

ALMA MATER STUDIORUM  
UNIVERSITÀ DI BOLOGNA

---

DOTTORATO DI RICERCA IN  
MONITORAGGIO E GESTIONE DELLE STRUTTURE E  
DELL'AMBIENTE - SEHM<sup>2</sup>

INTELLIGENT SENSOR SYSTEMS  
FOR STRUCTURAL HEALTH  
MONITORING APPLICATIONS

*Settore concorsuale: 09/E3 - Elettronica*

*Settore Scientifico Disciplinare: ING-INF/01 - Elettronica*

*Presentata da:*

Federica Zonzini

*Supervisore:*

Prof. Ing. Luca De Marchi

*Coordinatore Dottorato:*

Prof. Ing. Alessandro Marzani

*Co-supervisore:*

Prof. Ing. Alessandro Marzani

In reference to IEEE copyrighted material which is used with permission in this thesis, the IEEE does not endorse any of University of Bologna's products or services. Internal or personal use of this material is permitted. If interested in reprinting/republishing IEEE copyrighted material for advertising or promotional purposes or for creating new collective works for resale or redistribution, please go to [http://www.ieee.org/publications\\_standards/publications/rights/rights\\_link.html](http://www.ieee.org/publications_standards/publications/rights/rights_link.html) to learn how to obtain a License from RightsLink.

Federica Zonzini: *Intelligent Sensor Systems for Structural Health Monitoring Applications*, Dissertation for the degree of Doctor of Philosophy in Structural and Environmental Health Monitoring and Management (SEHM2), © February 2022

Intelligent Sensor Systems  
Structural Health Monitoring  
Embedded Signal Processing  
Vibration Diagnostics  
Guided Waves–based Digital Communications  
Acoustic Emission Monitoring



Dedicated to the loving memory of Ernesto.



## ABSTRACT

---

The convergence between the recent developments in sensing technologies, data science, signal processing and advanced modelling has fostered a new paradigm to the Structural Health Monitoring (SHM) of engineered structures, which is the one based on *intelligent sensors*, i.e., embedded devices capable of stream processing data and/or performing structural inference in a self-contained and near-sensor manner.

To efficiently exploit these intelligent sensor units for full-scale structural assessment, a joint effort is required to deal with instrumental aspects related to signal acquisition, conditioning and digitalization, and those pertaining to data management, data analytics and information sharing.

In this framework, the main goal of this Thesis is to tackle the multi-faceted nature of the monitoring process, via a full-scale optimization of the hardware and software resources involved by the SHM system. The pursuit of this objective has required the investigation of both: i) transversal aspects common to multiple application domains at different abstraction levels (such as knowledge distillation, networking solutions, microsystem HW architectures), and ii) the specificities of the monitoring methodologies (vibrations, guided waves, acoustic emission monitoring). The key tools adopted in the proposed monitoring frameworks belong to the embedded signal processing field: namely, graph signal processing, compressed sensing, ARMA System Identification, digital data communication and TinyML.

## SOMMARIO

---

La convergenza tra i recenti avanzamenti tecnologici nell'ambito dei sistemi di misura, dell'analisi dati e avanzate capacità di modellazione, ha promosso un nuovo paradigma per la valutazione di integrità strutturale (SHM) di strutture ingegnerizzate: quello basato su *sensori intelligenti*. Questi ultimi consistono in dispositivi embedded in grado sia di processare i dati in streaming che di verificare le condizioni di integrità strutturale in modo autonomo ed in stretta prossimità al punto in cui l'informazione strutturale viene misurata.

Per poter sfruttare efficientemente tali nodi sensore e fornire una diagnosi strutturale complessiva, è necessario uno sforzo implementativo congiunto in grado di far fronte sia ad aspetti strumentali - legati all'acquisizione, condizionamento e digitalizzazione dei segnali raccolti -, sia di garantire una opportuna gestione, elaborazione e condivisione dei dati acquisiti.

In tale contesto, scopo primario del presente lavoro di Tesi è quello di affrontare le diverse sfide aperte nel settore, mediante l'ottimizzazione complessiva delle risorse hardware e software del sistema di monitoraggio. Il raggiungimento di tale obiettivo ha richiesto l'analisi di: i) aspetti trasversali, comuni ai diversi domini applicativi, definiti a diversi livelli di astrazione (e.g., riduzione della complessità computazionale, definizione di nuove soluzioni di networking e comunicazione dati, microarchitetture di calcolo); ii) principi funzionali di diverse tecniche di ispezione (vibrazioni, onde guidate, emissioni acustiche). Gli strumenti chiave adottati nelle soluzioni proposte appartengono al campo dell'elaborazione del segnale con sistemi integrati: tra questi, la teoria del graph signal processing, la tecnica del compressed sensing, l'identificazione di sistemi dinamici basata su modelli ARMA, l'utilizzo di meccanismi di comunicazione digitale alternativi e l'implementazione di algoritmi di intelligenza artificiale a minimo costo energetico e computazionale (TinyML).



## LIST OF ACRONYMS

---

ADC	Analog-to-Digital
AE	Acoustic Emissions
AI	Artificial Intelligence
AIC	Akaike Information Criterion
AENN	Autoassociative Neural Network
APG	Adversarial Point Generator
AR	Autoregressive
ARMA	Autoregressive Moving Average
AR+Noise	Autoregressive with Noise
ARSNR	Average Reconstruction Signal-to-Noise-Ratio
ARX	Autoregressive with eXogenous Input
ASK	Amplitude Shift Keying
BER	Bit-error rate
BLE	Bluetooth Low Energy
BIC	Bayesian Information Criterion
BPSK	Binary Phase Shift Keying
BSS	Blind Source Separation
CAN	Controller Area Network
CapsNet	Capsule Neural Network
CapsNetToA	CapsNet-driven ToA estimator
CDM	Code Division Multiplexing
CF	Complementary Filters
CFRP	Carbon-fiber reinforced plastics
CH	Cluster Head
CNN	Convolutional Neural Network
COLA	Constant-Overlap-Add
CoSaMP	Compressive Sampling Matching Pursuit
CPSD	Cross-Power Spectral Density
CR	Compression Ratio
CS	Compressed Sensing
DCT	Discrete Cosine Transform
DFT	Discrete Fourier Transform
DL	Deep Learning

DoF	Degree of Freedom
DoP	Data-over-Power
DP	Dip Picking
DSP	Digital Signal Processing
DSS	Direct Spread Spectrum
DToA	Difference Time of Arrival
EOP	Enrивonmental and Operational
eS-TSQR	Embedded S-TSQR
eS-TSQR-OLS	Embedded Sequentail Tall-Skinny QR Decomposition for OLS
ERA	Eigensystem Realization
FDD	Frequency Domain Decomposition
FDM	Frequency Division Multiplexing
FEM	Finite Element Model
FFT	Fast Fourier Transform
FIR	Finite Impulse Response
FPU	Floating Point Unit
FRF	Frequency Response Function
FSAT	Frequency steerable acoustic transducers
FSK	Frequency Shift Keying
GSP	Graph Signal Processing
GW	Guided Waves
HR	Hannann-Rissanen
HW	Hardware
IHT	Iterative Hard Thresholding
IIR	Infinite Impulsive Response
IMU	Inertial Measurement Unit
ISD	Itakura-Saito Spectral Divergence
IoT	Internet of Things
LDO	Low-dropout
LDTR	Low-depth Time Reversal
MAC	Modal Assurance Criterion
MRak-CS	Model-assisted Rak-CS
MCU	Microcontroller Unit
MEMS	Micro Electro-Mechanical Systems
MIMO	Multiple-In Multiple-Out
MISO	Multiple-In Single-Out

ML	Machine Learning
MTA	Memory-per-Time-over-Accuracy
NExT	Natural Excitation Technique
NN	Neural Network
OCC	One Class Classification
OCCNN	One Class Classification Neural Network
OFDM	Orthogonal Frequency Division Multiplexing
OOK	On-off keying
OLA	Overlap-Add
OLS	Ordinary Least Squares
OMA	Operational Modal Analysis
OMP	Orthogonal Matching Pursuit
PAM	Pulse Amplitude Modulation
PCA	Principal Component Analysis
PDF	Probability Density Function
PoSER	Post Separate Estimation Re-scaling
PP	Peak Picking
PPM	Pulse Position Modulation
PSD	Power Spectral Density
PSM	Power Saving Mode
PSN	Peripheral Sensor Node
PSNR	Peak Signal-to-Noise Ratio
PZT	lead zirconate titanate
QAM	Quadrature Amplitude Modulation
QPSK	Quadrature Phase Shift Keying
QR-OLS	QR for Ordinary Least Squares
Rak-CS	Rakeness-based CS
RAM	Random Access Memories
RDT	Random Decrement Technique
ReLU	Rectified Linear Unit
RMSE	Root Mean Square Error
SAN	Sensor Arena Network
SOBI	Second Order Blind Identification
SHM	Structural Health Monitoring
SN	Sink Node
SNR	Signal-to-Noise Ratio

SSI	Stochastic Subspace Identification
SSI-COV	Covariance-driven Stochastic Subspace Identification
SSI-DATA	Data-driven Stochastic Subspace Identification
STSM	Statistical Time Series Models
S-TSQR	Sequential Tall-Skinny QR
SVD	Singular Value Decomposition
SysId	System Identification
SysId2FDD	SysId-to-FDD algorithm
SW	Software
TDD	Time Domain Decomposition
TinyML	Tiny Machine Learning
TF	Tensorflow
TFLite	Tensorflow Lite
ToA	Time of Arrival
TR	Time reversal
USB	Universal Serial Bus
VoI	Value of Information
WT	Wavelet Transform
WPT	Wavelet Packet Transform
X-Corr	Cross-Correlation
XCVR	Tranceiver

# CONTENTS

---

1	INTRODUCTION	1
1.1	Background and motivation	1
1.1.1	Application perspectives and open issues	2
1.2	Thesis objectives	4
1.3	Thesis organization and contributions	4
<b>I</b>	<b>EDGE COMPUTING SOLUTIONS FOR VIBRATION-BASED DIAGNOSTICS</b>	<b>9</b>
2	A GENTLE INTRODUCTION TO VIBRATION-BASED SHM	11
2.1	Introduction	11
2.2	Review of OMA-driven feature extraction algorithms	13
2.2.1	Frequency-based methods	13
2.2.2	Time-based methods	16
2.3	Review of OMA-based damage detection algorithms	23
3	MODE SHAPE ASSEMBLY FOR CLUSTERED ARCHITECTURES: A GRAPH SIGNAL PROCESSING PERSPECTIVE	27
3.1	Introduction	27
3.2	Network topology for OMA	28
3.3	GSP-driven cluster-based modal analysis	30
3.3.1	Mode shape assembly for overlapped clusters: the PoSER approach	32
3.3.2	Mode shape assembly for non-overlapped clusters: the GSP-driven approach	32
3.4	Experimental validation	34
3.4.1	SHM network description	35
3.4.2	The use case: a simply supported steel beam	36
3.4.3	Results	38
3.5	Conclusions	40
4	DATA COMPRESSION FOR VIBRATION-BASED SHM	43
4.1	Introduction	43
4.2	Comparative analysis of data compression techniques for OMA	44
4.2.1	Spectral-based decomposition	44
4.2.2	Compressed Sensing	44
4.2.3	Principal Component Analysis	47
4.2.4	Additional methods	47
4.3	Physics-based CS for vibration-based SHM	48
4.3.1	Designing the optimal sensing matrix: From Rak-CS to MRak-CS	49
4.3.2	Designing the optimal sparsity basis: a structurally-shaped approach	54
4.4	MRak-CS and WPT sparsity basis: experimental validation	58
4.4.1	The use case: a simply supported steel beam	59
4.4.2	Results	61
4.5	From CS to CS-enabled SHM: an EDGE COMPUTING PERSPECTIVE	66
4.5.1	Design criteria for the CS coder/encoder block	68
4.5.2	CS at the extreme edge: an experimental validation	69
4.5.3	CS vs Noise in MEMS sensors	73

4.5.4	CS vs noise: an experimental validation . . . . .	74
4.6	Conclusions . . . . .	76
5	SYSTEM IDENTIFICATION AT THE EXTREME EDGE FOR NETWORK LOAD REDUCTION	79
5.1	Introduction . . . . .	79
5.2	Estimating Model parameter at the edge: from OLS to S-TSQR-OLS . . . . .	80
5.2.1	The OLS formulation . . . . .	80
5.2.2	From OLS to QR decomposition . . . . .	81
5.2.3	From QR to Sequential Tall-skinny QR decomposition . . . . .	82
5.2.4	Wrapping up: the eS-TSQR-OLS approach . . . . .	83
5.3	Prototyping SysId at the extreme edge . . . . .	85
5.3.1	Materials . . . . .	85
5.3.2	Algorithmic validation . . . . .	85
5.3.3	Execution time . . . . .	86
5.3.4	Structural validation . . . . .	88
5.3.5	The case study: a Windspot blade wind turbine . . . . .	88
5.3.6	Including the effect of instrumental noise . . . . .	88
5.3.7	Results . . . . .	88
5.4	Cost-benefit analysis . . . . .	90
5.4.1	Quantifying energy consumption in IoT applications . . . . .	90
5.4.2	Results . . . . .	91
5.5	Local-to-global mode shape reconstruction for SysId-based data compression	92
5.5.1	The SysId2FDD algorithm . . . . .	94
5.5.2	Experimental validation . . . . .	96
5.6	Conclusions . . . . .	99
6	FROM ML TO TINYML-ENABLED VIBRATION DIAGNOSTICS	101
6.1	Introduction . . . . .	101
6.2	From raw data to anomaly detection . . . . .	102
6.2.1	Structural identification . . . . .	102
6.2.2	Neural Network design . . . . .	104
6.3	Experimental validation: the Z24 bridge case study . . . . .	106
6.3.1	From CS to feature tracking . . . . .	106
6.3.2	Neural network models . . . . .	108
6.3.3	Noise density in MEMS accelerometers . . . . .	108
6.3.4	Results . . . . .	109
6.3.5	Effect of NN distillation . . . . .	110
6.4	Running structural inference at the extreme edge: a TinyML approach . . . . .	112
6.4.1	TinyML for vibration diagnostics . . . . .	112
6.4.2	Experimental validation . . . . .	113
6.5	Conclusions . . . . .	114
7	DATA FUSION TECHNIQUES FOR VIBRATION-BASED SHM	117
7.1	Introduction . . . . .	117
7.2	Prototyping A tilt Sensor Node Embedding a Data-Fusion Algorithm . . . . .	118
7.2.1	Combining accelerations and angular velocities via CF . . . . .	119
7.2.2	Embedding tilt estimation on edge devices . . . . .	120
7.2.3	Prototyping and Experimental validation . . . . .	123
7.3	Heterogeneous Sensor Network for PZT-driven modal analysis . . . . .	127

7.3.1	Piezoelectric technology for modal analysis . . . . .	127
7.3.2	MEMS and low-cost PZT discs for modal analysis: a physical relationship . . . . .	128
7.3.3	PZT-driven modal analysis for damage detection . . . . .	133
7.4	Conclusions . . . . .	138
<b>II</b>	<b>GUIDED WAVES-BASED DATA COMMUNICATION SYSTEMS</b>	<b>141</b>
<b>8</b>	<b>GW-BASED FOR DIGITAL DATA TRANSFER</b>	<b>143</b>
8.1	Introduction . . . . .	143
8.2	Fundamentals of Lamb waves . . . . .	145
8.3	Overview of GWs-based data communication systems . . . . .	146
<b>9</b>	<b>FREQUENCY DIVISION MULTIPLEXING FOR LOW-POWER MIMO COMMUNICATION AT THE EDGE</b>	<b>151</b>
9.1	Introduction . . . . .	151
9.2	Physics-informed carrier frequency selection . . . . .	152
9.2.1	Joint optimization of the square-wave excitation-sequence length . . . . .	153
9.3	Experimental validation . . . . .	154
9.3.1	Materials and methods . . . . .	155
9.3.2	Carrier frequency selection . . . . .	156
9.3.3	Impact of structural irregularity . . . . .	157
9.3.4	Impact of excitation-sequence length on the bit reconstruction accuracy . . . . .	159
9.4	Conclusions . . . . .	160
<b>10</b>	<b>DIRECT SPREAD SPECTRUM MODULATION AND DISPERSION COMPENSATION FOR GWS-BASED COMMUNICATION</b>	<b>161</b>
10.1	Introduction . . . . .	161
10.2	Dedicated processing flow for CDM-based and dispersion compensated transmission with GWs . . . . .	162
10.2.1	Direct Spread Spectrum pulse coding . . . . .	162
10.2.2	Dispersion compensation . . . . .	163
10.3	Experimental validation . . . . .	164
10.3.1	Materials and methods . . . . .	164
10.3.2	Results . . . . .	165
10.4	Conclusions . . . . .	166
<b>11</b>	<b>LOW-DEPTH TIME REVERSAL AND PULSE POSITION MODULATION TECHNIQUE FOR ULTRASONIC COMMUNICATION</b>	<b>167</b>
11.1	Introduction . . . . .	167
11.2	Detailing the Low-depth TR-Pulse Position Modulation scheme . . . . .	168
11.3	Experimental Validation . . . . .	171
11.3.1	Materials and Methods . . . . .	171
11.3.2	Results . . . . .	172
11.4	Conclusions . . . . .	175
<b>12</b>	<b>FREQUENCY STEERABLE ACOUSTIC TRANSDUCERS AND QUADRATURE AMPLITUDE MODULATION</b>	<b>177</b>
12.1	Introduction . . . . .	177
12.2	QAM signal processing for GWs propagation in isotropic plates . . . . .	178
12.3	Experimental validation . . . . .	180

12.3.1	Materials and Methods . . . . .	180
12.3.2	Results . . . . .	181
12.4	Conclusions . . . . .	186
<b>III ENHANCING ACOUSTIC EMISSION-BASED MONITORING VIA DEEP LEARNING</b>		187
13	ARTIFICIAL INTELLIGENCE ALGORITHMS FOR TIME OF ARRIVAL ESTIMATION IN ACOUSTIC EMISSION SIGNALS . . . . .	189
13.1	Introduction . . . . .	189
13.1.1	The problem of ToA estimation: from statistical methods to machine learning . . . . .	190
13.2	DL Models for ToA estimation . . . . .	191
13.2.1	Convolutional Neural Network . . . . .	191
13.2.2	Capsule Neural Network . . . . .	194
13.3	Experimental validation: a numerical framework . . . . .	198
13.3.1	Dataset generation . . . . .	198
13.3.2	Performance metrics . . . . .	200
13.3.3	Results . . . . .	201
13.4	Experimental validation: ToA for acoustic source localization . . . . .	203
13.4.1	Materials . . . . .	203
13.4.2	Methods . . . . .	204
13.4.3	Results . . . . .	208
13.5	Conclusions . . . . .	211
14	CONCLUSIONS, ONGOING RESEARCH AND FUTURE OUTLOOKS . . . . .	213
14.1	Main conclusions of Part i . . . . .	213
14.2	Main conclusions of Part ii . . . . .	215
14.3	Main conclusions of Part iii . . . . .	217
14.4	Ongoing research activities . . . . .	218
14.4.1	Objective 1: Tackling open issues . . . . .	218
14.4.2	Objective 2: Designing a custom monitoring network . . . . .	219
14.4.3	Objective 3: Testing the processing framework on real scenarios . . . . .	219
14.5	Future outlooks . . . . .	219
<b>IV APPENDIX</b>		221
A	THE ISSLAB SENSOR NETWORK . . . . .	223
A.0.1	Communication layer . . . . .	223
A.0.2	Sensor node architecture . . . . .	224
A.0.3	Sensing layer . . . . .	225
A.0.4	Sensor network interface . . . . .	227
<b>BIBLIOGRAPHY</b>		231



## LIST OF FIGURES

Figure 1	General overview of a SHM system, from the hardware up to the software layers. . . . .	2
Figure 2	Current challenges in state-of-the-art monitoring networks. . . . .	3
Figure 3	Graphical description of the thesis organization. . . . .	5
Figure 4	OMA-based processing flow for a toy structure: the quantities $f_p$ and $\Phi_p$ ( $p = 1, 2, 3$ ) indicate the natural frequencies of vibration and the associated mode shapes, respectively. [©2021 IEEE] . . . . .	12
Figure 5	Schematic representation of the FDD processing flow, from data collection up to modal parameter extraction. . . . .	15
Figure 6	Formulation of input-output (ARX) and output-only (AR, ARMA, AR+Noise) parametric models. . . . .	18
Figure 7	Schematic representation of the SSI-COV processing flow, from data collection up to modal parameter extraction. . . . .	20
Figure 8	Schematic representation of the SOBI processing flow, from data collection up to modal parameter extraction. . . . .	23
Figure 9	System topology for OMA-based SHM architectures: (a) centralized, (b) stand-alone and (c) divide-and-conquer scheme. . . . .	29
Figure 10	Schematic representation of the proposed cluster-based and Graph Signal Processing (GSP)-driven monitoring architecture for vibration analysis. [©2020 IEEE] . . . . .	31
Figure 11	Mapping between modal-related quantities and graph domain. Graph signal properties depend on the Adjacency and Degree matrices, whose entries are uniquely determined by the chosen edge weights $w_{n_a n_b}$ . . . . .	33
Figure 12	Topology of the monitoring network deployed for the validation of the GSP-based mode shape assembly algorithm. [©2020 IEEE] . . . . .	35
Figure 13	Experimental setup with two clusters of sensors (red and blue-labelled chains): overlapping networks in correspondence of node $A_5$ (case $O_v$ ) and non-overlapping (case A, B, C, D) configurations. Unhealthy conditions were induced by means of a concentrated roving mass laterally hanged at positions $x_{a,1}$ , $x_{a,2}$ , $x_{a,3}$ . [©2020 IEEE] . . . . .	38
Figure 14	Spectra of signals acquired with sensor cluster $C_1$ (top graph) and $C_2$ (bottom graph). The damaged configuration (continuous line) corresponding to operating conditions perturbed with additive mass $m_a = 2.591$ kg at $x_a = 400$ mm is superimposed to the nominal case (dotted line). Numerical predictions in both situations are also included.[©2020 IEEE] . . . . .	39

Figure 15	Assembled mode shapes for the altered beam with additive mass $m_a = 2.591$ kg at $x_{a,2}$ under non-overlapped configuration of case C. Raw modal coordinates are extracted by means of the FDD reconstruction method. Theoretical predictions in nominal (NP) and damaged status (DP) are also provided. [©2020 IEEE] . . . . .	41
Figure 16	Schematic representation of the CS encoding (green) and decoding (blue) operations. . . . .	46
Figure 17	General processing flow at the basis of the MRak-CS approach. The computation starts with the selection of the frequency regions of interest, as they can be predicted by a numerical model or zero-time structural campaigns, on the basis of which a band—pass-like correlation profile of the structure ( $C^y$ ) is synthetically designed. Then, the CS-based problem is entered by firstly extracting the sensing matrix correlation profile ( $C^S$ ). Hence, the latter value is used to sample each row of the sensing matrix $S$ from a multivariate Gaussian distribution with zero mean and correlation profile equal to $C^S$ . . . . .	50
Figure 18	Spectral profiles of the Rak-CS (red) and MRak-CS (blue) compression matrices superimposed to the energy distribution of the input signal (black curve). [©2021 IEEE] . . . . .	51
Figure 19	Model-assisted Rak-CS (MRak-CS) correlation matrices in case closely spaced modes (green diamond markers) falling in the same frequency bin need to be identified. . . . .	52
Figure 20	MRak-CS reconstructed PSD for two different working conditions of the Z24 bridge (subplots (a) and (b)). Diamond markers are used to highlight the location of the estimated structural peaks on the basis of a properly tuned FEM analysis: yellow, magenta and green colors indicate lateral, bending and torsion/bending modes, respectively. In both subplots, the blue dotted line depicts the sensing matrix correlation profile used in the MRak-CS method. Finally, the red dotted and blue continues lines represent the raw signal (i.e. compression-free) and CS-recovered spectrum for $CR = 4$ , respectively. . . . .	53
Figure 21	Depiction of the filtering procedure at the basis of WPT. . . . .	55
Figure 22	WPT sparsity basis for the Z24 bridge with different frequency resolution: coarser resolution (left) with $j = 4$ corresponding to $\Delta_f = 1.56$ Hz and finer resolution (right) with $j = 6$ corresponding to $\Delta_f = 0.39$ Hz. Reference frequency components are also enclosed to identify how the frequency bins are distributed with respect to the predicted structural modes. . . . .	58
Figure 23	CPSD profile of CS-reconstructed signals in nominal structural condition for the Z24 bechmark use-case: a coarser (cyan color line) and finer (blue colorline) WPT sparsity basis depicted in Fig. 22 are considered and superimposed to the raw spectrum profile (red dotted line). . . . .	59

Figure 24	Experimental setup for MRak-CS testing purposes: sensor installation plan (all dimensions in millimeters) inclusive of the damaging mechanism and positions. [©2021 IEEE] . . . . .	60
Figure 25	Trends in Gini index for WPT (red) and DCT (blue) transformed acceleration coefficients over different signal instances, superimposed to the normalised and rescaled signal energy (black curve) in the original time domain. Results are presented for sensing positions $S_1, S_2, S_3$ . [©2021 IEEE] . . . . .	62
Figure 26	Correlation profile of the CPSD matrix for the considered compression methodologies as a function of increasing CR values in nominal (top line) and altered (bottom line) conditions. Yellow markers are also included in order to better track identify the frequency shift experienced by the third vibration mode. [©2021 IEEE] . . . . .	64
Figure 27	Typical CS-enabled clustered architecture for vibration-based SHM. From left to right, the compression/decompression stages are allocated to the PSNs and the CHs, respectively. Then, the pure modal analysis is performed, firstly identifying cluster-related mode shapes $\Phi_{C_z}$ and then merging the local estimates into a full-scale mode shape matrix $\Phi$ . Finally, the current health status can be inferred by monitoring trends in MAC values over time. [Adapted from ©2021]	67
Figure 28	Cost analysis for the considered recovery algorithm. In the left-hand side, memory occupancy, execution time and ARSNR are displayed from top to the bottom. The MTA product between the three curves per CR is conversely displayed in the right panel. [©2021 Springer] . . . . .	71
Figure 29	Experimental testbed and related sensor installation plan, comprising two clusters (C1 and C2, respectively) of six accelerometers. An inset depicting the practical connection of three PSNs is also enclosed. [©2021 Springer] . . . . .	72
Figure 30	Left: trend in MAC values between CS-reconstructed and compression-free full-scale modal shapes as a function of the compression ratio, superimposed to the chosen accuracy level indicated by the black-dotted line at 90%. Red-rumbled, green-rounded and blue-squared line styles refer to the first, second and third modal shape, respectively. Right: reconstructed full-scale modal shapes for a representative selection of CR values. [©2021 Springer] . . . . .	72
Figure 31	Trends in MAC value as a function of different PSNR values for increasing compression factors. Each line refers to a different CR value (from bottom to the down, CR = 4, CR = 6 and CR = 10, respectively) while each column corresponds to one of three reconstructed modal shapes. Results deriving from structural simulations (continuous line) are superimposed to those pertaining to in-field measurements (squared markers). The black dotted line indicate the structural accuracy level, i.e., MAC value greater than 0.95. [©2021 IEEE] . . . . .	76
Figure 32	Processing flow at the basis of the S-TSQR decomposition approach adopted in this work for the sake of matrix dimension reduction. . . . .	83

Figure 33	eS-TSQR-OLS processing flow for model parameter estimation. From left to right: once signals have been acquired (step 1), the eS-TSQR decomposition process is entered and repeated $N_{ch}$ times: at each $i$ -th iteration, the regression matrix is firstly created as stated in Table 3 by selecting the proper signal frame (step 2.a), each comprising a sliding window of $N/N_{ch}$ samples at step size equal to the number of parameters $N_p$ . Then, the Householder decomposition of $Z_i$ is applied (step 2.b), paving the way for the subsequent update of the coefficient vector $\check{Y}$ . At the end of the $N_{ch}$ -th cycle, the upper triangular matrix $R_{N_c}$ and $Y_{N_{ch}}$ are used in the SysId phase to compute the model parameters $\beta$ (step 3.a) and the residual noise density $\sigma_e^2$ (step 3.b). The finite set of $N_p$ quantities can, thus, be transmitted at the receiving side, where the spectrum profile $S_y(f)$ of the acquired signal can be reconstructed and the sensor-related modal information are then extracted (e.g. the peak spectral values $f_p$ ). . . . .	84
Figure 34	Execution time for ARMA (blue scale curves) and AR (red scale curves) model running on STM32L5 MCU under different $N_p$ and $N_{s1p}$ configurations. . . . .	87
Figure 35	Spectra of the wind turbine blade working at the reference temperature of +25 °C under progressive damage tests (left), while the effects of temperature changes are underlined in the right hand image for the damage-free status. Signals at higher density levels, characterised by a smoother profile, are obtained by SysId running on sensor, whereas the ones appearing at the bottom part are computed by standard Welch's method for PSD. . . . .	89
Figure 36	Total energy expenditure with one hour duty-cycle for different IoT protocols, taking into account expenditure due to data processing and outsourcing. The acquisition of triple-channel signals are assumed with $N_{s1p} = 45$ , while sweeping $N_p$ in the interval [9, 57] (depicted with different markers). Three different background colors are used to indicate different data compression scenarios: SysId-based processing (blue), CS-based processing (gray) and compression-free (green). Missing points mean that the corresponding payload in the given Tx time is not supported by the corresponding protocol. . . . .	92

Figure 37	Typical SysId-enabled clustered architecture for vibration-based SHM. From left to right, the SysId local identification is allocated to the PSNs which transmit their related model parameters to the CH unit where global modal identification is performed through SysId2FDD. The latter is formulated as follows: firstly, the FRF associated to each $i$ -th node ( $H_{y_i}(f)$ ) is computed and passed as input for the calculation of the CPSD matrix, directly in the frequency domain. The absolute value $ \Phi $ of the mode shape matrix is retrieved via standard FDD, whilst the corresponding sign vector $\eta_i$ per given sampling position is yielded by the DP method applied to $H_{y_i}$ . The actual mode shapes corresponds to $\Phi = \eta \odot  \Phi $ . Finally, the Sink Node (SN) provides the sought structural bulletin via analysis of the aggregated information. . . . .	94
Figure 38	Rendering of the five-storey shear frame located at the research lab of the University of Bologna and relative sensor installation plan: two different sensor clusters (red and green colors) and one CH device (black box). An insight about the sensor-to-structure bolting is also enclosed, as well as labels indicating the beam removed during testing. . . . .	97
Figure 39	Color-map of the waterfall plot obtained from the cascade of PSD spectra as computed by ARMA parameters for different structural configurations of the five-storey frame. . . . .	98
Figure 40	Proposed framework for structural assessment: from left to right, data compression and recovery, modal feature extraction and selection with the final structural assessment block. The matrix $\hat{Y}$ is used to indicate the ensemble of CS-reconstructed signals from all the different acquisition points, as it is required by OMA algorithms to provide a global understanding of the structure under analysis. . .	103
Figure 41	General scheme of an AENN architecture. . . . .	106
Figure 42	General scheme of the OCCNN-driven monitoring framework adopted for the structural assessment of the Z24 bridge. A graphical description of OCCNN is provided at step 4 under the label "Structural assessment". . . . .	107
Figure 43	First (a) and second (b) frequency component vs temperature. . . .	108
Figure 44	Performances of OCCNN and AENN reference models with (TO,TA) and without ( $O_A, A_1$ ) temperature input values, for compression-free configurations. . . . .	110
Figure 45	Feature space distribution with compression-free (a) and CS-based (b) processing framework. . . . .	111
Figure 46	Sequence of steps to be implemented to transform a generic NN architectures from cloud/server-based Tensorflow programming to MCU-compliant ML models passing through Tensorflow Lite quantization. . . . .	114
Figure 47	Geometric relationship between tilt angles $\theta$ and accelerations along the z-direction for a device installed on the top of a structure. . . .	120
Figure 48	Schematic representation of signal processing method necessary to estimate tilt values from accelerations and angular velocities. . . .	121

Figure 49	Adopted OLA window necessary to shrink the computational burden of the data fusion algorithm while running on sensor: (a) Time-domain working principle of the OLA mechanism and (b) window spectral properties for overlapping fraction spanning in the interval $[0.1;0.5]$ . . . . .	121
Figure 50	Effect of proper cutoff frequency selection for OLA-based sensor data fusion (actual tilt value: $30^\circ$ ). . . . .	124
Figure 51	Experimental setup in pseudo-static conditions: anti-vibration table equipped with TUV level. . . . .	125
Figure 52	Comparison of spectra (obtained with FFT) resulting from the windowed and non-windowed approach with respect to the spectral content of radial acceleration. . . . .	126
Figure 53	(a) Effect of signal fusion in time and frequency domain and (b) Comparison of PSD profiles for tilt signals estimated by nodes located at different positions of the beam. . . . .	127
Figure 54	Experimental setup comprising one piezoelectric transducer connected to a piezoelectric sensor node (PZT) and a tri-axial Micro Electro-Mechanical Systems (MEMS) accelerometer (ACC) installed on a cantilever beam. [©2019 IEEE] . . . . .	129
Figure 55	Dynamic response of a cantilever beam induced by an additive mass. Signals acquired in time domain on each channel of a piezoelectric sensor node and a MEMS accelerometer (top) placed in the same position. [©2019 IEEE] . . . . .	130
Figure 56	Comparison between PZT and ACC averaged envelopes: original signals (top) and normalized acceleration time-derivative superimposed to normalized PZT signals (bottom). [©2019 IEEE] . . . . .	131
Figure 57	First order electrical model of a PZT sensor. ©2019 IEEE . . . . .	131
Figure 58	Comparison between spectral trend of $a_z$ acceleration signal (top) and $ch_1$ PZT sensor (bottom) computed with different processing techniques. [©2019 IEEE] . . . . .	132
Figure 59	Experimental setup deployed on a simply supported steel beam, with one gateway (GW, in magenta), five MEMS accelerometers (ACC red devices) and akin PZT transducers (blue ones) connected to two PZT sensor nodes (green ones). The light-grey wiring lines identify the PZT transducer-to-sensor connections, whereas the blue ones refer to the sensor-to-sensor communication cables. Four different positions $x_1, x_2, x_3, x_4$ were considered to simulate the presence of crack-like faults by means of hanged masses. [©2019 IEEE] . . . . .	133
Figure 60	A comparison of spectral trends resulting from ACC (red lines, circle markers) and PZT (green lines, triangle markers) signals in nominal (dotted lines, blue markers) and altered (solid lines, yellow markers) conditions. Data were acquired in correspondence of the mid-span. [©2020 IEEE] . . . . .	134

Figure 61	Relative error $\varepsilon_p$ between AR+Noise-driven experimental estimation and numerical prediction obtained in nominal and damaged conditions; from left to right: first, second, and third natural frequency of vibration. [Adapted from ©2020 IEEE] . . . . .	135
Figure 62	Processing flow adopted for PZT-based damage detection purposes. In the left column, the zero-time validation in nominal conditions comprising (1) the extraction of both the ACC and PZT raw mode shapes, (2) the PZT mode shape scaling factors estimation built on a (2.a) leave-one-out tuning procedure and (2.b) a final structural validation of the reconstructed PZT mode shapes. Procedures in the right column refer to the on-condition assessment in damaged configurations, where the previously estimated tuning factors (step 2.a) are employed to re-scale (step 4) the currently obtained raw PZT mode shapes (step 3); the comparison with reference values (step 5) is performed to notify damage alarms in case of occurrence. . . . .	137
Figure 63	Exemplary description of the principles enabling GW-based wireless data transfer in SHM applications. Beside the punctual structural inspection capabilities peculiar to GWs, the complementary ability of smart sensors/transducers to on-board process and generate signals can be exploited for cable-free data sharing among the players of the SHM network itself. . . . .	144
Figure 64	Dispersion curves for an aluminum square plate with 1 mm thickness: (a) phase velocity and (b) group velocity. . . . .	145
Figure 65	Performance comparison of GWs-based communications systems	148
Figure 66	Experimental setup and relative communication distances: top (a) and (b) lateral view of the CFRP with highlighted stiffener geometry; top view of the aluminum plate. . . . .	155
Figure 67	Spectra of the cumulative normalized intensity (arbitrary unit in the vertical axis) in the received signals and magnification with bold vertical lines indicating the selected frequency carriers. The transmission of two complementary messages is shown: 0100 and 1011 in the first and second line, respectively, while the column on the left is for the metallic plate and the one on the right pertains to the CFRP element. [©2020 IEEE] . . . . .	158
Figure 68	Average BER as a function of excitation-sequence length and data rate per frequency for the (a) aluminum and (b) CFRP structure. [©2020 IEEE] . . . . .	160
Figure 69	Overview of the processing flow adopted for CDM-oriented communication systems exploiting elastic waves. Beside modulation and demodulation steps which are performed according to classical DSS modulation principles, a compensation procedure is inserted to account for the detrimental effects of dispersion. . . . .	163
Figure 70	Experimental setup for CDM communication tests over a slender aluminum beam. Five different inter-communicating distances were considered, whereas the amplitude of the actuated signal was regulated by means of a waveform generator. . . . .	164

Figure 71	BER trends for the CDM-based and dispersion compensated communication scenario as functions of input voltages and distances. [©2019 IEEE] . . . . .	165
Figure 72	Received signals related to the transmission of a CDM-modulated single bit while (a) decreasing the amplitude of the actuated pulses with fixed communication distance of 105 cm and (b) increasing the inter-communication distance at a constant supplied voltage of 1 V.	166
Figure 73	Proposed four stages low-depth TR-PPM scheme. [©2020 IEEE]	168
Figure 74	Details of the two-way handshake LDTR-PPM communication scheme extending the description provided in Fig. 73. The channel index is dropped to simplify notation. . . . .	170
Figure 75	LDTR-PPM communication: simulated experimental setup with underlined communication distances. . . . .	171
Figure 76	TR-PPM. Low-depth thresholded version of the received Gaussian probe signal $p_r(t)$ travelling along the communication link TX <sub>3</sub> -RX for different quantization functions. [©2020 IEEE] . . . . .	173
Figure 77	LDTR-PPM. Average BER for increasing bit rate and varying thresholding procedures with Gaussian probe signal. [©2020 IEEE] . . .	174
Figure 78	Block diagram of the adopted QAM-based communication framework, specifically modelling the effects of wave dispersion. A schematic representation of the FEM model used to validate the frequency directivity of FSATs is also enclosed. . . . .	178
Figure 79	Radiation pattern and wavefield snapshot for (a) 130 kHz and (b) 150 kHz carrier frequency obtained with FEM simulation of the FSAT.	181
Figure 80	Simulation results for QAM with 150 kHz carrier frequency. Top left: normalized transmitted (blue) and received (red) signals for 8 bit symbols. Bottom left: FFT of the received signal. Right: original (blue circular markers) and demapped (red star) symbol constellation. . . . .	182
Figure 81	Simulation results for QAM with 130 kHz carrier frequency. Top left: normalized transmitted (blue) and received (red) signals for 8 bit symbols. Bottom left: FFT of the received signal. Right: original (blue circular markers) and demapped (red star) symbol constellation. . . . .	184
Figure 82	Simulation results for QAM with 150 kHz carrier frequency and SNR = 0 dB. Top left: normalized transmitted (blue) and received (red) signals for 8 bit symbols. Bottom left: FFT of the received signal. Right: original (blue circular markers) and demapped (red star) symbol constellation. . . . .	185
Figure 83	Proposed small CNN for ToA estimation from 5000-long time series. The quantities reported in the blue and pink boxes indicate the dimensions of the output features of the corresponding layer. .	193
Figure 84	Proposed small CNN for ToA estimation. The quantities reported in the blue and pink boxes indicate the dimensions of the output features of the corresponding layer. . . . .	194
Figure 85	Proposed CapsNetToA architecture for ToA estimation. . . . .	197



Figure 86	Example of synthetic signals generated with the ray–tracing algorithm. . . . .	200
Figure 87	RMSE error for ToA estimation on synthetic test dataset for varying SNRs. (left) Pre–trigger window used for training (i.e., pre–trigger window lower than 2500 samples) and (right) Increased pre–trigger window. . . . .	201
Figure 88	ToA predictions for AIC (blue), CNN (orange), CapsNetToA (red) and small CNN (green) with synthetic dataset: (left column) SNR = 30 dB and (right column) SNR = 10 dB, with second row depicting a magnified region of the time interval where ToA is located. . . .	202
Figure 89	Sensor deployment on a metallic laboratory plate for the sake of Acoustic Emissions (AE) source localization. . . . .	204
Figure 90	Geometrical representation of the adopted localization model via a three sensor array: the objective is to estimate the AE–to–sensor distance $d$ and its relative direction $\theta$ . . . . .	205
Figure 91	Ratios in the mean ( $R^\mu$ ) and standard deviation ( $R^\sigma$ ) of the absolute errors for ToA estimation in the framework of the laboratory metallic plate: (a) drill, (b) AWGN and (c) localization experiments. . . . .	208
Figure 92	Absolute errors for acoustic signal localization on a laboratory metallic plate under various noise levels. . . . .	209
Figure 93	ToA predictions for AIC (blue), CapsNetToA (red) and small CNN (green) for excitation point 5: (left column) SNR = 20 dB and (right column) SNR = 8 dB, with second row depicting a magnified region of the time interval where ToA is located. . . . .	210
Figure 94	Comparison between the GWs–based communication strategies implemented in this work and state–of–the–art companion alternatives. . . . .	217
Figure 95	Generic four building block architecture of the ISSLab sensor nodes [P4]. . . . .	224
Figure 96	lead zirconate titanate (PZT) transducer (left) with embedded pre–amplifier (right) and the lodging case (middle). . . . .	227
Figure 97	Schematic diagram of the SAN interface (a) and the relative prototype (b). . . . .	228

## LIST OF TABLES

---

Table 1	Summary of commonly adopted frequency domain–based algorithms for OMA, with highlighted characteristics and limitations. Algorithms are compared in terms of computational complexity ( $\searrow$ , $\rightarrow$ , $\nearrow$ indicate low, medium and high cost, respectively), mechanical properties of the target structure, architectural topology (Loc and Glob indicate edge–compliant and centralized solutions, respectively) and tolerated input noise levels (L, M and H indicate low, medium and high SNR, respectively). . . . .	14
---------	--	----

Table 2	Summary of commonly adopted time domain–based algorithms for OMA, with highlighted characteristics and limitations. Algorithms are compared in terms of computational complexity ( $\swarrow$ , $\rightarrow$ , $\nearrow$ indicate low, medium and high cost, respectively), mechanical properties of the target structure behavior and tolerated input noise levels (L, M and H indicate low, medium and high SNR, respectively). . . . .	16
Table 3	PSD functions corresponding to the ARX, AR/AR+Noise and ARMA parametric models. . . . .	19
Table 4	Summary of commonly adopted techniques for structural assessment: from conventional modal–related methods to AI–driven approaches. . . . .	26
Table 5	Relative error in FDD–driven natural frequencies estimation between experimental data and theoretical prediction for different scenarios. . . . .	40
Table 6	MAC values comparing numerical prediction and assembled mode shapes in presence of altered conditions with overlapped clusters (case $O_v$ -PoSER approach) and spatially independent clusters (case A, B, C, and D-GSP approach). . . . .	42
Table 7	Comparison between different methods for OMA–oriented data compression: $\checkmark$ and $\times$ indicate whether the corresponding strategy is implemented in an unsupervised or supervised manner, respectively. . . . .	45
Table 8	MAC values between compression free and MRak-CS reconstructed mode shapes with DCT and WPT sparsity basis (left and right column, respectively). . . . .	63
Table 9	MAC values between raw and reconstructed mode shapes for different structural configurations. From top to down group lines, RND–CS, PCA, Rak-CS and MRak-CS results. [©2021 IEEE] . . . .	65
Table 10	$\epsilon_p^{CS}$ between CS–reconstructed $f_p^{CS}$ and compression free $f_p^{Raw}$ modal frequencies for increasing CR values and various structural configurations. . . . .	66
Table 11	Regression matrix and model parameter vector for the ARX, AR and ARMA parametric models. . . . .	81
Table 12	ISD values (multiplied by $10^2$ ) for varying model order and number of samples per parameter. . . . .	86
Table 13	First six modal frequencies of the five–storey shear frame computed via SysId2FDD by averaging over the ten successive measurements per given structural configuration. . . . .	99
Table 14	Average MAC percentages ( $\mu_p$ ) and standard deviation ( $\sigma_p$ ) between FDD and SysId2FDD+DP reconstructed mode shapes for the laboratory five–storey frame. Different structural configurations are considered: nominal and B1, B2, B3–damaged scenarios. . . . .	99
Table 15	Mechanical features of the considered MEMS accelerometers types.	109
Table 16	Performance metrics of OCCNN models A, B, C, D with temperature input values and CS–processed configurations: beside the classical classification scores, the number of hyperparameters is enclosed.	111

Table 17	Performance metrics of OCCNN model while moving from cloud-based TF to Arduino: beside the classical classification scores, the overall complexity in terms of memory consumption, number of hyperparameters and execution time, are enclosed. . . . .	115
Table 18	Statistics obtained for tilt values in different pseudo-static configurations: mean value, relative error and standard deviation. . . . .	124
Table 19	Mean values $\mu$ and associated standard deviations $\sigma$ of MAC values obtained in nominal condition validation and damage detection assessment after applying the proposed PZT mode shapes tuning procedure. . . . .	138
Table 20	State-of-the-art of the most significant techniques employed for GWs-based digital data communication with highlighted characteristics and reported performances (column "C" indicates whether compensation procedures are encompassed). . . . .	149
Table 21	Comparison of normalized spectral intensity [ $V^2/Hz$ ] that is accumulated in a bin (width 2 kHz) around the carrier frequencies at both receivers. Besides the metallic (Al) plate, two sets of communication channels are considered for the CFRP element, one for the optimal (Opt) and one for the non optimal (Non Opt) set of carrier frequencies. [©2021 Springer] . . . . .	157
Table 22	Comparison of normalized spectral intensity [ $V^2/Hz$ ] that is accumulated in a bin (width 2 kHz) around the carrier frequencies at both receivers for the CFRP plate in two different configurations: setup A with receivers attached on two opposite sides with respect to the stiffener; setup B for receivers on the same side. [©2021 Springer] . . . . .	159
Table 23	LDTR-PPM technique vs varying impulsive probe signals: BER percentages are included for increasing bit-rate. . . . .	175
Table 24	LDTR-PPM technique vs chirp-like probe signals: BER percentages are included for increasing bit-rate. . . . .	175
Table 25	RMSE values as a function of decreasing SNRs for QAM data communication (carrier frequency equal to 130 kHz (first column block) and 150 kHz (second column block). . . . .	183
Table 26	Summary of the investigated techniques for GWs-based digital data communication with highlighted characteristics and reported performances. Column "Top" stands for the sensor network topology they require, whereas column "C" indicates whether compensation procedures were also encompassed. . . . .	216
Table 27	ISSLab sensor network portrait: electrical and network characteristics common to all the sensor nodes are included beside the main features of the inertial and piezoelectric sensor node. . . . .	226



## NOMENCLATURE

---

### List of operators

$(\cdot)^\dagger$	Moore-Penrose pseudoinverse
$(\cdot)^H$	Transpose conjugate
$(\cdot)^T$	Transpose
$ \cdot $	Absolute value
$\mathbb{E}[\cdot]$	Mean value
$\mathcal{F}\{\cdot\}$	Fourier transform
$\text{tr}(\cdot)$	Trace of a matrix
$\nabla(\cdot)$	Smoothness gradient
$\oplus$	Bit-wise xor operator
$\overline{(\cdot)}$	Complex conjugate

### Common Notation for OMA

$\sigma_e^2$	Variance of the broadband input stimulus
$e$	White Gaussian noise acting as structural stimulus
$E_g$	Signal energy
$F_s$	Sampling frequency
$N$	Number of samples
$N_s$	Number of sensing positions
$P$	Number of structural modes
$S_i$	Sampling position $i$
$T_s$	Sampling time
$x(t)$	Input source signal
$Y$	Matrix collection of output signals
$y_i$	$i$ -th output signal
$Y_i(f)$	Frequency spectrum of $i$ -th output signal
$\Phi$	Mode shape matrix
$\Phi_p$	$p$ -th mode shape vector

$\Phi_p^{c_i}$  p–th mode shape vector of cluster  $i$

$f_p$  p–th modal frequency

$\mathbf{f}$  Modal frequency vector

### Signal processing techniques for OMA

$\mathbf{U}$  Generic matrix of left singular vectors

$\mathbf{V}$  Generic matrix of right singular vectors

$\Lambda$  Generic matrix of singular values

$\Xi$  Generic matrix of eigenvectors

$\Omega$  Generic matrix of eigenvalues

$\omega_p$  p–th eigenvalues of  $\Omega$

$S_{y_i y_j}(f)$  CPSD between signal  $y_i$  and  $y_j$

$S_Y(f)$  CPSD matrix

$\Lambda_{S,1}$  FDD: Vector of first singular values

$\mathbf{U}_{S,1}$  FDD: Matrix of first singular vectors

$\mathbf{A}$  SSI: State matrix

$\mathbf{C}$  SSI: Output matrix

$\mathbf{G}$  SSI: Next state–output matrix

$\mathcal{O}$  SSI: Observability matrix

$\mathcal{C}$  SSI: Controllability matrix

$s_p(t)$  SOBI: p–th independent source

$S_s$  SOBI: Source matrix in SOBI

$\mathbf{W}$  SOBI: Whitening matrix

$R_S(0)$  SOBI: Zero–lag covariance matrix of the independent source matrix

$R_S(\tau)$  SOBI: Time–lagged covariance matrix of the independent source matrix

$R_Y(0)$  SOBI: Zero–lag covariance matrix of the output signals

$Y_w$  SOBI: Matrix of whitened output signals

$R_{Y_w}(0)$  SOBI: Zero–lag covariance matrix of the whitened output signals

$R_{Y_w}(\tau)$  SOBI: Time–lagged covariance matrix of the whitened output signals

$\mathbf{K}$  SOBI: Mixing matrix

$\mathbf{U}_i$  SOBI: Unitary matrix

$\kappa_{pi}$  SOBI: Mixing term for mode  $p$  and sensor unit  $i$

### Graph Signal Processing

$\alpha_p^{c_i}$  Scaling factor for mode shape  $p$  and cluster  $c_i$

$\epsilon$  Tolerance threshold for the update of the scaling coefficients

$\lambda_p$  Modal graph smoothness

$\mathbf{D}$  Degree matrix of graph structure

$\mathbf{L}$  Graph Laplacian operator

$\mathbf{W}$  Weighted Adjacency matrix of graph structure

$N_c$  Cluster number

$N_o$  Overlapping positions

$N_{Cs}$  Cluster size

$r_p$  Updating ratio of the scaling factor coefficient

$v_{n_a}$  Generic graph vertex

$w_{n_a n_b}$  Edge weight between graph node  $n_a$  and  $n_b$

### Compressed Sensing

$\Delta f^{\min}$  Minimum frequency distance between modal components

$\Gamma$  Relative frequency offset of the bin

$\Psi$  Sparsity basis

$\rho(s, y)$  Rakeness quantity

$B^*$  Frequency bands outside  $W_T$

$B_p$   $p$ -th frequency band of interest

$C^s$  sensing matrix correlation profile

$C^y$  Input signal correlation profile

$f_H$  Right value of  $\Delta f^{\min}$

$f_L$  Left value of  $\Delta f^{\min}$

$G_i$  Gini index

$j$  Decomposition level of the WPT

$k_k$  Sparsity level

$m$  Number of preserved samples

$Q$  Quality factor

$S$	Sensing matrix
$s$	Generic entry of the sensing matrix
$W_p$	Width of the $p$ -th frequency bin
$W_T$	Vector ensemble of the frequency bands of interest

### System Identification

$\alpha_i$	Householder reflector
$\beta$	Model parameters
$\eta_i$	Mode shape sign vector for sensor $i$
$\eta_{i,p}$	Mode shape sign entry for sensor $i$ and mode $p$
$\gamma$	Taps of the feed-forward filter
$\hat{Z}_i$	$i$ -th partition of the regression matrix
$\theta$	Taps of the feedback filter
$\zeta$	Regression vector
$E$	Error vector
$H(f)$	Frequency Response Function
$k$	Time index
$N_p$	Number of model parameters
$N_r$	Number of rows in $\hat{Z}_i$
$N_{ch}$	Number of chunks
$Q$	Orthogonal matrix of QR decomposition
$q_1$	Order of the filter numerator
$q_2$	Order of the filter denominator
$Q_i$	$i$ -th orthogonal matrix
$R$	Upper triangular matrix of QR decomposition
$R_i$	$i$ -th upper-triangular matrix
$S_y(f)$	Power spectral density
$Z$	Regression matrix

### Machine Learning

$E$	EOP vector
$F$	Frequency vector at the output of the modal identification phase



$H$	Frequency vector at the output of the feature tracking phase
$N_E$	Number of considered EOPs
$N_F$	Number of frequency at the output of the modal identification phase
$N_H$	Number of frequency at the output of the feature tracking phase
$N_I$	Number of signal instances
$\chi$	OCCNN: Vector of adversarial points
$N_\chi$	OCCNN: Number of adversarial points
$N_N$	OCCNN: Number of neuron per hidden layer
$\Omega$	OCCNN: Feature space boundaries
$N_A$	AENN: Number of neurons in the mapping layer
$N_B$	AENN: Number of neurons in the bottleneck layer

#### Data fusion

$\alpha$	Accuracy threshold to the frequency resolution
$\Delta_{ft}$	Frequency resolution non-windowed data
$\Delta_{fw}$	Frequency resolution windowed data
$\omega_G$	Absolute angular velocity
$\omega_x, \omega_y, \omega_z$	$x, y, z$ angular velocity components
$\theta$	Tilt angle
$\theta_A$	Acceleration-driven tilt
$\theta_G$	Gyroscope-driven tilt
$\xi_a$	Intrinsic accelerometer noise
$\xi_b$	Gyroscope bias
$\xi_c$	Crosstalk noise
$\xi_g$	Intrinsic gyroscope noise
$a_r$	Radial acceleration
$a_t$	Tangential acceleration
$a_x, a_y, a_z$	$x, y, z$ acceleration components
$f_\beta$	Cut-off frequency of the complementary filters
$H_G(f)$	High-pass part of the complementary filter
$H_L(f)$	Low-pass part of the complementary filter

$N_t$	OLA: Window size
$T_{ov}$	OLA: Time overlap
$T_{hop}$	OLA: Time stride
$w(t)$	OLA: Time domain mask
$W(f)$	OLA: Frequency domain mask
$F_{hop}$	OLA: Hop rate
$N_w$	OLA: Number of windowing iterations
$V_q$	Piezoelectric potential
$V_{out}$	Potential at the output of the PZT sensor
$R_L$	Load resistor
$C_L$	Load capacitance
$C_p$	Piezoelectric capacitance
$H(s)$	Input–output piezoelectric transfer function
$\alpha_{i,PZT}^{(p,kN)}$	Scaling coefficient for the $p$ -th PZT modal coordinate at sampling position $i$ and iteration $k$

### Guided-Waves–based Communication

$\rho$	Cross section of the waveguide
$\tau_d^M(f)$	Group delay
$b_i, \hat{b}_i$	Original and reconstructed bit
$c_g^M(f, \rho)$	Wave group dispersion curve for mode $M$
$d$	Communication distance
$F_c$	Carrier modulating frequency
$F_g$	Data rate
$K$	Number of transmission channels
$k$	Channel index
$M$	Undamped wave mode
$n$	Transmitter index
$N_{bit}$	Total number of bits in a single message
$N_{err}$	Total number of mis–reconstructed bits in a single message
$S_n(f, 0)$	Spectrum of the actuated signal

$S_n(f, d)$	Spectrum of the actuated signal after travelling a distance $d$
$S_n^{\text{comp}}(f, d)$	Spectrum of the actuated-compensated signal after travelling a distance $d$
$L_k$	FDM: Sequence length of the $k$ -th transmission channel
$t_k$	FDM: Duration of the $k$ -th rectangular pulse
$T_k$	FDM: Total excitation-sequence duration of the $k$ -th rectangular pulse
$r_k$	FDM: Inactive/Active ratio for the $k$ -th carrier frequency
$F_{\text{ch}}$	CDM: Chipping frequency
$L$	CDM: PN sequence length
$s_n^{(i)}, \tilde{s}_n^{(i)}$	CDM: DSS modulated and demodulated signal
$p(t)$	LDTR-PPM: probe signal
$T_p$	LDTR-PPM: Duration of the probe signal
$h^k(t)$	LDTR-PPM: impulse response function of channel $k$
$p_r^k(t)$	LDTR-PPM: channel-operated probe signal
$N_{\text{lev}}$	LDTR-PPM: Number of quantization levels
$\alpha$	LDTR-PPM: scaling factor for the Max-based quantization algorithm
$p_{q\text{TR}}^k(t)$	LDTR-PPM: Time reversed version of $p_q^k(t)$
$N_g$	PPM: Number of encoding pulses
$\Delta$	PPM: Time delay for bit encoding
$p_q^{(k)}(t)$	LDTR-PPM: Quantized version of $p_r^k(t)$
$g^{(k)}(t)$	LDTR-PPM: Channel-actuated LDTR-PPM signal
$\tau_0$	LDTR-PPM: Demodulation time
$g_r(t)$	LDTR-PPM: Received LDTR-PPM signal
$\gamma^k$	LDTR-PPM: Energy normalization coefficient
$E_{1,n}, E_{0,n}$	LDTR-PPM: Energy for decoded pulse 1 and 0
$A_n$	QAM: Amplitude modulation
$\phi_n$	QAM: Phase modulation
$I_n, I_n^r$	QAM: Original and retrieved in-phase component
$Q_n, Q_n^r$	QAM: Original and retrieved in-quadrature component
$s_{I_n}(t)$	QAM: in-phase modulated signal

$s_{I_n}^r(t)$	QAM: in-phase demodulated signal
$s_{Q_n}(t)$	QAM: in-quadrature modulated and demodulated signal
$s_{Q_n}^r(t)$	QAM: in-quadrature demodulated signal
$s_n^{QAM}(t)$	QAM: QAM modulated signal
$s_n^r(t)$	QAM: Synchronized version the received signal

### AE signal characterization via AI

$c_{ij}$	Coupling coefficient between local digit capsules
$N_{class}$	Number of classes
$N_{DC}$	Number of digit capsules
$N_{filter}$	Number of filters in one convolutional block
$N_{in}$	Dimension of the input data
$N_{ks}$	Kernel size
$N_{PC}$	Number of primary capsules
$N_{stride}$	Stride size
$p_{AE}$	Probability value for the AE class
$R_{ij}$	Weight routing matrix
$s_j$	Digit capsule j
$u_i$	Primary capsule i
$v_j$	Output of the squashing function
$W_{ij}$	Weight opinion matrix
$N_{pre}$	Number of pre-trigger samples
$d, \hat{d}$	True and estimated AE-to-source localization distance
$\theta$	Angle of arrival
$D_{ij}$	Distance between sensor i and sensor j
$t_i$	Travel time of the acoustic wave to sensor i
$T_0$	Actuation time of the acoustic wave
$\delta t_{ij}$	DToA between $ToA_i$ and $ToA_j$
$R^\mu$	Ratio in the mean values
$R^\sigma$	Ratio in the standard deviation

## INTRODUCTION

---

*The fascinating thing about living organisms is that  
they perceive their environment,  
react to it and even  
heal themselves when injured.  
We want to instill these qualities in materials and infrastructures.*

— Mark Tibbitt<sup>1</sup>

### 1.1 BACKGROUND AND MOTIVATION

The conceptualization of structures as intelligent organisms has inspired many researchers and it is fostered by the recent technological advancements which are making conceivable the design of self-aware and autonomous structures capable of "*perceiving* their status and the environment, *reacting* to changes and [possibly] even *healing* themselves when damaged".

What made this progress possible is the vertical coalescence between the research contributions in sensing technologies, data science, signal processing and advanced modelling. As a result, a new paradigm to the integrity assessment of structures has emerged in recent years, which is the one of *smart structures*. This definition comes from the fact that, in the next generation, engineered structures will be equipped with *intelligent sensors*, which are not merely in charge of passively capturing the structural response, but are uniquely provided with on-board processing and decision making functionalities, emulating - to a certain extent - the cognitive behavior of the human brain. It is, then, from the information sharing between these near-sensor intelligent units that the full-scale structural status can be inferred and continuously assessed during the whole life-cycle. The implementation of such *Structural Health Monitoring (SHM)* systems requires perfect coordination among the sensing, the communication and the decision subsystems to achieve a timely and reliable diagnosis.

Therefore, the deployment of SHM systems is an intrinsically interdisciplinary task, whose fulfillment requires innovative tools and approaches, constantly adapted to the evolving structural design. As a first instance, resilient monitoring strategies are needed to detect structural damages while filtering out environmental noise or instrumental non-idealities, which most often represent a primary cause of uncertainty during structural characterization. Possible solutions to tackle these topics are based on the exploitation of highly customised sensing devices, such as shaped transducers equipped with spatial filtering functionalities, or miniaturized system-in-package inertial modules, just to name a few. In addition, effective data acquisition and storage techniques must be employed in order to cope with the heterogeneity of the sensing devices and with the amount of data produced by collecting raw signals. Finally, damage detection and characterization

---

<sup>1</sup> *Biodegradable bridges: Living structures that respond to the environment*. Available at <https://techxplore.com/news/2020-01-biodegradable-bridges-environment.html>

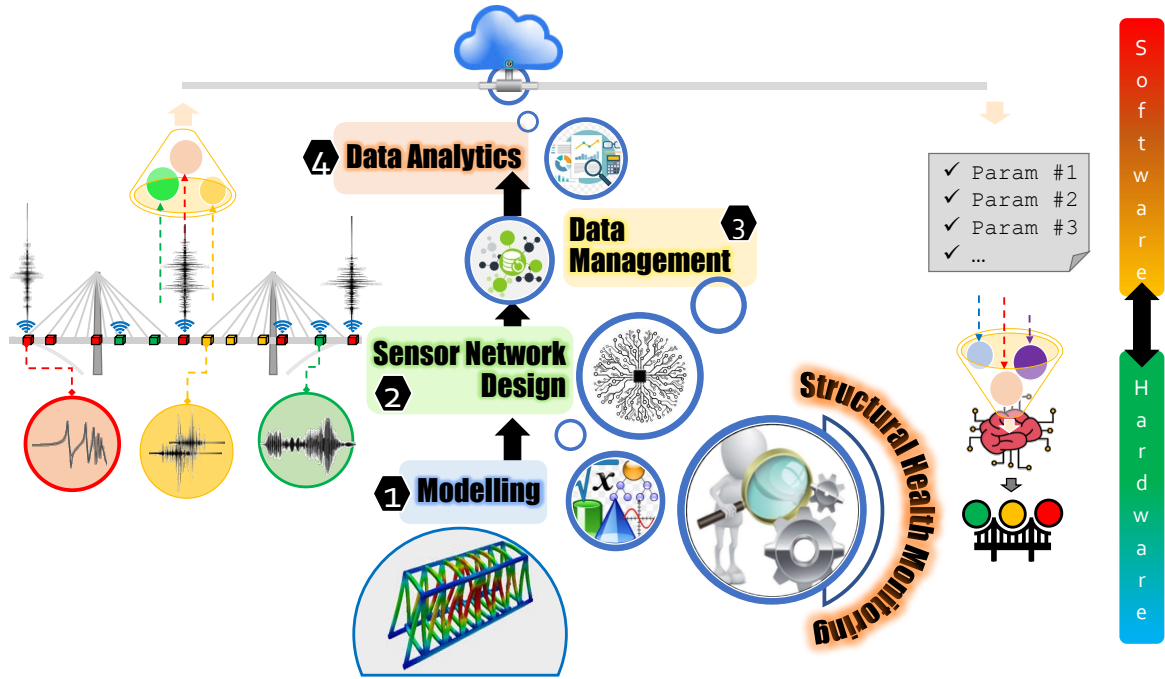


Figure 1: General overview of a SHM system, from the hardware up to the software layers.

tasks may be computed via data-driven algorithms that can complement the model-based alternatives conventionally leveraged in the diagnostic process.

Consistently, the effectiveness of the SHM architecture is based on the optimal combination between the required Hardware (HW) resources for signal acquisition, conditioning and digitalization, and the associated Software (SW) infrastructure in charge of data management, data analytics and structural assessment. As schematically depicted in Fig. 1, this is realized via implementation of multi-layered architectures exploiting the intrinsic capability of the above-mentioned smart devices to measure, pre-elaborate and forward physical data to virtual aggregating units [1]. From a HW standpoint, the selection of the specific sensors to be deployed and their relative positioning strictly depend on the characteristics of the structure to be inspected, the complexity of which may demand the combination of different sensing technologies, as well as several diagnostic approaches. At higher abstraction levels, considerable research efforts have been made to (i) enhance the reliability in retrieving and sharing structural information collected at multiple locations, (ii) increase the quality of the extracted structural parameters while reducing the computational latency and, in turn, the data-to-user transfer time, and (iii) bridge the gap between human and computer-aided prognostics about the remaining useful life, possibly combining them with dedicated interfaces [2].

### 1.1.1 Application perspectives and open issues

In this framework, the main challenge which is faced by the SHM community is to ensure long-lasting monitoring functionalities, while adapting to the constantly evolving complexity of modern *mesoscale* structures [3], i.e., structures with very large geometries, where deluge of data collected from increasingly denser sensor networks makes their management a primary issue. Significant advancements have been achieved in recent

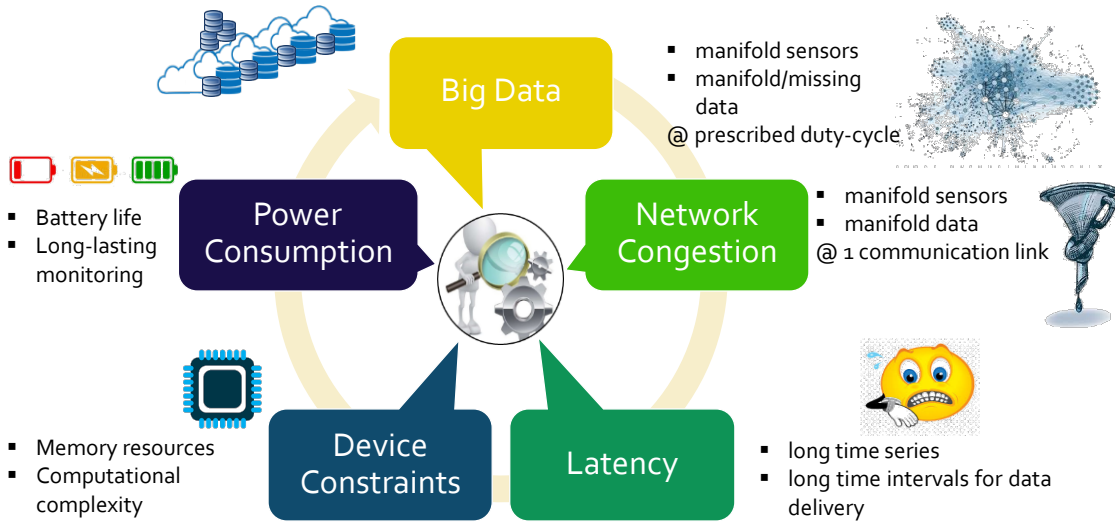


Figure 2: Current challenges in state-of-the-art monitoring networks.

years in the implementation of autonomous, reliable and cost-effective SHM systems [4] [5], through the joint optimization of data sampling rates, on-board storage and computational resources, and communication data payloads. The advent of *Internet of Things (IoT)* technologies [6] may ease the development of real-time and continuous monitoring systems, allowing for the seamless sharing of information between users, sensors and structures [7]. Nevertheless, a number of issues remain to be tackled in order to enhance the responsiveness and the resilience of the designed monitoring architectures [8]. As schematically depicted in Fig. 2, five main and mutually inter-related challenges can be listed: (i) the big data volume implied by dense sensor networks deployed on large-scale infrastructures, (ii) the consequent probability of network congestion due to limited and shared communication channels between multiple devices, (iii) the growing latency in the data-to-user transfer process, (iv) device constraints, i.e., limited memory space and computational resources available on sensors in order to meet the requirements of (v) low-power and low-cost hardware that can ensure a long-lasting monitoring action. These aspects are even more crucial in case of wireless monitoring systems [9], where the usage of battery-operated devices allow for higher versatility in the deployment process, while posing more stringent limitations on the power consumption.

As a consequence of the above-mentioned challenges, which affect multiple layers of the SHM system, sensor network improvement is mandatory for each step of the monitoring process. In this context, the HW-SW co-design of embedded computing systems has promoted a rapid shift from standard hierarchical approaches, relying on cloud-based data analytics, performed on remote servers via time- and energy- onerous procedures, to near-sensor data compression and/or inference, empowered to smart sensors in charge of stream processing the raw data.

In the SHM field, data compression techniques have been investigated as a means to address these issues by performing global network optimization. However, most of the related works ([10]–[13]) are based on offline data processing, while the edge and extreme edge computing perspective, i.e., investigating whether and how compression could be practically implemented on resource-constrained sensor boards, has only recently gained attention. Compression at the extreme edge is particularly attractive because, among the different contributions to the energy budget, the one related to wireless data transmission

is largely dominant due to the significant power consumption necessary to cover long transmission distances with minimal payload degradation.

Another macro-trend in SHM concerns the possibility to integrate different sensing technologies to provide a deeper insight about various aging phenomena occurring in the same structure [14], [15]. Indeed, heterogeneous monitoring platforms may overcome the inherent shortcomings of individual sensing principles. Despite their beneficial impact on the quality of the structural assessment process, such scenarios demand for dedicated mixed-signal processing enabling for data merging and global feature reconstruction from multi-source measurements. For these measurements, the role of smart sensors is pivotal since they might perform data fusion without centralized data retrieval.

Finally, continuously growing attention is nowadays attracting the key concept of Value of Information (VoI), i.e., quantifying how the information extracted from the SHM system can actually provide optimal decision support [16]. In these terms, the VoI assumes a crucial importance since it allows to evaluate, in a quantitative and no more qualitative manner, the real benefit that the HW-SW improvement demanded by the next generation of SHM systems can bring to the integrity assessment process and, by extension, it instructs the SHM users about the most convenient maintenance action.

## 1.2 THESIS OBJECTIVES

The main goal of this Thesis is to tackle the multi-faceted and undoubtedly entangled nature of the monitoring process, via a full-scale improvement of the HW and SW resources involved by the SHM system.

As depicted in Fig. 3, the pursuit of this objective has required the investigation of both: (i) transversal aspects common to multiple application domains at different abstraction levels (such as knowledge distillation, networking solutions, microsystem HW architectures), and (ii) the specificities of the monitoring methodologies (vibrations, guided waves, acoustic emission monitoring).

## 1.3 THESIS ORGANIZATION AND CONTRIBUTIONS

The content of this dissertation is organized into three major parts (see Fig. 3), each of them trying to offer tangible solutions to different issues related to as many non-destructive structural evaluation methods. In Part i (Chapters 2 to Chapter 7), the focus is on the HW/SW sensor network optimization for vibration-based monitoring. In Part ii (Chapters 8 to Chapter 12), inspection strategies built on guided elastic waves are presented, investigating the opportunity to exploit piezoelectric transducers for probing the inspected structures and, at the same time, for communicating data in a self-contained manner. Finally, Part iii (Chapter 13) is entirely dedicated to the problem of onset time estimation in acoustic signals, since it represents a pivotal parameter for the accurate localization of the acoustic events caused by structural aging.

For each part, an introductory section is enclosed, in which the basic principles of the driving monitoring technique, as well as a review of the most relevant signal processing methodologies to cope with it, are discussed. The aim is to provide a detailed overview of the state-of-the-art in the field, on which the novel solutions proposed in the manuscript are grafted.

An executive summary of each chapter-related content is provided as follows:



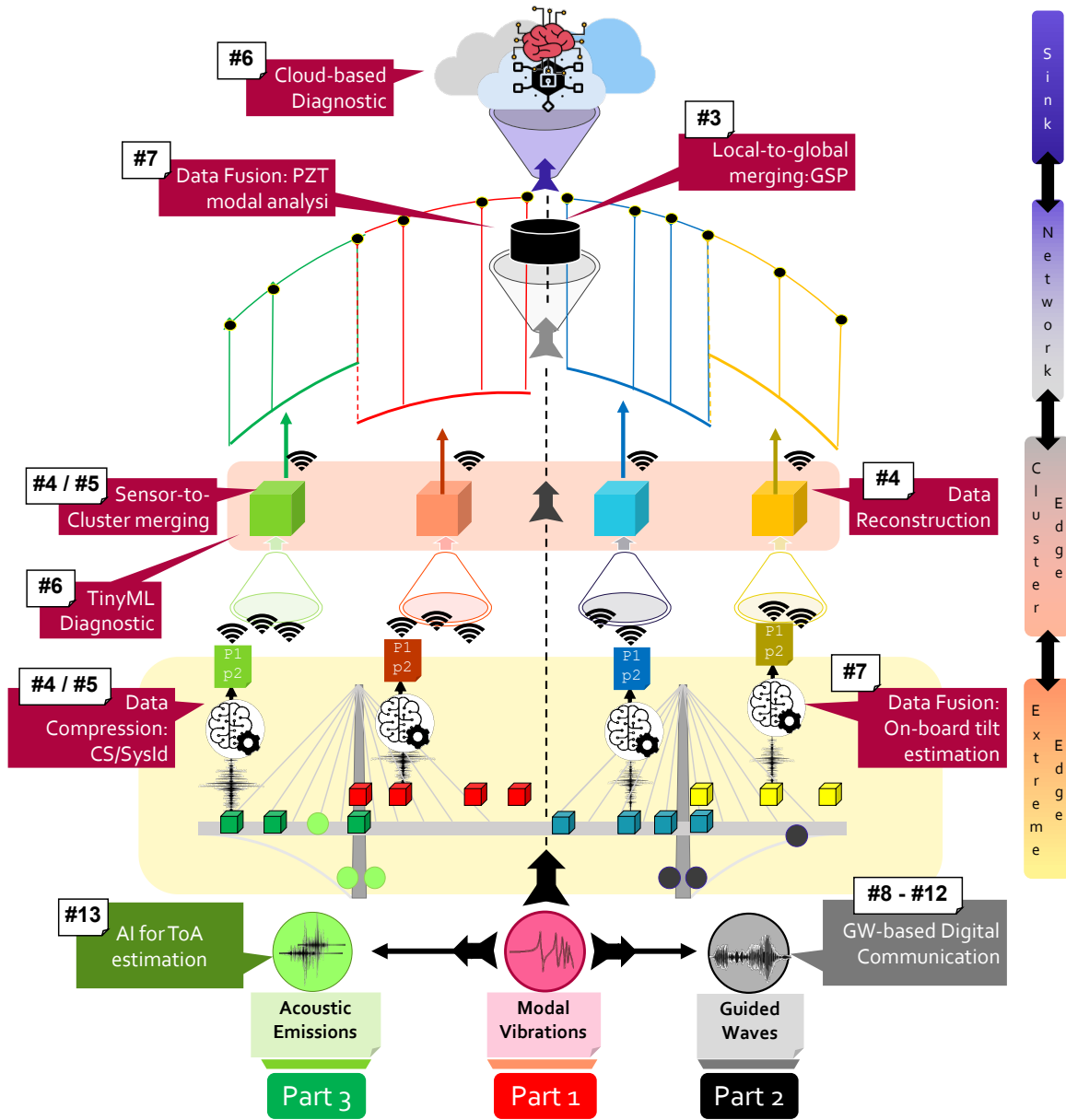


Figure 3: Graphical description of the thesis organization.

- Chapter 2 outlines the theory at the basis of vibration diagnostics under the cap of Operational Modal Analysis (OMA), which serves the fundamental goal of feature extraction for the following structural assessment process. An overview of the most-established signal processing techniques available for OMA is provided, with specific emphasis on those strategies actually exploited in this work. Accordingly, the damage assessment problem is finally discussed together with a general introduction about the available algorithms to finalize it.
- Chapter 3 deals with a critical task in clustered architectures for modal analysis, which is the reconstruction of global modal features from local estimates. In particular, a novel method inspired by the Graph Signal Processing theory is proposed for the sake of full-scale mode shape retrieval in case of non-overlapped clusters of sensors, thus overcoming the limitation of many state-of-the-art alternatives in the field. In these terms, the Chapter introduces a first level of sensor network optimization: indeed, by removing the constraint of cluster interleaving, not only the cumulative number of sensors might be reduced, but also the sensor deployment can be better adapted to the geometry of the inspected structure.
- Chapter 4 investigates solutions for sensor life-cycle extension, especially for battery-operated devices, where the need for real-time and over-time serviceability barely copes with the limited memory and power budget available on edge devices permanently attached to the structure. To this end, an innovative technique for vibration data compression at the extreme edge driven by the Compressed Sensing (CS) paradigm is introduced. The method adapts the compression mechanism to the structural characteristics, but it achieves this goal in a conservative manner, i.e., taking into account the possible changes in the structural signature, as required in long-term monitoring. Alongside, the effectiveness of CS strategies in presence of an operative framework are assessed. To this end, the compliance of CS-enabled clustered architectures with global structural features reconstruction is firstly investigated. Then, its robustness against instrumental noise is thoroughly assessed.
- Chapter 5 approaches the task of data compression as a system identification (SysId) problem. SysId is capable of encapsulating the meaningful vibration content in a very reduced set of values, called model parameters, which are fully descriptive of the underlying physical dynamics. To validate this concept with near-sensor implementations, an ad-hoc processing flow encompassing dense linear algebra operators is devised to shrink both the memory and computational complexity of the involved algorithms. Relying on that, the actual embodiment of system identification models on a low-power resource-constrained device is successfully achieved and validated against structural deterioration. Finally, a cost-benefit analysis concludes the Chapter: the objective is to provide a comprehensive measure of the energy savings brought by this technique, taking into consideration the power consumption due to data transmission, as required by state-of-the-art communication protocols for IoT scenarios.
- Chapter 6 fulfills the last step of the monitoring architecture, with specific emphasis on the damage assessment process. Suitable artificial intelligence solutions are reviewed and adopted via the TinyML approach, yielding to the porting of the sought inference models on a low-cost edge device. The aim is to move the artificial in-

telligence in strict proximity where information is actually sensed, overtaking the requirement of centralized integrity evaluation [17]. Moreover, in order to provide a comprehensive framework for vibration-based inspection from acquisition to damage characterization, the diagnostic performance of the designed models paired with data compression procedures is tested.

- Chapter 7 discusses the importance of heterogeneous monitoring networks for vibration analysis as a viable solution to counteract the intrinsic limitations of single sensing principles and, thus, to enhance the depth and the quality of the structural insight. Therefore, two data fusion techniques are presented to aggregate multi-type measurements: the former is a methodology for on-board tilt angle estimation by fusing linear acceleration and angular velocities; the latter consists of a purposely designed strategy for the combination of cost-effective piezoelectric discs with inertial sensors, with the ultimate objective of promoting the realization of up-scalable and minimally invasive monitoring architectures.
- Chapter 8 delineates the working principles at the basis of Guided Waves (GWs)-based monitoring, which serve as a starting point to discuss the inherent wireless communication capabilities made available by smart transducers without the need of external, bulky and costly, radio modules. Hence, this peculiar communication-related property could be used in a next generation of autonomous and self-aware sensor networks for GW inspection: the near-sensor processing and actuating functionalities of the transducers can be exploited both for data acquisition and characterization in a preliminary stage and, subsequently, to share the result of the inspection in form of damage indicators, by propagation through the mechanical medium itself.
- Chapter 9 focuses on the extreme edge implementation of the Frequency Division Multiplexing technique as a suitable strategy for multi-user communication scenarios. Physics-informed strategies for the selection of the best set of carrier frequencies are proposed to maximize the communication performance. The effects of structural irregularities on the propagation channels and the achievable transmission rates are explored.
- Chapter 10 exploits the standard Code Division Multiplexing technique in combination with a dispersion compensation procedure to be suitable for GWs-based scenarios: this solution allows for the best compromise between channel availability while transmitting with defect resolution while evaluating the structural integrity.
- Chapter 11 counteracts the intrinsic complexities of GW propagation, which might be responsible for significant degradation in the quality of the delivered information, via the concurrent transmission-compensation approach offered by the Time Reversal-Pulse Position Modulation method by virtue of the channel reciprocity. In particular, a novel low-depth variant of the same methodology is suggested in the Chapter to meet the signal synthesis capabilities of low-cost actuators and, consequently, to support its edge implementation.
- Chapter 12 combines the communication robustness of Quadrature Amplitude Modulation with the frequency steering efficiency of Frequency Steerable Acoustic Transducers to implement, in hardware, spatial multiplexing functionalities, as it is the

case of modern 5G communications. The final objective of the work is to demonstrate how the amalgam of an innovative sensor design and advanced signal processing might allow to achieve important transmission rates while ensuring high immunity to unfavorable propagation environments.

- Chapter 13 concentrates on a pivotal problem in Acoustic Emission monitoring, that is the estimation of the Time of Arrival in acoustic signals, since it delivers a primary tool both for damage identification and acoustic source localization. Notwithstanding conventional statistical methods, three neural network models are purposely proposed to tackle this task: two are based on a standard Convolutional Neural Network, whereas the other is built on a CapsNet architecture, further combined with a CNN-based logic for the retrieval of the sought onset time. The algorithms are firstly tested on a labelled, synthetic dataset, and then evaluated on experimental data for acoustic event localization, showing superior performances in both cases.

Finally, Chapter 14 concludes the manuscript, depicts the current status of the work, briefly describes ongoing research directions and opens to future challenges.

Part I

EDGE COMPUTING SOLUTIONS FOR VIBRATION-BASED  
DIAGNOSTICS



## ABSTRACT

*In this Chapter, the working principles of vibration-based structural assessment are reviewed. Signal processing techniques necessary to extract the structural features of interest, which fall under the cap of the so-called operational modal analysis field, will be discussed. Then, the most relevant strategies typically employed for damage detection basing on either vibration features or machine learning algorithms will be tackled, with the final objective to provide a comprehensive overview of the current challenges in the field.*

## 2.1 INTRODUCTION

Vibration-based monitoring refers to the process of inferring the integrity status of a structural system by the continuous and, possibly, automated monitoring of its dynamics. For this reason, it is classically adopted for structures that operate in the dynamic regime, such as bridges [18], [19], wind turbines [20], [21], mechanical rotors [22], etc.

The diagnostic procedure passes through the tracking, over time, of a representative set of vibration features, which are taken as damage indicators since they can reflect even subtle changes in the mechanical properties of the underlying physical structure. Most typically, such features pertain to frequency-related quantities, the so-called *modal parameters* [23]. Accordingly, the structural characterization task is usually referred to as *modal identification*, as it aims at extracting, for each vibration component of interest, namely a *mode* of the structure, a representative set of quantities. The latter comprehend, but are not limited to, the associated modal frequency value, the mode shape, i.e., the specific spatial pattern of vibration exhibited by the structure at that modal frequency [24], and the damping ratio, i.e., the rate at which the mode decays after excitation.

In structural analysis, three to five dominant modal components at relatively low spectral bands are usually identified, since this is typically sufficient for an accurate detection of global changes in the observed structure [25] (e.g. changing load path, loss in global stiffness). An additional reason is that, despite being useful for integrity characterization owed to their more pronounced sensitivity to structural anomalies, higher-order modes are intrinsically more complicated to be identified with enough accuracy because of the complex vibration behavior exhibited by the structure at these modal frequencies.

There are two different ways to perform modal analysis. The *input-output* approach (known as experimental modal analysis) recovers modal parameters from the simultaneous collection of the actuating force and the output response. Conversely, identification techniques that extract modal information from the measured vibration response, also referred to as *output-only* methods, fall within the class of Operational Modal Analysis (OMA) solutions [24]. OMA aims to identify structural properties under the assumption that the input signal can be described as a white Gaussian noise term  $e(t) \sim \mathcal{N}(0, \sigma_e^2)$  with zero-mean and prescribed variance  $\sigma_e^2$ . In this case, which is though a crucial requirement in practical scenarios and in-service inspection, no controlled input signal is artificially

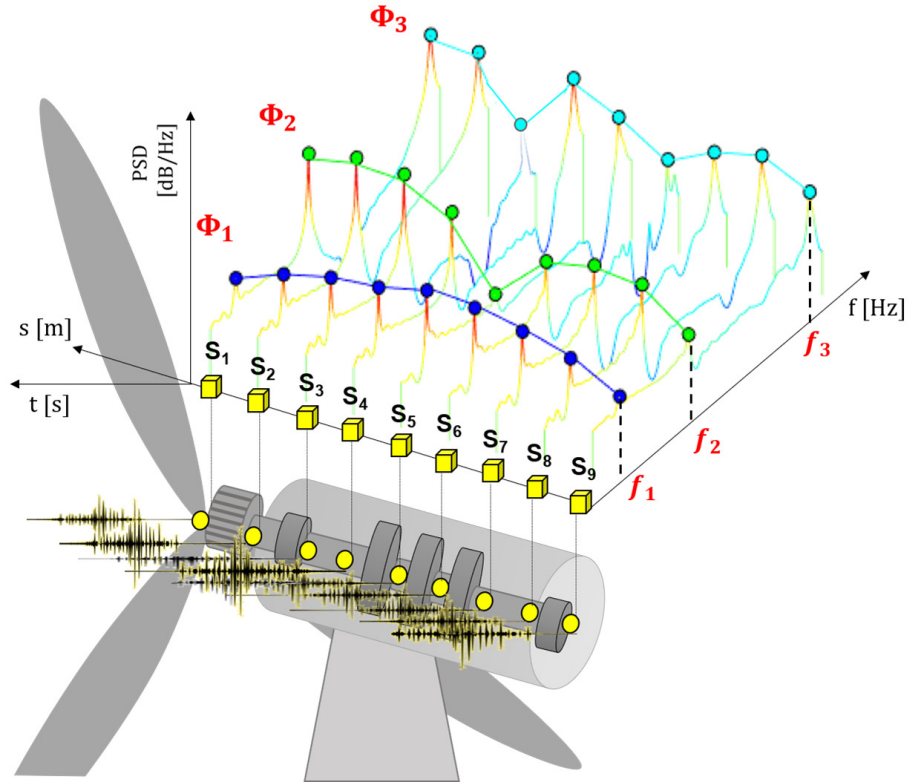


Figure 4: OMA-based processing flow for a toy structure: the quantities  $f_p$  and  $\Phi_p$  ( $p = 1, 2, 3$ ) indicate the natural frequencies of vibration and the associated mode shapes, respectively. [©2021 IEEE]

applied to the structure, which is left to vibrate in its normal operative conditions. This strategy strives to overcome the practical difficulties in measuring the exciting force, as the latter most often derives from the combination of operational (e.g., vehicles) and environmental (e.g., wind) stimuli and it is, therefore, challenging to be captured properly.

Since the modal components illustrate how the structural energy distributes over the frequency spectrum, one of the most efficient way to identify these quantities is to look at the Power Spectral Density (PSD) of the acquired vibration signals. Accordingly, in its most basic form, a typical structural identification process works as schematically depicted in Fig. 4, where an illustrative case of  $N_s = 9$  sensing positions and  $P = 3$  modal components is considered. Vibration signals ( $y_i(t)$ ,  $i = 1 \dots N_s$ ) acquired at individual sampling positions ( $S_i$ ) are the only inputs required by the system. As can be noticed, the set of frequencies  $f = [f_1 \dots f_P] \in \mathbb{R}^{1 \times P}$  is identified from the collection of the  $P$  dominant peaks appearing in the spectral profile of the gathered vibration data. A global estimation of the cumulative vibration frequencies can finally be obtained as a point-by-point average of the peak frequency values estimated at each sensor of the network, namely  $f_p = \sum_{i=1}^{N_s} f_{p,i}$ . On the other hand, the absolute value of the  $p$ -th mode shape vector  $|\Phi_p| \in \mathbb{R}^{N_s \times 1}$ , corresponding to the equally-indexed modal frequency  $f_p$ , can be trivially reconstructed by interpolating in the spatial domain the previously computed peak spectral values. Notably, it must be underlined that, from the pure spectral analysis, just the absolute value of the mode shape can be extracted. Hence, in order to reconstruct the actual envelope of the mode, more advanced techniques are demanded.



Accordingly, from the knowledge of the frequency vector  $\mathbf{f}$  and the mode shape matrix  $|\Phi| = [|\Phi_1| \dots |\Phi_p|] \in \mathbb{R}^{N_s \times P}$ , obtained by vertically stacking the individually computed  $\Phi_p$  mode shape vectors, the structural integrity status can be assessed. Alternatively, recent structural characterization solutions stemming from the Artificial Intelligence (AI) processing field are based on innovative strategies which do not rely on the extraction of modal features and are purely data-driven [26].

## 2.2 REVIEW OF OMA-DRIVEN FEATURE EXTRACTION ALGORITHMS

Many algorithms were proposed in the literature in the last decades for OMA. In general terms, they can be classified into three main groups depending on the processing domain: *frequency-domain*, *time-domain*, and *time-frequency domain* methods. The three categories differ in terms of computational complexity, capability to handle noise levels hidden in vibration data, and aptness to deal with intricate spectral signatures which are likely to characterise the underlying structure. Thus, the selection of one method over the others should balance between the maximum admitted latency in providing the sought structural information and the necessity to cope with possible non-stationary and non-linear structural behaviors.

In the next subsections, the most-established techniques within the class of frequency-based and time-based will be reviewed in a comprehensive and schematic manner by discussing their main features and their compliance with either centralized or decentralized monitoring networks. A more rigorous mathematical formulation will be enclosed only for those techniques actually employed in this work. The aim is to provide to the reader the theoretical background and introduce the criticality in state-of-the-art signal processing solutions for OMA-based SHM.

### 2.2.1 Frequency-based methods

Algorithms built on the representation of vibration signals directly in the frequency domain found great success in OMA applications due to their frequency-driven nature. A list of frequency-based methods and their main peculiarities have been summarized in Table 1.

#### 2.2.1.1 Peak Picking

The simple working principle combined with the apparently low computational complexity made Peak Picking (PP) [32] one of the most widely applied algorithms for vibration analysis. In essence, PP identifies the location-magnitude pair of the dominant modes appearing in the frequency representation of the signal [27], the latter being either the spectral profile of the measured vibration data or, in the most basic case, simple Fourier-transformed signals. Nevertheless, some factors might limit the effectiveness of this technique for modal identification. A primary reason is due to the practical difficulties in capturing very faint and poorly energetic structural modes, which easily blend into the surrounding noise floor even for a relatively highly Signal-to-Noise Ratio (SNR). Secondly, multiple modes of different entity and nature (e.g., torsional, bending, etc.) contribute to the overall vibration response of a structure. This condition might lead the number of local maxima in the spectrum to increase rapidly; thus, the approach becomes more suscepti-

Table 1: Summary of commonly adopted frequency domain-based algorithms for OMA, with highlighted characteristics and limitations. Algorithms are compared in terms of computational complexity (↘, →, ↗ indicate low, medium and high cost, respectively), mechanical properties of the target structure, architectural topology (Loc and Glob indicate edge-compliant and centralized solutions, respectively) and tolerated input noise levels (L, M and H indicate low, medium and high SNR, respectively).

Method	Characteristics				Limitations	Ref
	Cost	SNR	Top.	Target Structure		
Peak Picking	↘	H	Loc	weakly damped with well-separated modes	<ul style="list-style-type: none"> <li>- Fixed frequency resolution</li> <li>- Only stationary signals</li> <li>- Supervised approach</li> <li>- Bad damping ratio estimation</li> </ul>	[27]
Frequency Domain Decomposition	→	L M H	Glob	from well-separated to relatively-spaced modes	<ul style="list-style-type: none"> <li>- Fixed frequency resolution</li> <li>- Only broadband input excitation</li> <li>- Supervised approach</li> </ul>	[28]
Complex Mode Indication Function						[29]
Least Squares Complex Frequency-Domain						[30]
Multiple Signal Classification	↗	L M H	Loc	from well-separated to closely-spaced modes	<ul style="list-style-type: none"> <li>- Processing time</li> <li>- Only natural frequencies are identifiable</li> <li>- Calibration is required</li> </ul>	[31]

ble to false identification in case artifact peaks, in the surrounding of the most energetic values, remain significantly above the other physical, yet less energetic, modes.

As previously introduced, another key point to be considered is that, in its elementary spectral conceptualization, PP only applies to real quantities: such limitation hampers the possibility to recover complex values, first among all the phase and, thus, the sign of the mode shapes, even though this quantity might represent a pivotal damage indicator. Hence, a desirable condition for the successful application of PP-based strategies is the one characterized by clearly smooth frequency trends with high spectral resolution, the latter requirement being barely guaranteed by standard frequency estimators. Another important aspect is that, owing to its decentralized nature which may be advantageous from an edge-computing perspective, PP requires the implementation of specific policies capable to merge local estimates into global modal parameters.

#### 2.2.1.2 Frequency Domain Decomposition

The Frequency Domain Decomposition (FDD) technique has been firstly proposed by Brincker *et al.* in [28] to provide a more accurate and exhaustive spectral characterization with respect to the one offered by PP alone. Noteworthy, the advantages of FDD are not merely circumscribed to the gain in the quality of the computed spectra, but they extend to its centralized processing. Indeed, FDD returns global modal parameters and, consequently, does not require additional local-to-global procedures necessary for the full-scale assessment of the structure.

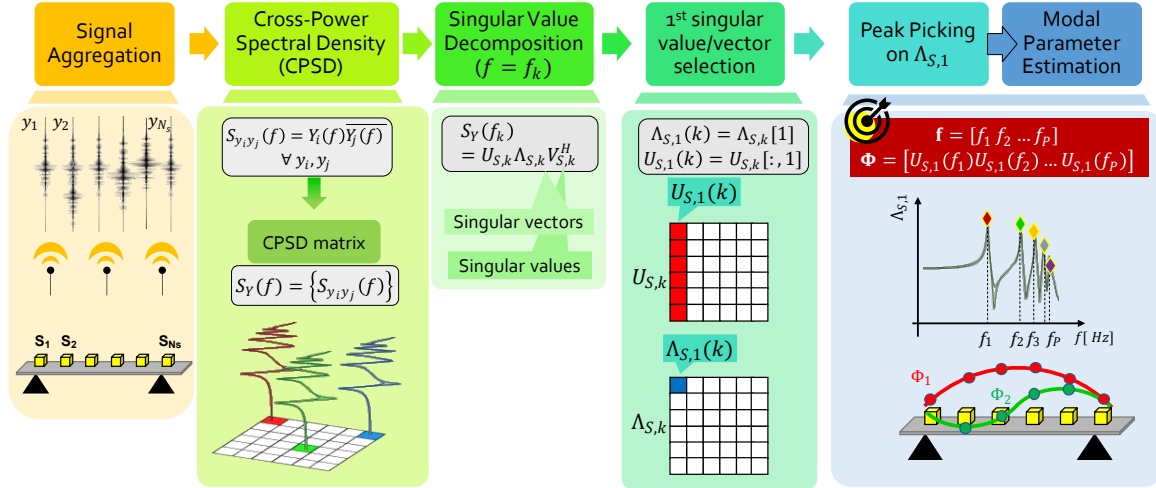


Figure 5: Schematic representation of the FDD processing flow, from data collection up to modal parameter extraction.

This peculiar characteristic has been highlighted in Fig. 5, in which the basic steps implied by the FDD processing flow are sketched. As can be observed, the starting point of the procedure encompasses the aggregation of vibration signals collected at various points of the structure. Let's call with  $Y \in \mathbb{R}^{N \times N_s}$  the matrix obtained by the vertical concatenation of the different responses  $y_i, \dots, y_{N_s}$ . Thereafter, the Cross-Power Spectral Density (CPSD) function  $S_{y_i y_j}(f) = Y_i(f)\overline{Y_j(f)}$  expresses the complex product<sup>1</sup> between the frequency spectra  $Y_i(f) = \mathcal{F}\{y_i\}$  and  $Y_j(f) = \mathcal{F}\{y_j\}$  of any pair of signals  $y_i$  and  $y_j$ . Most commonly,  $S_{y_i y_j}(f)$  is computed directly in the time domain as the Fourier transform of the cross-correlation function between the two signals.

The CPSD is computed for all the possible sensor combinations ( $i-j$ ), and then stored in the three-dimensional CPSD matrix  $S_Y(f) = \{S_{y_i y_j}(f)\} \in \mathbb{R}^{N_s \times N_s \times N}$ .  $S_Y(f)$  is then processed via Singular Value Decomposition (SVD), repeatedly for each of the  $N$  frequency points in the spectrum (i.e.,  $f = f_k, k = 1, \dots, N$ ), corresponding to as many  $N_s \times N_s$  horizontal slices of the complete CPSD matrix. Every single decomposition reads as  $S_Y(f_k) = U_{S,k} \Lambda_{S,k} V_{S,k}^H$ <sup>2</sup>, yielding the square matrix of  $N_s$  left ( $U_{S,k}$ ) and right ( $V_{S,k}$ ) singular vectors and the diagonal matrix of  $N_s$  singular values  $\Lambda_{S,k}$  (singular values appearing in descending order).

Supposing that a large fraction of the signal energy is captured by the first singular component, only the vector  $U_{S,1} = U_{S,k}[1] \in \mathbb{R}^{N_s \times 1}$  and the scalar  $\Lambda_{S,1} = \Lambda_{S,k}(1)$ , are preserved at each iteration. At the end of the process, the cumulative matrix  $U_{S,1} \in \mathbb{R}^{N_s \times N}$  of first singular vectors and the  $N$ -dimensional vector of singular values  $\Lambda_{S,1} \in \mathbb{R}^{1 \times N}$  are created and used in the following modal parameter extraction phase. The final step involves the application of the PP algorithm to  $\Lambda_{S,1}$ , returning modal frequencies as the frequency points associated with the  $P$  most energetic peaks; the mode shape matrix  $\Phi$  is, instead, recovered by taking the column entries in  $U_{S,1}$  at the mutual frequency point locations.

The weak point of FDD lies in its dependence from PP, such that it could be somehow difficult to identify closely-spaced modal components in a fully automatic manner.

<sup>1</sup> Overline stands for the complex conjugate operator.

<sup>2</sup> Superscript <sup>H</sup> stands for the transpose conjugate of a matrix.

Table 2: Summary of commonly adopted time domain-based algorithms for OMA, with highlighted characteristics and limitations. Algorithms are compared in terms of computational complexity ( $\swarrow$ ,  $\rightarrow$ ,  $\nearrow$  indicate low, medium and high cost, respectively), mechanical properties of the target structure behavior and tolerated input noise levels (L, M and H indicate low, medium and high SNR, respectively).

Method	Characteristics				Limitations	Ref
	Cost	SNR	Top.	Target Structure		
Statistical Time Series Models – AR – ARMA – ARX <sup>3</sup> – AR+Noise	$\rightarrow$	L M H	Loc	from well-separated to closely-spaced modes	– Local-to-global merging is required – Strict dependence on selected model order – Absolute value of mode shape	[33], [34]
Stochastic Subspace Identification – SSI-COV – SSI-DATA	$\nearrow$	L M H	Glob	from well-separated to closely-spaced modes, with slightly non-stationary response	– Processing time – Calibration is required – Generation of artifact modal components	[35]
Free-decay Response – Natural Excitation Technique (NEXT) – Eigensystem Realization (ERA) – Random Decrement Technique (RDT) – Ibrahim-Time Domain	$\rightarrow$	M H	Loc	moderately damped with well-spaced modes	– Processing time – Only stationary or slightly non-stationary signals – High sensitivity to input noise	[36]
Blind Source Separation – SOBI – ICA – PCA	$\rightarrow$	L M H	Glob	moderately damped with well-spaced modes	– Processing time – Number of identifiable modes limited to the number of available sensors	[37]
TDD	$\nearrow$	M H	Glob	from well-separated to relatively-spaced modes	– Supervised approach	[38]

To overcome this limitation, supervised or semi-supervised approaches are followed, in which a preliminary guess about the frequency bands of interest is provided as additional input of the PP algorithm to favor better peak selection.

Alternative techniques are available to address OMA-based identification in the frequency domain, such as those listed in the last lines of Table 1. However, they are not popular within the SHM community, mainly because of their higher computational cost, and their poor capability to retrieve the modal parameters of interests in a consistent manner.

### 2.2.2 Time-based methods

Methods labeled as *time-domain* make use of time-dependent operators to identify modal parameters. A comprehensive collection of such techniques is provided in Table 2. As

a general comment, these strategies are based on more computationally-involved and time-consuming procedures than their frequency counterparts. This is one of the primary obstacle limiting their implementation in a near-sensor manner.

### 2.2.2.1 System Identification based on Statistical Time Series Models

Structural analysis built on System Identification (SysId) relies on the idea that the mechanical and physical laws governing the equations of motion admit an abstract, but still completely equivalent, mathematical representation as causal linear time-invariant filters [39]. In line with this formulation, the objective of parametric system identification is to estimate that set of filter coefficients, or *model parameters*, which can exactly reproduce the measured input-output relationship. SysId based on Statistical Time Series Models (STSM) resorts to regression techniques to identify the sought model parameters, by minimizing the error between the predicted and actually measured system response according to certain heuristics.

In analytical terms, denoting  $x[k]$  and  $y[k]$  the generic input-output pair<sup>4</sup> gathered at time stamp  $kT_s$  (with  $T_s$  indicating the sampling period), a basic and most general variant of a univariate discrete-time parametric model at a generic sample  $k \in \{0, \dots, N-1\}$  reads:

$$y[k] + \sum_{t=1}^{q_1} \theta_t y[k-tT_s] = \sum_{s=0}^{q_2} \gamma_s x[k-sT_s] \quad (1)$$

in which  $q_1$  and  $q_2$  specifically determine the number of parameters preserving memory of the past  $q_2$  input and  $q_1$  output instances, while  $\theta_t$  and  $\gamma_s$  are the feedback and feed-forward taps of the corresponding filter.  $q_2$  and  $q_1$  are also known as the orders of the filter numerator and denominator polynomials, while their summation  $N_p = q_2 + q_1 + 1$  equals the total amount of model coefficients to be determined.

It is, therefore, from the algebraic manipulation of Eq. (1) that all the structural features of interest can be obtained, either in the time or frequency domain, by virtue of the dual relationship between the filter impulse response function and its associated Frequency Response Function (FRF):

$$H_y(f) = \frac{\sum_{s=0}^{q_2} \gamma_s e^{-i2\pi f s T_s}}{1 - \sum_{t=1}^{q_1} \theta_t e^{-i2\pi f t T_s}} \quad (2)$$

Finally, an estimate of the system's PSD  $S_y(f)$  can be delivered via the square of the magnitude of the FRF as:

$$S_y(f) = |H_y[f]|^2 \quad (3)$$

from which the modal frequency features are retrieved.

Different identification strategies have been defined depending on the nature of the processed signals and the features of interest. In the following, four STSM will be reviewed, which are classically applied in the context of modal analysis. For the sake of clarity, Table 3 summarizes the mathematical expressions of the PSDs involved in Eq. (2) and (3).

Here, a concise description of their working principle is delivered:

<sup>4</sup> The subscript  $i$  in  $y$  is dropped to simplify notation.

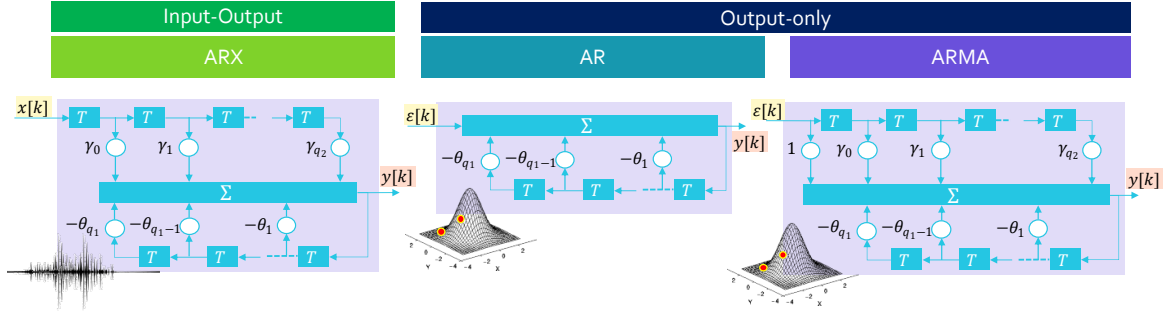


Figure 6: Formulation of input–output (ARX) and output–only (AR, ARMA, AR+Noise) parametric models.

- *Autoregressive with eXogenous Input (ARX)*. ARX models are applicable for experimental modal analysis. Their block diagram representation, depicted in the first box of Fig. 6, stems from the filter definition and clearly shows the feedback-feedforward nature of these system models, whose characteristic equations coincide with those offered in (1) and (2). Despite being an extremely accurate tool, two main factors limit broad applicability of the ARX scheme. Firstly, the practical difficulty in measuring, with sufficient precision, the input signal (excitation) of the structure under operational conditions, due to unmeasured, arbitrary and/or very weak excitation sources. Secondly, a decentralized processing requires that the input signal is made available to all the sensing nodes during a pre–processing step, thus increasing the amount of data to be transmitted in case of decentralized sensor networks.
- *Autoregressive (AR)*. An AR model essentially comprises an all–pole Infinite Impulsive Response (IIR) filter obtained by zeroing the contribution of the external input  $x[k]$  in Eq. (1), which turns into:

$$y[k] + \sum_{t=1}^{q_1} \theta_t y[k - tT_s] = e[k] \quad (4)$$

The drawback of this model is that a high number of parameters is typically required in order to produce accurate results, or at least comparable to the ones yielded by ARX.

- *Autoregressive with Noise (AR+Noise)*. The AR+Noise method was firstly proposed in [34] to tackle the inherent noise levels in real data, which are relevant in some application contexts. This can be considered as an error-in-variables identification problem, meaning that the locus of allowable solutions should be strictly compatible with the second–order characteristics of the acquired signals. Furthermore, beside sharing the same filter representation, it outperforms similar AR strategies thanks to the combined feedback–feedforward prediction model employed during the parameter estimation process. Thus, it ensures the congruence of the obtained solution with the second–order statistics of the noisy data with a negligible increase in the algorithmic complexity.
- *Autoregressive Moving Average (ARMA)*. ARMA models are superior to the basic AR ones in that they introduce a moving average term in the output equation, with the

Table 3: PSD functions corresponding to the ARX, AR/AR+Noise and ARMA parametric models.

ARX	AR/AR+Noise	ARMA
$S_y(f) = \left  \frac{\sum_{s=0}^{q_2} \gamma_s e^{-i2\pi f s T_s}}{1 - \sum_{t=0}^{q_1} \theta_t e^{-i2\pi f t T_s}} \right ^2$	$S_y(f) = \frac{\sigma_e^2}{ 1 - \sum_{t=0}^{q_1} \theta_t e^{-i2\pi f t T_s} ^2}$	$S_y(f) = \left  \frac{1 + \sum_{s=0}^{q_2} \gamma_s e^{-i2\pi f s T_s}}{1 - \sum_{t=0}^{q_1} \theta_t e^{-i2\pi f t T_s}} \right ^2$

benefit to provide smoother and clearly defined spectral curves. The regression form is given by:

$$y[k] + \sum_{t=1}^{q_1} \theta_t y[k - tT_s] = e[k] + \sum_{s=0}^{q_2} \gamma_s e[k - sT_s] \quad (5)$$

Since no other information apart from the one encoded in the model parameters is available, which is then converted in a more convenient frequency-driven form, the obtained PSD profiles can be passed as input to the PP algorithm allowing for the retrieval of the sought modal features. In this regard, STSM are used as an equivalent means for power spectrum estimation. Until that point, SysId based on STSM has been treated as a sensor-wise process, in compliance with its original formulation and to better stress its suitability for edge and extreme edge implementations. Nevertheless, all-signal-inclusive variants have also been formulated to tackle those scenarios in which the shortcomings of PP are too detrimental for an accurate estimate. They can be found in the literature with prefix *vector* (e.g., vector ARMA) and their governing equations can be constructed from the multi-variate form of the previously presented time series models.

#### 2.2.2.2 Stochastic Subspace Identification

Approaching the problem of SysId from a slightly different perspective, Stochastic Subspace Identification (SSI) strategies leverage a state-space representation of the model parameters provided by STSM to identify modal parameters in a centralized manner.

State-space models in stochastic form, where the adjective comes from the stochastic nature of the white noise term supposed as input of the structural system, exploit the concept of state variables  $z[k]$  for casting the driving structural equations into a mathematical system of first-order differential equations:

$$z[k + 1] = Az[k] + Be[k] \quad (6a)$$

$$y[k] = Cz[k] \quad (6b)$$

This formulation follows the dynamics of the underlying physical system as generally described in Eq. 1, with a  $q_2$ -dimensional set of input-dependent quantities transferring the effect of the input driving source  $e[k]$  to the output observed instance  $y[k]$ . The quantities  $A \in \mathbb{R}^{q_2 \times q_2}$ ,  $B \in \mathbb{R}^{q_2 \times 1}$  and  $C \in \mathbb{R}^{q_1 \times q_2}$  represent, in order, the square state companion matrix of the filter numerator polynomial, the input matrix and the output matrix. Among the various SSI implementations, the Covariance-driven Stochastic Subspace Identification (SSI-COV) method in Fig. 7 deserves particular attention owing to its

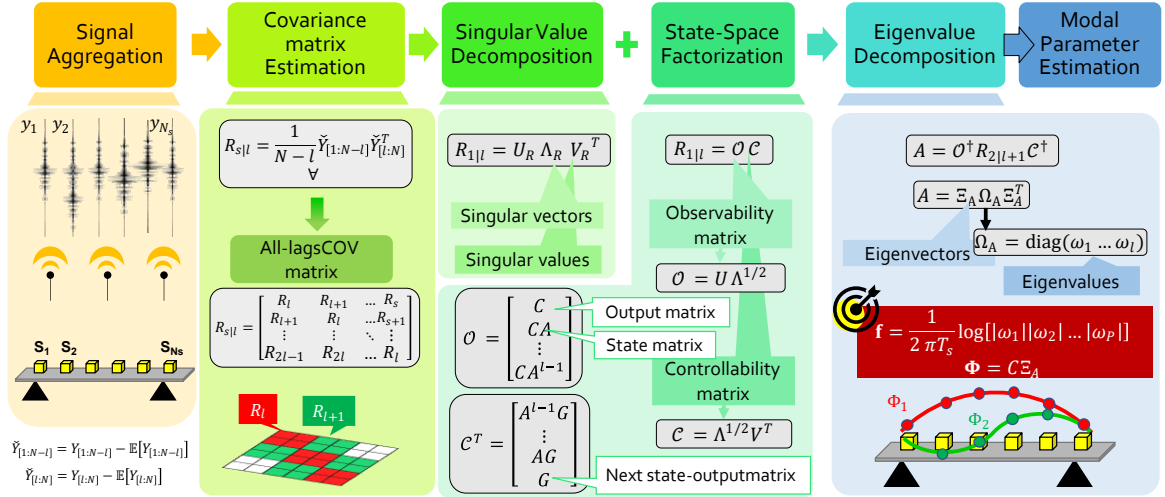


Figure 7: Schematic representation of the SSI-COV processing flow, from data collection up to modal parameter extraction.

robust recovery without affecting the processing time. SSI-COV takes its name from the calculation of the covariance function of the measured data, that represents the core function of the entire algorithm.

The approach involves the following steps:

1. Compute, for fixed time lag  $l$  and time shift  $s$ , the block Toeplitz matrix of dimension  $N_s l \times N_s l$

$$R_{s|l} = \begin{bmatrix} R_l & R_{l+1} & \dots & R_s \\ R_{l+1} & R_l & \dots & R_{s+1} \\ \vdots & \vdots & \ddots & \vdots \\ R_{2l-1} & R_{2l} & \dots & R_l \end{bmatrix} \quad (7)$$

in which the internal  $N_s \times N_s$  blocks:

$$R_l = \frac{1}{N-l} [Y_{[1:N-l]} - \mathbb{E}[Y_{[1:N-l]}]] [Y_{[l:N]} - \mathbb{E}[Y_{[l:N]}]]^T \in \mathbb{R}^{N_s \times N_s} \quad (8)$$

are nothing but the covariance matrix between the aggregated output signals  $Y$  acquired in the interval  $[1 : N - l]$  and  $[l : N]$ , respectively.

2. Perform the SVD decomposition of  $R_{1|l}$  ( $s = 1$ ), returning  $R_{1|l} = U_R \Lambda_R V_R^H$ , with  $U_R \in \mathbb{R}^{N_s l \times N_p}$  the rectangular matrix of left singular vectors and  $\Lambda_R \in \mathbb{R}^{N_p \times N_p}$  the diagonal matrix of singular values.
3. Apply the state-space factorization of the covariance matrix. Starting from the pure algebraic manipulation of the SVD, one may write  $R_{1|l} = U_R \Lambda_R V_R^H = O C$ . This means that  $R_{1|l}$  can be decomposed into the product of two matrices: the so-called observability matrix  $O = U \Lambda^{1/2}$  and controllability matrix  $C = \Lambda^{1/2} V^T$ . The advantage in pursuing such factorization is that the two latter quantities admit an alternative state-space formulation as  $O^T = [C \ CA \ \dots \ CA^{l-1}]$  and  $C = [A^{l-1}G \ \dots \ AG \ G]$  uniquely determined by the state-space matrices  $A, C$



and the next state–output matrix  $G \in \mathbb{R}^{N_p \times N_p}$ . While  $C$  and  $G$  can be easily extracted from the first  $N_p$  rows (columns) of the controllability and observability matrix, respectively, the computation of  $A$  is less straightforward and requires the additional computation of the time-lagged covariance matrix  $R_{2|l+1}$ ; it can be estimated as  $A = \mathcal{O}^\dagger R_{2|l+1} \mathcal{C}^\dagger$  ( $\dagger$  being the Moore–Penrose pseudoinverse operator).

4. Execute the eigenvalue decomposition of the above computed state matrix. This is decomposed as  $A = \Xi_A \Omega_A \Xi_A^T$ , corresponding to the product of the eigenvector matrix  $\Xi_A \in \mathbb{R}^{N_p \times N_p}$  and the diagonal matrix of  $N_p$  eigenvalues  $\omega_p$ , namely  $\Omega_A = \text{diag}[\omega_1, \dots, \omega_{N_p}]$ .

The described procedure draws foundations in the point–wise correspondence existing between the mathematical state–space matrices in (6) and their physical counterparts prescribed by the classical modal analysis theory. Indeed, once the state–space transformation driven by the solution of the eigenvalue problem of the state matrix  $A$  at step 4 of the procedure is applied, the mathematical system can be transformed into the "true" physical system, namely the one dictated by modal parameters, as:

$$z[k+1] = \Omega z[k] + \Pi^T e[k] \quad (9a)$$

$$y[k] = \Phi z[k] \quad (9b)$$

in which  $\Omega$  is the diagonal matrix of the eigenvalues of  $e^{A T_s}$ ,  $\Pi^T$  the modal participation vector<sup>5</sup> and  $\Phi$  the mode shape matrix.

In compliance with this akin transformation, natural frequencies of vibration  $f$  and mode shapes  $\Phi$  are finally given by:

$$f = \frac{|\log(\text{diag}(\Omega_A))|}{2\pi T_s} \quad (10a)$$

$$\Phi = C \Xi_A \quad (10b)$$

As a competitive variant to SSI-COV, in Data–driven Stochastic Subspace Identification (SSI-DATA) the computation of the covariance matrix is replaced by the projection of the row space of future outputs into the row space of past outputs. The problem with this method is that it involves the factorization of a very large matrix and, hence, becomes very computationally onerous. For this reason, SSI-COV inherently provides a much faster and efficient algorithmic solution, since the derivation of  $R_{s|l}$  can easily be obtained via the Fast Fourier Transform (FFT) algorithm. This is the reason why SSI-COV is preferred over SSI-DATA in an edge–computing perspective.

### 2.2.2.3 Blind Source Separation

The objective of Blind Source Separation (BSS) techniques is to identify the unknown signal sources  $S_s = [s_1(t), \dots, s_p(t)]$  from their observed mixtures  $Y$ , assuming that they are independent and identically distributed variables. Under this condition, each individual time series can be seen as the linear superposition of  $P$  distinct components combined via the mixing terms  $\kappa_{pi}$ :

<sup>5</sup> The modal participation vector is defined as the percentage of the system mass that participate in a particular mode.

$$\mathbf{y}_i(t) = \sum_{p=1}^P \kappa_{pi} s_p(t) \quad (11)$$

Transformed in matrix notation, Eq. (11) becomes  $\mathbf{Y} = \mathbf{K}\mathbf{S}_s$ , with  $\mathbf{K}$  connoting the mixing matrix to be estimated. The peculiar statistical distribution of  $s_p(t)$  implies that the zero-lag covariance matrices of  $\mathbf{S}_s$  and  $\mathbf{Y}$  coincide with  $\mathbf{R}_S(0) = \frac{1}{N}[\mathbf{S}_s - \mathbb{E}[\mathbf{S}_s]][\mathbf{S}_s - \mathbb{E}[\mathbf{S}_s]]^T = \mathbf{I}$  and  $\mathbf{R}_Y(0) = \mathbf{K}\mathbf{K}^T$ , respectively.

There are two reasons for leveraging BSS-driven methods in the context of OMA. Firstly, a clear advantage of BSS lies in its almost *agnostic* (in this sense, *blind*) nature, that is, very limited knowledge is required about the characteristics of the structure to be analysed. Secondly, assuming that the structure behaves as a linear system, its multi-modal response can be seen as the linear superposition of  $P$  independent components individually contributing to the overall energy. If this condition applies, it is immediate to observe that Eq. (11) has an equivalent counterpart in terms of modal parameters:

$$\mathbf{y}_i(t) = \sum_{p=1}^P \Phi_{pi} s_p(t) \quad (12)$$

where  $\Phi_{pi}$  indicate the modal coordinate for the  $p$ -th vibration mode  $s_p(t)$  at sensing location  $i$ . The importance of Eq. (12) is that, if the vibration behavior of the structure under analysis is linear and the superposition principle valid, "the modal coordinates may act as a virtual sources regardless of the number and type of the physical excitation forces" [37]. Therefore, a point-to-point correspondence exists between the mixing matrix  $\mathbf{K}$  returned as output of the BSS-based processing and the mode shape matrix, i.e.,  $\mathbf{K} = \Phi$ .

Among the different BSS solutions, Second Order Blind Identification (SOBI) deserves particular interest for vibration analysis, thanks to its capability to extract sources with a very different spectral content. This working principle perfectly matches the way in which structural energy distributes over the frequency spectrum, especially for underdamped systems undergoing free response. Indeed, in such cases, the signal sources, namely, the vibration modes, can be represented as harmonic decaying functions, each of them having a different amplitude. In these terms, what makes SOBI more effective is the exploitation of the temporal structure of the sources for facilitating their separation, a goal which is achieved by manipulating the acquired vibrations via second-order statistics [37].

A detailed description of the SOBI strategy is illustrated in Fig. 8 and mainly constitutes of two macro-phases. In the first step, the eigenvalue decomposition of  $\mathbf{R}_Y(0) = \Xi_R \Omega_R \Xi_R^T$  is performed and the eigenvectors/eigenvalues are employed to compute the so-called whitening matrix  $\mathbf{W} = \Omega_R^{1/2} \Xi_R^T$ . Once applied to the original time series matrix, the latter quantity has the effect of producing a new set of observed signals  $\mathbf{Y}_W = \mathbf{W}\mathbf{Y}$ , whose covariance matrix  $\mathbf{R}_{Y_w}(0) = \mathbf{W}\mathbf{K}\mathbf{K}^T\mathbf{W}^T$  at time lag zero now equals the identity matrix, whereas its  $\tau$ -lagged companion reads as  $\mathbf{R}_{Y_w}(\tau) = \mathbf{W}\mathbf{K}\mathbf{R}_S(\tau)\mathbf{K}^T\mathbf{W}^T$ .

At this point, let's introduce the unitary matrix  $\mathbf{U}_i = \mathbf{W}\mathbf{K}$ , which simplifies  $\mathbf{R}_{Y_w}(\tau) = \mathbf{U}_i\mathbf{R}_S(\tau)\mathbf{U}_i^T$ . On the other hand, the eigenvalue decomposition of the whitened time-lagged covariance matrix reads as  $\mathbf{R}_{Y_w}(\tau) = \Xi_{R_w} \Omega_{R_w} \Xi_{R_w}^T$ . The identity principle applied to these quantities states that, being  $\mathbf{R}_S(\tau)$  a diagonal matrix, the selected unitary matrix is nothing but the eigenvector matrix of  $\mathbf{R}_{Y_w}(\tau)$ , i.e.,  $\mathbf{U}_i = \Xi_{R_w} = \mathbf{W}\mathbf{K}$ . The latter can be uniquely determined via an appropriate choice of the time-lag value.

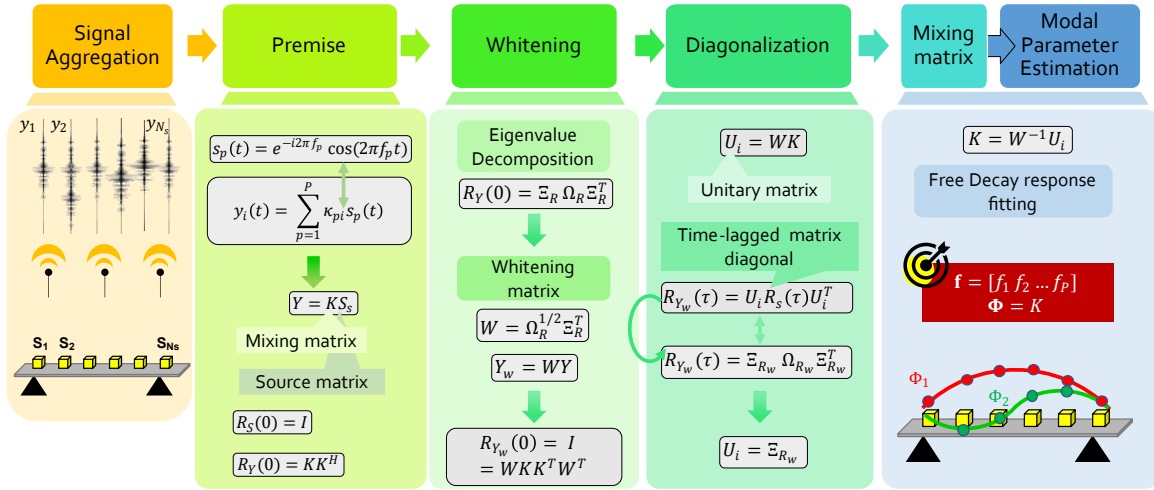


Figure 8: Schematic representation of the SOBI processing flow, from data collection up to modal parameter extraction.

Finally, the sought mode shape matrix can be easily retrieved as  $K = W^{-1} U_i$ , while further computation is necessary to estimate natural frequencies. To solve this task, considering a scenario characterised by free decay approximation as anticipated before, strategies based on time series fitting represent a valid solution. Some powerful methods addressing this specific problem are listed in Table 2 in the "Free-Decay Response" group: they can be used either standalone or, more often, in cascade to compensate from possible inaccuracies.

Another time-domain method is also worthy of mention: the Time Domain Decomposition (TDD) approach. It can be considered as the time variant of the FDD, with the substantial difference of being based on a recursive band-pass filtering of the input data, directly performed in the time domain and centered at the spectral bands of interest. Filtered signals are then used for the computation of the cross-correlation matrix, eventually replacing the CPSD matrix in the standard FDD workflow. TDD could be particularly profitable when very dense sensor networks are employed, since the initial filtering stage promotes the better isolation of the expected structural modes. On the other side, it requires a precise knowledge of the structure under inspection and this could limit its extensive applicability.

### 2.3 REVIEW OF OMA-BASED DAMAGE DETECTION ALGORITHMS

Once modal features have been extracted, the structural assessment process encompasses the following five steps: (i) detection, (ii) localization, (iii) classification and (iv) quantification of potential damages that may have been occurred, with the ultimate objective of (v) forecasting the remaining useful time in a predictive manner [40], [41]. Two alternative approaches are typically leveraged to reveal the presence of damages in vibrating structures: the former depends on the computation of modal-related metrics, whereas the latter tackles the problem from an agnostic perspective and, therefore, it relies on purely data-driven tools.

Conventionally applied for their inherent simplicity, modal-based methods can be subdivided into three main groups on the basis of the driving structural parameter [42]:

1. *frequency-based* solutions: these strategies look for local variations in the frequency values recovered at the monitoring time with respect to the ones collected in a reference structural status. In particular, when the difference between  $\mathbf{f}^{ref}$  and  $\mathbf{f}$  (i.e., the vectors of modal frequencies estimated in pristine and current in-operation conditions, respectively) is more than 5%, this is considered a remarkable deviation in the expected modes of vibration and a possible indication that the investigated structure is damaged [43].
2. *mode shape-based* methods: they exploit the spatial insight provided by mode shapes to provide a full-scale assessment of the structure. This is most commonly achieved via the computation of the Modal Assurance Criterion (MAC) [44] value, which quantifies in a global manner the level of superposition between the  $p$ -th experimental ( $\Phi_p$ ) and baseline ( $\Phi_p^{ref}$ ) mode shape vectors. MAC for mode  $p$  is defined as the normalized point-wise scalar product:

$$MAC_p = \frac{\left| \sum_{i=1}^{N_s} \Phi_p^{(i)} \Phi_p^{(i,ref)} \right|^2}{\sum_{i=1}^{N_s} \Phi_p^{(i),2} \sum_{i=1}^{N_s} \Phi_p^{(i,ref),2}} \quad (13)$$

while its all-embracing definition is usually expressed in form of a MAC matrix, presenting in the main diagonal the modal correlation between equally indexed components and, in the remaining entries, the cross level of similarity between distinct modes, which should be zero in the ideal case. For this reason, only the values in the main diagonal are considered, one scalar for each modal component. If variations in environmental conditions and/or structural defects are absent, the MAC factor returns a value of 100%; therefore, mode shape-driven damage identification strategies track reductions in modal fitting. More precisely, when MAC falls below 90%, the structural integrity may be significantly compromised. Equivalently, MAC values can be expressed as decimal quantities. Hereinafter, both formats will be used interchangeably.

3. *modal strain energy-based* methods, which sense for local variations in the energy sampled at local structural elements.

These modal-dependent procedures suffer from the fact they cannot handle in a robust manner the important effects induced by Environmental and Operational (EOP) agents hidden in vibration data, whose influence may mask the consequences of true structural degrade. It follows that such kinds of approaches have become inaccurate in multiple circumstances.

Fortunately, the fast development of AI technologies opens new perspectives for fully automated structural assessment. In OMA scenarios, it is appropriate to distinguish between modal parameter-dependent strategies, in which AI is used only at the end of the diagnostic process, and purely data-driven, in which no intermediate feature extraction step is encompassed and the structural status is inferred directly from time series via black-box models returning the integrity condition.

As the human brain understands patterns and hidden relationships amid variables, the task of inferring information from data by means of intelligent algorithms is commonly referred to as Machine Learning (ML). The abstract representation of an AI-network consists of the following three main elements: an input layer, several hidden layers where the actual processing part is executed, and a final output layer where the mined information can be retrieved. In more detail, each layer consists of a certain number of neurons which produce an output depending on a specific activation (transfer) function (a compelling selection of activation functions is provided in [45]). In compliance with this general architecture, the term Deep Learning (DL) is used to indicate all the ML implementations in which many layers and/or very dense neuron size are stacked to solve the goal; in this sense, they are considered *deep* variant of the standard ML architectures.

The AI procedures are differentiated on the basis of their learning approach, which can be either supervised (i.e., data are labelled), unsupervised, when no prior information is available about the distribution of data in the feature space, or semi-supervised, when only partial training is classified. Supervised learning tackles the problems of *classification* and *regression* from data, as it is aimed at forecasting which class the current instance belongs to on the basis of a ML model trained on labelled input. Indeed, regression is used to retrieve the mutual dependency between different variables, such as the correlation between structural features and environmental parameters. Conversely, *clustering*, i.e., the capability to group features according with their distribution in the feature space, and *association analysis*, i.e., the capability to retrieve valuable relationships from data, are byproducts of unsupervised ML. Finally, *novelty detection* is the task of identifying outliers in a given data distribution and it can be considered as a semi-supervised method owing to its dependency on a baseline model.

In Table 4, the most commonly applied algorithms fulfilling the above discussed AI task are schematized; a detailed description of these procedures can be found in [46].

Table 4: Summary of commonly adopted techniques for structural assessment: from conventional modal-related methods to AI-driven approaches.

Type	Approach	Task	Method	Ref
Modal Methods	frequency-based methods	Local Detection	Frequency shift	[43]
	mode shapes-based methods	Global Detection	Modal Assurance Criterion	[47]
		Localization	Modal Shape Curvature	
Machine Learning	Supervised	<ul style="list-style-type: none"> <li>- Classification</li> <li>- Regression</li> </ul>	Autoassociative Neural Network	[48]
			Support Vector Machine	[49]
			Bayesian Network	[50]
			Decision Tree	[51]
			$k$ -nearest	[52]
			Random Forest	[53]
	Unsupervised	<ul style="list-style-type: none"> <li>- Clustering</li> <li>- Association Analysis</li> </ul>	$k$ -clustering	[54]
			Density-based Clustering	[55]
			Fuzzy clustering	
Semi-supervised	<ul style="list-style-type: none"> <li>- Novelty detection</li> <li>- Outlier removal</li> </ul>	Mahalanobis Squared Distance	[56]	
		Gaussian Mixture Model	[48]	
		Control Chart	[57]	
		Reconstruction-based methods	[58]	
		Density-based methods		
Regression-based methods	[59]			
Deep Learning	Supervised Unsupervised Semi-supervised	<ul style="list-style-type: none"> <li>- Detection</li> <li>- Classification</li> <li>- Novelty detection</li> </ul>	Convolutional Neural Network	[60]
			Recurrent Neural Network	[61]
			Deep Autoencoder	[62]
			Restricted Boltzmann Machine	[63]

## MODE SHAPE ASSEMBLY FOR CLUSTERED ARCHITECTURES: A GRAPH SIGNAL PROCESSING PERSPECTIVE

---

### ABSTRACT

*In this Chapter, novel signal processing techniques for inter and intra-cluster data assembly are introduced to solve the critical task of full-scale structural assessment in presence of clustered monitoring architectures. In particular, a dedicated method based on the emerging Graph Signal Processing theory is specifically proposed to favor the deployment of non-overlapped sensor clusters. Such approach eases the sensorization process of complex structures despite the electrical and geometrical constraints which are still affecting state-of-the-art alternatives. The strategy is unique in that it maps the intrinsic smoothness characteristic of vibration signals to the smoothness assumption inherent in graph signals.*

The content of this Chapter is based upon the research work [P1]:

"Cluster-based vibration analysis of structures with graph signal processing"  
by Zonzini F., Girolami A., De Marchi L., Marzani A. and Brunelli, D. In *IEEE Transactions on Industrial Electronics*, vol. 68, no. 4, pp. 3465-3474, April 2021.  
©2020 IEEE

from which part of the text is drawn.

### 3.1 INTRODUCTION

A fundamental condition for the applicability of modal identification techniques is the synchronization of the acquired data. Such a requirement is particularly crucial for the reconstruction of mode shapes, since they convey a global structural understanding via the aggregation of different estimates taken at multiple sensing positions. Noteworthy, a lack of synchronicity generates unacceptable phase shifts which strongly impinge on the accuracy of the reconstructed modal features. To cite an example, authors in [64] pointed out that the maximum tolerable delay to not alter the accuracy of signal processing outcomes should be inferior to dozens of  $\mu\text{s}$ . Correspondingly, Krishnamurthy *et al.* [65] found that the detrimental effect of synchronicity faults can even exceed the sensor noise or intrinsic oscillations in internal clocks. In particular, it was demonstrated that the major consequences of these uncertainties are associated to higher modes of vibration [66], which are extremely sensitive to time synchronization errors independently from the sensors' positions.

Besides synchronization, the extraction of modal parameters is complicated in large scale or hazardous scenarios, where the high amount of data and sensing devices, combined with the inherent structural complexity and the possible difficulties in powering the sensor network, requires advanced and versatile hardware solutions. Moreover, high spatial resolution of sensors is beneficial for a precise damage assessment. In such context, thanks to their capability to easily adapt to the geometric characteristics of the inspected

structure, clustered sensor networks have been gradually developed to reduce the computational and energy budget associated to the gathering of sensor data and their transmission to a central processing unit. Therefore, the optimization of computational and communication resources is of the utmost importance for the design of a resilient and long-lasting monitoring system.

The aim of this Chapter is to alleviate the main drawbacks of state-of-the-art clustered architectures by means of advanced signal processing techniques, inspired by the emerging and more versatile graph signal representation, to be used in a post-processing phase to compensate for physical constraints. In these terms, it allows for a first level of sensor network optimization.

### 3.2 NETWORK TOPOLOGY FOR OMA

A compelling description of the architectural topologies commonly applied for OMA-based SHM scenarios is provided in [64], in which three main strategies are discussed:

1. *centralized data processing* (Fig. 9a): vibration data acquired at different sensing positions by extreme edge Peripheral Sensor Node (PSN)s are transferred with the proper timestamp to a central sink unit (SN). Either wired sensor networks or complex wireless synchronization protocols are required. This strategy, often adopted in the past for its architectural simplicity, may become unfeasible in current scenarios, where an increasing number of devices are simultaneously connected [67], [68].
2. *stand-alone schemes* (Fig. 9b): each sensor acts both as a sensing and a processing unit, hence minimizing the effects of limited bandwidth and communication constraints. Nevertheless, this solution hampers the possibility to perform data cross-correlation (e.g., extract mode shapes) between surrounding nodes since no synchronization command is usually broadcasted to the sensors [69].
3. *"divide-and-conquer"* strategies (Fig. 9c): taking advantage of a hierarchical design, data collection is performed by leaf devices at the extreme edge, subsequently forwarding locally elaborated features to a corresponding Cluster Head (CH) unit [70], [71]. These edge devices execute preliminary processing steps on data pertaining to their controlled area and finally transmit structural parameters to a common aggregating unit (SN), which is used to combine cluster-dependent information and to globally evaluate the structural integrity. Data fusion techniques, feature compression and communication protocols, if effectively combined and customized in such a distributed paradigm, may achieve the best possible compromise between inspection performances and bandwidth [54], [72].

It is worth noting that the last strategy perfectly handles the mode shapes reconstruction process. Specifically, although the processing is performed by multiple sub-networks referred to correspondent physical sub-structures, the presence of an additional assembly step is crucial to extract the global features of the monitored structure [73]. A plurality of schemes, which differ in terms of topology and task assignment, were implemented obeying to this hierarchical logic. In the following, some of the most noticeable solutions are reviewed, whereas additional examples are extensively described in [74]–[76].



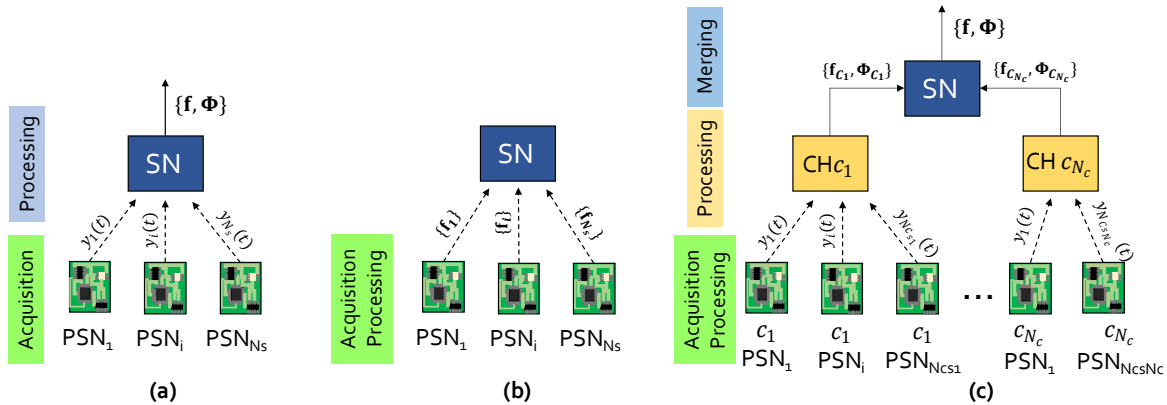


Figure 9: System topology for OMA-based SHM architectures: (a) centralized, (b) stand-alone and (c) divide-and-conquer scheme.

The multilevel cyber-physical system proposed in [77] is based on three main components: (i) edge nodes collect raw vibration samples and, after carrying out power spectrum analysis, transmit local modal features to their (ii) CH, which aggregates information concerning its controlled area; finally, (ii) a unique SN calculates all-embracing modal parameters. A similar, decentralized data aggregation procedure was implemented using a cluster-based wireless sensor network deployed on a truss structure [78]. Analogously, a study of a 14-bay girder was conducted with a two-layered cluster network [72], evidencing a favorable trade-off between the energy requirements and the quality of modal information. Alongside, a multi-channel monitoring architecture was exploited in [79] for the localization of impacts in aircraft composite structures. The hierarchical interoperability of several leaf nodes, few CH nodes and one multi-radio SN enabled the resulting architecture to achieve a reliable global assessment of the structural integrity. A different variant of akin configurations is reported in [80], in which the authors implemented a parallel processing architecture based on clusters of sensors that collaborate to compute structural dynamics under the orchestration of a central node. Their solution is characterized by a voting step, necessary to prevent local drifts that may contribute to the misestimation of vibrating frequencies. Conversely, the system in [81] exploits a different distribution of the computational tasks between the CHs and the central SN. In detail, CHs alone are in charge of feature extraction and decision making about structural health, whereas the SN coordinates them to ensure highly synchronized samples.

In this context, designing a network of partially overlapped clusters is a widely adopted strategy [72], [73] because it leads to two main benefits: (i) the possibility to make the monitoring system fault tolerant and resilient; (ii) the exploitation of native correlation between sampling points, which simplifies the task of concatenating modal data for the extraction of the global structural signature with minimal data transfer among CHs.

Mode shape concatenation in case of overlapped clusters rely on reference measurement positions shared by multiple clusters, a requirement which represents their main limitation. In fact, the presence of overlapping sampling positions unavoidably implies an increase in the number of devices to be installed. More importantly, in practical application scenarios, it might be impossible to deploy geometrically overlapped clusters due to the presence of geometrical obstacles and other building complexities [82].

The development of alternative and more effective solutions should cope with spatially-disjoint sub-networks conformable to the structural characteristics at hands and capable

of minimizing both the architectural costs and the electrical and communication constraints. In order to tackle these limitations affecting state-of-the-art clustered strategies, the purpose of this Chapter is to introduce a novel approach, which leverages the intrinsic capability of GSP techniques to model the inherent geometrical connectivity between different, non-overlapped clusters, despite the physical distance.

Several application fields have recently benefited from this emerging signal representation domain, including smart cities, traffic networks and environmental processes [83]. However, its application in SHM, and more precisely to vibration-based SHM contexts, still represents a pioneering field of research [83]–[85].

### 3.3 GSP-DRIVEN CLUSTER-BASED MODAL ANALYSIS

The cluster-based and GSP-driven monitoring solution, which has firstly been proposed in [P2], is schematically depicted in Fig. 10. The primary step (*clustered sampling*) consists in defining the most suitable cluster topology and the associated sensor-to-cluster assignment (usually depending on sensor proximity), while neglecting the requirement of reference sensing positions. From the chosen sensing positions, vibration signals  $y_i(t)$  are gathered at the CH level ready to be used for the following feature extraction phase. Indeed, according to the divide-and-conquer paradigm, an initial step is required in which the identification of modal parameters pertaining to each cluster (*local evaluation*) is fulfilled. To this purpose, any of the methodologies mentioned in Section 2.2 can be applied.

If  $N_C$  is the number of clusters, which has to be defined depending on the number of available sensors, their proximity on the structure and the minimum number of frequencies to be extracted,  $N_C$  sets of  $P$  natural frequencies ( $f_p^{c_i}$ ) and mode shapes ( $\Phi_p^{c_i}$ ) are obtained in the local identification step; then, a merging procedure has to be executed in order to characterize the whole monitored structure (*global evaluation*) in terms of global natural frequencies ( $\mathbf{f}$ ) and global mode shapes ( $\Phi$ ). It is worth stressing that, even if the local feature estimation process can provide a first-order indication about the macro-area inside which a damage could have occurred, it is, however, usually not possible to estimate with sufficient precision its location. The main reason is that, in order to keep the power consumption as low as possible, the sensor density inside each sub-cluster is preferably limited to the number of modes of interests  $P$ , a quantity which hardly exceeds five to ten devices. Regrettably, this operative constraint barely meets the requirement of dense sensor deployment which is at the basis of the majority of the damage localization technique discussed in Section 2.3. Consequently, full-scale parameters have to be preferred.

Two different procedures are performed in parallel to compute  $\mathbf{f}$  and  $\Phi$ :

1. The computation of the cumulative  $P$ -tuple of natural frequencies is simply obtained by averaging cluster-related frequency values per  $p$ -th modal component.
2. The estimation of  $\Phi$  is performed by concatenating the mode shape portions extracted within adjacent clusters and by properly setting a scaling factor  $\alpha_p^{c_i}$  for each cluster  $c_i$  and mode  $p$ , namely  $\tilde{\Phi}_p = [\alpha_p^{c_1} \Phi_p^{c_1}, \dots, \alpha_p^{c_{N_C}} \Phi_p^{c_{N_C}}]$ .

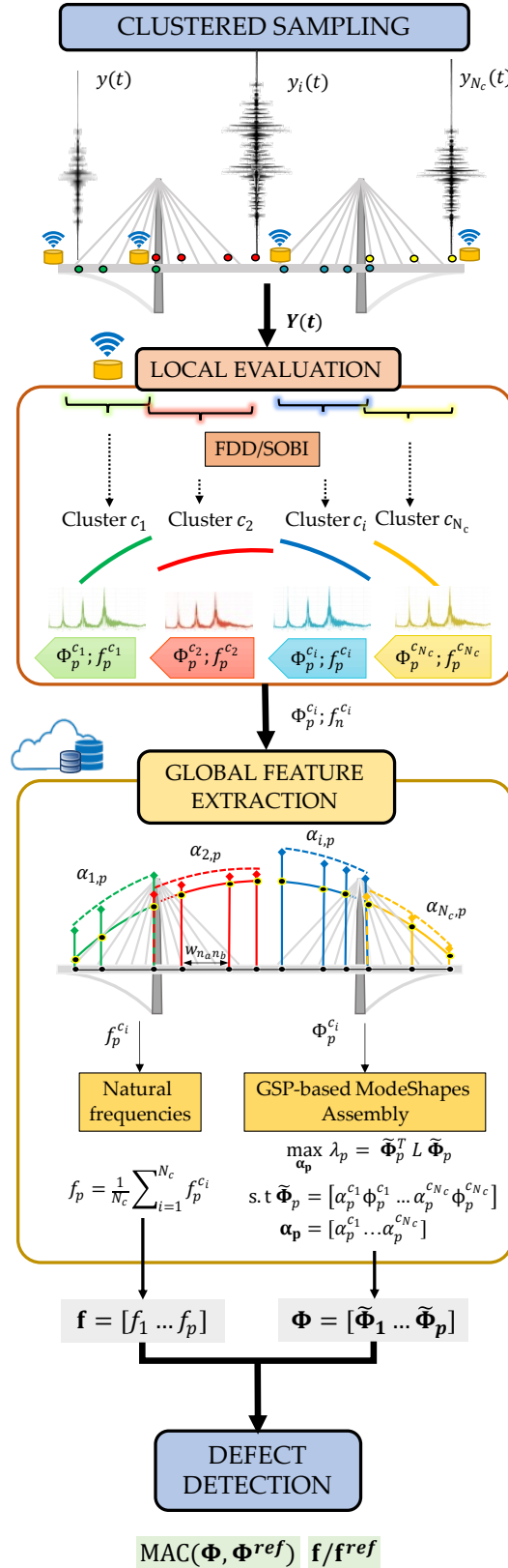


Figure 10: Schematic representation of the proposed cluster-based and GSP-driven monitoring architecture for vibration analysis. [©2020 IEEE]

After the computation of global parameters, the presence of damage can be assessed (*damage detection* phase) by comparing the extracted modal parameters, and in particular the mode shapes that are more robust damage indicators, with reference values; the latter can be derived either from the structural response in healthy (baseline) conditions [86] or as a result of numerical simulations for the designed (undamaged) structure.

Therefore, the problem of mode shape concatenation from multiple clusters converts in the estimation of the corresponding scaling factors  $\alpha_p^{c_i}$ : the GSP-driven algorithm is specifically designed to deal with this task. In the following, one state-of-the-art method used in case of partially overlapped clusters is reviewed since it represents a benchmark in the field and, then, the details of the novel GSP-driven method for non-overlapping clustered schemes are presented.

### 3.3.1 Mode shape assembly for overlapped clusters: the PoSER approach

The Post Separate Estimation Re-scaling (PoSER) algorithm [87] is a noteworthy procedure for mode shape concatenation based on partially overlapped clusters. According to this approach, two consecutive mode shape branches are re-scaled by minimizing in a least-squares sense the discrepancies between mode shape estimations at common reference positions [88]. Other covariance-driven methods draw their fundamentals on the second-order statistical properties of measured data, such as [89]. However, all these strategies rely on reference measurement positions.

With this assumption in mind, each set of real mode shape vectors inside a single cluster is decomposed via PoSER into overlapped and roving entries, indicated with subscripts *ov* and *rov* respectively. Equation (14) is provided in [90] to compute scaling factors  $\alpha_p^{c_i}$  in the  $c_i$ -cluster with respect to the same modal coordinates estimated in a predefined reference cluster  $c_R$ :

$$\alpha_p^{c_i} = \frac{\Phi_{ov,p}^{c_i}{}^T \Phi_{ov,p}^{c_R}}{\Phi_{ov,p}^{c_i}{}^T \Phi_{ov,p}^{c_i}} \quad (14)$$

where  $^T$  indicates the transpose operator. Once the scaling factors are computed, the global mode shape vector is assembled as:  $\tilde{\Phi}_p = [\alpha_p^{c_1} \Phi_{rov,p}^{c_1}, \dots, \alpha_p^{c_{N_c}} \Phi_{rov,p}^{c_{N_c}}]$ .

### 3.3.2 Mode shape assembly for non-overlapped clusters: the GSP-driven approach

The devised GSP-driven monitoring solution overcomes already existing architectures in terms of energy efficiency and flexibility in the deployment of sensor networks on complex structures. In fact, owing to its reference-free sensing topology, the achieved reduction of sensing positions lessens the energy demand, supporting more efficient power management strategies. In the sensor network deployment, the advantage is twofold. First of all, since it is based on non-overlapped clusters, the difficulties in wiring sensor nodes on complicated or hazardous scenarios can be easily bypassed. Secondly, as an immediate byproduct, the minimal cluster size that can be selected is uniquely dictated by the level of structural detail necessary to ensure a reliable inspection process, and not by the divide-and-conquer strategy itself.

Furthermore, the proposed approach is not influenced by operational uncertainties, such as temperature fluctuation and asynchronicity among clusters. Combining the versatility of the circuitry with the advantages of graph signal processing, the resulting system

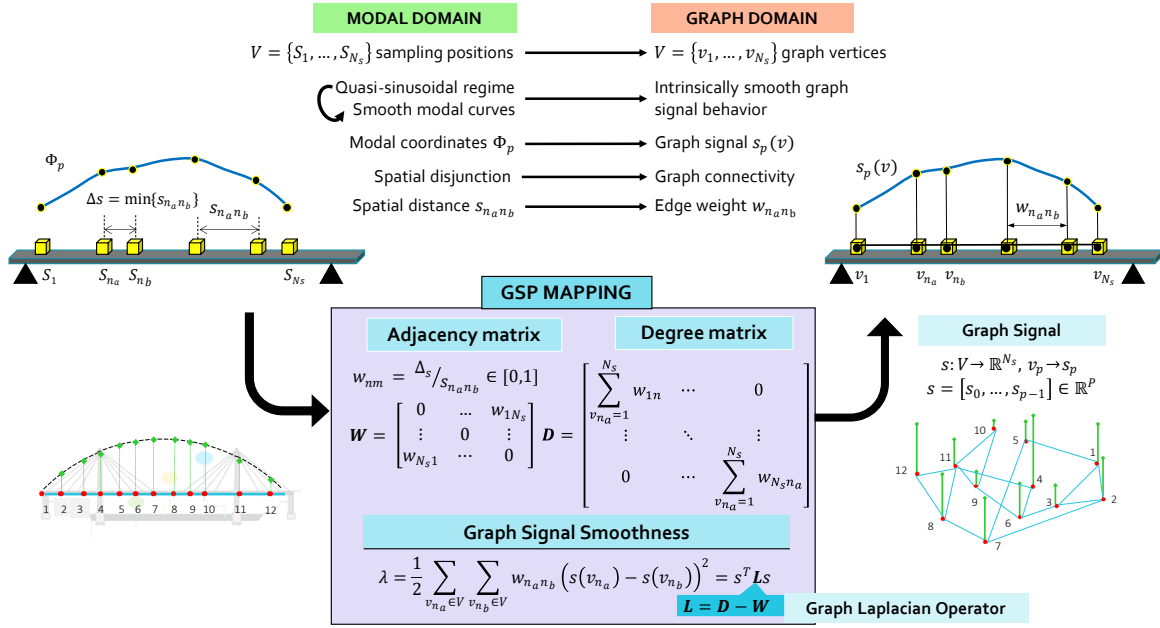


Figure 11: Mapping between modal-related quantities and graph domain. Graph signal properties depend on the Adjacency and Degree matrices, whose entries are uniquely determined by the chosen edge weights  $w_{n_a n_b}$ .

is suitable for different and complex application-fields, revealing to be a competitive alternative to traditional monitoring frameworks.

### 3.3.2.1 Mapping modal features in the graph domain

The analysis of signals defined on graphs has been gaining increasing attention due to its capability of modeling inherent patterns coded in the acquired data as similarities between adjacent vertices [84], [91]. A *graph* is a mathematical entity described by a set of vertices connected by edges, whose algebraic representation is expressed through the *Adjacency* and *Degree* matrices [91]. The weighted Adjacency matrix  $\mathbf{W}$  expresses the vertex connectivity between two generic nodes  $v_{n_a}$  and  $v_{n_b}$  by means of a correspondent edge weight  $w_{n_a n_b}$ . Conversely, each entry of the Degree matrix  $\mathbf{D}$  is given by the sum of all the weights incident on a specific vertex.

In this framework, the selection of the proper graph topology represents the foremost step. To this end, since the sensor network topology not only exploits strategic structural positions, but it is also known in advance, it offers a powerful means to define a graph structure: mode shape values corresponding to the different sensor node locations are mapped as graph signals associated to graph vertices and edge weights are defined as the inverse of the sensor nodes' spatial distances. This modal-to-graph mapping is clarified in Fig. 11, in which the similarities between the two domains, i.e., the modal and the graph one, are underlined with point-to-point correspondences. The utmost advantage of such transformation is that the physical disjunction between non-overlapped clusters of sensors can be compensated by the logical connection of adjacent vertexes via a proper estimation of the corresponding arches.

The focal point of the modal-to-graph transformation is inspired by the idea to move the smooth modal pattern (given by the quasi sinusoidal vibration behaviour) of mode

shapes into the smoothness assumption (i.e., smooth changes between connected vertices) [92] intrinsic in graph signals. This similarity led to the formalization of the mode shape smoothness  $\lambda_p$ , defined as:

$$\lambda_p = \frac{1}{2} \sum_{n_a=1}^{N_s} \sum_{n_b=1}^{N_s} w_{n_a n_b} (\tilde{\Phi}_p(n_a) - \tilde{\Phi}_p(n_b))^2 = \tilde{\Phi}_p^T \mathbf{L} \tilde{\Phi}_p \quad (15)$$

where  $\tilde{\Phi}_p$  is the  $p$ -th mode shape vector, and  $\mathbf{L} = \mathbf{D} - \mathbf{W}$  is the so called graph Laplacian operator.

Indeed, considering the quasi-sinusoidal dynamic regime typical of vibrating structures, mode shapes inherently exhibit a smooth profile. However, when they are assembled from the pure concatenation of the values collected from different clusters (i.e., when the scaling factors are all equal to 1), discontinuities or abrupt jumps may result. To this end, it is worth considering that, even if this jagged effect is particular prominent for higher-order modes, especially when a very sparse instrumentation is available, the nature of the underlying mode shapes to be reconstructed is still characterized by a sinusoidal pattern, which is the main assumption to be satisfied for the applicability of the method. Indeed, the conceived GSP-driven algorithm aims at compensating these discontinuities and to maximize the mode shape smoothness.

Given a generic mode shape  $p$ , such algorithm involves the following steps:

1. During the initialization phase, scaling factors  $\alpha_p^{(0)} = [\alpha_p^{c_1}, \dots, \alpha_p^{c_{N_c}}]$  are set to 1.
2. Then, mode shapes are assembled and the smoothness function  $\lambda_p$  is computed according to (15).
3. A prediction phase updates the scaling coefficients: the values  $\alpha_p^{(k)}$  at iteration  $k$  are computed as:

$$\alpha_p^{(k)} = \alpha_p^{(k-1)} - r_p^{(k)} \nabla \lambda_p(\alpha_p^{(k-1)}) \quad (16)$$

in which  $r_p^{(k)} = r_p^{(k-1)} \left( 1 + \frac{\lambda_p^k - \lambda_p^{k-1}}{\max\{\lambda_p^k, \lambda_p^{k-1}\}} \right)$  and  $\nabla \lambda_p(\cdot)$  are the updating ratio and the smoothness gradient, respectively.

4. Steps 2) and 3) are repeated until the smoothness variation between subsequent iterations is smaller than a predefined tolerance  $\epsilon$ . Apart from setting  $\epsilon$ , the process is fully automated.

The same procedure has to be executed for every mode shape, finally yielding the sought matrix of assembled mode shape  $\tilde{\Phi} = [\tilde{\Phi}_1 \dots \tilde{\Phi}_p]$ .

### 3.4 EXPERIMENTAL VALIDATION

The effectiveness of the GSP-driven methodology has been validated with experimental data from a simply-supported steel beam. First of all, a description of the monitoring architecture in terms of network topology and developed electronics is enclosed. Then, the actual algorithmic analysis is entered, in which the novel mode shape assembly technique is tested.

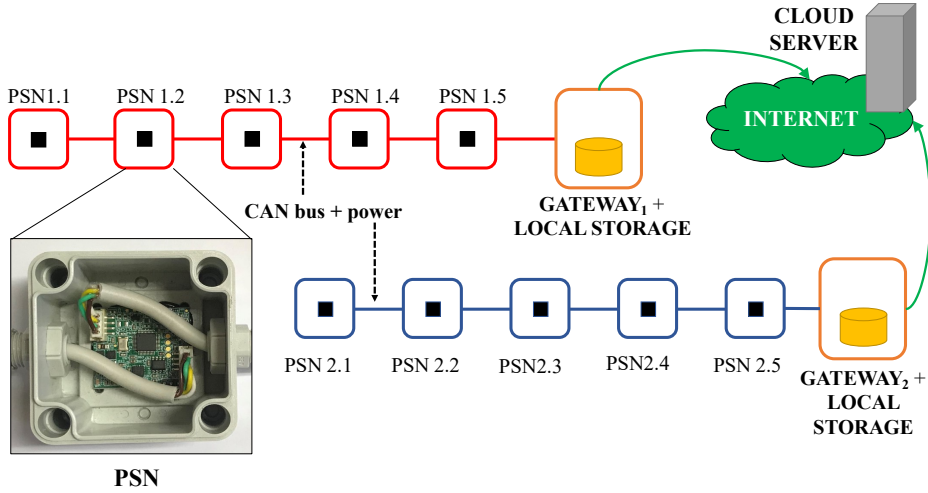


Figure 12: Topology of the monitoring network deployed for the validation of the GSP-based mode shape assembly algorithm. [©2020 IEEE]

### 3.4.1 SHM network description

#### 3.4.1.1 Network topology

The monitoring architecture includes linked chains of connected sensors organized in different clusters, each of them coordinated by a gateway unit which acts as a corresponding CH (Fig. 12). The signal acquisition chain is organized as follows. Each PSN, shown in the bottom left corner of Fig. 12, uses a 32-bit ARM Cortex M4 microcontroller to digitally filter the samples coming from the accelerometer, precisely employing a Finite Impulse Response (FIR) filter implemented with the Floating Point Unit (FPU). Consequently, the gateway collects filtered signals provided by the sensors and forwards data to a cloud server by means of a wireless channel. At this common data-aggregation level, a corresponding virtual SN is in charge of feature extraction and data merging.

As already mentioned, the sensor network design depends on three major factors: energy efficiency, computational complexity and structural properties. From an electronic point of view, two quantities mainly contribute to the total energy budget, namely the power adsorbed by active nodes for sampling and transmitting data, and the gateway communication costs. The computational effort is a function of the total volume of samples to be collected within a specific time-frame (which is an application-dependent quantity) and of the cluster size. More specifically, the sensor network can be described through the following set of parameters: the total amount of available devices  $N_s$  and the number of clusters  $N_c$ . The corresponding cluster size  $N_{C_s}$  and the overlapping factor  $N_o$  need to be optimized taking into account the practical difficulties which can be associated to the installation of sensors, the maximum admitted distance between the devices and the presence of nodal points of mode shapes. In particular, the lower bound for  $N_{C_s}$  is given by the number  $P$  of modes which is sufficient to characterize the dynamic behaviour of the structure under test [72], i.e.  $N_{C_s} \geq P$ . For the overlapping factor, the cases of  $N_o = 0$  and  $N_o = 1$  are the ones that correspond to the minimal sensor redundancy and, for this reason, these cases have been evaluated in the experimental campaign.

### 3.4.1.2 *Electronic equipment*

At its core, each PSN (whose architecture has firstly been disseminated in [P<sub>3</sub>]) integrates a three-axes accelerometer, the LIS344ALH MEMS device manufactured by ST Microelectronics and characterized by the lowest noise density in its class ( $50 \mu\text{g}/\sqrt{\text{Hz}}$ ). This device enables a maximum operative band of 1.8 kHz in a dynamic range of  $\pm 2 \text{ g}$ . In case of civil structures, where principal modal frequencies are typically below 30 Hz, using a data rate of  $F_s = 100 \text{ Hz}$  is reasonable for elaborating all the fundamental modes of vibration and, thus, this sampling rate was selected.

Moreover, in order to optimize the performances of the circuitry and to meet the same features of expensive piezoelectric accelerometers characterized by a high full-scale to noise-floor ratios, an oversampling strategy with multiplication factor of 256 was implemented. In this way, the 12-bit Analog-to-Digital (ADC) conversion resolution of the Microcontroller Unit (MCU) inside the PSN was improved up to 16-bit, correspondingly incrementing the signal to quantization noise ratio. The procedure was practically realized by setting an ADC sampling frequency of 25.6 kHz in conjunction with an internal DMA data management, configured to move 12-bit conversion from the ADC to a circular buffer in the memory. Finally, a digital low-pass multistage decimation FIR filter was developed to generate, at the desired sampling frequency, the final stream of three-axes 16-bit acceleration data. According to the capacity of the transmission channel at the selected sampling frequency, a maximum number of 19 sensors can be connected to each Controller Area Network (CAN) port provided by the gateway. In terms of power consumption, when powered at 5 V in normal operating mode, the current drawn by each node and the gateway device amounts to 32.5 mA and 340 mA, respectively.

Moving to the gateway device, its most relevant functionality is the synchronization of the set of peripheral sensors, which are connected through a CAN bus. This protocol is used for the communication from the PSNs to the CH, allowing for a native synchronization between clocks and compliant with the simultaneous acquisition from various PSNs at a regular and high data rate of 250 000 baud over 40 m cable. These transmission properties are enough for instrumenting most of the residential and industrial buildings in case of vibration analysis. As such, each cluster automatically embeds its own timestamp, to be used in a post processing phase for data cross-correlation, and no-coordination between different groups of sensors is yet necessary.

## 3.4.2 *The use case: a simply supported steel beam*

### 3.4.2.1 *Material*

The performance of the developed GSP-driven cluster-based monitoring system was evaluated on a 2142x10x60 mm pinned-pinned steel beam, with an effective distance of 2052 mm between the supports. Such a setup represents a widely adopted vibration analysis test-bed, because it permits the use of a simple numerical model for the analytical prediction of modal parameters. At the same time, numerical models are readily implementable for this structure even in damaged conditions, without needing to practically impair it. It is also worth considering that, regardless of its structural simplicity, the dynamics of a simply supported beam can also be representative of that exhibited by many larger structures, including precast concrete beams and small bridges [72].



The sampling frequency imposed a Nyquist bandwidth of 50 Hz, that was sufficient to retain the first three modes; accordingly, the parameter  $P$  was set equal to 3. Assuming the nominal mechanical properties already described in [P3], [P4], the first three flexural frequencies of vibrations,  $f_1 = 5.32$  Hz,  $f_2 = 21.32$  Hz,  $f_3 = 47.92$  Hz, and the first three mode shapes ( $\Phi_1, \Phi_2, \Phi_3$ ) were analytically predicted by using closed form formulae. Experimentally, the structure was excited with impact hammer and free vibration responses were acquired in a time window of 100 s.

#### 3.4.2.2 Methods

Faulty conditions were mimicked by hanging a dead mass on the beam at different positions, thus simulating the formation of localized damages. Changes in the dynamic response of the structure were consequently induced, primarily due to the non symmetric mass distribution. This extra weight, in fact, causes variations in the mode shapes that scatter across the mass placement. Correspondingly, spectral shifts with respect to mass-free modal frequencies occur, proportionally to the induced perturbation. Notably, the adopted damaging method might produce variations which are remarkably more pronounced to the ones which can occur in real scenarios; however, it serves as an efficient means to investigate the actual anomaly detection capability of the method in a non-destructive manner.

The effects of the mass position  $x_a$  and the mass values  $m_a$  were evaluated. In detail, three different positions  $x_{a,1} = 200$  mm,  $x_{a,2} = 400$  mm and  $x_{a,3} = 600$  mm were considered. Besides, the following mass values were hanged step by step at location  $x_{a,2}$ :  $m_{a,1} = 1.078$  kg,  $m_{a,2} = 1.847$  kg,  $m_{a,3} = 2.591$  kg. The deviations induced in natural frequencies and mode shapes were *a priori* estimated through an ad-hoc finite element numerical model, taking into account the effect of the added mass on the stiffness and rigidity of the beam. To accomplish this task, the numerical model discussed in [93] was revised including the extra impingement of the electronic equipment (e.g., the mass of the sensor). Accordingly, experimental modal parameters were extracted and compared to simulation results in order to validate the suitability of the proposed scheme under potential defective conditions.

#### 3.4.2.3 Clustering scheme

In the considered experiments, a sensor network consisting of two clusters (specifically labelled by red and blue markers) was designed, whose grouping schemes are depicted in Fig. 13. In particular, case  $O_v$  sketches a network with overlapped clusters, each consisting of 5 sensor nodes ( $S_{1,\dots,5}$  and  $S_{5,\dots,9}$ , respectively) installed at nine different positions uniformly distributed along the entire length of the beam. In this case, modal parameters were extracted with the  $P_{oSER}$  procedure, and accelerometer  $A_5$  was used as the reference point for re-scaling. Conversely, cases A-D are related to non-overlapped clusters with different (and irregular) sensor spacing to examine the influence of sensor placement in modal parameter estimation. In detail, case D is a particularly unfavourable arrangement with minimal clusters' size and significant inter-cluster distance, while case A is the most redundant and denser configuration.

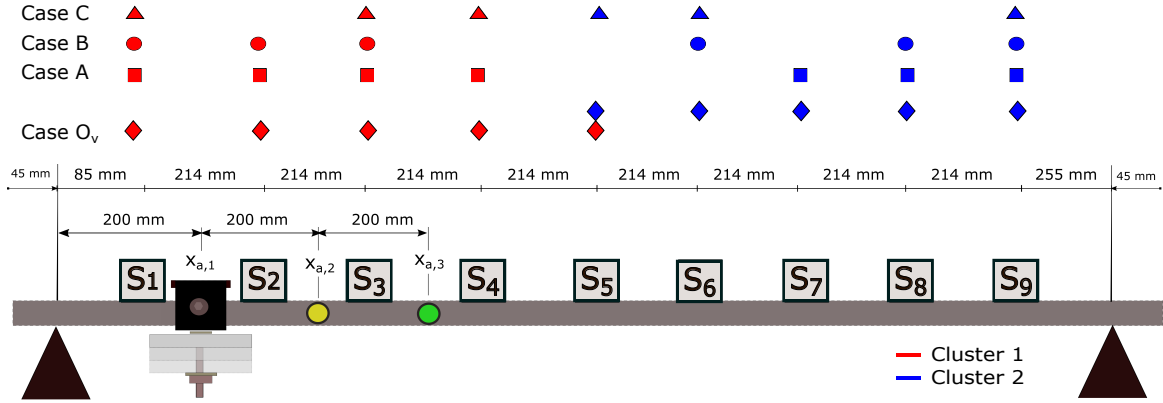


Figure 13: Experimental setup with two clusters of sensors (red and blue-labelled chains): overlapping networks in correspondence of node  $A_5$  (case  $O_v$ ) and non-overlapping (case A, B, C, D) configurations. Unhealthy conditions were induced by means of a concentrated roving mass laterally hanged at positions  $x_{a,1}$ ,  $x_{a,2}$ ,  $x_{a,3}$ . [©2020 IEEE]

Resilience against thermal fluctuations, excitation uncertainty and cluster asynchronicity were additionally investigated<sup>1</sup>. For this purpose, the experiments were designed to acquire acceleration signals separately with the two clusters in two different moments: sensors at positions  $S_{1,\dots,5}$  (cluster  $C_1$ ) were activated at operating conditions characterized by high temperatures ( $29^\circ\text{C}$ ) and low input force, whereas sensors  $S_{5,\dots,9}$  (cluster  $C_2$ ) worked at relatively low temperatures ( $17^\circ\text{C}$ ) and stronger excitation energy.

### 3.4.3 Results

#### 3.4.3.1 Frequency estimation

A frequency-based assessment was firstly conducted. The spectral profiles depicted in Fig. 14 were generated with the FDD algorithm and demonstrate the capability of the system to identify variations in natural frequencies due to the presence of added masses. In fact, the results reveal good vertical alignment between experimental spectral peaks and numerically predicted modal components. The relative differences with respect to theoretical simulations in the same operating conditions are reported in Table 5. For all the tested configurations, an average discrepancy of 1.183% is observed considering all the three modes.

#### 3.4.3.2 Mode shape reconstruction

The analysis was then extended to the reconstruction of mode shapes. The signal processing techniques FDD and SOBI mentioned in Section 2.2 were applied to extract the modal parameters related to each cluster. The mode shapes were thereafter concatenated according to the algorithmic procedures detailed in Section 3.3. For each inspected configuration, MAC percentages computed between numerically expected and experimentally estimated mode shapes were employed to quantify the correspondent degree of structural coherence.

<sup>1</sup> Supposing the behavior of the beam is stationary, asynchronicity is tested at a cluster level, meaning that, according to what has been discussed in Section 3.1, sensors within each cluster are perfectly synchronized via the CAN bus; in absence of this condition, the retrieval of cluster-dependent mode shapes is not viable.

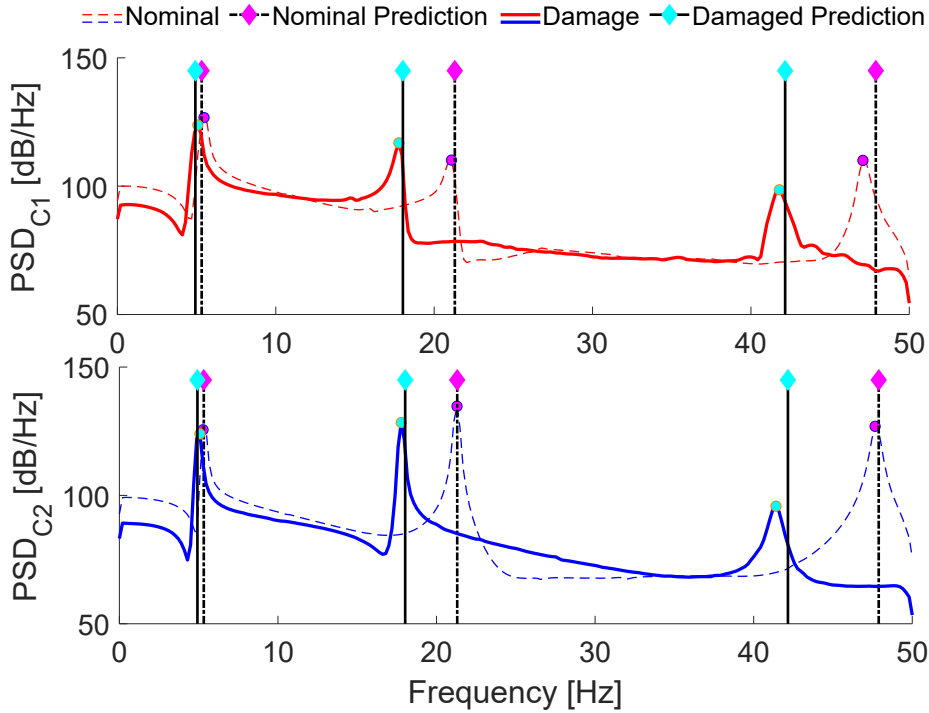


Figure 14: Spectra of signals acquired with sensor cluster  $C_1$  (top graph) and  $C_2$  (bottom graph). The damaged configuration (continuous line) corresponding to operating conditions perturbed with additive mass  $m_a = 2.591$  kg at  $x_a = 400$  mm is superimposed to the nominal case (dotted line). Numerical predictions in both situations are also included.[©2020 IEEE]

### 3.4.3.3 Overlapped configuration

The performance of the PoSER approach [87] in case of overlapped clusters is reported in Table 6 (case  $O_v$ ). Noticeably, an almost perfect superimposition to theoretical predictions is achieved, attested by modal correlation indexes which are always above 98% even in the worst case, associated with strongly perturbed tests performed with the heaviest mass. It is worth highlighting that the estimated SOBI-based mode shapes also fit the model nearly perfectly in all the scenarios, showing its robustness for modal analysis purposes in spite of its fully unsupervised approach.

### 3.4.3.4 Non-overlapped configurations

Moving to non-overlapped network configurations (case A, B, C and D), the very same damaged conditions were tested. In these cases, modal coordinates were extracted by means of the already discussed graph smoothness maximization method. A tolerance error  $\epsilon = 10^{-4}$ , an initial updating ratio  $r^{(0)} = 0.5$  and a starting smoothness gradient  $\nabla\lambda_p = 1$  were empirically estimated to achieve the best trade-off between the resulting modal accuracy and the algorithmic convergence velocity.

The potential of GSP tools elicits from their intrinsic capability to derive the proper graph topology compliant to the best graph signal smoothness in all the considered sensor arrangements. An example of graph-combined mode shapes (black dots) is drawn in Fig.15, where raw modal coordinates (black stars) are extracted through the FDD technique for case C. The numerical values drawn above arches connecting adjacent vertices repre-

Table 5: Relative error in FDD-driven natural frequencies estimation between experimental data and theoretical prediction for different scenarios.

Mode	Fixed mass $m_{a,1}$			Fixed position $\chi_{a,1}$	
	$\chi_{a,1}$	$\chi_{a,2}$	$\chi_{a,3}$	$m_{a,2}$	$m_{a,3}$
	[%]	[%]	[%]	[%]	[%]
$f_1$	2.003	1.525	1.235	1.109	1.186
$f_2$	0.957	0.687	0.938	0.006	1.436
$f_3$	0.710	1.279	1.436	1.222	1.348

sent the corresponding edge weights. Going deeper into the analysis, an evident greater level of superimposition is achieved after GSP operators are applied for the reconstruction of the complete mode shapes. In order to perform a quantitative evaluation, cases A-D in Table 6 synthetically report computed MAC values between numerical expectations and graph-assembled modal branches, the highly accurate fitting among them being proved by modal correlation indexes averagely above 95%.

Another aspect should further be underlined: despite isolated cases related to the reconstruction of the third vibration mode when the heaviest masses are hanged, the effectiveness of the proposed GSP algorithm attains very high scores both starting with supervised (FDD) and unsupervised (SOBI) modal inspection methods. In particular, the maximum deviation between these two categories amounts to less than 7 point percentages, without exceeding the tolerance interval of 90% considered as a damage threshold. Furthermore, conducting a comparative analysis with respect to already existing methodologies, albeit a slight decrease in modal fitting occurs among traditional overlapped solutions and unconventional disjoint configurations, the coherence of the GSP method averagely worsens for less than 1.1% compared to covariance-based alternatives. As a matter of fact, it is reasonable that the worst performance is associated to sparser sampling configurations, longer intra-cluster distances, and minimal cluster sizes (i.e.  $N_{C_s} = P$ ). Nevertheless, the proposed processing achieved a maximum deviation of approximately 7% (related to the reconstruction of the third mode for sensing case D, again in the tolerance range), hence showing its suitability for damage monitoring tasks.

### 3.5 CONCLUSIONS

In this Chapter, a novel cluster-based vibration monitoring system, suitable for structural integrity assessment, is described. The system stands out for its modularity, level of integration and versatility, supporting the design of divide-and-conquer strategy for modal analysis. In particular, a dedicated GSP-driven method for the combination of modal parameters in case of non-overlapped sensor clusters was proposed as a means for joint - electrical and structural - improvement of the monitoring network.

The accuracy of the monitoring system was evaluated through an experimental campaign designed to take into account non-stationary phenomena, such as the effect of thermal excursions, blind excitation, and lack of synchronization between clusters. In ad-

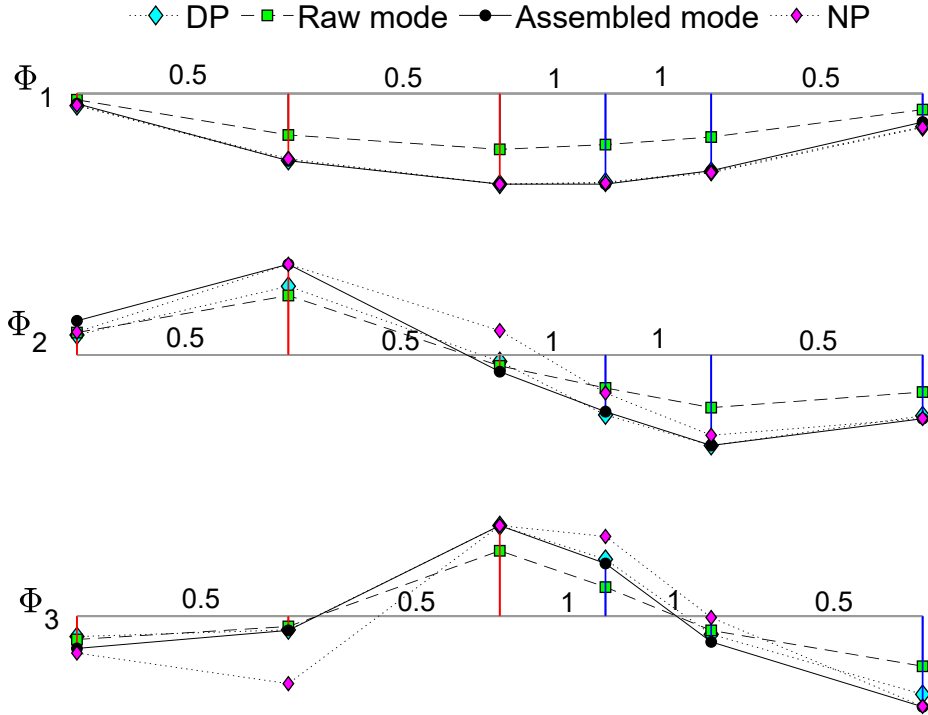


Figure 15: Assembled mode shapes for the altered beam with additive mass  $m_a = 2.591$  kg at  $x_{a,2}$  under non-overlapped configuration of case C. Raw modal coordinates are extracted by means of the FDD reconstruction method. Theoretical predictions in nominal (NP) and damaged status (DP) are also provided. [©2020 IEEE]

dition, the nominal properties of the structure were altered by simulating the presence of a defect through the insertion of concentrated masses. The properties of the developed hardware and software solutions used in the experimental setting proved to output reliable results. In fact, the spectral and modal signatures estimated at the end of the GSP-driven and cluster-based monitoring architecture showed a significant concordance to theoretical predictions. For this reason, the presented mode shape assembly procedure candidates as a promising strategy to overtake the current limitations of state-of-the-art, overlapped and decentralized platforms for vibration diagnostics.

Table 6: MAC values comparing numerical prediction and assembled mode shapes in presence of altered conditions with overlapped clusters (case  $O_v$ -PoSER approach) and spatially independent clusters (case A, B, C, and D-GSP approach).

Case	Mode	Fixed mass $m_{a,1}$			Fixed position $x_{a,2}$		
		$x_{a,1}$	$x_{a,2}$	$x_{a,3}$	$m_{a,2}$	$m_{a,3}$	
$O_v$	FDD	f <sub>1</sub>	99.93	99.92	99.82	99.94	99.94
		f <sub>2</sub>	99.15	99.25	99.46	99.13	98.21
		f <sub>3</sub>	99.49	99.72	98.44	99.27	99.11
	SOBI	f <sub>1</sub>	99.96	99.93	99.91	99.95	99.95
		f <sub>2</sub>	99.25	99.16	99.21	94.15	98.85
		f <sub>3</sub>	99.75	99.41	98.84	99.00	97.40
A	FDD	f <sub>1</sub>	99.83	99.63	99.58	99.54	99.58
		f <sub>2</sub>	99.17	97.31	96.62	97.01	98.55
		f <sub>3</sub>	98.56	98.54	99.16	97.20	97.49
	SOBI	f <sub>1</sub>	99.95	99.92	99.89	99.85	99.90
		f <sub>2</sub>	99.18	98.18	97.31	97.83	96.87
		f <sub>3</sub>	98.86	98.66	98.89	97.21	96.04
B	FDD	f <sub>1</sub>	99.90	99.82	99.66	99.54	99.81
		f <sub>2</sub>	99.61	99.41	98.13	98.53	97.36
		f <sub>3</sub>	99.13	98.73	98.27	96.71	97.00
	SOBI	f <sub>1</sub>	99.92	99.88	99.85	99.83	99.88
		f <sub>2</sub>	99.78	99.43	98.80	98.64	97.46
		f <sub>3</sub>	99.57	98.74	98.68	97.09	96.25
C	FDD	f <sub>1</sub>	99.95	99.92	99.76	95.77	95.84
		f <sub>2</sub>	99.33	99.49	98.29	98.48	97.40
		f <sub>3</sub>	99.30	99.51	95.42	99.11	99.39
	SOBI	f <sub>1</sub>	99.97	99.95	99.92	96.07	99.97
		f <sub>2</sub>	99.40	99.43	98.48	98.64	97.35
		f <sub>3</sub>	98.65	99.44	95.61	98.69	93.06
D	FDD	f <sub>1</sub>	97.13	97.54	96.79	96.64	97.72
		f <sub>2</sub>	99.15	99.06	97.68	98.18	96.90
		f <sub>3</sub>	99.33	98.96	98.74	96.38	94.87
	SOBI	f <sub>1</sub>	97.00	97.39	97.35	97.33	97.63
		f <sub>2</sub>	99.11	99.18	98.48	98.29	97.02
		f <sub>3</sub>	99.29	98.58	98.72	95.86	90.13

## INTRODUCTION

*This Chapter deals with the problem of network load reduction for vibration-based SHM systems. Accordingly, advanced data compression techniques driven by the Compressed Sensing paradigm are presented and a novel model-assisted method for the design of the best adapted compression schemes is coherently proposed. The effectiveness of the strategy for structural assessment is validated in different experimental campaigns. A hardware-oriented perspective is endorsed, thus investigating the embodiment of the analysed method in resource-constrained devices.*

The content of this Chapter is based upon the research work [P5]:

"Model-Assisted Compressed Sensing for Vibration-Based Structural Health Monitoring" by Zonzini F., Zauli M., Mangia M., Testoni N. and De Marchi L. in *IEEE Transactions on Industrial Informatics*, vol. 17, no. 11, pp. 7338-7347, Nov. 2021. ©2021 IEEE

from which part of the text is drawn.

## 4.1 INTRODUCTION

Data compression is particularly promising in the field of vibration-based assessment because structural responses exhibit peculiar spectral profiles characterized by a sparse frequency content and, therefore, the total structural energy is concentrated in a few and highly localized harmonics which can provide quite an accurate snapshot of the current health status. Accordingly, it is possible to envision a monitoring system capable of compressing in real-time vibration signals by preserving only the information associated with these most energetic modes. This might reduce to a large extent the amount of data to be transmitted along the network, without hampering the quality of the monitoring process.

Moreover, it is worth noticing that data compression strategies can be fruitfully employed both for wired and wireless architectures. In the former case, in particular for multiplex wiring systems, the reduction of data packets to be transmitted paves the way to an increase in the number of sensors simultaneously connected to the same central unit via daisy-chaining. In wireless communication systems, instead, exploiting a data reduction approach may be beneficial to extend battery life, and to inherently tackle the problem of data loss due to transmission fails [94].

On another note, it is worth to emphasize that, to be applicable, data compression techniques must be suitable for implementation on the extreme edge sensor nodes, such that it is possible to compensate at a software level hardware constraints. Therefore, data compression may be combined with the enhancement undertaken at a global level by the GSP-driven mode shape assembly algorithm for clustered monitoring architectures presented in Chapter 3.3.

This new Chapter starts with a brief review of the most common solutions available for vibration data compression. From this prospective solutions, the method built on the Compressed Sensing (CS) paradigm will be selected for the following analyses, owing to its favorable compatibility with near-sensor implementations and the promising results already achieved in the field. Coherently, a physics-based and highly optimized strategy inspired by the adapted CS theory will be proposed and tested with real-field data.

## 4.2 COMPARATIVE ANALYSIS OF DATA COMPRESSION TECHNIQUES FOR OMA

A consistent deal of research has been spent in the last two decades, seeking to design the most effective compression scheme for vibration monitoring [99], [101]. However, the investigation of how these solutions could be practically implemented on self-contained sensor boards has only recently gained attention [95]. In the current Section, a general overview about some of the most established techniques for data compression in OMA applications is depicted, whilst a consistent comparison is summarised in Table 7 and further commented in Section 4.4.2.2. Hereinafter, the acronym CR will be used to quantify the compression ratio, i.e., the ratio between the considered signal length ( $N$ ) and the actual amount of transmitted data.

### 4.2.1 Spectral-based decomposition

Spectral-based decomposition refers to the ensemble of methodologies built on the selection of a small batch of parameters out of the spectral representation of the input signal. This procedure can be performed by applying PP algorithms directly on Fourier-transformed data and, then, by extracting the topmost peak spectral values. A seminal work in this field is provided in [80] and further validated with a near-sensor implementation on prototyping boards. However, these methods present a crucial limitation since they assume that the vibration components to be analysed are well-spaced, highly energetic and significantly decoupled, a condition which barely holds when dealing with the majority of real SHM scenarios under operative conditions. In this sense, their effect is to 'decompose' a multi-degree-of-freedom system into the linear summation of single structural components, which can be treated independently.

### 4.2.2 Compressed Sensing

Approaches based on the CS theory define the problem on a pure mathematical basis by resorting to linear algebra transformations as a means for data reduction [102], [103]. The underpinning principle behind CS is that, under the premise that the processed class of signals is *sparse* (or, at least, *compressible*) in a given domain, only a few coefficients suffice to capture the signal content. If this condition applies, a shrunk version of a long time series can be obtained by projecting it onto a lower-dimensional subspace through a suitable compression matrix [104]. Since the spectral representation of vibration data is inherently sparse in the frequency domain, the CS paradigm appears to be particularly suited for vibration data manipulation.

The operative principles of CS are schematized in Fig. 16. The sparsity hypothesis assumes that a basis  $\Psi \in \mathbb{R}^{N \times N}$  exists in which a signal instance  $y \in \mathbb{R}^{N \times 1}$  can be accurately



Table 7: Comparison between different methods for OMA-oriented data compression: ✓ and ✗ indicate whether the corresponding strategy is implemented in an unsupervised or supervised manner, respectively.

Method	Advantages	Drawbacks	Type	Ref.
PP	<ul style="list-style-type: none"> <li>– Naive logic, usually computationally efficient</li> <li>– Massive CR</li> </ul>	<ul style="list-style-type: none"> <li>– Prior structural knowledge is required to instruct PP</li> <li>– Loss of mode shapes sign</li> </ul>	✗	[80]
STCS	<ul style="list-style-type: none"> <li>– Well-balanced resource distribution</li> <li>– Sparsity adapted at acquisition time</li> </ul>	<ul style="list-style-type: none"> <li>– Additional payload due to the transmission of coordination variables</li> <li>– High computational complexity of the data recovery algorithm</li> </ul>	✓	[95]
RND-CS	<ul style="list-style-type: none"> <li>– Straightforward implementation of the decoder</li> <li>– Suitable for data loss recovery</li> </ul>	<ul style="list-style-type: none"> <li>– High sensitivity to input noise level</li> </ul>	✓	[96]
BSS-CS	<ul style="list-style-type: none"> <li>– Mode shapes recovered from low-rate measurements</li> </ul>	<ul style="list-style-type: none"> <li>– High computational complexity</li> <li>– Number of observable modes inferior to the cluster size</li> </ul>	✓	[97]
MRak-CS	<ul style="list-style-type: none"> <li>– Soft adaptation process to the input signal energy profile</li> <li>– Robustness with respect to structural variations</li> <li>– Low computational cost for the encoder</li> </ul>	<ul style="list-style-type: none"> <li>– Structural models are required to design the sensing matrix</li> </ul>	✗	[P5]
PCA, history PCA	<ul style="list-style-type: none"> <li>– Adaptation to the input signal energy profile</li> <li>– Straightforward decoding process</li> <li>– Low computational cost for the encoder</li> </ul>	<ul style="list-style-type: none"> <li>– Large and sufficiently representative training set is required</li> <li>– Spectral deviations hardly captured</li> </ul>	✗	[98], [99]
PSBS	<ul style="list-style-type: none"> <li>– Modal parameters extracted directly from compressed data</li> <li>– Low computational complexity of the encoder</li> </ul>	<ul style="list-style-type: none"> <li>– High computational complexity and memory requirements for the decoder</li> </ul>	✓	[100]
RD	<ul style="list-style-type: none"> <li>– Low computational cost of the encoder</li> <li>– Low memory requirements</li> <li>– Data loss inherently handled</li> </ul>	<ul style="list-style-type: none"> <li>– Poor performance in the recovery of noisy acquisitions</li> <li>– Short frame length is required</li> </ul>	✓	[13]
WT	<ul style="list-style-type: none"> <li>– Low computational cost</li> <li>– Readily implementable through filter banks</li> </ul>	<ul style="list-style-type: none"> <li>– Threshold selection</li> <li>– Wavelet basis selection</li> </ul>	✓	[13]

approximated by at most  $k_k \ll N$  non-negligible components belonging to the signal support, i.e.,  $y = \Psi c$  ( $c$  being the  $N$ -dimensional coefficient vector and  $k_k$  the sparsity level). Hence, by harnessing this signal prior, the information hidden within raw acquired data can be condensed into a measurement vector  $y_{cs} \in \mathbb{R}^{m \times 1}$ ,  $m \geq 2k$ , resulting from the

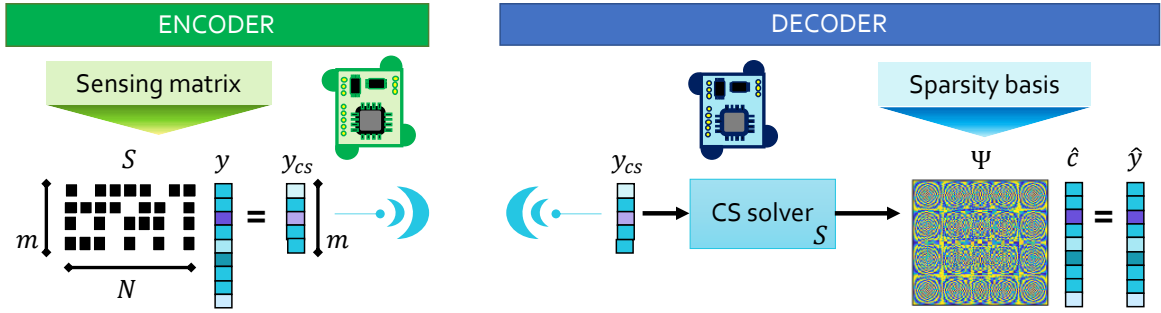


Figure 16: Schematic representation of the CS encoding (green) and decoding (blue) operations.

linear combination of  $m \ll N$  samples by means of a sensing matrix  $S \in \mathbb{R}^{m \times N}$ , namely  $y_{cs} = S\Psi c$ . The recovery can be accomplished with an inverse CS solver, either based on convex optimization problems or gradient-based alternatives, the solution of which consists of the set of sparsest coefficient vector  $\hat{c}$  guaranteeing the highest accuracy between the sensed and the currently predicted measurement vector  $\hat{y}_{cs} = S\Psi\hat{c}$ . The original signal is finally reconstructed as  $\hat{y} = \Psi\hat{c}$ .

From such formulation, it is worth saying that CS performs a lossy compression and its effectiveness is conditional upon the selection of two fundamental ingredients, namely the optimal compression matrix ( $\Psi$ ) and the sparsity basis ( $S$ ). Notably, since the signal sparsity may vary due to structural and environmental factors, methods capable to adapt these defining features over time should be preferred. Even if these two operators are conventionally supposed constant, this is not applicable for SHM scenarios, where the non-stationary and usually non-predictable behaviour of the underlying dynamics demand for their adaptation. Methods exist which try to adapt them in a streaming fashion to better track the actual sparsity condition of the input instances [105]. However, since this adaptation is difficult to be accomplished on the fly, the compression-accuracy trade-off is commonly solved by relaxing the Compression Ratio (CR) to favour a higher signal to reconstruction noise ratio. As a consequence, typical CRs for vibration-based SHM hardly exceed one fifth of the total amount of samples [99].

The potential usefulness of CS in vibration monitoring is demonstrated by the high number of published papers in the field. Indeed, in the last few years, many researchers investigated the suitability of different CS techniques and tried to cast them under the framework of clustered SHM architectures. Among the most representative examples, authors in [95] explored the advantages of a combined spectro-temporal compression approach (ST-CS) leveraging a bidirectional feature transmission scheme. A distributed CS paradigm was proposed, which involves several peripheral nodes under the orchestration of a master aggregating unit. Alongside, it has recently been demonstrated that the data recovery problem can be formalized into a standard supervised-learning task [106], therefore featuring a tight interweaving between standard CS operations and subspace learning techniques driven by the artificial intelligence [107].

Alternatively, a CS-based sparse coding strategy was efficiently complemented with a non-convex shrinkage algorithm to reconstruct the original data from incomplete measurements in the field of large-span structures [108]. Furthermore, researchers explored the possibility to extract modal parameters, and in particular mode shapes, directly from low-rate random measurements by tackling the modal identification task with a CS-

driven and BSS-oriented approach (an example is the work by Yang and Nagarajaiah [97]).

Beside their technicality and the additional improvements brought by each specific implementation, all the mentioned solutions exploit standard compression matrices, whose entries can be taken either from Gaussian or Bernoulli distributions [109], or obey to random sampling (RND-CS), namely the selection of an arbitrarily-indexed subset of samples [110]: the latter sensing strategies (RND-CS-based) are inherently suitable to counteract the additional loss of packets affecting the communication channel. Indeed, assuming that data loss can be modeled as a random stochastic process, its effect can be seen as the output of a random sampler that arbitrarily selects few packets from the whole payload.

#### 4.2.3 *Principal Component Analysis*

The compression of vibration signals can also be tackled as a pure eigenvalue problem by applying Principal Component Analysis (PCA) [98]. Eigenvalue strategies compress data by projecting them onto the signal subspace spanned by those directions related to the most energetic components. For example, authors in [111] stressed the potential of PCA for feature compression and reconstruction in the context of predictive maintenance and anomaly detection. These methods show good recovery performances even under significant compression ratios. Noteworthy, both the PCA encoding and decoding side can be easily implemented through a simple matrix-vector multiplication, a procedural characteristic which fostered its success for simple on-sensor deployment. However, their main limitation is in the huge amount of data they require for the statistical characterization of the input signal energy profile, which implies exhaustive and accurate baseline measurement campaigns necessary to characterize the structure in pristine conditions [105].

Addressing this issue, the so called *history* PCA has very recently been proposed for network load reduction. Such method exploits the eigenvalue decomposition of the correlation matrix between signal components to extract the primary information to be preserved. Outstanding results were obtained in [99] via adoption of history PCA in the context of bridge inspection, where a 10x compression factor was achieved with satisfying reconstruction accuracy while embedding the algorithm on network end nodes.

#### 4.2.4 *Additional methods*

Other noticeable solutions for data compression in OMA scenarios are the power spectrum blind sampling (PSBS) and the random demodulator (RD) approach, which are sub-Nyquist techniques specifically suited for hardware implementations. PSBS [100] extracts second order statistics (i.e., modal information) directly from multi-coset sampled data without any additional hypothesis on the nature of the involved phenomenon. Conversely, in RD [13], random alternation of samples' sign is combined with low-pass filtering and low-rate sampling. Such technique was proposed to account for data loss, and it is based on accumulate and dump operations that can readily be implemented in smart sensor platforms. The main drawback of RD strategies is that they assume stationary or piece-wise stationary vibration signals; more importantly, the sampling pattern is not only difficult to be analytically computed in advance, but it also scales poorly when the CR decreases.

Furthermore, the seminal work in [112] approaches the problem from a filter bank perspective by resorting to Wavelet Transform (WT). In more detail, WT operates in the time–frequency domain and provides a means for multi–resolution analysis, namely WT is used to describe mathematically the increment in information needed to move from a coarser to a higher signal approximation [113].

In essence, WT constitutes of the cascade of filtering steps acting on subsequently thinner spectral bands such that the frequency resolution is finer in the higher parts of the spectrum and coarser in the lower ones. The values retrieved at the output of each WT step are called wavelet coefficients: these coefficients capture different energy content depending on the spreading of the structural modes across the spectrum. Following this rule, WT paired with thresholding algorithms offers a powerful tool for data compression. The reason is that, at each decomposition step, those coefficients whose magnitude is significantly lower a prescribed threshold can be disregarded since they do not convey meaningful insight about the analysed signal. WT has been successfully applied in the context of gear box monitoring [112] and, as underlined by the authors, one of the most critical part of this method is the selection of the most appropriate threshold, which is typically very hazardous to predict in advance and it is very application–dependent. This task is most often achieved only via experimental demonstrations that, in turn, might suffer from the variability of the measured structural responses in terms of content and magnitude and, thus, not very stable.

#### 4.3 PHYSICS-BASED CS FOR VIBRATION-BASED SHM

The CS–based method proposed in this work draws foundation on the Rakeness–based CS (Rak-CS) approach [114], which is an adapted CS method offering the peculiar capability to adapt the statistical distribution of the sensing mechanism in a way that maximizes the total energy which may be "raked" from the different components of the input signal. As a matter of fact, a close analogy exists between the *sparse–and–localized* signal assumption unique to Rak-CS and the energy distribution of vibration data in the frequency domain, where modal peaks are not only sparse, but highly localized in the spectrum. Analysed from a structural perspective, the latter observation means that Rak-CS provides the ideal tool to encode modal information by leveraging the inherent vibration signature of the structure.

There is an additional reason for preferring Rak-CS over alternative CS methods. Indeed, a distinctive advantage of Rak-CS consists of its relatively soft exploration–localization trade–off [115], such that the compression scheme is prevented from overspecializing data against potential spectral variations, which are very likely to occur in real scenarios.

In line with the above observations, a novel variant of Rak-CS, named after as MRak-CS approach, is advanced. The name derives from the fact that it exploits numerical estimations of the structural dynamics to design the compression matrix. In parallel, the design of a physics–based sparsity basis is also encompassed, to favor the sparsification of vibration data in the direction of the expected topmost frequency components of the structure. This solution overcomes the necessity to collect large training datasets for the same task. In this sense, and in line with the so–called theory–guided data science paradigm [116], the knowledge derived by numerical simulations or by semi–analytical methods is seamlessly blended with the signal statistics characterization process.

Finally, it is important to underline that the proposed method works on the optimization of the encoding stage not only for the primary - and declared - aim to alleviate data load transmission, but to precisely meet the limited memory space available on resource-constrained and battery-operated sensors and, as a third byproduct, better tolerate the inherent noise levels affecting real vibration data.

#### 4.3.1 Designing the optimal sensing matrix: From Rak-CS to MRak-CS

Compared to the standard CS theory [109], that adopts a measurement matrix  $S$  whose entries are instances of independent zero-mean Gaussian random variables, the Rak-CS approach [115] generates each row  $s$  of the measurement matrix  $S$  as a zero-mean random vector, but with a correlation profile  $C^s = \mathbb{E}[ss^T]$  tightly matched to the second-order statistic  $C^y = \mathbb{E}[yy^T]$  of the raw input vector  $y$ . The method relies on the maximization of the rakeness quantity

$$\rho(s, y) = \text{tr}(C^s C^y) \quad (17)$$

which measures the average energy of the projections of instances of  $y$  over independently drawn rows of  $S$  ( $\text{tr}(\cdot)$  stands for the matrix trace operator) [114]. The analytical solution of the Rak-CS problem discussed in [114] yields the correlation profile of the sensing matrix to coincide with

$$C^s = \frac{N}{2} \left( \frac{C^y}{\text{tr}(C^y)} + \frac{I_N}{N} \right) \quad (18)$$

where  $I_N$  indicates an  $N \times N$  identity matrix.

In the rakeness approach, whose processing flow is sketched in the last column of Fig. 17, a fundamental step is the computation of the correlation matrix  $C^y$  of the vectors to be acquired. This matrix is typically estimated from a sufficiently large number of signal instances which are expected to be representative of the different measured realizations [115]. Alternatively, the proposed MRak-CS method numerically derives  $C^y$  by hinging on *a priori* considerations. If an approximate model of the dynamic response of the structure is available, a condition that usually holds for the majority of industrial and civil plants, a simplified correlation profile can be analytically designed, as detailed in the following (see first column block of Fig. 17).

Let's assume  $P$  modes are expected to identify the spectral signature of the structure. Coherently,  $P$  rectangular frequency bins are designed, whose spectral width  $W_p$  is related to the modal frequency  $f_p$  so that the quality factor  $Q = f_p/W_p$  is constant. Then, since  $C^y$  should be, approximately, a positive semi-definite Toeplitz (i.e., block diagonal) matrix, the value on its  $i$ -th diagonal is computed as:

$$C^y[i] = \sum_{p=1}^P \int_{f_p - \Gamma W_p}^{f_p + (1-\Gamma)W_p} \cos(2\pi f i) df \quad (19)$$

where  $\Gamma$  is a parameter which can be used to offset the central frequency of the bin with respect to the modal frequency. Such parameter is introduced to adapt the sensing matrix to the typical evolution of the spectral content in vibration signals.

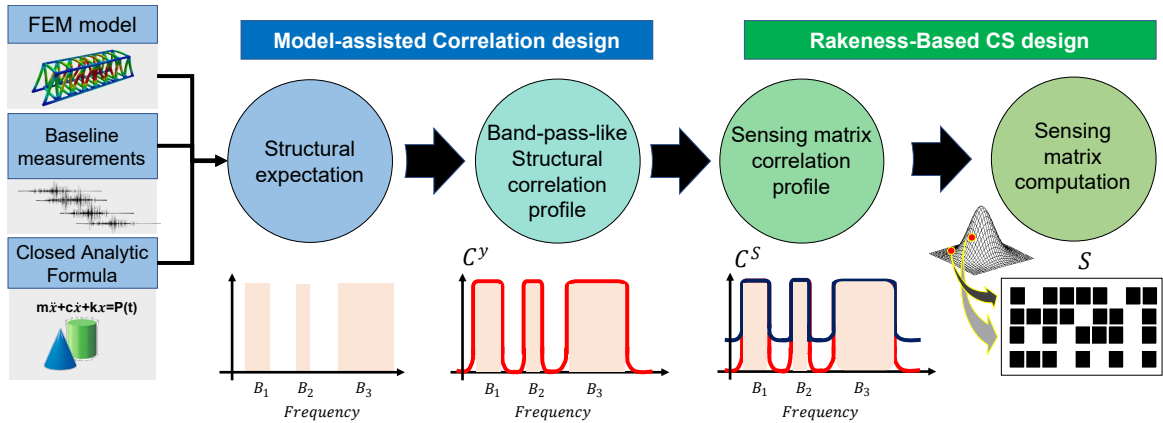


Figure 17: General processing flow at the basis of the MRak-CS approach. The computation starts with the selection of the frequency regions of interest, as they can be predicted by a numerical model or zero-time structural campaigns, on the basis of which a band-pass-like correlation profile of the structure ( $C^y$ ) is synthetically designed. Then, the CS-based problem is entered by firstly extracting the sensing matrix correlation profile ( $C^S$ ). Hence, the latter value is used to sample each row of the sensing matrix  $S$  from a multivariate Gaussian distribution with zero mean and correlation profile equal to  $C^S$ .

Once the input matrix correlation profile is defined, the eigenvalues and eigenvectors of  $C^S$  are computed as illustrated in [114]. In Fig. 18, the PSD of the Rak-CS (red line) and MRak-CS (blue line) compression matrices for a simple problem are enclosed, to show how the two design procedures may adapt to the second-order statistics of the input signal (black dotted curve).

#### 4.3.1.1 Frequency binning and MRak-CS parameter selection

The frequency binning of the MRak-CS adaptation procedure, namely the selection of the location and width of the frequency bands  $B_p$  to be preserved, behaves in the following manner. If a rough expectation about the possible vibration content of the monitored structure suggests that the two closest modal peaks should lie in the frequency band  $B_p = [f_L; f_H]$ , a minimum frequency distance  $\Delta f^{\min} = f_H - f_L$  has to be preserved, imposing  $W_p \geq \frac{\Delta f^{\min}}{2}$ . Consequently, the design process of the input signal correlation profile simply takes the average value  $f_p = \frac{f_H - f_L}{2}$  as reference spectral peak to shape the corresponding frequency bin as stated in Eq. (19). Given  $B_p$  and  $f_p$ , the quality factor can be retrieved and kept constant for all the remaining modes.

On the other hand, the quantity  $\Gamma$  assumes a paramount importance for practical SHM applications since it favors better adaptation to possible spectral changes induced by degrading phenomena. This is the case of civil structures that can be modeled as one-dimensional elements, for which the structural dynamics theory dictates that damages tend to produce downshifts in the modal frequencies as a consequence of stiffness reduction [117]. One may argue that this assumption is too simplistic; however, mono-dimensional representations are rather common even for more complex real scenarios, especially for long-span bridges [72], whose vibration response can be well approximated to that of 1D beam elements. In these cases, it is suggested to select this parameter in the interval  $0.5 < \Gamma < 1$ , so that the down shifting of the frequency peaks can be tracked.

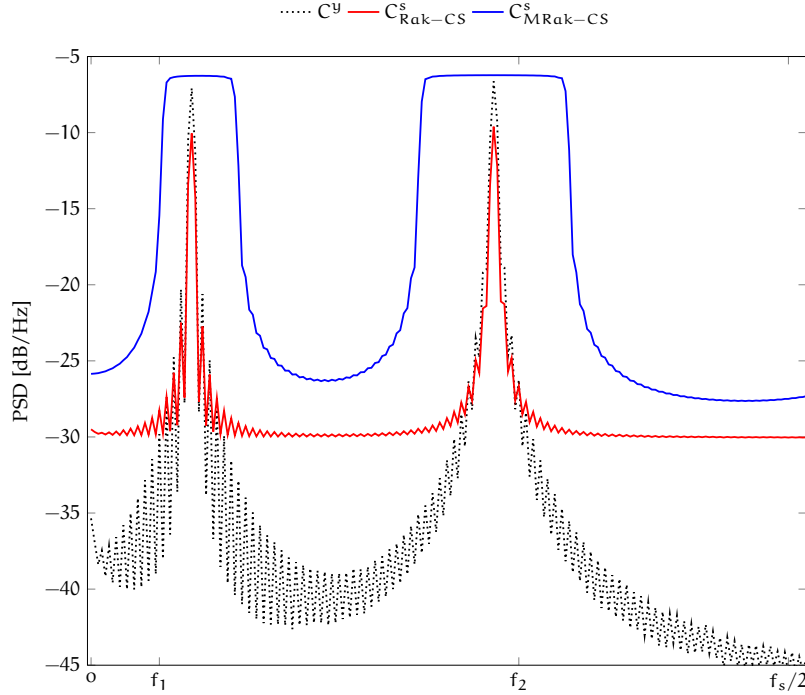


Figure 18: Spectral profiles of the Rak-CS (red) and MRak-CS (blue) compression matrices superimposed to the energy distribution of the input signal (black curve). [©2021 IEEE]

Conversely, when it is impossible to make an educated guess about the future trend of the modal frequencies, the best option is to select  $\Gamma = 0.5$ , so that the right and left side of the central frequency band are equally spaced from  $f_L$  to  $f_H$ . To summarize, the input signal correlation matrix in Eq. (19) can be constructed by selecting  $f_p$  as the central frequency of the band  $B_p$  in which the modal frequencies are expected to be located, while  $\Gamma$  and  $W_p$  are selected so that the spectrum of the sensing matrix is flat in  $B_p$ . The latter property allows the MRak-CS process to be inherently adapted to all the spectral components in that band.

It is important to stress the fact that MRak-CS is a considerably conservative approach, which is not affected by the actual number of vibration peaks appearing in a specific spectral region. Such robustness makes the method suitable for real-field implementations, where it is commonly rather complicated to predict in advance and in a precise manner how the energy content of the structure might evolve over time. For the same reason, the proposed MRak-CS strategy performs reliably even in presence of structural variations, avoiding the overfitting to the originally estimated spectral content, as could be the case for purely data-driven alternatives. This means that the described strategy can be extended to the case of multiple, closely spaced modal frequencies.

As an example, let's consider the toy case in Fig. 19, where  $f_L = 3$  Hz and  $f_H = 4$  Hz are supposed in compliance with possible real scenarios, leading to a maximum frequency distance of  $\Delta f^{\min} = 1$  Hz. If  $f_1 = 3.1$  Hz and  $f_2 = 3.7$  Hz are the true vibration modes to be identified, we have an actual frequency distance of 0.6 Hz. Coherently,  $f_p = 3.5$  Hz,  $\Gamma = 0.5$  and  $W_p = 2\Delta f^{\min} = 2$  Hz are selected so that, even in case of wrong estimation in the original prediction, or strong deviations in the nominal structural behavior, the frequency content can be accurately tracked. The band-pass profile of the input signal correlation matrix  $C^y$  (grey line in Fig. 19) is the one defined by Eq. (19) and the analytical solution of

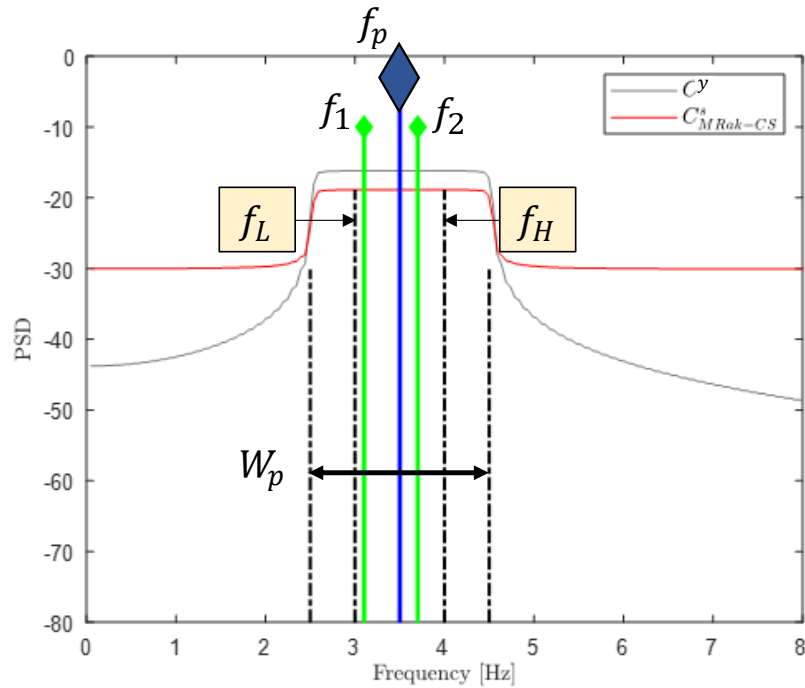


Figure 19: MRak-CS correlation matrices in case closely spaced modes (green diamond markers) falling in the same frequency bin need to be identified.

the MRak-CS problem statement is solved via Eq. (18), which provides the corresponding sensing matrix correlation profile  $C_{MRak-CS}^s$  (red curve). It follows that all the structural modes that will fall inside the frequency band  $[f_p - 0.5W_p; f_p + 0.5W_p]$  are likely to be reconstructed with high accuracy, independently from their proximity and/or quantity.

The pros and cons of standard data compression methods with respect to the MRak-CS strategy are summarized in Table 7, taking into consideration the procedures discussed in Section 4.2. In essence, MRak-CS is a hybrid approach between the purely random sampling which characterizes the conventional CS and the data compression methods requiring an extensive preliminary characterization of the structural response, as in PCA. There is a trade-off involved in the MRak-CS implementation, that is related to the definition of the frequency bin span: the larger the span, the closer the compression performance will be to the (relatively poor) one achieved with standard CS strategies. Conversely, by narrowing the span, the attainable compression level can be improved, but the risk is to lose the capability to track the changes in the structural dynamics. Noteworthy, the same risk characterizes PCA-based compression procedures. Nonetheless, as it will be shown in the results section, the MRak-CS approach has great potentialities for SHM implementations thanks to its adaptability, at least when the numerical model of the structure can be derived with sufficient accuracy.

#### 4.3.1.2 Proving the robustness of MRak-CS against structural variations

To validate the effectiveness of the the MRak-CS method even in presence of closely-spaced modes or in view of changes in the spectral profile of the structure, real-field data taken



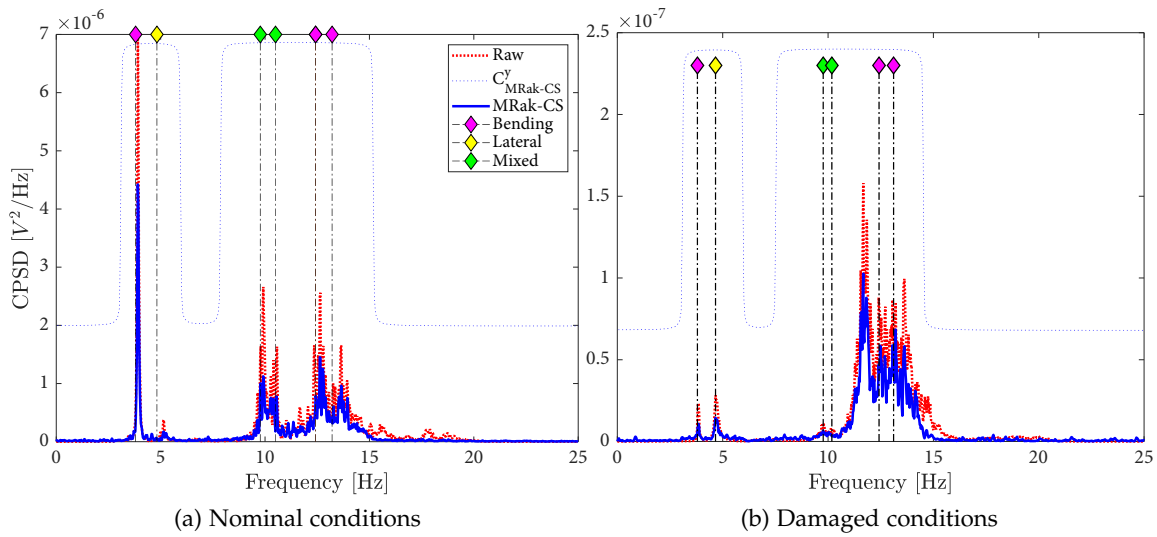


Figure 20: MRak-CS reconstructed PSD for two different working conditions of the Z24 bridge (subplots (a) and (b)). Diamond markers are used to highlight the location of the estimated structural peaks on the basis of a properly tuned FEM analysis: yellow, magenta and green colors indicate lateral, bending and torsion/bending modes, respectively. In both subplots, the blue dotted line depicts the sensing matrix correlation profile used in the MRak-CS method. Finally, the red dotted and blue continues lines represent the raw signal (i.e. compression-free) and CS-recovered spectrum for  $CR = 4$ , respectively.

from the Z24 benchmark use case were exploited. The Z24 bridge is well known in the SHM community, since a dataset related to the long-term monitoring of this structure with vibration sensors was made openly available. A complete description of the bridge as well as a thorough report about the conducted experimental campaign can be found in [118], while major details will be provided in Section 6.3 of this manuscript, where a dedicated processing will be presented. At this stage, only the information necessary for the methodological validation of the MRak-CS approach against practical complexities will be introduced.

Modal analysis studies applied to this dataset proved that the majority of the modal components are located below 20 Hz. In particular, at a reference temperature value of 25°C and in nominal working conditions, the three dominant bending modes (magenta markers in Fig. 20) are located at 3.87 Hz, 12.42 Hz and 13.21 Hz, while the most energetic lateral mode arises at 4.82 Hz (yellow marker in Fig. 20). Two closely spaced mixed torsion/bending modes (green markers in Fig. 20) are found at 9.77 Hz and 10.50 Hz, respectively. By taking into consideration these modal frequencies, two main spectral bands can be identified: the former one spans the interval 3.5–5 Hz, while the latter has wider dimensions and includes all the components from 9.5 Hz to 13.5 Hz. Therefrom, the sensing matrix is designed as illustrated in Section 4.3.2: two central frequencies are defined, i.e.  $f_1 = 4.25$  Hz and  $f_2 = 11.5$  Hz, with related bandwidths of  $W_1 = 2.70$  Hz and  $W_2 = 7.31$  Hz, respectively, imposed by  $Q = 1.5$ . The choice on  $Q$  is ruled by the necessity to be compatible with the minimum spectral insight at the two sides of the leading peaks ( $W_1 \geq 1.5$  Hz and  $W_2 \geq 4$  Hz), simultaneously guaranteeing a proper tracking of frequency deviations which were intentionally provoked during the monitoring campaign.

The acquired waveforms, which are too long to be processed in a single shot, are divided into 512-sample segments (sampling frequency equal to 50 Hz) with a compression ratio equal to 4. The reason for selecting these values is that the goal, at this stage, is to determine the effect of the sensing design procedure itself with respect to conventional methods, rather than probing for the attainable compression levels. From the piece-wise reconstruction of the original time series, the CPSDs reported in Fig. 20 are obtained for two rather distinct working conditions. As can be observed, the spectral content of the MRak-CS-reconstructed signal is remarkably accurate if compared to the spectrum of the original (uncompressed) signal, and even low energy peaks can be satisfactorily identified. The recovery is very effective also when, as a consequence of the induced structural damage, the peak localization of the reference modes significantly changes (subplot 2ob).

#### 4.3.2 *Designing the optimal sparsity basis: a structurally-shaped approach*

The selection of the optimal sparsity basis plays a crucial role in boosting the compression performance as much as possible. Vibration signals with low damping factors are sparse in the Fourier domain [119], a condition which led to the conventional selection of the Discrete Cosine Transform (DCT) or the Discrete Fourier Transform (DFT) matrices as sparsifying basis [106], [120].

In compliance with the time-frequency localization trade-off stated by Heisenberg's inequality, the main drawback inherent to the adoption of the aforementioned Fourier-driven sparsity domains is given by their poor time resolution, namely their incapability to recover time-localized discontinuities associated with important non-stationary phenomena. For this reason, assuming that side effects typically manifest at the highest frequencies, wavelet-dependent alternatives have been proposed [121], [122]. They permit a more versatile tiling of the time-frequency plane, as the spectral resolution increases the lower the frequency bands, and better track non-stationary phenomena. Nevertheless, the dyadic frequency split at the basis of the discrete wavelet transform is still incapable of adapting to the specific frequency peak distribution which characterizes the spectral profile of vibrating structures. This means that no possibility persists to recover with enough precision vibration modes above half of the Nyquist frequency ( $F_s/2$ ), since the corresponding frequency resolution is fixed at the first decomposition level  $j$  and, thus, it cannot be greater than  $F_s/2^{j+1}$ ,  $j = 1$ . For modal identification purposes, this constraint could prevent the identification of high-order coupled components, which usually characterize the majority of industrial and civil infrastructures.

More recently, several approaches started to be explored to overcome this limitation and design a best-adapted signal representation in favor of a better sparsification. They include sparse coding [123] and dictionary learning [124]. Wavelet Packet Transform (WPT) is another suitable tool, particularly apt at performing this adaptation to the signal characteristics in a very flexible way [125].

As schematically illustrated in Fig. 21, WPT is conceived as a nested filtering operator applied to both the detail  $y_H$  (i.e., high-frequency) and approximation  $y_G$  (i.e., low-frequency) components of a signal. Filters  $h$  and  $g$  are usually given in pair since they belong to the class of quadrature mirror filters, providing a sufficient condition for the perfect signal reconstruction, and are uniquely determined upon the selection of an appropriate wavelet basis, also called mother wavelet. The sequence (tree) of filtering stages can be purposely pruned to match the intrinsic multi-scale nature of the signal; in these

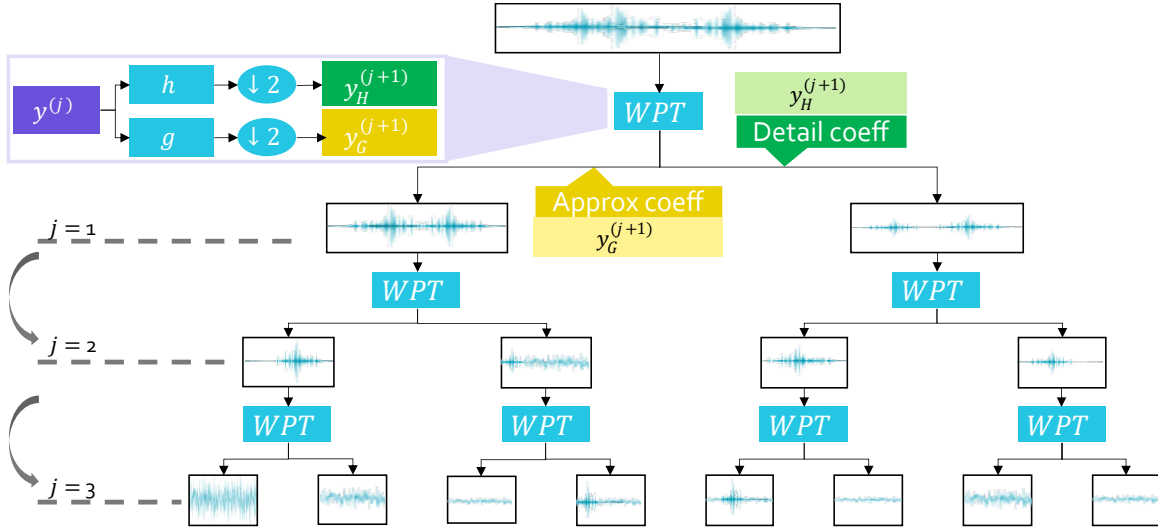


Figure 21: Depiction of the filtering procedure at the basis of WPT.

terms, the WPT operator splits the signal in multiple packets (frequency bands), which can deliver an efficient representation for signals specifically localized at distinct sub-bands distributed over the entire spectrum.

One question may arise at this point, which is: *what is it the enabling reason supporting WPT as candidate tool for the creation of the optimal sparsity basis?*

Let's answer to this pivotal question.

Firstly, the optimization steps entailed by WPT can be performed by learning the most suited representation from uncompressed [126] or compressed data [127]. Even if these methods proved to be robust and promising for an effective signal recovery process in the context of data compression, they require a consistent amount of data to be used during the training phase.

Hence, as sparsifying basis for CS, adopting a WPT-based method has several advantages in terms of computational cost, theoretical capability to reconstruct the signal perfectly (except for the math processor finite word length approximations) and capability to adapt the frequency resolution in a very flexible way driven by the very same structural knowledge at the basis of the MRak-CS encoding mechanism. In this case, the WPT operator allows to zoom the frequency resolution in the sub-bands where the structural information has been estimated to lie (i.e., the frequency regions of interest), while imposing a coarser frequency detail in the remaining portions where none but noise is expected to appear. As a consequence, the final signal representation can be considered maximally sparse in the sense that just a very few signal coefficients, i.e., those pertaining to pre-selected frequency bands with maximum resolution, are sufficient to retrieve almost all of the structural energy. Thereby, it can be effectively combined with the Rak-CS method which leverages the signal localization property to design the sensing matrix.

#### 4.3.2.1 The WPT adaptation algorithm

In the proposed strategy, structural numerical models are exploited to shape the WPT decomposition process according with the PSD of vibration signals. The WPT adaptation procedure is listed in Algorithm 1. The following quantities

are required as inputs: the vector ensemble of the frequency bands of interest  $W_T = \bigcup_{p=1}^P B_p = \bigcup_{p=1}^P [f_p - \Gamma W_p, f_p + (1 - \Gamma)W_p]$ , the sampling frequency  $F_s$  and the frame size  $N$ . The sought decomposition level  $j$  and the frequency interval of each wavelet packet are returned as outputs according with the following three-stage procedure:

1. *Centre*: select the decomposition level  $j$  as the maximum value allowing one wavelet packet to capture the first modal frequency while keeping the corresponding frequency bin  $\Delta_f = F_s/2^{j+1}$  below the distance  $\Delta_f^{\min}$  between the closest modal frequencies. The minimum span of the WPT frequency bin has an inferior bound given by the length of the frame size:  $\Delta_f^{\min} = \frac{F_s}{2^{\log_2 N + 1}}$ . In turn,  $N$  is limited by the memory space available in embedded sensors; thus, attainable values for  $\Delta_f^{\min}$  range from one to few tenths of Hertz, depending on the adopted sampling rate. In typical OMA applications, such values are usually sufficient to locate strongly coupled modal frequencies in separated WPT bins.
2. *Divide*: create the overcomplete wavelet tree up to depth  $j$ , yielding to  $2^j$  successive wavelet packets, each of them being identified by a corresponding frequency interval and width. Define with  $B^*$  the ensemble of packet bands falling outside the frequency region of interests, i.e.,  $B^* \cap W_T = \emptyset$ .
3. *Merge*: climb back the full tree level-by-level. At each filtering stage, merge those children packets associated with a father node whose frequency band belongs to  $B^*$ . Repeat this procedure until the dyadic grouping is permitted. This pruning step is encompassed for two main reasons: (i) relax the frequency resolution constraint in expected low-energy intervals, and (ii) minimize the frequency overlap between side lobes of adjacent filter masks, which might be responsible of artifact alias components in the reconstructed signal.

#### 4.3.2.2 Proving the robustness of WPT-driven sparsity against complex vibration patterns

It is worth highlighting that the design of the WPT sparsity basis could be effective even in presence of closely-spaced modal frequencies. In this case, the selection of the appropriate decomposition depth  $j$  is very important, because such parameter dictates the minimum reachable frequency resolution. Whenever the peak proximity is expected to be extremely narrow and no precise prediction is available for the target structure, the selection of  $j = \log_2 N$  ensures the greatest attainable frequency resolution equal to  $\Delta_f^{\min}$ . Under this assumption, the detection capability of the WPT basis coincides with that attainable with standard Fourier basis.

Just to make an example, for 512-long signals acquired at a sampling frequency equal to 200 Hz (that correspond to very common parameters for OMA applications), this leads to a frequency resolution  $\Delta_f = \frac{200}{2^{\log_2 512 + 1}} = 0.20$  Hz, which is largely compliant with the above discussed frequency distances for strongly coupled modes in vibrating structures.

Furthermore, even in case the frequency resolution of the WPT filter-bank is not sufficient to discriminate closely spaced modal frequencies, this fact does not hamper the possibility to perform mode discrimination after the signal recovery. Indeed, the modal

**Algorithm 1** Adapted WPT decomposition process**Input:**  $W_T, F_s, N$ **1. Centre:**

```

1:  $p = 1, j = \lfloor \log_2 n \rfloor$ 
2:  $\Delta_f = F_s/2^j, \Delta_f^{\min} = \min_{j \in [1, \dots, P-1]} (f_{j+1} - f_j)$ 
3: while  $\Delta_f < \Delta_f^{\min}$  do
4:   if  $\exists k \in [1 \dots 2^{j+1}] : \left( \frac{f_1}{\Delta_f} - \frac{k}{2} \right) < \varepsilon$  then
5:      $j \leftarrow j - 1$ 
6:      $\Delta_f = \Delta_f/2$ 
7:   end if
8: end while
9: return  $j$ 
10:  $L = 2^{j+1}, \Delta_f = F_s/2^{j+1}$ 

```

**2. Divide:**

```

11: for all  $i \in [1, \dots, L]$  do
12:    $b_i = \{f \in [0, F_s/2] : f \in [\Delta_f(i-1), \Delta_f]\}$ 
13:    $f_{b_i} = i\Delta_f/2$ 
14:    $W_{b_i} = b_i/\Delta_f$ 
15: end for

```

**3. Merge:**

```

16:  $B^* = \{b_i : b_i \cap W = \emptyset\}$ 
17:  $n \leftarrow j$ 
18: while  $n > 0$  do
19:   for all  $(b_i, b_{i+1}) \in B^* : W_{b_i} = W_{b_{i+1}}$  do
20:      $f_c = (f_{b_i} + f_{b_{i+1}})/2$ 
21:     if  $\exists k \in \mathbb{N}^+ : f_c = \frac{F_s}{2^{n+1}} \left( 1 + \frac{k}{2} \right)$  then
22:        $b_i \leftarrow b_i \cup b_{i+1}$ 
23:        $f_{b_i} = f_c$ 
24:        $W_{b_i} \leftarrow 2W_{b_i}$ 
25:        $L \leftarrow L - 1$ 
26:     end if
27:   end for
28:    $n \leftarrow n - 1$ 
29: end while

```

**Output:**  $b_i, \forall i \in [1, \dots, L]$ 

identification algorithms discussed in Section 2.2 extract the modal parameters by processing multiple signal instances, thus mitigating possible inaccuracies in isolated windows.

This behavior is proven in Fig. 23, where the CPSD profile for finer (blue line) and coarser (cyan line) frequency resolution of the WPT basis (see Fig. 22b and 22b, respectively) are depicted and superimposed to the original spectrum (red dotted line) of the Z24 bridge in nominal condition (i.e., the same condition used in Fig. 20a). In Fig.23, the case with  $j = 4$  is an example in which the frequency resolution is coarser than the minimum distance between the closest modal components, namely  $\Delta_f^{\min} = 1.56 \text{ Hz} \geq \max\{f_{p,i+1} -$

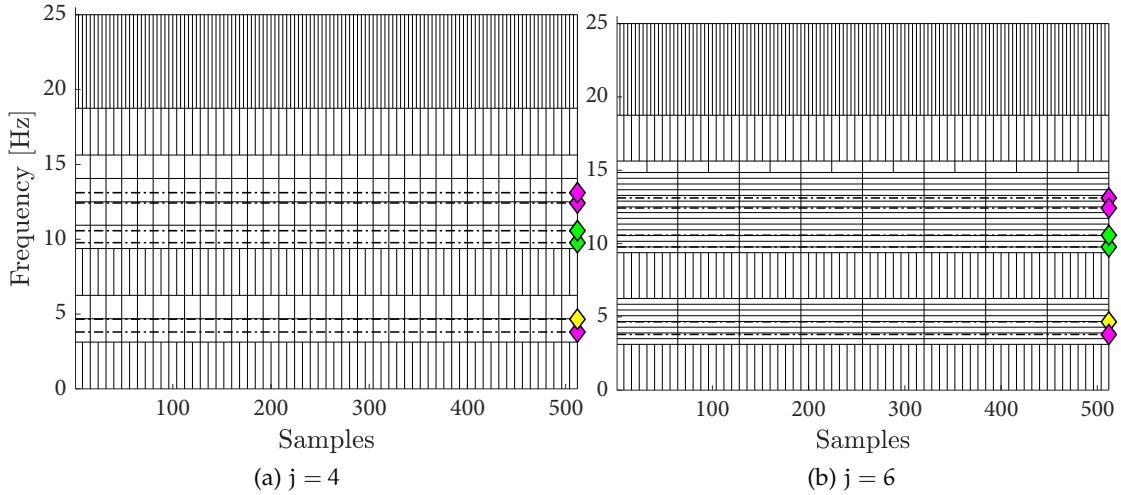


Figure 22: WPT sparsity basis for the Z24 bridge with different frequency resolution: coarser resolution (left) with  $j = 4$  corresponding to  $\Delta_f = 1.56$  Hz and finer resolution (right) with  $j = 6$  corresponding to  $\Delta_f = 0.39$  Hz. Reference frequency components are also enclosed to identify how the frequency bins are distributed with respect to the predicted structural modes.

$f_{p,i} \approx 0.8$  Hz. This is evident in the time–frequency plane of Fig. 22a, where it can be observed how the two peaks around 10 Hz fall within the same frequency bin for  $j = 4$ , whereas a thinner frequency resolution is achieved with  $j = 6$  in Fig. 22b. The power spectrum confirms that modal peaks can still be correctly identified even when the spectral resolution is coarser, at the expenses of a slight reduction in the preserved signal energy.

#### 4.4 MRAK-CS AND WPT SPARSITY BASIS: EXPERIMENTAL VALIDATION

In this Section, the practical effectiveness of the novel CS-based methodology is validated with experimental data, proving how the combination of the optimal sensing matrix design and the WPT-driven structurally-shaped sparsity basis could be beneficial for network load reduction while attaining an accurate level of structural characterization.

Four main objectives were pursued within the validation phase:

- (i) proving the superiority of the devised WPT sparsifying basis with respect to the classical DCT operator;
- (ii) assessing the validity of both the Rak-CS and MRak-CS scheme in the framework of vibration-based structural inspection;
- (iii) comparing the performance of the proposed sampling schemes against basic eigenvalue-based methodologies and alternative CS-based solutions for OMA, in terms of compression ratio and quality of the reconstructed structural information;
- (iv) verifying the actual capability of the MRak-CS-based and WPT-driven compression approach against both structural changes (due to damage and/or environmental agents) and very complicated vibration patterns.

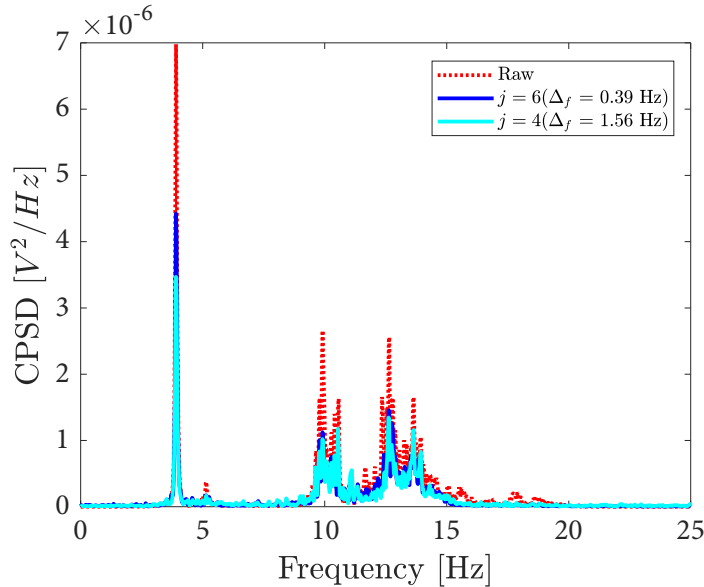


Figure 23: CPSD profile of CS-reconstructed signals in nominal structural condition for the Z24 bechmark use-case: a coarser (cyan color line) and finer (blue colorline) WPT sparsity basis depicted in Fig. 22 are considered and superimposed to the raw spectrum profile (red dotted line).

To address task (iii), the classical PCA [105] was considered as the main competitor among the standard eigenvalue approaches because of its fully-symmetric and low-complexity approach. In this case, the compression factor CR should be intended as the ratio between the total frame size and the number of preserved principal components. A direct comparison with the sensing matrix design criterion prescribed by RND-CS is also included, since it represents a benchmark methodology for CS-based OMA.

#### 4.4.1 The use case: a simply supported steel beam

##### 4.4.1.1 Materials and methods

Mastered by one CH unit, a chain of six ISSLab inertial sensor nodes, extensively detailed in Appendix A and here configured as tri-axial accelerometers, was used to experimentally validate the effectiveness of the conceived algorithmic strategies. As schematically depicted in Fig. 24, a pinned-pinned steel beam, whose mechanical and geometrical characteristics have already been presented in 3.4.2.1, was instrumented and exploited as representative test-bed. In this case, the useful beam span led the three fundamental modes to be localised at the following frequencies:  $f_1 = 5.52$  Hz,  $f_2 = 22.08$  Hz and  $f_3 = 49.68$  Hz, as predicted by a closed analytic formula [128].

Each time series was acquired at a data rate of  $F_s = 200$  Hz over a sampling period of 75 s (i.e., 15 000 samples in each iteration). The beam was left to oscillate under pure environmental noise (i.e., ground motion excitation), therefore mimicking the classical exciting mechanism required by output-only modal analysis. Moreover, since the bounding conditions force the structure to vibrate along the vertical direction, devices were programmed to collect accelerations only on the  $z$  axis.

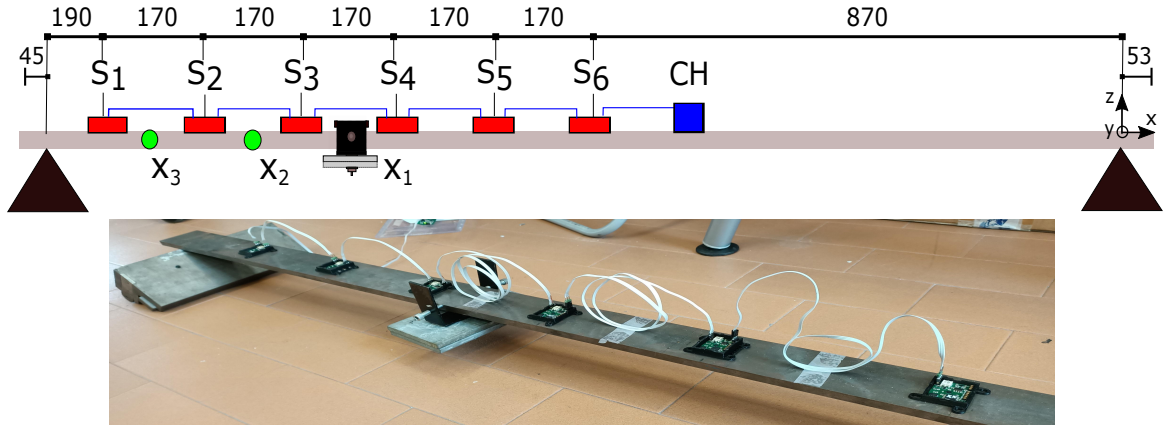


Figure 24: Experimental setup for MRak-CS testing purposes: sensor installation plan (all dimensions in millimeters) inclusive of the damaging mechanism and positions. [©2021 IEEE]

The frame size was fixed to  $N = 512$  samples, a quantity that corresponds to the best compromise between the necessary spectral resolution and the sensor node memory capability. The number of measurements  $m$  sets the compression ratio. In particular, the results achieved by varying from  $CR = 4$  to  $CR = 10$  are reported. To further shrink the memory requirements and ease the computational complexity of the entailed vector-matrix operations in view of near-sensor implementations, a sensing matrix populated with highly digitized Rak-CS antipodal entries (i.e.  $S_{i,j} \in \{-1, 1\}$ ) [115] was preferred. The SPGL1 algorithm<sup>1</sup> was conversely employed during the recovery stage for its superior performances.

Two datasets were acquired, in nominal and altered structural configurations. The former, associated to the healthy status, was used to estimate off-line the correlation matrix corresponding to the given structure, as required by the Rak-CS sampling mechanism. Conversely, the latter was employed during the real testing phase. For this reason, acceleration data deriving from intact vibration behavior were collected along with those pertaining to structural anomalies, which were induced by laterally hanging a progressively heavier dead mass ( $m_A = 1.042$  kg,  $m_B = 1.808$  kg) to the beam at different positions ( $x_1 = 1.8$  m,  $x_2 = 1.6$  m,  $x_3 = 1.4$  m). Thereafter, the caption  $m_d@t_g$  will be used to indicate a generic damage configuration resulting from mass  $m_d$  hinged at position  $x_g$ , with  $d \in \{A, B\}$  and  $g \in \{1, 2, 3\}$ .

The effects due to aging for the category of structures involved in the experimental campaign are such that vibration frequencies tend to decrease at the occurrence of damages [129]. For this reason, considering the MRak-CS approach, the parameter  $\Gamma$  was assumed equal to 0.75 to better track possible frequency downshifts. Accordingly, a band ratio  $Q = 5$  was chosen to ensure a significant frequency inspection in the neighborhood of the estimated peaks. For the pure modal estimation task, the FDD technique [130] was adopted to extract the set of natural frequencies  $f$  and the associated mode shapes  $\Phi_p$ .

<sup>1</sup> <https://www.cs.ubc.ca/~mpf/spgl1/index.html>



## 4.4.2 Results

### 4.4.2.1 Sparsity basis: DCT vs WPT

Exploiting the structural priors detailed in Section 4.4.1.1 as inputs for the adapted WPT decomposition process discussed in Section 4.3.2, the sparsity basis  $\Psi$  was derived. In particular, the Fejér–Korovkin mother wavelet with 22 taps was chosen because of its highly vanishing high-order lobes [117] (i.e., minimal filter overlap between adjacent packets) with respect to smoother alternatives (e.g., Daubechies, Symlet). The decomposition level was set equal to 6, consequently the minimum packet bandwidth is  $200/2^7 = 1.57$  Hz, which allows for a good discrimination of the modal components.

To quantify the sparsifying effect of the signal representation domain [131], the Gini index for an  $N$ -dimensional vector  $\mathbf{a}$  was selected:

$$Gi = 1 - 2 \sum_{n=1}^N \frac{a_n}{\|\mathbf{a}\|_1} \left( \frac{N - n + 0.5}{N} \right) \quad (20)$$

The Gini index was preferred over energy-dependent alternatives because of its higher statistical relevance in presence of noisy measurements ( $\|\cdot\|_p$  stands for the  $\ell_p$  norm of the vector). This is the case of the considered scenario, where recorded acceleration data are characterized by weak amplitudes as a direct consequence of the considered beam loading conditions.

For the sake of clarity, vector  $\mathbf{a}$  consists in the projection coefficients of the acceleration data calculated as  $\mathbf{a} = \Psi^{-1}\mathbf{y}$ . In particular, the Gini term was computed both for the DCT and WPT representations, considering multiple time frames and sampling locations. Such a multi-sensor assessment procedure was necessary to prevent the analysis from being influenced by sensing positions proximal to the nodal points of the investigated mode shapes, in which the energy of the modal components is vanishing.

The outcomes of the sparsity analysis are depicted in Fig. 25, in which each of the three panels represents the actual trends in the  $Gi$  index for the adapted WPT (red line -  $Gi_{WPT}$ ) and DCT (blue line -  $Gi_{DCT}$ ) basis over subsequent signal frames - sensor locations  $S_1$ ,  $S_3$ ,  $S_6$  are considered. As  $Gi$  approximates the unit value, the sparsity ratio is more pronounced. The global frame energy  $E_g$  (black curve) is also illustrated, so that the obtained sparsity indicators can be compared to the magnitude of the measured acceleration data in the original time domain.<sup>2</sup> Apart from low energy segments, in which the blue and red curves are almost overlapped, the sparsifying effect of the WPT basis is clearly superior for all the considered sensor positions, with  $Gi_{WPT}$  larger than  $Gi_{DCT}$  of more than 0.1 points on average.

The sparsifying effect of the WPT basis is meant to enhance the performance of the CS-recovery in a structurally-oriented manner. To verify this statement, the quality of the results was judged in structural terms by computing MAC values, either using the DCT or the WPT sparsifying basis, as input for the MRak-CS approach in nominal conditions (compression-free signals are taken as reference). The results are reported in Table 8 and prove that DCT-based recovery is much less accurate in capturing the signal characteristics, especially as far as the third mode is concerned, which is instead a more sensitive damage indicator.

<sup>2</sup> For pure visualization purposes, this parameter has been rescaled to be comparable with Gini index values.

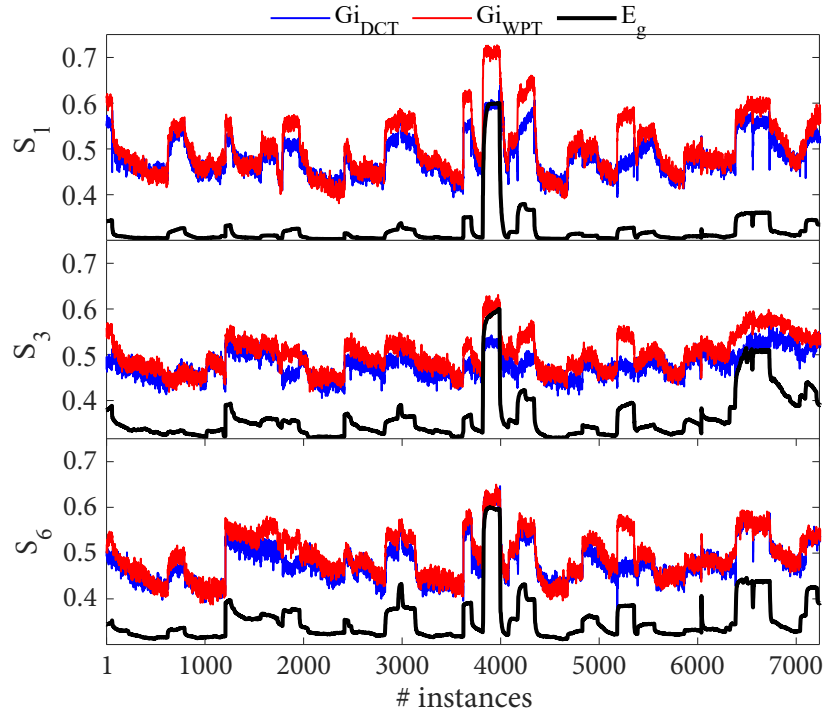


Figure 25: Trends in Gini index for WPT (red) and DCT (blue) transformed acceleration coefficients over different signal instances, superimposed to the normalised and rescaled signal energy (black curve) in the original time domain. Results are presented for sensing positions  $S_1$ ,  $S_2$ ,  $S_3$ . [©2021 IEEE]

#### 4.4.2.2 Compression approach: Rakness-based vs benchmark solutions

Rather than focusing on the classical Average Reconstruction Signal-to-Noise-Ratio (ARSNR), which assesses the consistency of the reconstructed data in the original time domain, a more robust mode shape-related metric was computed to measure the quality of the proposed solution as a function of the compression ratio. The rationale behind this choice is that structural assessment based on mode shapes is widely understood to be more robust against environmental uncertainties, which may unavoidably alter the mere frequency peak localization. The quality of the signal recovery was assessed by taking MAC as main metric, with a safety threshold raised to 0.95 since it is necessary to ensure the highest possible congruence to compression-free monitoring approaches.

The performance was evaluated in all the tested configurations (nominal and altered). Exemplary spectra in nominal conditions for one data record are reported in the upper charts of Fig. 26, in which each of the three charts relates, from left to right, to the Rak-CS, MRak-CS and PCA reconstructed acceleration data. The curves in each panel indicate the frequency distribution of the CPSD matrix among the six sampling positions, stepping from lower (blue) to higher (red) CR values, overlapped to the raw measurements' profile (black).

One fundamental result needs to be underlined, which is the filtering effect inherent to the PCA strategy. Noticeably, the structural information which is retained after the PCA compression-decompression process is limited to the acceleration content appearing in the estimated input correlation profile used during the training phase. Consequently, spurious components, which can be induced either by frequency shifts from pristine vi-

Table 8: MAC values between compression free and MRak-CS reconstructed mode shapes with DCT and WPT sparsity basis (left and right column, respectively).

CR	DCT			WPT		
	f <sub>1</sub>	f <sub>2</sub>	f <sub>3</sub>	f <sub>1</sub>	f <sub>2</sub>	f <sub>3</sub>
4.00	0.99	1.00	0.94	0.98	1.00	1.00
5.00	0.99	1.00	0.94	0.97	1.00	0.99
6.00	0.97	0.99	0.48	1.00	0.98	0.98
7.00	0.98	1.00	0.95	0.98	0.98	0.97
8.00	0.95	0.97	0.82	0.96	0.99	0.93
9.00	0.94	0.98	0.45	0.96	0.96	0.92
10.00	0.93	1.00	0.92	0.92	0.92	0.90

bration conditions or by outbreaks of unexpected modal components due to possible structural deterioration, are canceled out by the signal compression/decompression. Conversely, Rak-CS and MRak-CS can capture these unpredictable but highly probable vibration anomalies.

It is also important to refresh that more pronounced variations in the modal frequencies imply a greater sensitivity in defect detection. Therefore, recalling the importance of reconstructing with significant accuracy the highest modal components, and despite the extremely accurate results appearing in Table 9 under the columns associated with modal components  $f_1$  and  $f_2$ , the remaining poor performance in correspondence of the third mode hampers the robust applicability of PCA as suitable candidate for OMA-based vibration diagnostics.

Indeed, PCA-based compression schemes provide a strict signal adaptation process, where the term *strict* means that the only spectral components that can be retrieved in the decompression stage are those captured by the first  $m$  most energetic eigenvalues identified in the training phase. In this context, as long as the variations in the structural modes are modest and effectively represented by the eigenvalues belonging to the subset of preserved components, the PCA compression is compatible with an effective reconstruction of the corresponding spectral information. On the contrary, as soon as this condition is no more satisfied, because of strong system perturbation, the decoded information loses any consistency with respect to the original signal content. In the tested use case, it can be observed that the first two vibration modes experience rather limited downshifts. In more detail, the maximum reduction in  $f_1$  and  $f_2$  was estimated equal to 0.72 Hz ( $m_A@x_3$ ) and 1.94 Hz ( $m_B@x_2$ ), respectively. On the other hand, a consistently higher contraction of 5.29 Hz ( $m_B@x_2$ ) was observed for the third mode, a quantity which justifies the poor reconstruction performance of PCA in the bottom panel of Fig. 26, as well as the low MAC values associated to the third modal component. This is also coherent with the fact that the MAC values between experimental mode shapes reconstructed from the original signals (without compression) in nominal and defective configuration are very high for the first two modal components: 0.978 and 0.965, respectively, whereas a significant reduction is observed for the third mode with MAC degrading down to 0.879.

It is worth noting that the input signal correlation matrix used for altered conditions is the same that was adopted for the nominal ones. In this way, it was possible to evaluate

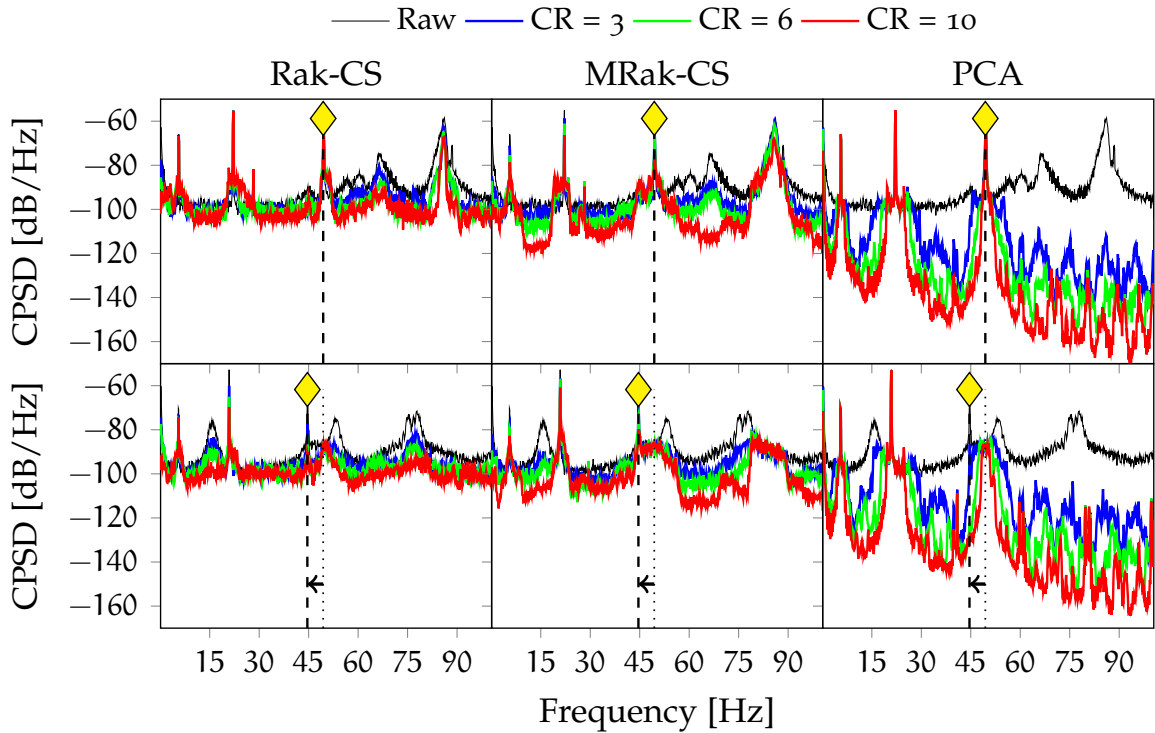


Figure 26: Correlation profile of the CPSD matrix for the considered compression methodologies as a function of increasing CR values in nominal (top line) and altered (bottom line) conditions. Yellow markers are also included in order to better track identify the frequency shift experienced by the third vibration mode. [©2021 IEEE]

how the distinct encoding/decoding mechanisms may cope with spectral changes which may occur in long-term monitoring tasks. For instance, the third vibration mode appearing in the panels altered with the mass  $m_B$  hanged at position  $x_2$  (highlighted in the bottom subplots of Fig. 26 with yellow diamond markers) is downshifted from 49.68 Hz in nominal conditions to 44.39 Hz, corresponding to a frequency reduction above 10%. Notably, such a significant change cannot be tracked by the PCA strategy, while Rak-CS and MRak-CS are capable to detect such mode even for high CRs.

MAC factors computed by correlating mode shapes coming from uncompressed vs recovered measurements for the three dominant vibration modes are reported in Table 9. As can be seen, a poor reconstruction performance characterizes the RND-CS method: very low MAC values (often below 0.9) are achieved in all the considered structural configurations if CR is higher than 5. This is coherent with the compression levels reported in previous studies conducted on long-span structures [96].

In the comparison among the rakeness-driven solutions, it is possible to observe a more pronounced denoising effect of the MRak-CS method, while the noise floor of Rak-CS is slightly higher. This effect is more evident for higher CRs. The improvement brought by the adoption of the MRak-CS design is also evident in the results reported in Table 9. In detail, MAC values achieved with MRak-CS are larger than those attained with Rak-CS in almost all the altered cases. In particular, it might be shown that MRak-CS provides sufficient MAC factors (i.e.  $MAC \geq 0.9$ ) when CR is increased up to  $CR = 7$ , which guarantees a sufficient modal consistency for all the inspected modes. This result compares favorably

with alternative solutions presented in the literature, where the estimated CR values were consistently below  $CR = 5$  [95].

Table 9: MAC values between raw and reconstructed mode shapes for different structural configurations. From top to down group lines, RND-CS, PCA, Rak-CS and MRak-CS results. [©2021 IEEE]

CR	Nom			$m_A@x_1$			$m_A@x_2$			$m_A@x_3$			$m_B@x_1$			$m_B@x_2$			
	$f_1$	$f_2$	$f_3$	$f_1$	$f_2$	$f_3$	$f_1$	$f_2$	$f_3$	$f_1$	$f_2$	$f_3$	$f_1$	$f_2$	$f_3$	$f_1$	$f_2$	$f_3$	
RND-CS	4.00	0.96	0.93	0.96	0.99	0.99	0.98	0.96	0.96	0.94	0.98	0.98	0.97	0.97	0.91	0.98	0.98	0.99	0.83
	5.00	0.95	0.94	0.92	0.99	0.97	0.96	0.96	0.78	0.26	0.98	0.91	0.87	0.97	0.84	0.63	0.98	0.97	0.58
	6.00	0.94	0.94	0.97	0.99	0.91	0.63	0.88	0.95	0.73	0.95	0.99	0.36	0.95	0.70	0.42	0.94	0.95	0.92
	7.00	0.83	0.89	0.80	0.98	0.89	0.77	0.98	0.66	0.99	0.99	0.90	0.49	0.92	0.73	0.44	0.93	0.93	0.94
	8.00	0.73	0.97	0.98	0.96	0.91	0.50	0.96	0.85	0.81	0.92	0.94	0.37	0.98	0.76	0.35	0.96	0.91	0.44
	9.00	0.61	0.95	0.97	0.99	0.73	0.87	0.90	0.20	0.49	0.99	0.49	0.96	0.95	0.25	0.20	0.95	0.92	0.86
	10.00	0.58	0.94	0.81	0.96	0.86	0.78	0.93	0.72	0.30	0.87	0.77	0.54	0.91	0.76	0.41	0.91	0.96	0.75
PCA	4.00	1.00	1.00	1.00	1.00	1.00	0.80	1.00	1.00	0.99	1.00	1.00	1.00	1.00	1.00	0.36	1.00	1.00	0.96
	5.00	1.00	1.00	1.00	1.00	1.00	0.67	1.00	1.00	0.78	1.00	1.00	0.98	1.00	1.00	0.47	1.00	1.00	0.37
	6.00	1.00	1.00	1.00	1.00	1.00	0.66	1.00	1.00	0.73	1.00	1.00	1.00	1.00	1.00	0.48	1.00	1.00	0.34
	7.00	1.00	1.00	1.00	1.00	1.00	0.70	1.00	1.00	0.84	1.00	1.00	1.00	1.00	1.00	0.50	1.00	1.00	0.34
	8.00	1.00	1.00	1.00	1.00	1.00	0.71	1.00	1.00	0.83	1.00	1.00	1.00	1.00	1.00	0.79	1.00	1.00	0.51
	9.00	1.00	1.00	1.00	1.00	1.00	0.72	1.00	1.00	0.83	1.00	1.00	1.00	1.00	1.00	0.68	1.00	0.98	0.50
	10.00	1.00	1.00	1.00	1.00	1.00	0.71	1.00	1.00	0.81	1.00	1.00	0.91	1.00	1.00	0.73	1.00	0.48	0.49
Rak-CS	4.00	1.00	1.00	0.99	1.00	1.00	0.98	1.00	0.98	0.97	0.99	0.98	0.97	0.99	0.98	0.95	0.97	0.98	0.96
	5.00	1.00	1.00	0.99	1.00	1.00	0.95	1.00	0.96	0.37	0.99	0.95	0.99	0.98	0.99	0.93	0.97	0.98	0.94
	6.00	1.00	1.00	0.99	1.00	1.00	0.88	1.00	0.96	0.93	0.99	0.98	0.87	0.99	0.93	0.92	0.98	0.99	0.93
	7.00	1.00	1.00	0.99	1.00	1.00	0.89	0.99	0.91	0.46	0.99	0.79	0.86	0.99	0.99	0.94	0.99	0.88	0.88
	8.00	1.00	1.00	0.99	1.00	0.87	0.94	0.99	0.96	0.36	0.98	0.96	0.39	0.99	0.98	0.83	0.97	0.97	0.97
	9.00	0.99	1.00	0.97	1.00	1.00	0.83	1.00	0.96	0.45	0.96	0.78	0.92	0.95	0.92	0.91	0.99	0.86	0.47
	10.00	1.00	1.00	0.97	1.00	0.91	0.31	1.00	0.89	0.46	0.99	0.31	0.71	0.96	0.91	0.51	0.97	0.97	0.53
MRak-CS	4.00	0.98	1.00	1.00	1.00	1.00	0.99	0.99	0.99	0.97	1.00	0.98	0.96	1.00	0.99	0.99	1.00	0.98	0.99
	5.00	0.97	1.00	0.99	0.99	1.00	0.97	0.99	0.98	0.98	0.99	0.98	0.96	0.99	0.99	0.99	1.00	0.99	0.98
	6.00	1.00	0.98	0.98	0.97	0.97	0.98	0.99	0.97	0.99	0.98	0.99	0.96	0.94	0.98	0.81	0.99	0.97	0.97
	7.00	0.98	0.98	0.97	0.98	0.99	0.98	0.97	0.97	0.97	0.94	0.98	0.92	0.98	1.00	0.95	0.99	0.99	0.97
	8.00	0.96	0.99	0.93	0.99	0.98	0.95	0.98	0.98	0.99	0.99	0.96	0.95	0.93	0.99	0.99	0.99	0.99	0.97
	9.00	0.96	0.96	0.92	0.97	0.81	0.96	0.86	0.96	0.95	0.98	0.97	0.96	0.95	0.97	0.67	0.99	1.00	0.95
	10.00	0.92	0.92	0.90	0.96	0.85	0.92	0.97	0.95	0.66	0.99	0.89	0.83	0.96	0.99	0.40	0.99	0.99	0.92

Additionally, the matching between the theoretical modal frequencies and those extracted via FDD was assessed with experimental data coming from compression-free nominal tests. The extracted frequencies were  $\hat{f}_1 = 5.47$  Hz,  $\hat{f}_2 = 22.07$  Hz and  $\hat{f}_3 = 49.37$  Hz, showing a maximum relative percentage error with respect to the theoretical values equal to  $\varepsilon_1 = 100 \left( 1 - \frac{\hat{f}_1}{f_1} \right) = 0.843\%$  in correspondence of the first mode (see Table 10).

Table 10:  $\varepsilon_p^{CS}$  between CS-reconstructed  $f_p^{CS}$  and compression free  $f_p^{Raw}$  modal frequencies for increasing CR values and various structural configurations.

CR	Nom			$m_A@x_1$			$m_A@x_2$			$m_A@x_3$			$m_B@x_1$			$m_B@x_2$		
	$f_1$	$f_2$	$f_3$	$f_1$	$f_2$	$f_3$	$f_1$	$f_2$	$f_3$	$f_1$	$f_2$	$f_3$	$f_1$	$f_2$	$f_3$	$f_1$	$f_2$	$f_3$
4.00	0.84	0.04	0.73	0.65	0.08	0.98	2.58	0.90	0.65	1.56	0.41	1.89	0.81	0.25	0.38	1.52	0.21	0.36
5.00	0.84	0.04	0.73	0.65	0.10	0.98	2.58	0.90	0.65	1.56	0.41	1.89	0.81	0.25	0.59	1.52	0.21	0.94
6.00	2.61	0.04	0.73	0.65	0.10	0.98	2.58	0.90	0.65	1.56	0.41	1.89	0.81	0.25	0.59	1.52	0.21	0.94
10.00	2.61	0.04	0.53	1.42	0.11	0.98	1.52	0.21	0.94	1.56	2.94	0.69	0.81	0.25	0.38	0.81	0.25	0.59

#### 4.5 FROM CS TO CS-ENABLED SHM: AN EDGE COMPUTING PERSPECTIVE

In this Section, some major challenges implied by the practical embodiment of the CS encoding/decoding mechanisms in edge devices within the framework of clustered sensor networks are tackled. The first issue relates to the proper orchestration of the computing resources of the network, since the computational complexity and the memory requirement of the compression and decompression operations are remarkably different. Secondly, the algorithmic effectiveness of the CS strategy may be impaired by the detrimental effects due to noise sources characterizing the electronic equipment. Hence, coping with this instrumental limitations is crucial to define the proper locus of admissible application contexts.

The content of this Section is based upon the research works [P6], [P7]:

"Hardware-Oriented Data Recovery Algorithms for Compressed Sensing-Based Vibration Diagnostics" by Zonzini F., Carbone, A., Romano, F., Zauli M. and De Marchi L. (2021). In Saponara S., De Gloria A. (eds) *Applications in Electronics Pervading Industry, Environment and Society. ApplePies 2020*. Lecture Notes in Electrical Engineering, vol 738. Springer, Cham.<sup>3</sup>

"Compressive Sensing and On-Board Data Recovery for Vibration-Based SHM" by Zauli, M., Zonzini F., Testoni, N., Marzani, A. and De Marchi L. (2021). In Rizzo P., Milazzo A. (eds) *European Workshop on Structural Health Monitoring. EWSHM 2020*. Lecture Notes in Civil Engineering, vol 127. Springer, Cham.<sup>4</sup>

As a matter of fact, CS is a two-step procedure consisting of (i) an initial *encoding* step, in which the actual compression operation takes place, followed by a (ii) second signal recovery phase in which the original time series is retrieved for further elaboration. In cascade, the usual modal assessment process finally takes place. Given this well-defined task assignment, CS inherently embraces the design of a decentralized sensor network topology, in which multiple PSNs, directly deployed on the structure, are arranged in multiple clusters, each of them being coordinated by a corresponding CH unit. Such monitoring architecture is thoroughly schematized in Fig. 27, in which  $C_z$  expresses the generic cluster.

<sup>3</sup> Adapted by permission from Springer Nature Customer Service Centre GmbH: Springer, Lecture Notes in Electrical Engineering, Hardware-Oriented Data Recovery Algorithms for Compressed Sensing-Based Vibration Diagnostics, ©2021

<sup>4</sup> Adapted by permission from Springer Nature Customer Service Centre GmbH: Springer, Lecture Notes in Electrical Engineering, Compressive Sensing and On-Board Data Recovery for Vibration-Based SHM, ©2021

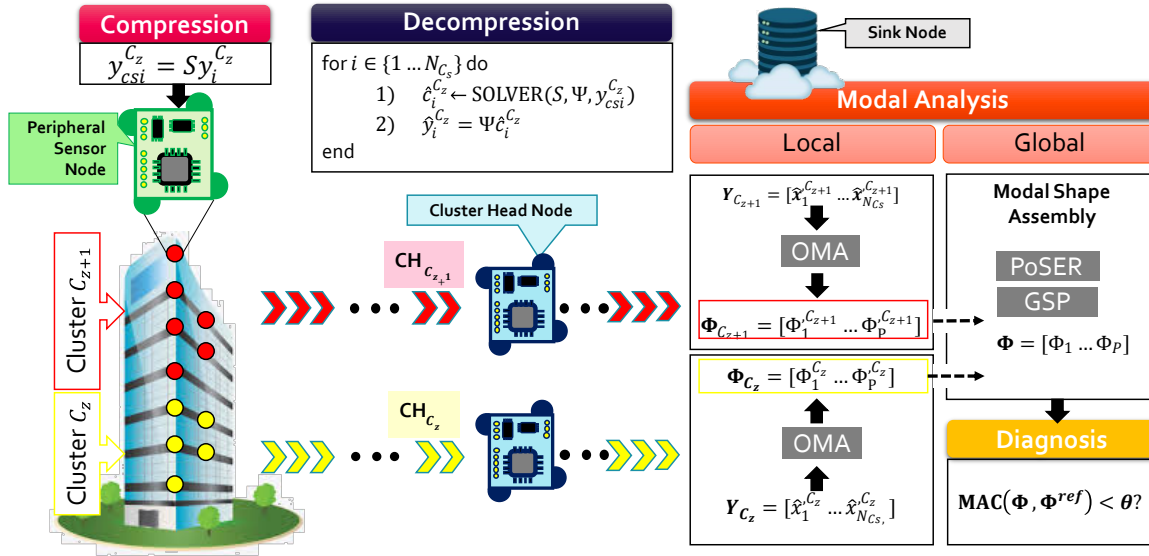


Figure 27: Typical CS-enabled clustered architecture for vibration-based SHM. From left to right, the compression/decompression stages are allocated to the PSNs and the CHs, respectively. Then, the pure modal analysis is performed, firstly identifying cluster-related mode shapes  $\Phi_{C_z}$  and then merging the local estimates into a full-scale mode shape matrix  $\Phi$ . Finally, the current health status can be inferred by monitoring trends in MAC values over time. [Adapted from ©2021]

The advantages of such a hierarchical approach are the following: (i) the computational complexity is minimized, a condition which is ensured by the inherent cluster parallelism, i.e., the capability to retrieve local information prior than returning the full-scale structural parameters; (ii) communication congestion is avoided while the local channel availability is increased, i.e., the sensor density  $N_{C_s}$  per cluster is significantly lower than the cumulative one; (iii) the available HW and SW resources of the network are optimally allocated, subdividing the computational task between the PSNs and their master CH.

As a main result, it is possible to reduce the latency in providing a final structural bulletin and the power budget of the whole system, thanks to the combination of the streaming data processing and the limited amount of data which is exchanged through the network (namely, only sensors' pre-processed modal features assembled by the CH nodes are transmitted to the SN rather than the entire signal waveform).

As far as the algorithmic part is concerned, the proposed workflow involves the cascade of the compression/decompression stages, on top of which the pure modal identification process is stacked. Once the sensor-to-cluster assignment has been defined, i.e., sensor node  $i$  has been assigned to cluster unit  $C_z$ , the following tasks need to be accomplished:

1. *Compression*: each PSN acquires and on-board compresses vibration data, eventually returning  $y_{csi}^{C_z} = S y_i^{C_z}$ ;
2. *Decompression*: upon receiving the compressed signals, one for each of its  $N_{C_s}$  mastered sensor nodes, every  $CH_{C_z}$  recovers the original time series  $\hat{y}_i^{C_z}$ , and arranges them in a form which is suitable for the following modal identification task. Let's suppose a suitable choice is the column matrix  $\hat{Y}_{C_z} = [\hat{y}_1^{C_z}, \dots, \hat{y}_{N_{C_s}}^{C_z}]$ ;

3. *Local Modal Analysis*: given  $\hat{Y}_{C_z}$ , the matrix  $\Phi_{C_z} = [\Phi_1^{C_z}, \dots, \Phi_p^{C_z}]$  of cluster-dependent mode shape vectors is extracted by resorting to one of the available modal identification method (without loss of generality, a similar consideration could be done for modal frequencies);
4. *Global Modal Analysis*: the full-scale mode shape matrix  $\Phi = [\Phi_1 \dots \Phi_p]$  is computed at the SN side by merging together local mode shape estimations  $\Phi_{C_z}$  as prescribed by the mode shape assembly algorithms presented in Section 3.3;
5. *Diagnosis*: the health status of the structure can be finally quantified, e.g., by computing the MAC between the currently estimated  $\Phi$  and the reference mode shape matrix  $\Phi^{ref}$  in case modal-based methods are worthy of application.

Note that the described processing framework corresponds to the conventional CS approach, whereas more advanced solutions could also be envisioned in which the latter steps are skipped and the integrity status directly derived from compressed data. Solutions capable of providing such an alternative only recently started to be investigated, thanks to the significant advancements brought by the AI field. For this reason, the classic scenario beforehand described is taken as operative groundwork in this work.

#### 4.5.1 Design criteria for the CS coder/encoder block

##### 4.5.1.1 Porting CS encoder on extreme edge devices

Analog implementations of the CS encoder have barely been investigated in the literature: a primary reason for this lack is the requirement of had-hoc hardware which renders the sensor design and its deployment process time consuming, more complicated and less versatile in massive sensor networks. A seminal work in this direction is the one in [13], in which the authors proposed a customized version of the Imote2 sensor platform reaching good performance for the on-line assessment of long-span structures. Similarly, in [96], the Narada wireless sensor was employed as a prototyping board for acceleration compression in the framework of bridge assessment.

Conversely, implementing CS in a digital manner is the most efficient strategy for porting on edge devices, owing to the multiply-and-add nature of the involved operations, ensured by the fact that the computation of  $y_{cs}$  is the result of a pure matrix-vector multiplication. The advantage is that, in this case, the sensing matrix can be statically loaded into the non volatile memory of the MCU at the network start-up phase and accessed at run-time to execute compression operations as new signal instances are available. Thus, the favorable algorithmic complexity of the software implementation makes the encoding mechanism readily portable on PSNs. On the other hand, the memory footprint entailed by this solution imposes the frame size and the compression level to be properly evaluated in advance, since extreme edge devices are usually equipped with very limited memory slots which can, in turn, be rapidly saturated. To make a practical example, the selection of  $N = 512$  and a reasonable compression ratio equal to 4 may require more than 250 kB of memory for 32 bit data, which is poorly compatible with most of cut-off-the-shelf devices.

What enables the off-line estimation of the sensing matrix is the long inertia with which the effects of aging manifest on the structural signature. Indeed, despite being subject to



variability over-time, the major causes of changes in the modal characteristics of the structure can be categorized into two main groups: i) structural-dependent factors, i.e., damages which reflect real structural degradation, and ii) EOP agents. The vast majority of the phenomena generating damages (such as corrosion, bolt loosening, cracks) have a slow genesis and progression; therefore, structural failure usually occurs at the end of a long-degrading process. Hence, such processes are associated to relatively long time-constants. Similarly, environmental factors undergo slow variations over time when compared to the structural dynamics itself [132]. For this reason, and from a signal processing perspective, vibration analysis is usually approached as a quasi-stationary system identification problem, exhaustively described by modal parameters associated with the peak spectral values. This is particularly true when the structural analysis task is conducted under normal operating conditions, namely when wind, traffic loading, etc., are used as natural or environmental excitation to the structure (as it is the assumption of output-only modal analysis).

#### 4.5.1.2 *Porting CS decoder on edge devices*

Differently from the encoder, the decoding task is more computationally-onerous. For this reason, it cannot be assigned to extreme edge devices but, rather, its deployment appears more adequate on CH edge boards, where both the processing power and the memory resources are superior.

However, for edge-oriented implementations, the best trade-off between the algorithmic complexity, the memory storage and the retrieved signal accuracy, has to be pursued. Among the many possible solutions (a compelling review of CS-solving algorithms is provided in [133]), iterative algorithms could be particularly suitable due to their faster convergence: this property is essential in real-time inspection scenarios where the latency due to the mere processing should be kept to the minimum. In particular, three main approaches deserve particular interest:

- (i) Orthogonal Matching Pursuit (OMP): considered as one of the most effective serial greedy strategies, the rationale behind this procedure is to update step-by-step the values and positions of the non-zero signal coefficients by exploiting a least-square method.
- (ii) Compressive Sampling Matching Pursuit (CoSaMP): overcoming the main limitations given by the sequential approach at the basis of OMP, CoSaMP jointly refreshes all the non-null entries by refining, at each iteration, their value in the direction of the minimum residual error.
- (iii) Iterative Hard Thresholding (IHT): in essence, IHT is similar to CoSaMP, the main difference being related to the exploitation of a thresholding operator for the simultaneous update of the estimated set of signal coefficients.

#### 4.5.2 *CS at the extreme edge: an experimental validation*

In the following, different experimental tests aimed at corroborating the suitability of CS operations into clustered sensor networks are presented [P6]. Two main goals will be pursued: (i) prove the structural consistency of CS-operated data while combined with mode

shape merging procedures; (ii) comprehensively validate iterative CS-solver algorithm when coded in an hardware-oriented manner. In both cases, the steel beam presented in Section 4.4.1.1 is exploited and the MRak-CS approach employed at the encoding side.

#### 4.5.2.1 HW-oriented implementation of iterative recovery algorithms

For validation purposes, the code implementing the decompression techniques mentioned in Section 4.5.1.2 was programmed in the C++ language to be compatible with the digital signal processing functionalities embedded in edge devices. To this end, all the mathematical procedures and functions were purposely written in order to customise the signal processing framework to the embedded resources of the network.

The three main metrics chosen to quantify the performance of each data recovery method are: (i) the memory footprint  $\text{Mem}$ , namely the total number of initialised data and temporary variables required for the complete reconstruction of a single set of coefficients  $\hat{c}$ , (ii) the running time  $T$ , i.e., the time needed to restore one single frame, and (iii) the ARSNR, which is computed off-line in a post-processing phase. The latter is conventionally used to quantify the noise levels introduced by the CS processing operations according with:

$$\text{ARSNR} = 20 \log \left( \frac{\|y\|_2}{\|y - \hat{y}\|_2} \right) \quad (21)$$

in which  $\|\cdot\|_2$  stands for the  $\ell_2$  norm of the vector. Finally, the Memory-per-Time-over-Accuracy (MTA) factor

$$\text{MTA} = \frac{\text{Mem} \cdot T}{e^{\text{ARSNR}/20}} \quad (22)$$

was introduced with the primary goal of providing an overall evaluation: the lower the MTA, the higher the recovery performance of the sought algorithms are. For the sake of clarity, ARSNR values were computed back in the linear scale to account for the singular values implied by the logarithmic operator, i.e.,  $\text{ARSNR} = 0$  or  $\text{ARSNR} < 0$ .

The same dataset used for the validation of the MRak-CS/WPT approach (Section 4.4.1.1) is employed for testing. The obtained results are depicted in Fig. 28, where the panels in the left-hand side refer, from top to bottom, to the memory occupancy, the mean execution time and the ARSNR computed by averaging among the six accelerometers, respectively. The memory occupancy here reported only accounts for the variables involved in the data recovery algorithms themselves. Thus, assuming that the CS operators are pre-loaded, it has been estimated that, in the worst cases associated to limited compression scenarios (e.g.  $\text{CR} = 3$ ), the IHT, CoSaMP and OMP solutions may require a buffer size up to 1 MB due to the huge dimensions of the sensing matrix and the sparsity basis.

The MTA quantity is displayed in the right chart and provides an overall cost analysis. As can be seen, the OMP implementation largely outperforms the other alternatives at all the levels of evaluation; its MTA is at least half of the total burden associated to IHT and CoSaMP for all the considered CRs. It is also worthy mentioning that, despite the characteristics of IHT appear to be competitive in terms of memory size, its associated reconstruction accuracy is lower and it requires a larger execution time.

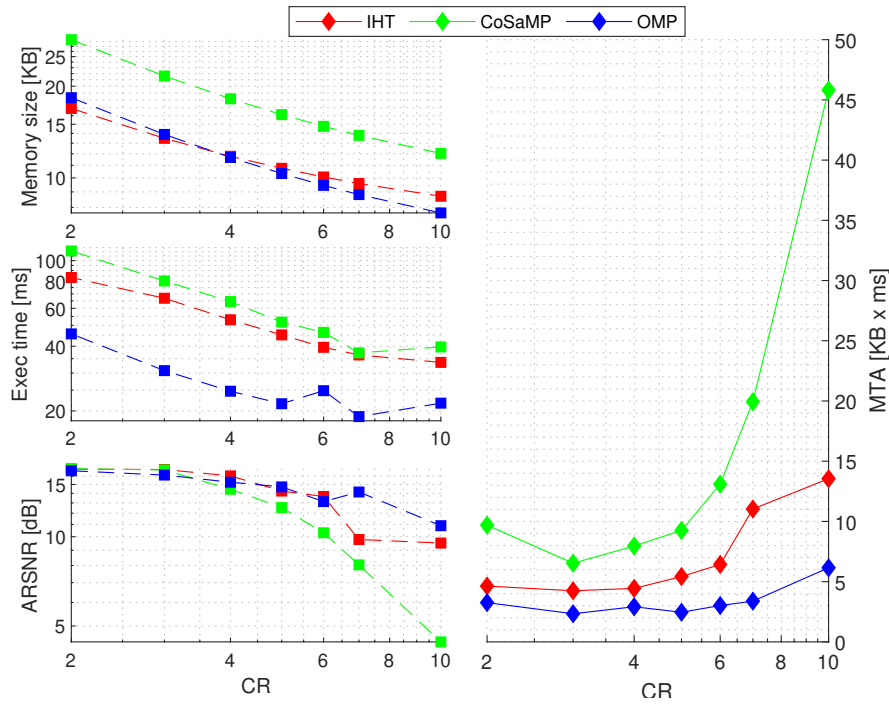


Figure 28: Cost analysis for the considered recovery algorithm. In the left-hand side, memory occupancy, execution time and ARSNR are displayed from top to the bottom. The MTA product between the three curves per CR is conversely displayed in the right panel. [©2021 Springer]

#### 4.5.2.2 Combining CS with mode shape assembly

A double chain of six PSNs was used to instrument the structure, each of them being orchestrated by a purposely devoted CH (Fig. 29). Worthy to be noticed, the two clusters are overlapped in correspondence of their terminal position (position 'PA'), and, for this reason, the PoSER approach was applied for convenience.

Concerning the entailed CS operations, both the sensing matrix  $S$  and the DCT sparsity basis  $\Psi$  were thought to be pre-charged into the nodes memory at the network startup, as justified above. The OMP solver algorithm was used instead during the recovery process for the superior performances shown in Section 4.5.2.1

Acceleration data along the  $z$  axis were acquired, repeatedly, over time windows of 75 s (i.e., each time series consisted of 15 000 samples), and then framed into data segment of  $N = 512$  samples. The compression factor was varied in the interval  $[2;10]$ .

Experiments were designed to leave the beam vibrating under ground borne vibration, so as to mimic the typical vibration conditions imposed by the operative environment. Results in terms of MAC values are reported in the left panel of Fig. 30, superimposed to the benchmark level of 90% in order to better track the quality of the identified structural information. Besides, the three vertical charts in the right side of Fig. 30 refer to the different modal components, each of them including exemplary full-scale reconstructed mode shapes for a selection of compression factors.

It is worth noting that an abrupt reduction in modal fitting occurs for compression factors exceeding  $CR = 4$ . It is also evident that the performance is heavily dependent on the selected mode shape. In fact, if the MAC trend affecting the second mode shape (green-rounded line) is just slowly decreasing with increasing CRs, the behaviour associated with

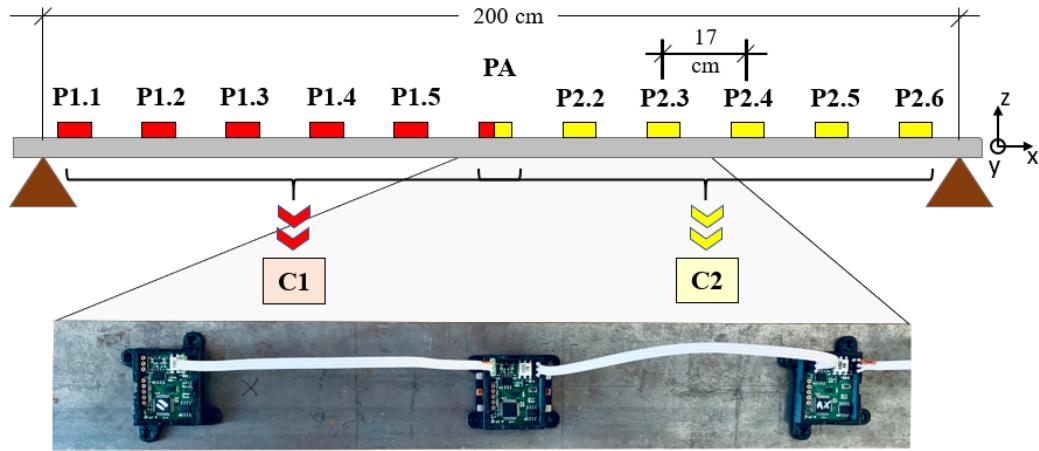


Figure 29: Experimental testbed and related sensor installation plan, comprising two clusters (C1 and C2, respectively) of six accelerometers. An inset depicting the practical connection of three PSNs is also enclosed. [©2021 Springer]

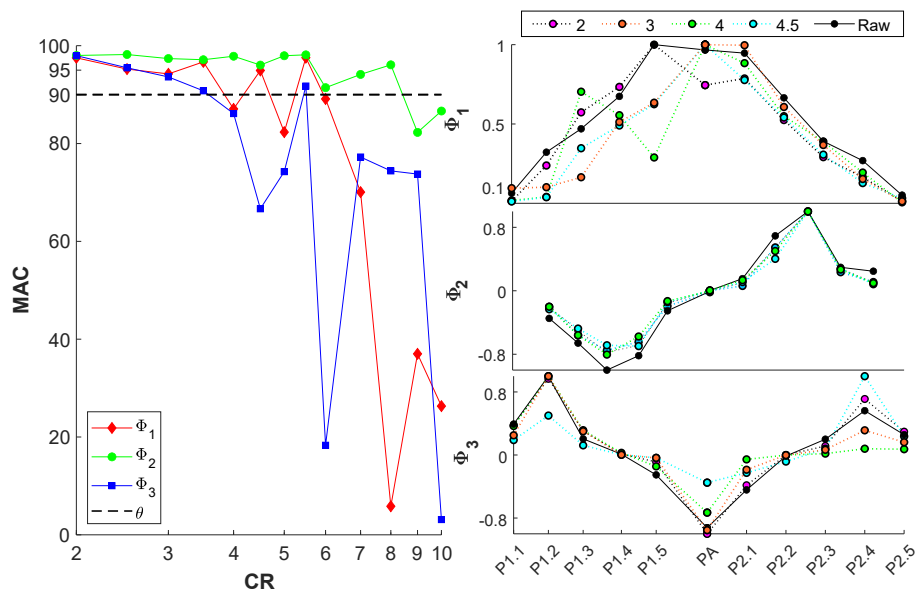


Figure 30: Left: trend in MAC values between CS-reconstructed and compression-free full-scale modal shapes as a function of the compression ratio, superimposed to the chosen accuracy level indicated by the black-dotted line at 90%. Red-rumbled, green-rounded and blue-squared line styles refer to the first, second and third modal shape, respectively. Right: reconstructed full-scale modal shapes for a representative selection of CR values. [©2021 Springer]

the first mode shape (red-rumbled curve) shows a more pronounced decreasing trend. A more peculiar pattern characterises the MAC curve associated to the third mode shape (blue-squared line). This phenomenon can be attributed to the fact that the energy of the third mode is very weak with respect to the other two components. Indeed, in this case, the random effects due to sampling uncertainties and the instrumental noise generate the oscillations in the estimated modal coordinates.

On the contrary, MAC percentages for low CRs (i.e.  $CR \in [2;4]$ ) are always above 90% for all the inspected mode shapes, apart from the limit case  $CR = 4$  where the modal fitting of the first and third mode slightly falls nearby 87%. An additional proof of the obtained outcomes is provided by the good level of superposition in the corresponding mode shapes depicted in the left-hand side of Fig. 30.

#### 4.5.3 CS vs Noise in MEMS sensors

The content of this sub-Section is based upon the research work [P8]:

"HW-Oriented Compressed Sensing for Operational Modal Analysis: The Impact of Noise in MEMS Accelerometer Networks" by Zonzini, F., Zauli, M., Mangia, M., Testoni, N., and De Marchi, L. (2021, August). *2021 IEEE Sensors Applications Symposium (SAS), 2021, pp. 1-5*. ©2021 IEEE

from which part of the text is drawn.

Real-world signals are inherently affected by structural non-idealities and ambient-related disturbances, which may hamper the applicability of CS strategies, in the sense that they undermine the sparsity assumption. A major cause for this can be due to the important noise floors and undesired operative interference which might frequently corrupt the environment in the surrounding of the monitored structure.

On the other side, this environmental limitation, that holds regardless of the adopted monitoring solution, often combines with an additional source of noise, the one affecting electronic devices. This is exactly the case of accelerometer - or, more generally, inertial sensors - realized in MEMS technology: the latter has become, in recent years, the dominating sensing technology for vibration-based applications enabling for the widespread development of low-cost, dense and miniaturized sensor networks. Indeed, MEMS devices are characterized by high-sensitivity, low-power consumption and very high integration levels: all these properties made this sensing technology a cost-effective yet reliable and extremely advantageous alternative to the piezoelectric counterpart for the design of accelerometer sensors [134]. The problem with MEMS is that, notwithstanding their successful adoption, signals acquired by these accelerometers are affected by comparatively higher intrinsic noise density values, which thus need to be properly coped with in the CS signal processing chain.

Furthermore, it is worth mentioning that works trying to explore the effects of such instrumental noise in OMA-oriented architectures are very scarce in the literature. In line with this, the same concepts have already been emphasized and validated against the reconstruction accuracy of controlled mechanical and industrial sites [135] [136]. Nonetheless, the results discussed in the above-referenced manuscripts have not tangibly related the instrumental noise to the specificity of the exciting sources. Aiming at bridging this

gap, the analysis presented in [P8] is one of the few works discussing the importance of noise levels in CS-based approaches for OMA scenarios, moreover extending the analysis to the actual sensing capabilities of cut-of-the-shelves MEMS accelerometer devices.

#### 4.5.4 CS vs noise: an experimental validation

The experimental campaign conducted in [P8] was aimed at establishing a practical bound to the effectiveness of the Rak-CS technique in presence of practical noise levels deriving from both instrumentation specifications and structural vibration conditions. Consistently, numerical simulations and experiments were performed for the structure described in 4.4.1.1 in nominal working conditions.

For the sake of clarity, the selection of the Rak-CS solution over the MRak-CS draws foundation in two main aspects. From one side, since the objective, at this stage, is to evaluate the effect of noise levels themselves on CS, results obtained in Section 4.4.2.2 demonstrate that designing the sensing matrix as prescribed by the Rak-CS approach provides a more severe test to be passed. Secondly, and in line with the above consideration, working in nominal conditions allows the effects of structural degradation to be disregarded such that it is possible to restrict the attention on the mere impact of instrumental noise: in this case, the two methods perform similarly.

##### 4.5.4.1 Materials

Resorting to a simplistic test-bed has the one exploited in this experimental campaign yielded two main benefits: the relatively simple shape of the beam enables for the fast design of a corresponding Finite Element Model (FEM) and, secondly, this kind of structure shows a localized and identifiable vibration behavior, a condition which permits to assess the Rak-CS performances when corrupted by different electronic/exciting noise levels whilst neglecting the additional complexities inherent to the structure itself.

The mechanical and geometrical properties of the beam were presented in [137] and the synthetic acceleration responses at sampling positions  $S_{1,\dots,6}$  were then predicted through an ad-hoc FEM analysis tool. Being capable to create such a model was advantageous from a signal processing perspective, too. Remarkably, Rak-CS is an adapted CS method which requires the availability of a prior batch of signals for the derivation of the correlation profile of the sensing matrix. However, this procedure could be quite time-consuming while performed only via experimental data. Hence, using a numerical tool could be effective to expedite the deployment phase.

##### 4.5.4.2 Methods

The compression mechanism has been configured as follows. Striving to reduce the computational burden associated to the compression stage, an antipodal derivation of the sensing matrix [138] was preferred (as in Section 4.4.2.2). As a sparsifying basis, the one drawn from DCT was conversely selected. Signal instances were subdivided into  $N = 512$  sample-long segments, whereas the compression ratio was varied in  $\{4, 6, 10\}$ .

To simulate the presence of noise sources, the simulated vibration responses were corrupted with white Gaussian noise. The SNR was imposed in the  $[-25;30]$  dB range. The selected noise values were meant to simulate practical and typical working conditions

when the structure is excited by operational/environmental forces. A thorough description of the typical acceleration ranges can be found in many technical recommendations (see, for example, the American National Standard ISO 4866:2010<sup>5</sup>). Thus, since the entity of this excitation is most frequently very low, even the corresponding structural responses are usually poorly energetic and might easily overlap to the residual noise density hidden in electronic devices. For these reasons, severe SNR levels were taken into consideration.

A total number of 1000 noise-free signal instances were numerically generated for the computation of the correlation matrix  $C^s$  by varying along the beam span the point at which the external stimulus was applied. The noise power  $\sigma_e^2$  was estimated, too. In the simulated case, it was simply derived as the noise power ensuring a prescribed SNR. Conversely, for in-field data, it was computed as the median absolute value of a time series acquired during a zero-time measuring phase in which no vibrations were induced.

MAC values among compression-free ( $\Phi_{p,raw}$ ) and compressed/reconstructed mode shapes ( $\Phi_{p,CS}$ )<sup>6</sup> were quantified. An additional metric has been introduced to measure the quality of the decompressed structural parameters as a function of the prescribed SNR and CR: the Peak Signal-to-Noise Ratio (PSNR). Borrowed from the image processing field, the conventional definition of PSNR [139] has been purposely specialised for each  $p$ -th structural frequency to deal with the multi-modal nature of vibration data. Here, the quantity:

$$\text{PSNR}_p = 10 \log(S_y(f_p)) - 10 \log(\sigma_e^2) \quad (23)$$

is used to express to what extent the power spectral density  $S_y(f_p)$  occurring at the peak of the structural mode  $f_p$  is distinguishable with respect to the noise power  $\sigma_e^2$ .

#### 4.5.4.3 Results

Trends in MAC index are reported in Fig. 31 as a function of the different PSNR values, moving from lower to higher compression factors (CR = 4, CR = 6 and CR = 10 in first, second and third line, respectively). Each column refers to the Rak-CS reconstructed mode shapes, namely  $\Phi_{1,CS}$ ,  $\Phi_{2,CS}$ ,  $\Phi_{3,CS}$ , corresponding to vibration frequencies  $f_1$ ,  $f_2$ ,  $f_3$ .

It can be noticed that, independently from the adopted CR value, the PSNR varies in a broader interval the higher the order of the structural component. As prescribed by the structural dynamics theory [130], this outcome proves that high-order vibration frequencies are more sensitive to noise levels due to the intrinsic lower energy they may carry.

Apart from the pure noise level comparison, a significant structural coherence, namely MAC values above 0.95 (black dotted line in Fig.31), occurs between uncompressed and reconstructed mode shapes both for synthetic and real data, and for increasing compression factors. Despite one isolated case corresponding to CR = 6 at relatively low PNSR, the fittings in the simulated/experimental MAC are acceptable in the remaining configurations.

To summarize, the noise-to-structure cross-analysis reveals that the Rak-CS approach can be useful for data compression in vibration-based SHM implementations even for relatively deep compression levels. This statement holds if a PNSR\* of at least 20 dB

<sup>5</sup> <https://www.iso.org/standard/38967.html>.

<sup>6</sup> A minimum accuracy threshold of 0.95 has been considered here to ensure a modal fitting as close as possible to compression-free scenarios

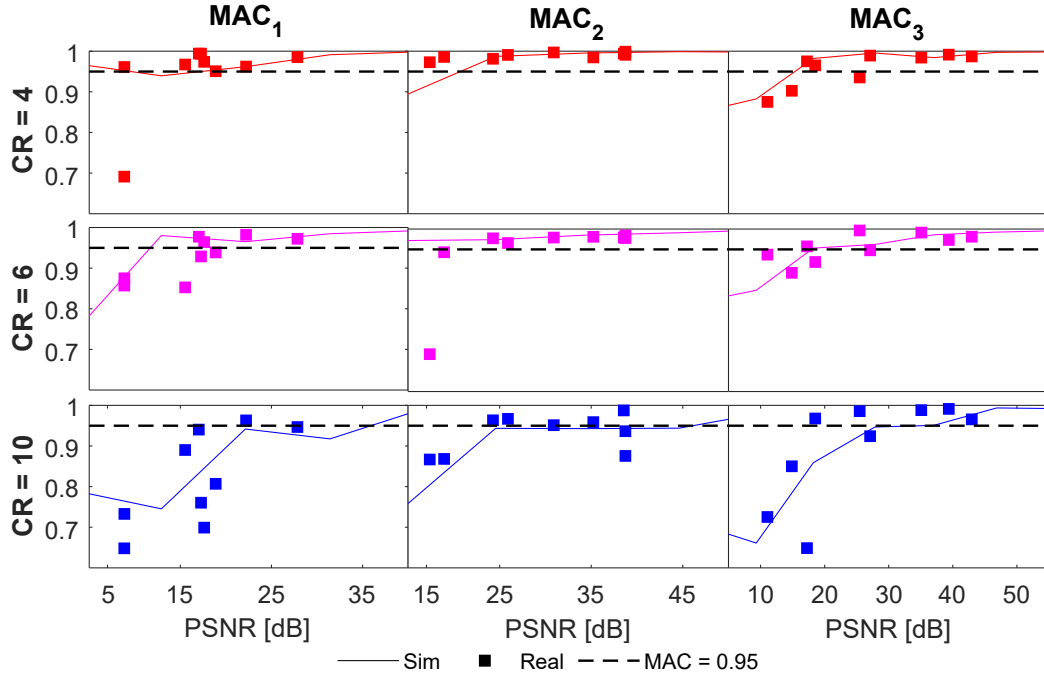


Figure 31: Trends in MAC value as a function of different PSNR values for increasing compression factors. Each line refers to a different CR value (from bottom to the down, CR = 4, CR = 6 and CR = 10, respectively) while each column corresponds to one of three reconstructed modal shapes. Results deriving from structural simulations (continuous line) are superimposed to those pertaining to in-field measurements (squared markers). The black dotted line indicate the structural accuracy level, i.e., MAC value greater than 0.95. [©2021 IEEE]

characterizes the spectral magnitude of the sought modal components. Accordingly, a relationship between the useful signal magnitude  $y^*$  and the intrinsic sensor noise floor value  $y_e$  can be stated as:

$$\text{PNSR}^* \geq 20 \log(y^*) - 20 \log(y_e) \quad (24)$$

In particular, assuming that  $y^*$  is  $g$  times the minimum detectable acceleration value  $y_{\min}$  ( $y^* = g y_{\min}$ ), the amplification factor  $g$  can be obtained as  $g \geq \frac{y_e}{y_{\min}} \cdot 10^{(\text{PNSR}^*/20)}$ . Focusing on the application at hand and assuming the sensor characteristics mentioned in Appendix A, for the chosen sampling rate of 200 Hz,  $y_{\min} = 0.061 \text{ mg}$  and  $y_e = 80 \mu\text{g}\sqrt{200} = 1.128 \text{ mg}$  can be estimated. These values yield to  $g \geq 185$ , i.e.,  $y^* \geq 11.24 \text{ mg}$ . This signal entity meets the typical acceleration ranges involved in OMA-based scenarios, where the common magnitudes are in the order of thousands of  $\mu\text{g}$ , such as human-related activities, earthquakes, ground blastings [140].

#### 4.6 CONCLUSIONS

This Chapter focused on the optimization of state-of-the-art CS solutions for data compression in the field of vibration monitoring. This objective has been achieved by combining a novel model-assisted CS strategy, the MRak-CS method, capable of adapting, in a conservative manner, to the specific spectral signature of the target structure. Besides,



a structurally-shaped algorithm for the design of the sparsity basis based on the WPT has been presented, favoring a better sparsity level of the processed signals and, thus, allowing for a higher compression level.

The validity of the proposed data compression system was assessed during an experimental campaign aimed at verifying the integrity conditions of a pinned-pinned steel beam. The obtained results highlight that the concurrent optimization of the signal representation domain, together with the advantages of the MRak-CS sensing scheme, can disclose increased compression ratios while attaining superior performances in the quality of the reconstructed structural parameters if compared with conventional approaches. The effectiveness of the methods was also shown in defective configurations.

Finally, the practical issues to be coped with while deploying CS operators in decentralized monitoring systems were investigated. In more detail, it has been proven that: *(i)* CS is a local optimization tool compatible with mode shape merging procedures for the consistent retrieval of global modal features; *(ii)* the effect of instrumental and environmental influences could play a crucial role for the effective CS-driven manipulation of vibration data collected in operative scenarios.



## SYSTEM IDENTIFICATION AT THE EXTREME EDGE FOR NETWORK LOAD REDUCTION

---

### ABSTRACT

*Overcoming the main shortcomings of CS techniques for vibration diagnostics, the current Chapter explores SysId as an innovative strategy for data compression suitable to be performed at the extreme edge. Solutions taken from the dense linear algebra are exploited to run input–output and output–only SysId models on a resource constrained device. Besides, a cost–benefit analysis is also presented, in which the energy saving brought by SysId running on peripheral sensor nodes is comprehensively measured against the power consumption due to data transmission, as implied by state–of–the–art communication protocols for IoT ecosystems.*

The content of this Chapter is based upon the research work [P9]:

"System Identification at the Extreme Edge for Network Load Reduction in Vibration Monitoring" by Zonzini F., Dertimanis, V., Chatzi, E. and De Marchi L. (2021). *Submitted to IEEE Internet of Things Journal, 2021.*

from which part of the text is drawn.

### 5.1 INTRODUCTION

In Section 2.2.2.1, it has been asserted that:

The objective of parametric system identification is to estimate that set of filter coefficients, also known as *model parameters*, which can exactly reproduce the measured input–output system relationship.

This statements specifies that the power of time series models (or, simply, parametric models, as they are commonly addressed in the literature) is to instill structure and to encapsulate, in this way, the meaningful portion of the signal content in a reduced set of values (the model parameters), which fully capture the underlying system dynamics.

The key reason for their exploitation in SHM applications is that, since the number of parameters typically settles below a couple of dozens [141], massive compression levels could be potentially attained considering the length of the time series to be collected. Hence, SysId represents a compelling alternative to standard Fourier–driven, as well as CS or eigenvalue–based approaches, in the context of vibration monitoring.

It is worth pinpointing that the benefit in pursuing parametric identification strategies is not restricted to the reduction of the data payload to be transmitted, but more importantly extends to the significant enhancement in the quality of the retrieved spectral properties [142]. In this sense, a twofold advantage is brought. Firstly, the spectrum is analytically generated from the computed filter coefficients, as opposed to the conventional approach of applying a Fourier transformation on the raw data, where the influence of noise might

be detrimental. Thus, spectra deriving from parametric methods inherently allow for a significant increase in the SNR. Secondly, it follows that the delivered spectral profiles are characterized by a much sharper and smoother trend with respect to non-parametric approaches; as pinpointed in Section 2.2.1.1, this trait facilitates the subsequent feature extraction phase, especially when dealing with PP algorithms.

Notwithstanding these advantages, there are very few examples of SysId implementations on edge or extreme edge devices available in the literature. A possible explanation is in the high computational complexity and memory requirement of the involved algorithms, which render their embodiment in resource-constrained sensors a non-trivial task.

A noteworthy exception is the work presented in [12], where the authors exploit parametric system modeling, running on the Imote sensor platform, for the structural assessment of civil infrastructures. Nevertheless, despite showing promising results, the very restrictive memory footprint of this sensor board was not compliant with the execution of the algorithms required by output-only SysId. To tackle this issue, the same authors adopted simple correlation-based methods, at the expenses of a lower communication efficiency, implied by the necessity of broadcasting a reference signal to multiple nodes.

Conversely, in the strategy proposed in this work, such requirements are alleviated and accounted for by means of efficient linear algebra operations. Coherently, the expedients resorted to for the embodiment of SysId in extreme edge devices are investigated, and their performances thoroughly evaluated from an algorithmic, structural and energy point of view.

## 5.2 ESTIMATING MODEL PARAMETER AT THE EDGE: FROM OLS TO S-TSQR-OLS

### 5.2.1 The OLS formulation

SysId makes use of regression techniques to identify the sought model parameters, as typically those minimizing the error between the predicted and actually measured system response according to certain heuristics.

Accordingly, the expression provided in Eq.(1) can straightforwardly be converted into a linear regression formulation, as follows:

$$\mathbf{y}[k] = \zeta[k]^T \boldsymbol{\beta} + \varepsilon[k] \quad (25)$$

with  $\zeta[k]^T \in \mathbb{R}^{1 \times N_p}$  designating the regression vector and  $\boldsymbol{\beta} \in \mathbb{R}^{N_p \times 1}$  denoting the coefficient vector to be estimated. Assuming that the time series spans an observation window of  $N$  samples, a full-scale variant of (25) is given as:

$$\mathbf{Y} = \mathbf{Z}\boldsymbol{\beta} + \mathbf{E} \quad (26)$$

where  $\mathbf{Z} = [\zeta[1] \dots \zeta[N]]^T \in \mathbf{R}^{N \times N_p}$  is a rectangular matrix with regression vectors arranged as horizontal entries, per row;  $\mathbf{Y} = [\mathbf{y}[1] \dots \mathbf{y}[N]]^T \in \mathbf{R}^{N \times 1}$  and  $\mathbf{E} = [\mathbf{e}[1] \dots \mathbf{e}[N]]^T \in \mathbf{R}^{N \times 1}$  correspond, instead, to the observation and error vector. Hence, a final estimate of the sought coefficient vector is yielded via Ordinary Least Squares (OLS), according to:

Table 11: Regression matrix and model parameter vector for the ARX, AR and ARMA parametric models.

ARX	AR	ARMA
$Z[k] = \begin{bmatrix} -y[k-1] \\ \vdots \\ -y[k-q_1] \\ u[k] \\ \vdots \\ u[k-q_2] \end{bmatrix} \quad \beta = \begin{bmatrix} \theta_1 \\ \vdots \\ \theta_{q_1} \\ \gamma_0 \\ \vdots \\ \gamma_{q_2} \end{bmatrix}$	$Z[k] = \begin{bmatrix} -y[k-1] \\ \vdots \\ -y[k-q_1] \end{bmatrix} \quad \beta = \begin{bmatrix} \theta_1 \\ \vdots \\ \theta_{q_1} \end{bmatrix}$	$Z[k] = \begin{bmatrix} -y[k-1] \\ \vdots \\ -y[k-q_1] \\ e[k] \\ \vdots \\ e[k-q_2] \end{bmatrix} \quad \beta = \begin{bmatrix} \theta_1 \\ \vdots \\ \theta_{q_1} \\ \gamma_1 \\ \vdots \\ \gamma_{q_2} \end{bmatrix}$

$$\beta = (Z^T Z)^{-1} Z^T \mathbf{Y} \quad (27)$$

while a recovery of the prediction error is returned as

$$\mathbf{E} = \mathbf{Y} - Z\beta \quad (28)$$

with variance  $\sigma_e^2 = \mathbf{E}^T \mathbf{E}$ . As such, any parametric model is completely characterized by a set of  $N_p + 1$  values. Obviously, the regression quantities  $\beta$  and  $Z$  strictly depend on the adopted SysId model: for ARX, AR and ARMA, they have been collected in Table 11.

#### 5.2.1.1 OLS for ARMA models: the Hannan–Rissanen algorithm

The regression technique described above is only applicable for single-stage parametric models, such as ARX and AR, and may not be implemented for evaluation of the ARMA counterpart. In fact, in the latter case,  $y[k]$  is regressed not only on its past values, but also on the preceding unobserved quantity  $e[k]$ , which thus needs to be implicitly calculated. In this case, the Hannan–Rissanen (HR) algorithm [143] provides a simple and yet asymptotically stable solution. HR is based on the cascade of two successive OLS steps: firstly, a high-order AR model is fitted to the measured response and an estimate of the noise term is derived, as dictated by Eq. (28). Knowing  $\mathbf{E}$ , the next step involves matching a low-order ARX model to the same time series, finally returning an estimate of the ARMA parameters. To be consistent, the order of the first-step AR model should be at least twice the one adopted in the second ARX stage.

#### 5.2.2 From OLS to QR decomposition

The canonical OLS algorithm, which is given in Eq. (26), might be prone to numerical instability, rounding effects and bad conditioning, primarily due to the required inverse matrix operation. To partly alleviate these effects, the QR factorization of the regression matrix is usually suggested as a viable procedure. Indeed, the QR [144] factorization aims at decomposing a full-rank matrix in the product of two independent matrices, namely an orthogonal matrix  $Q$  and an upper triangular matrix  $R$ , with the advantage of converting any complex linear system into a simple back-substitution procedure.

For the problem at hand,  $Z = QR$  can thus be computed and, once plugged into (26), the QR-based variant of OLS (QR for Ordinary Least Squares (QR-OLS)) becomes:

$$\beta = R^{-1}Q^T Y \quad (29)$$

The dimensions of the two factorizing matrices depend, in turn, on the arrangement of the matrix to be decomposed. In our case, the ratio between the number of rows ( $N = N_{s1p}N_p$ ) and columns ( $N_p$ ) of the regression matrix exactly amounts to  $N_{s1p}$ , i.e., the number of samples per parameter, which is empirically suggested to be a quantity larger than 20 in order to guarantee a sufficiently accurate estimation of the model parameters. Given this, the upper triangular structure of  $R$  imposes that only its upper  $[N_p \times N_p]$  partition differs from zero. As such, an economy-size variant of the standard QR has to be preferred, returning  $Q \in \mathbb{R}^{N \times N_p}$  and  $R \in \mathbb{R}^{N_p \times N_p}$ .

Several algorithms are available to accomplish QR decomposition. The Householder reflection method [144] is specifically suggested for edge solutions, granting the most-favorable compromise among the modified Graham-Schmidt orthogonalization, which is readily implementable but extremely prone to numerical errors, and Givens rotation, that, conversely, shows great stability but sensitivity to overflow/underflow in single-precision floating-point values [99], [145]. The choice was driven by the necessity to handle very weak and faint signals, sometimes close to the sensor sensitivity, as would be the case for vibration responses that are induced by ambient loads.

### 5.2.3 From QR to Sequential Tall-skinny QR decomposition

QR-OLS is efficient in terms of processing, owing to its conceptual and algorithmic simplicity. However, in this form, it appears impractical for near-sensor embodiment because of its elevated memory requirements imposed by the large dimensions of the matrices to be processed. It should be noted that the dimension of  $Z$  increases with the square power of the number of parameters, i.e.,  $\dim\{Z(\cdot)\} \propto N_p^2 N_{s1p}$ , while the Random Access Memories (RAM), in low-power and low-cost MCUs, are typically below a couple of hundreds of kB, even for the devices with the largest storage capabilities. It follows that, when  $N_p$  is in the order of a few tens and a minimum number of samples per parameter ( $N_{s1p}$ ) is set, the available memory is rapidly consumed. As an example, assuming a single piece of data is represented as a word of 4 B (i.e., 32-bit parallelism), the combination of  $N_p = 20$  and  $N_{s1p} = 20$  requires at least  $4N_p^2 N_{s1p} = 32$  kB of memory entirely dedicated to the storage of the regression matrix.

To overcome these restrictions, a MCU version of the classical Sequential Tall-Skinny QR (S-TSQR) decomposition [146] is proposed. S-TSQR was originally conceptualized to bypass the limitations of parallel architectures (in particular, of MapReduce) to provide a communication-avoiding solution for dense linear algebra problems enabling data transfer reduction by means of local grid operations. In this work, the standard S-TSQR has been adapted to single-core embedded platforms, in which the computing power and the memory allocation policy of the processor are dramatically lower. Such goal was achieved by exploiting efficient coding techniques such as loop unrolling, register blocking, buffered multiplications, vector outer product and matrix addition merging and transposed multiplications enabling fast arithmetic and optimal memory re-use.

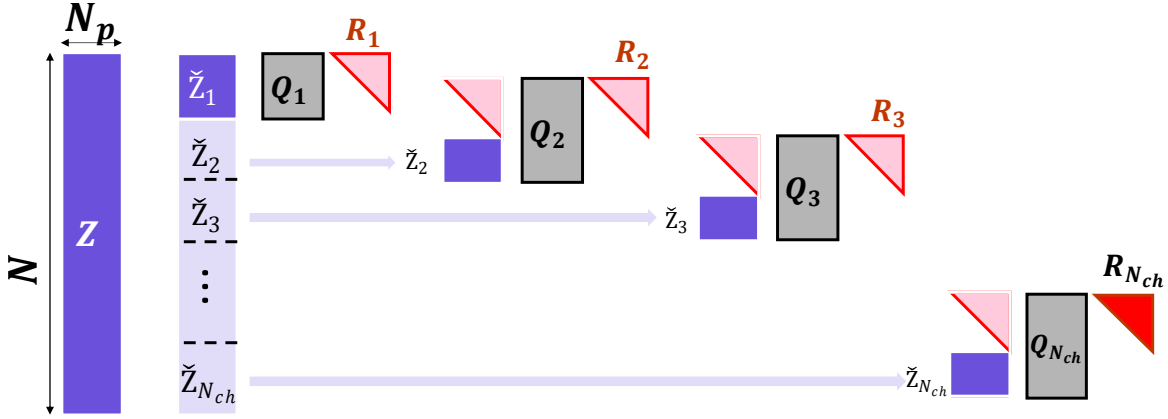


Figure 32: Processing flow at the basis of the S-TSQR decomposition approach adopted in this work for the sake of matrix dimension reduction.

In general terms, S-TSQR leverages the key concept of *reproducibility*, i.e., the ability to obtain bit-wise identical results from different runs of the same algorithm given identical input data, regardless of how the computing resources are scheduled. In this sense, the ruling principle at the basis of S-TSQR (schematically depicted in the block diagram of Fig. 32) is to partition the full-scale decomposition of  $Z$  in the subsequent decomposition of small-size  $\tilde{Z}_i \in \mathbf{R}^{N_r \times N_p}$  ( $i \in \{1, N_{ch}\}$ ) matrices comprising at most  $N_r = N/N_{ch} + N_p$  rows dictated by the selected number of chunks  $N_{ch}$ . The procedure is described as follows. Apart from the initial step acting directly on the first  $N/N_c$  rows of  $Z$ , in all the remaining  $N_c - 1$  iterations QR is performed on the newly generated matrix  $Z_i = [R_{i-1} | \tilde{Z}_i]^T$  obtained from the horizontal concatenation of the previously computed  $R_{i-1}$  matrix and the current block rows  $\tilde{Z}_i$ . Accordingly, the original  $Q$  and  $R$  terms, referring to the complete regression matrix, can be recovered as  $R = R_{N_{ch}}$  and  $Q = Q_1 Q_2 \dots Q_{N_{ch}}$ . This means that, while  $R$  can be taken directly at the output of the last iteration in a very efficient way, the computation of  $Q$  according with the canonical S-TSQR procedure [146] is not affordable because it consumes a memory space exactly equal to the original regression matrix to be decomposed, and because it implies the storage of all the intermediate  $Q_i$  matrices.

To overcome this limitation, a new and memory efficient procedure has been implemented in a novel manner. The proposed solution, referred to as Embedded S-TSQR (eS-TSQR), is inspired by the sparse structure of the  $Q_i$  matrices, whose non-null and non-unitary entries are the *Householder reflectors*  $\alpha_i$  [144], i.e., those vectors which are used to perform the orthogonal triangularization of the matrix  $R$ . In particular, at the end of each TSQR iteration, an additional step (the coefficients vector update) is introduced, so that the matrix product  $Q^T \mathbf{Y} = Q_{N_c}^T \dots Q_2^T Q_1^T \mathbf{Y}$  is substituted by two dot-products  $\mathbf{Y}_i = \alpha_i \alpha_i^T \mathbf{Y}_{i-1}$  ( $\mathbf{Y}_0 = \mathbf{Y}$ ).

#### 5.2.4 Wrapping up: the eS-TSQR-OLS approach

A complete description of the implemented Embedded Sequential Tall-Skinny QR Decomposition for OLS (eS-TSQR-OLS) procedure is depicted in Fig. 33, where the two main phases, namely eS-TSQR and  $\text{SysId}$ , are underlined. Note that ARX and AR form direct methods meaning that one single cycle of eS-TSQR-OLS is necessary to obtain the sought model

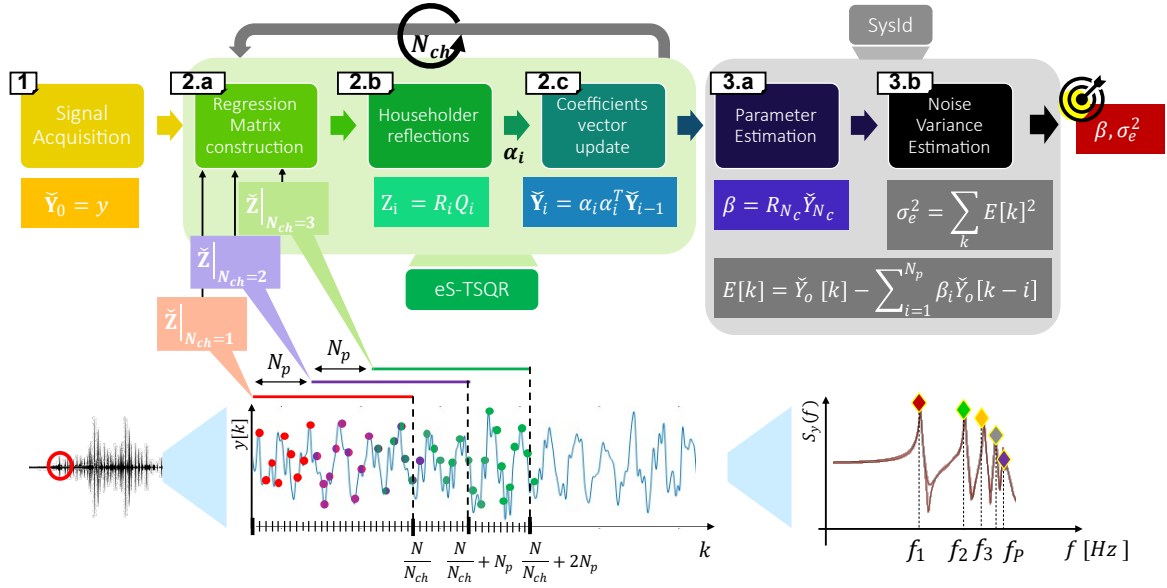


Figure 33: eS-TSQR-OLS processing flow for model parameter estimation. From left to right: once signals have been acquired (step 1), the eS-TSQR decomposition process is entered and repeated  $N_{ch}$  times: at each  $i$ -th iteration, the regression matrix is firstly created as stated in Table 3 by selecting the proper signal frame (step 2.a), each comprising a sliding window of  $N/N_{ch}$  samples at step size equal to the number of parameters  $N_p$ . Then, the Householder decomposition of  $Z_i$  is applied (step 2.b), paving the way for the subsequent update of the coefficient vector  $\tilde{Y}$ . At the end of the  $N_{ch}$ -th cycle, the upper triangular matrix  $R_{N_c}$  and  $\tilde{Y}_{N_{ch}}$  are used in the SysId phase to compute the model parameters  $\beta$  (step 3.a) and the residual noise density  $\sigma_e^2$  (step 3.b). The finite set of  $N_p$  quantities can, thus, be transmitted at the receiving side, where the spectrum profile  $S_y(f)$  of the acquired signal can be reconstructed and the sensor-related modal information are then extracted (e.g. the peak spectral values  $f_p$ ).

parameters. Conversely, ARMA models imply a recursive two-stage procedure. In this case, the entire procedure needs to be repeated twice: firstly, AR is adopted to retrieve the (unknown) noise exciting force, which is then used in a second eS-TSQR-OLS iteration built on the ARX model in order to derive the ARMA parameters.

#### 5.2.4.1 Selecting the chunk size

The optimal number of partitions  $N_{ch}$  for the eS-TSQR decomposition is a function of the selected number of samples per parameter. In order the Householder algorithm to be applicable, it must be ensured that the number of rows in the regression matrix is strictly higher than the number of columns, corresponding to  $N_p$ . This condition is always satisfied in the second iteration of the S-TSQR, due to the fact that the regression matrix constitutes of the horizontal concatenation of the previously computed Householder matrix  $R$  and the new block row. While, in the first iteration,  $N_{ch}$  should be selected such that

$$\frac{N_{s1p}N_p - N_p}{N_{ch}} \geq N_p \quad (30)$$

from which it is easy to derive that  $N_{ch}^* \leq N_{s1p} - 1$ . Hereinafter,  $N_{ch} = N_{ch}^*$  will be assumed.



### 5.3 PROTOTYPING SYSID AT THE EXTREME EDGE

During the prototyping phase, the algorithmic accuracy of the proposed eS-TSQR-OLS is firstly assessed, then investigating the effectiveness of the entire methodology for damage assessment even in presence of noisy signals.

#### 5.3.1 Materials

The parametric models presented in Section 2.2.2.1 were embedded in the STM32L522ZE-Q Nucleo board, which is one of the latest products released by ST Microelectronics for the prototyping of embedded applications requiring ultra-low-power consumption and higher security levels. It integrates, at its core, an STM32L5 MCU [147] based on an ARM<sup>®</sup> Cortex<sup>®</sup>-M33 processor with a single-precision FPU and upgraded level of performances thanks to the enhanced Digital Signal Processing (DSP) functionalities. The equipped memory amounts to 256 kB of RAM and 512 kB of FLASH, which are enough to accommodate both static and volatile data for typical duty-cycles of SHM scenarios.

#### 5.3.2 Algorithmic validation

##### 5.3.2.1 Model order selection

The selection of the proper model order is a critical point for the efficacy of parametric models, since both under or over-estimation may hamper the actual retrieval of the hidden structural information [148]. A plurality of methods has been proposed to tackle this challenge, which are usually based on statistical metrics, such as the Bayesian Information Criterion (BIC) adopted in this work [149]. Once estimated on a meaningful batch of data, the model order is assumed constant; as discussed before, such approach is enabled by the slow-varying structural properties characterizing the vast majority of civil and industrial structures [132].

##### 5.3.2.2 Performance metrics

From the computed set of parameters, modal information can be retrieved by analysing the associated PSD. As such, the quality of the identified structural properties was assessed by means of the Itakura-Saito Spectral Divergence (ISD) [150]. ISD represents a cumulative measure of the point-wise spectral distance between two different PSD curves. For  $N$ -long frequency vectors, it is defined as:

$$\text{ISD} = \frac{1}{N} \sum_{c=1}^N \left[ \frac{S_y(f)}{\hat{S}_y(f)} - \log \left( \frac{S_y(f)}{\hat{S}_y(f)} \right) - 1 \right] \quad (31)$$

The goal of this analysis is to demonstrate the equivalence of fast running remote servers processing high-depth signals and extreme edge-processing computation in vibration monitoring; thus,  $S_y(f)$  and  $\hat{S}_y(f)$  are the PSDs computed via SysId as detailed in Section 5.2, by using the model parameters estimated by the MCU with the eS-TSQR-OLS approach, and via built-in MATLAB<sup>®</sup> functions addressing the same task, respectively. ISD ranges between 0 and 1: spectral superposition is considered perfect in case the ISD equals to zero, whereas higher values highlight possible misalignments.

Table 12: ISD values (multiplied by  $10^2$ ) for varying model order and number of samples per parameter.

$N_{s1p}$	$N_p$						
	9	17	25	33	41	49	57
25	1.36	1.42	1.40	1.42	1.39	1.40	1.36
30	1.15	1.15	1.16	1.12	1.12	1.17	1.12
35	0.95	0.99	0.95	0.93	0.93	0.93	0.93
40	0.82	0.83	0.82	0.82	0.80	0.79	0
45	0.73	0.69	0.71	0.71	0.71	0	0

### 5.3.2.3 Results

The effectiveness of the implemented extreme-edge processing with respect to off-line computation has been verified in the first phase of the experimental validation. In particular, attention is focused on the validation of the ARMA model estimation because, given the dual-stage structure of the HR algorithm, the retrieval of ARMA parameters implicitly confirms the validity of both the AR and ARX implementations.

This was accomplished by loading into the STM32L5 FLASH memory one noise-corrupted vibration signal, which was generated via simulation of a six-storey shear frame under white noise base excitation. All the possible combinations of  $N_p$  and  $N_{s1p}$  values were explored by varying the former quantity in between 9 and 57 (step size equal to 8), whereas the latter was swept in the interval [25;50] (step size equal to 5). The performance was evaluated in spectral terms via the ISD and the corresponding results are reported in Table 12.

As can be observed, ISD values are below  $1.5 \cdot 10^{-2}$  even for the worst-performing configuration, while reaching perfect superposition in some cases (e.g.,  $N_p = 49$  and  $N_{s1p} = 45$ ).

### 5.3.3 Execution time

To measure the execution time, the  $N_p$  and  $N_{s1p}$  pairs discussed in Section 5.3.2 were selected, obtaining the processing times depicted in Fig. 34 for the AR<sup>1</sup> (red scale curves) and ARMA (blue scale curves) model.

The reported trends confirm that the time consumed by the ARMA model is nearly double the time required by the MCU for execution of the AR variant, when a mutual number of samples per parameter and total amount of parameters is used for both models. This outcome is, once again, consistent with the AR-ARX nature of the adopted HR algorithm. From Fig. 34, it can be seen that the relationship between the processing time and  $N_p$  is cubic, whereas the variation due to  $N_{s1p}$  is a linear function of the selected number of samples per parameter.

The maximum reported computation time amounts to 129 s and is associated with an ARMA model involving  $N_p = 57$  and  $N_{s1p} = 45$ , i.e., 57 parameters are to be extracted from the time series (2565 samples). For real-field deployment, where algorithms are to be executed with low latency, such computation time is barely compatible with high

<sup>1</sup> Execution time for ARX model were not included since it is equal to the one required by AR for the same total number of parameters.

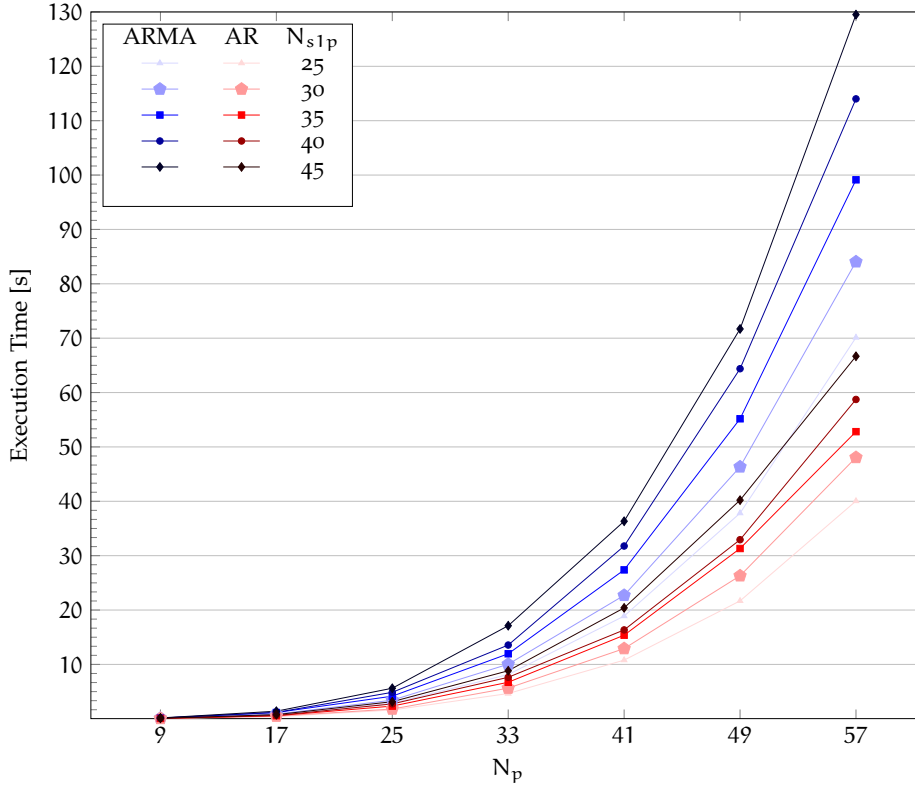


Figure 34: Execution time for ARMA (blue scale curves) and AR (red scale curves) model running on STM32L5 MCU under different  $N_p$  and  $N_{s1p}$  configurations.

sampling rates. For the sake of an example, acquiring 2565 samples at 50 Hz requires about 50 s, which is slightly more than one third of the time taken for processing them.

It is worth noting that, in many practical applications, a viable way to speed up identification is to apply a band-pass filtering operation before running the actual parametric identification task. This reduces the true content of the signal, owing to the focus on some selected spectral bands and, in turn, lowers the number of parameters that are necessary to accurately model the system dynamics, which implies a decrease in the computation time according to  $N_p^3$ . In addition, as mentioned above, computing such a large number of parameters is hardly required in typical SHM scenarios, where model orders are usually confined below a couple of dozens even for the most complicated vibration patterns, such as the ones characterised by highly coupled modes or very rich profiles [141]. As such, SysId remains an efficient means for data compression even in presence of rapidly varying structural behavior. This possibility is granted by the fact that, by processing successive time frames with comparably shorter size, it is possible to identify potential anomalies in the structure by tracking how the spectral content extracted from the corresponding model parameters changes over subsequent signal instances.

### 5.3.4 *Structural validation*

#### 5.3.5 *The case study: a Windspot blade wind turbine*

The proposed edge solution for data compression was validated on an actual operating structure. This objective was pursued by exploiting field data collected for a small-scale wind turbine hosted in the IBK laboratory at ETH Zürich. In more detail, the considered test-bed consists in a 3.5 kW Windspot prototype blade, manufactured by Sonkyo Energy [151]. Its structural behaviour has been extensively investigated against artificially-induced dynamic excitation, as well as varying environmental conditions under both pristine ("healthy") and damaged scenarios<sup>2</sup>. In the referenced work, the vibration response signals, induced by white noise excitation (effective frequency bandwidth between 0 and 400 Hz) are considered to emulate a practical OMA scenario, which requires use of a broad-band (ambient) excitation.

In [151], an experimental study has been performed on the considered blade structure, which reveals that the vibration pattern experienced by this structure is remarkably complex, as it is characterized by multiple and closely-spaced spectral regions undergoing significant changes due to varying temperature and operational effects. This suggests that simple AR models would be either ineffective in capturing all the significant components with enough resolution or, conversely, too complex to approximate a reasonable solution. Hence, an ARMA model was applied, whose model order - according to the BIC criterion - has been estimated equal to 20 ( $N_p = 40+1$ ), for processing time frames of 3000 samples, acquired at a sampling frequency of 833 Hz. The corresponding compression factor amounts to  $CR = 3000/40 = 75$ .

#### 5.3.6 *Including the effect of instrumental noise*

Similarly to the approach adopted in the preliminary validation step, data were statically loaded into the MCU non-volatile memory at the start-up after conversion to the float32 bit format. Moreover, since the response signals were acquired via use of commercial instrumentation involving PCB Piezotronics accelerometers that feature high sensitivity and high resolution levels, which are not compliant with long-term and low-cost monitoring systems, the datasets were corrupted with white Gaussian noise. This is meant to replicate the intrinsic electronic and mechanical drifts that are common in commercial digital MEMS devices for low-cost and low-power embedded applications. In particular, the following features were considered: sensor noise equal to  $80 \mu\text{g}/\sqrt{\text{Hz}}$ , a constant offset bias of 40 mg, 16-bit ADC resolution corresponding to 0.061 mg/LSB, zero-g level and sensitivity change versus temperature of  $\pm 0.1 \text{ mg}/^\circ\text{C}$  and  $\pm 0.01 \text{ \%}/^\circ\text{C}$ , respectively.

#### 5.3.7 *Results*

The effectiveness of ARMA models for data compression has been evaluated by verifying whether the spectral signatures, that were reconstructed by the ARMA parameters that were computed by the STM32L5 device under varying conditions, are capable to track the corresponding shifts in the peak spectral values. The rationale behind this choice

<sup>2</sup> The collected signals have been made publicly available at <https://zenodo.org/record/3229743#.YLpz8vkzaUm>)

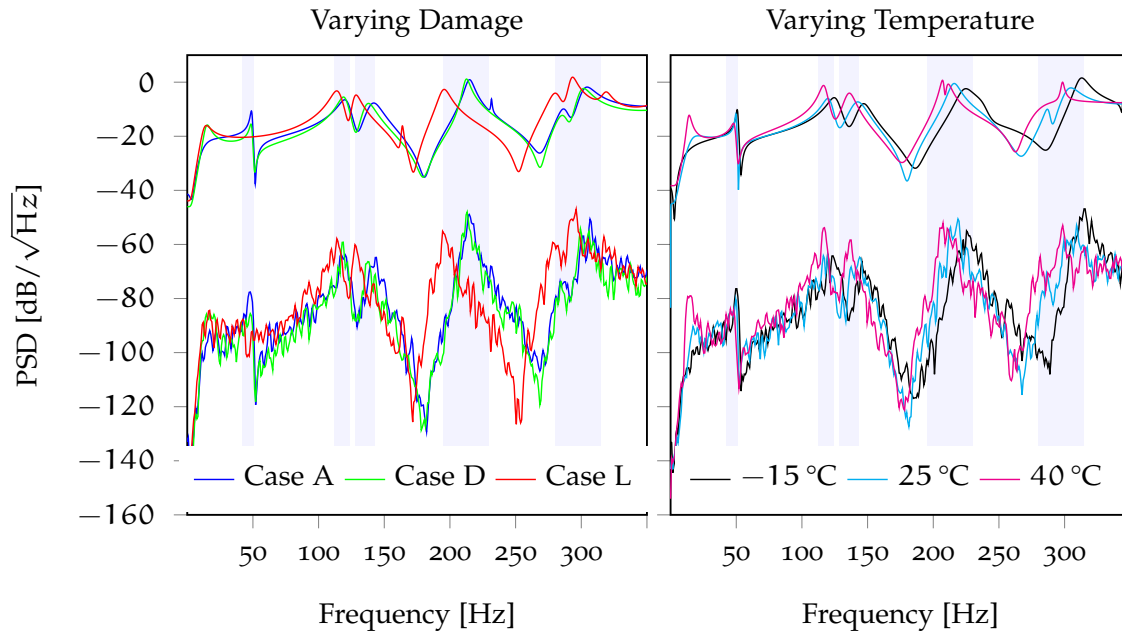


Figure 35: Spectra of the wind turbine blade working at the reference temperature of +25 °C under progressive damage tests (left), while the effects of temperature changes are underlined in the right hand image for the damage-free status. Signals at higher density levels, characterised by a smoother profile, are obtained by SysId running on sensor, whereas the ones appearing at the bottom part are computed by standard Welch's method for PSD.

is that variations in the frequencies that are associated with the most energetic modal components form important indicators of possible damages or, in other words, are proxies of anomalies (defects).

Two different analyses were performed and the obtained spectral profiles are shown in Fig. 35. In Fig. 35a, the capability of the adopted ARMA model to follow the frequency variations induced by man-made damages is investigated. Three reference cases, denoted in the figure with label A, D and L and characterised by the same temperature value of +25 °C, correspond to three different damaged status simulating, in sequence, the presence of one added mass (case A), the formation of one single crack (case D) and the concurrent occurrence of three cracking phenomena (case L). On another study, three signals for the healthy blade were processed while varying the temperature range between -15 °C, +25 °C and +40 °C (see Fig. 35b). In both cases, the perturbation in the spectrum is clearly evident and increases for higher natural frequencies. This is additionally noted via use of grey background boxes whose width increases while moving toward higher frequencies.

Comparing the spectral curves derived from ARMA parameters and the ones computed via the more conventional Welch estimator (lower part of the spectrum), a good agreement is noticeable: indeed, despite a vertical shift due to a bias in the estimated noise density  $\sigma_e^2$ , the peak locations remain clearly centered as well as the global trends superimpose in quite a precise manner. The main difference between the two spectral estimators is given by the filtering effect of the parametric method, which finally provides a PSD plot that can be more reliably used for extraction of the structural modes in both regimes.

## 5.4 COST-BENEFIT ANALYSIS

The energy consumption of a sensor node strongly depends on the executed tasks, which may pertain to data acquisition, data processing and data transmission, with each task contributing to the overall power budget. Indeed, it has been demonstrated [152] that outsourcing data in wireless devices is the most demanding operation, due to the significant amount of power required by the transmission module to travel long distances with minimal payload degradation.

When no operation needs to be executed, the sensor node enters a quiescent mode in which the energy expenditure is kept minimal to preserve battery life-cycle. Furthermore, this discrepancy increases when considering the power spent in idle state. In this condition, which is imposed when no overriding task is executed, the sensor node enters a sleep phase to minimize the power consumption: no more than a couple of  $\mu\text{W}$  are usually consumed in this modality, which is more than three order of magnitude less expensive than transmitting.

The energy consumption is also strongly influenced by the execution time of compression and/or identification tasks. Unfortunately, while the elapsed times for acquiring and transmitting information are deterministic quantities (related to the total frame size, the compression technique and the communication protocol), the accurate estimation of the DSP time is non-trivial. The reason is that some dependencies between different portions of the code (i.e., break instructions, conditionals) can be thoroughly evaluated only at run-time.

### 5.4.1 *Quantifying energy consumption in IoT applications*

Overwhelming the common approach usually focusing only on the mathematical technicalities, the specific impact of extreme edge signal processing for SysId to the power budget has been comprehensively evaluated in conjunction with the one of transmission, by taking into consideration the communication protocols that are best suited for IoT applications. In doing this analysis, the energy spent for sampling can be neglected, as it is proportional to the length of the signal to be acquired, which is supposed equal for all the adopted compression algorithms.

Further to SysId solutions (label SysId), compression-free scenarios (label No DSP), as well as compressed sensing solutions (label CS) are considered, the latter representing the main (and most commonly adopted) competitor for data compression in this field.

#### 5.4.1.1 *IoT-protocols for WSN*

To accomplish this goal, the IoT analyzer toolbox<sup>3</sup> presented in [152] has been specifically exploited since it provides an open source platform which allows to simulate the working principles of different IoT-oriented protocols for wireless sensor networks, and to quantify the energy consumption of the corresponding hardware modules. The complete list of protocols and related hardware considered in this work includes: the nrf52840 multiprotocol System on Chip [153] supporting both Bluetooth Low Energy (BLE) 5.0 with Long Range connectivity and the 802.15.4 stack; the MAX2830 module [154] enabling 802.11 Power Saving Mode (PSM); the very recent SX-NEWAH [155] module implementing the

<sup>3</sup> <https://gricad-gitlab.univ-grenoble-alpes.fr/morinelo/iot-analyzer>

communication based on 802.11ah Wi-Fi HaLoW; finally, the SX1272 transceiver [156] was chosen for LoRaWAN technology. These devices differentiate both in terms of maximum power consumption (from 30 mW to 700 mW in transmission mode), available data rates (from 125 kbps to 10 Mbps) and maximum packet size (from 120 to 1280 Bytes).

#### 5.4.1.2 Setting the simulation scenario

The periodic acquisition of  $N$ -sample time series per hour from a tri-axial accelerometer device is simulated to mimic real vibration-based monitoring scenarios. Here,  $N = N_{s1p}N_p$  is the total length of the waveforms to be acquired in case of the SysId method. The communication-related energy consumption computed by the analyzer (for a transmission distance of 200 m to be compliant with the communication ranges supported by all the considered protocols) is thus complemented with the one associated with the DSP task. To this end, the execution times reported in Fig. 34 were specifically employed and multiplied by the average power consumption of the STM32L5 device in normal operative mode, which has been experimentally measured equal to 15 mA, while powered at 3.3 V; a compression ratio equal to 5 has been chosen for CS processing. In what follows, among the various tried configurations, results are presented only for the most critical one, corresponding to ARMA model with  $N_{s1p} = 45$ : this leads to a gain in the compression factor of 9x and 45x comparing with CS and No DSP, respectively.

#### 5.4.2 Results

In Fig. 36, the trends representing the total energy consumption deriving from the communication and processing operations are shown. The different background colors are used to identify the three considered working configurations, namely blue, gray and green are associated to SysId, CS and No DSP, respectively. Additionally, the markers are used to indicate the same transmission payload (per given  $N_{s1p}$ , while varying  $N_p$  in the interval [9, 57], in steps of 8), such as it is easier to compare the considered approaches. The plot indicates that the power saving of SysId with respect to CS can reach 10x, increasing up to 100x in case of no data compression.

It is further worth mentioning that SysId yields the most efficient performance for all the considered communication protocols. Apart from a horizontal bias due to hardware characteristics, the same consumption curve characterizes BLE 5.0, 802.15.4 and WiFi HaLoW by exhibiting a sharp increase for data payload higher than 1 kB. The trend is slightly different for 802.11 PSM, where the estimated energy profile is almost constant with a minimal increase in case of very large packet sizes. The reason is that this protocol works at a very high data rate (11 Mbps) with a large packet size (1280 B).

The gain in the saved energy for the least power-hungry protocol (i.e., 802.15.4) has been highlighted in Fig. 36 for the two extreme cases of  $N_p = 9$  and  $N_p = 57$ . As can be observed, the energy savings are always favorable, moving from a minimum gain of 1.07x up to a maximum improvement of 1.19x in the comparison with CS-driven solutions, as dictated by the minimum and maximum number of parameters. Notably, these gains rise up to 1.38x (minimum  $N_p$ ) and 2.78x (maximum  $N_p$ ) while considering compression-free scenarios.

The SysId-based approach yields a significant advantage with respect to the other solutions, especially in the LoRa case. As a general observation, the restrictions in terms

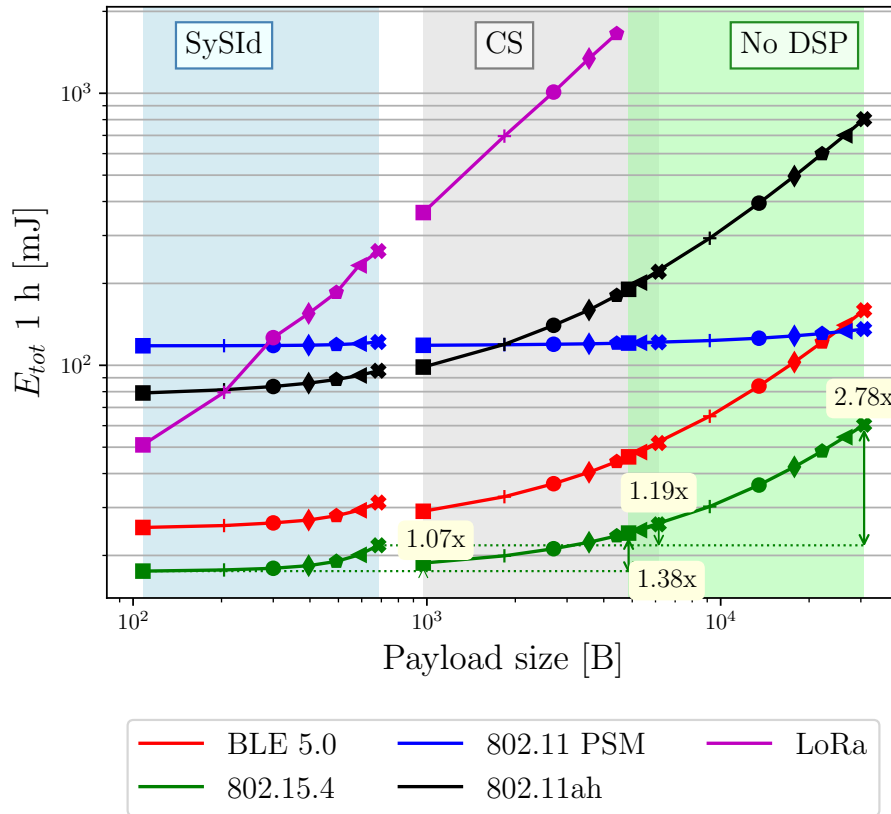


Figure 36: Total energy expenditure with one hour duty-cycle for different IoT protocols, taking into account expenditure due to data processing and outsourcing. The acquisition of triple-channel signals are assumed with  $N_{s1p} = 45$ , while sweeping  $N_p$  in the interval  $[9, 57]$  (depicted with different markers). Three different background colors are used to indicate different data compression scenarios: SysId-based processing (blue), CS-based processing (gray) and compression-free (green). Missing points mean that the corresponding payload in the given Tx time is not supported by the corresponding protocol.

of sub-band occupancy imposed by ETSI<sup>4</sup> for protocols working in the sub-1 GHz band makes LoRaWAN less effective for this kind of applications. Despite this practical limitation, denoted by the absence of markers in the purple curve for high payload sizes, the chart shows that, when SysId data compression is leveraged, even this long-range communication technology could become feasible for the assumed transmission rates.

### 5.5 LOCAL-TO-GLOBAL MODE SHAPE RECONSTRUCTION FOR SYSID-BASED DATA COMPRESSION

To be applicable in the context of data compression, the computation of parametric models is inherently performed in a sensor-driven logic. Conversely, the structural assessment process must be accomplished in a global manner, aiming at providing a comprehensive overview of the overall integrity condition of the structure. Therefore, a local-to-global merging action needs to be performed to combine all the locally retrieved information.

<sup>4</sup> European Telecommunications Standards Institute: <https://www.etsi.org/>



This assertion assumes particular significance while tackling mode shapes, which are spatial dependent quantities whose profile is determined by the relative position of the sensors with respect to the modal response of the structure.

However, one fundamental point is worthy of discussion prior than entering the actual algorithmic part of the local-to-global procedure: it relates to the algebraic formulation of output-only SysId models. Indeed, when performed on a decentralized and OMA-driven basis, the reconstruction of mode shapes from local modal coordinates is implicitly an ill-posed problem. In modal terms, the issue is that, contrarily to input-output models where a known and shared exciting force is used to normalize each local output with respect to a common reference, retrieving the complex modal contribution, namely both the relative magnitude and phase of each mode at distinct sensing positions, becomes impossible.

Such drawback arises from the fact that, from the pure knowledge of the model parameters, it is in principle not possible to recover a unique estimate of the variance  $\sigma_e^2$  associated to the true white stochastic process exciting the structure. Consequently, no common scaling factor is available and, thus, there is no guarantee that the hierarchy in the relative energy distribution across different sensors is preserved after the computation of the SysId power spectrum. On the other hand, it should be considered that the variance of the assumed white noise is usually very low, owing to the fact that such quantity statistically coincides with an error term (see Eq. (28)), ideally assuming null values in case of perfect prediction. The importance of the latter observation is pivotal because it allows naive PP algorithms to be applied to single PSD estimates for the fruitful reconstruction of the absolute value of the mode shapes.

Despite offering the naivest approach to extract modal coordinates in decentralized systems, PP suffers from the same problems highlighted in Section 2.2.1.1, namely it is extremely prone to local drifts and inaccuracies, which obstacle the accurate identification of the peak spectral values. When this algorithmic instability combines with the additional uncertainties due to output-only processing, the results yielded by this approach cannot be considered sufficiently reliable.

Moreover, what is more detrimental is the fact that all the phase delays associated with the individual SysId filters for output-only identification are zeroed, irrespective of the physical relationship between each measured vibration response and the common exciting source. Hence, the relative temporal shifts between multiple sensing positions, corresponding to as many phase rotations in the phase diagram of the corresponding FRF, are completely missed; this hampers the possibility to compute back the sign of the mode shapes. Note that, since phase rotations are phasor of unitary value, this phase hindrance has no effect on the magnitude of the FRF (and, thus, the relationships in the magnitude of energy collected at different sampling points could be preserved, in principle, less than the noise term). As such, the mode shape identification problem turns, in essence, to the divination of the sign of the mode shapes.

With these intrinsic shortcomings in mind, the pursuit of this Section is to offer a suitable strategy for the estimation of the global mode shapes under the premise that (i) the adopted SysId model is known and (ii) only the locally computed model parameters are accessible at the cluster edge for aggregation.

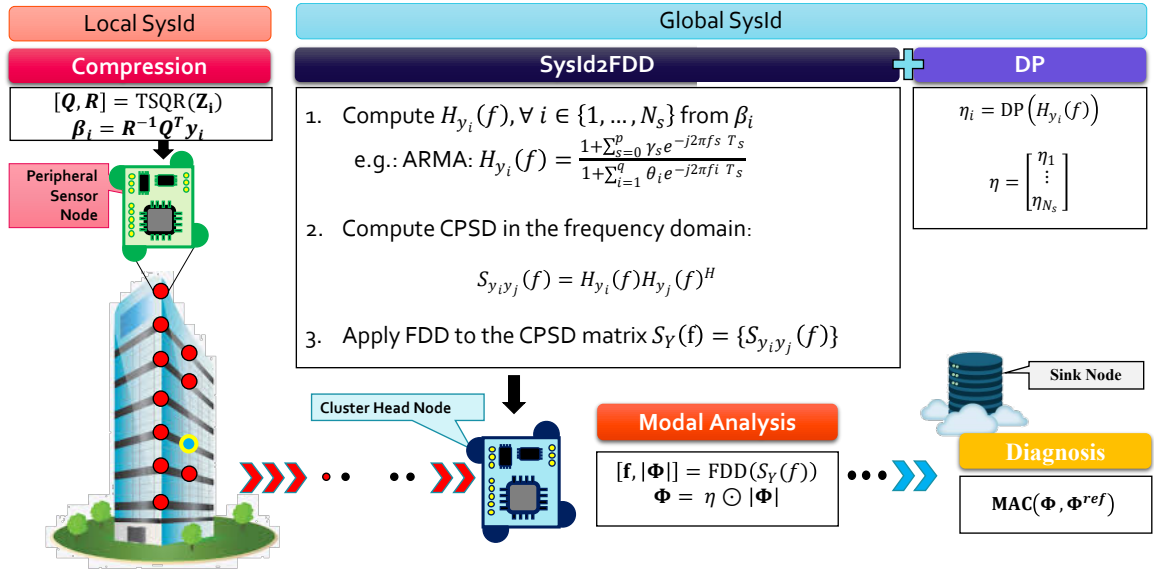


Figure 37: Typical SysId-enabled clustered architecture for vibration-based SHM. From left to right, the SysId local identification is allocated to the PSNs which transmit their related model parameters to the CH unit where global modal identification is performed through SysId2FDD. The latter is formulated as follows: firstly, the FRF associated to each  $i$ -th node ( $H_{y_i}(f)$ ) is computed and passed as input for the calculation of the CPSD matrix, directly in the frequency domain. The absolute value  $|\Phi|$  of the mode shape matrix is retrieved via standard FDD, whilst the corresponding sign vector  $\eta_i$  per given sampling position is yielded by the DP method applied to  $H_{y_i}$ . The actual mode shapes corresponds to  $\Phi = \eta \odot |\Phi|$ . Finally, the SN provides the sought structural bulletin via analysis of the aggregated information.

### 5.5.1 The SysId2FDD algorithm

Overcoming the main drawbacks of PP algorithms, the methodology devised in this Section for the sake of global mode shape reconstruction from SysId is original in that it takes advantage of the centralized nature of FDD with the superior resolution in the spectral profiles delivered by SysId. Leveraging on this dual properties, the technique will be addressed, in the following, as SysId-to-FDD algorithm (SysId2FDD).

The operative framework is identical to the one depicted in Fig. 29; the only variation is that, since the core point of the method is to demonstrate the actual retrieval of mode shapes, the simplistic case with one single cluster is considered. Once model parameters are identified at the PSN level and outsourced to the CH node, the SysId2FDD algorithm can be run at the cluster node involving the following steps:

1. *FRF retrieval*: for all the mastered nodes, the complex quantity  $H_{y_i}(f)$  is computed according with the selected SysId model<sup>5</sup>.
2. *CPSD matrix estimation*: differently from its canonical definition in the time domain introduced in Section 2.2.1.2, the generic CPSD function  $S_{y_i, y_j}(f)$  is computed directly in the frequency domain as the complex product between FRF  $H_{y_i}(f)$  and  $H_{y_j}(f)$

<sup>5</sup> The expressions to be employed to this end coincide with the PSD equations in Table 3 less than the square magnitude operator.

collected at node  $i$  and  $j$ , respectively. For analogy with Fig. 5, let's denote the CPSD matrix as  $S_Y(f)$ .

3. *Mode shape magnitude retrieval*: the remaining operations invoked by FDD are then performed, yielding the modal frequency vector  $\mathbf{f}$  and the absolute value  $|\Phi|$  of the mode shape matrix.

In order to reconstruct the sign of the mode shape, an effective strategy is suggested by the Dip Picking (DP) algorithm. DP has been proposed in the literature as the dip-driven counterpart of the more famous PP strategy. In essence, DP aims at identifying phase rotations in a given spectral representation by probing for the presence of antiresonant frequencies [157], the latter corresponding to those frequencies whose vibration amplitude is theoretically null. If  $\Phi_i = [\Phi_{i,1}, \dots, \Phi_{i,p}]$  represents the row vector of  $P$  modal coordinates identified for PSN  $i$ , a phase change among two successive modal coordinates  $\Phi_{i,p}$  and  $\Phi_{i,p+1}$  can be revealed via DP in case one antiresonant frequency is identified between their peak spectral values  $f_p$  and  $f_{p+1}$ . Therefore, the sought mode shape sign vector  $\eta_i$  can be structured as a row-wise antipodal vector containing, for each entry  $\eta_{i,p}$  ( $p \geq 2$ ), a value equal to  $-1$  or  $1$  depending on whether or not one antiresonant point is identified between the modal component  $p$  and the preceding  $p - 1$ ; the method assumes  $\eta_{i,1} = 1$  for all the sensor locations<sup>6</sup>.

The complete mode shape matrix is finally fetched as:

$$\Phi = \eta \odot |\Phi| \quad (32)$$

where  $\eta$  is a row matrix containing - in each  $i$ -th row - the mode shape sign vector  $\eta_i$ , and  $\odot$  indicates the point-wise Hadamard product.

Noteworthy, there are three aspects to be considered for the actual effectiveness of the DP technique. The former is that the spectral profile of the structure at the antiresonant frequencies is clearly distinguishable, a condition which depends, in turn, on the selection of the most appropriate model order, whose estimation becomes the tricky point of the overall processing flow. The second one pertains, instead, to the relative spectral distance between the modal components of interest, which might impede, in case of closely-spaced modes, the actual frequency tracking activity of DP. Finally, being DP nothing but a PP method adapted to search negative rather than positive peak quantities, it might be affected by the same drawbacks.

Nevertheless, in the SysId2FDD realization, since modal frequencies are provided in one-shot by the FDD algorithm, the antiresonance check implied by DP takes advantage of the centralized retrieval of the frequency bands, which are known in advance and can be proficiently exploited during the sign retrieval step to focus the attention on the proper spectral regions. Conversely, the standalone application of PP is less robust since, in this case, one initial step of global frequency identification needs to be executed to select common modal components out of local frequency representations that might be affected by artifact components, which most likely occur in case of unfavorable sensing locations or instrumental failures.

From an edge processing perspective, another point is worthy of discussion, which is the low computational complexity implied by SysId2FDD, which is substantially identical

<sup>6</sup> Coherently, the method is applicable for structures whose first peak spectral value correspond to a clear bending mode.

to the one required by the classical FDD plus the additional cost due to the computation of the FRFs. The latter is negligible if compared to the other operations; hence, the method appears affordable even at a hardware-oriented level. Additionally, it is important to observe that such methodology is also compatible with the possibility to adapt the number of parameters in a sensor-wise manner to better capture vibration modes irrespective of the sensor position. This is viable since the retrieval of modal parameters only depends on the computed FRFs, independently from the actual number of parameters required for their computation.

### 5.5.2 *Experimental validation*

In the following, the effectiveness of the proposed SysIdzFDD+DP method is discussed and proved against damage detection capabilities. Since the objective of this analysis is to verify the correctness of the local-to-global workflow, such validation was performed offline in the MATLAB® environment. ARMA models were considered due to their superior performances in OMA scenarios.

#### 5.5.2.1 *The use case: a laboratory high-rise shear structure*

Vibration responses collected for a metallic shear frame located at the research labs of the Department of Civil Engineering of the University of Bologna, Italy, are employed. The facility consists of a high-rise five-story frame composed of five identical cubic modules with nominal height of 1 m, arranged in a way that imposes quite a rigid mechanical response. Combined with the symmetric design, all these structural properties led to the presence of tightly coupled modal components and, for this reason, it provides a challenging scenario for the actual validation of the SysIdzFDD+DP strategy.

#### 5.5.2.2 *The monitoring network*

This structure represents one of the pillar test-beds of the MAC4PRO project for the monitoring and predictive maintenance of industrial sites and civil engineering structures by means of a customized sensor-to-cloud architecture. Pursuing this objective, the ISSLab sensor network presented in Appendix A was selected as candidate player for the data measuring layer thanks to its low-cost, light-weight and versatile characteristics. More details about the complete monitoring platform, from the first field validation to recent improvements, can be uncovered in [P10] and [P11].

The structure was instrumented with a double chain of six inertial nodes fixed in correspondence of the junction elements. One out of two CH units were preferred to minimize the total electrical consumption while exploiting the beneficial multi-drop capabilities of the communication bus. Furthermore, a favorable deployment strategy was followed to halve the electrical load seen by the CH device. The final installation plan is sketched in Fig. 3, where the two clusters of sensors have been differentiated with red (cluster 1, label C1) and green (cluster 2, label C2) colors, while the CH unit is identified by the gray rectangle drawn at the mid-span of one bar on the third floor.

Notably, the geometrical rigidity of the elements imposes quite a stiffened dynamic behavior. Thus, a sampling frequency  $F_s = 833$  Hz was selected (among the available ones) to extend the spectral analysis in a frequency range compatible with the high-order

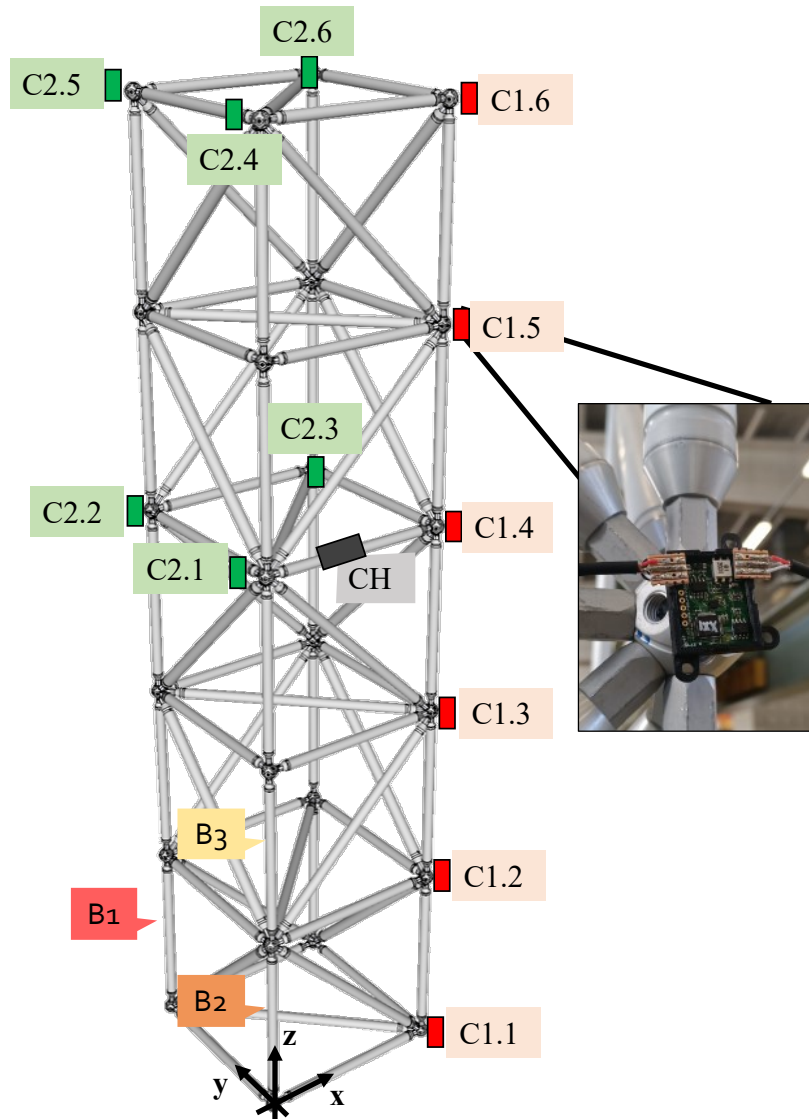


Figure 38: Rendering of the five-storey shear frame located at the research lab of the University of Bologna and relative sensor installation plan: two different sensor clusters (red and green colors) and one CH device (black box). An insight about the sensor-to-structure bolting is also enclosed, as well as labels indicating the beam removed during testing.

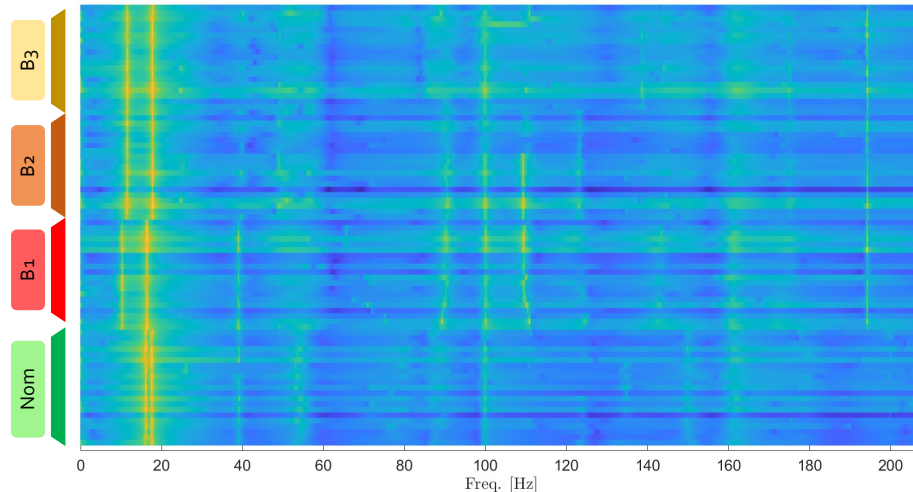


Figure 39: Color-map of the waterfall plot obtained from the cascade of PSD spectra as computed by ARMA parameters for different structural configurations of the five-storey frame.

modes of vibration. Time series were acquired continuously with a fixed batch size of 2000 samples along each axis.

#### 5.5.2.3 *The testing protocol*

Preliminary studies conducted on this structure revealed that, as a consequence of the bonding mechanism that forces the structure to vibrate along the in plane axes, highly lateral displacements are favored while the vertical and rotational ones are minimized [P10]. As such, the meaningful signal content is hidden in acceleration signals measured along the  $x$  and  $y$  direction, which are the only one considered in this analysis. Moreover, since the sensor distribution of cluster  $C_2$  is not sufficient to reconstruct with enough accuracy mode shapes associated to torsional modes, attention has been restricted on lateral bending modes, which can conversely be well-captured by cluster  $C_1$ .

In order to replicate operative scenarios affected by EOP factors, a fan motor simulating the effects of wind was used to excite the structure. Beside tests in nominal condition, the experimental campaign was extended to damaged ones in which beams  $B_1$ ,  $B_2$ ,  $B_3$  were, in order, removed and re-inserted to create defective configurations, one at a time. The primary effect of this action is to induce an asymmetric mass distribution and a loss in the mechanical stiffness of the structure, which causes mode decoupling manifesting as a significant change in the observable spectral content. For each structural configuration, ten different measurements were registered.

These effects are evident in the waterfall plot of Fig. 39, which shows the cascade of PSD profiles as computed by ARMA parameters ( $N_p = 32$ ) extracted at node  $C_{1.6}$  for varying structural conditions, from the nominal (case Nom) to the damaged ones (label  $B_1$ ,  $B_2$ ,  $B_3$ ). From this graph, it is immediate to observe the abrupt change in the first vibration mode, which moves from almost 16.22 Hz to 10.19 Hz as beam  $B_1$  is removed. The frequency shift is less pronounced for the remaining modal components, which undergo variations in the order of a couple of Hertz.

Table 13: First six modal frequencies of the five-storey shear frame computed via SysId2FDD by averaging over the ten successive measurements per given structural configuration.

Configuration	$f_1$	$f_2$	$f_3$	$f_4$	$f_5$	$f_6$
Nom	16.22	17.68	39.10	86.53	100.06	110.45
B1	10.19	16.43	39.10	85.70	99.44	110.24
B2	11.65	17.89	39.94	86.11	100.27	110.03
B3	11.65	17.68	40.14	86.53	100.69	110.03

Table 14: Average MAC percentages ( $\mu_p$ ) and standard deviation ( $\sigma_p$ ) between FDD and SysId2FDD+DP reconstructed mode shapes for the laboratory five-storey frame. Different structural configurations are considered: nominal and B1, B2, B3-damaged scenarios.

Conf.	$\Phi_1$		$\Phi_2$		$\Phi_3$		$\Phi_4$		$\Phi_5$		$\Phi_6$	
	$\mu_1$	$\sigma_1$	$\mu_2$	$\sigma_2$	$\mu_3$	$\sigma_3$	$\mu_4$	$\sigma_4$	$\mu_5$	$\sigma_5$	$\mu_6$	$\sigma_6$
Nom	99.60	0.02	98.60	0.34	97.94	1.19	95.64	0.74	98.08	0.53	97.53	1.80
B1	99.29	0.10	98.49	0.07	98.31	0.39	88.51	2.41	97.14	0.70	94.60	2.27
B2	99.58	0.12	98.97	0.12	98.35	0.87	42.83	35.61	98.02	0.44	95.29	1.03
B3	99.62	0.07	99.06	0.06	97.96	1.80	43.31	30.95	98.64	0.21	95.28	1.02

#### 5.5.2.4 Modal parameter identification

To better quantify the damage tracking capability of SysId2FDD+DP and fulfill the global identification task, modal parameters were extracted and compared to the ones obtained via application of the standard FDD technique, which serves as a benchmark approach, to the vector ensemble of measured data. Indeed, since an updated numerical model of the structure was not available, this prevented a direct comparison with numerical predictions.

The frequency distribution in Fig. 39 also suggests that six modal components are present below 120 Hz: their evolution over time is summarized in Table 13, which reports the frequency values (averaged over the ten data logs) taken as output of the SysId2FDD.

Then, the analysis was extended to the reconstruction of the global mode shapes, which are intrinsically more complicated to be recovered with sufficient accuracy. Average MAC percentages ( $\mu_p$ ) per working status and the associated standard deviation ( $\sigma_p$ ) over the ten measurements are reported in Table 14. MAC values always above 94% demonstrate that, apart from the isolated case related to the fourth modal component, for all the remaining modes and irrespective of the structural configuration, mode shapes from SysId2FDD+DP are remarkably superimposed to the ones provided by FDD. The quality of the results is further corroborated by the low standard deviation among the different tests, which remains stably beneath 2.5%.

Accordingly, the promising outcomes yielded by this novel approach demonstrate that a viable solution could exist to the problem of global structural identification and assessment even in presence of SysId-based data compression performed at the extreme edge.

## 5.6 CONCLUSIONS

In this Chapter, the implementation of SysId schemes as a means for data compression in the context of vibration-based SHM has been presented and validated on both synthetic

and experimental structural responses. Embedded versions of linear algebra techniques, namely the eS-TSQR decomposition combined with least-squares estimators, have been specifically proposed to tackle the memory constraints of the involved algorithmic procedures and meet the computational and storage resources of extreme edge devices.

The potential power savings due to the network load reduction achieved by running SysId in a near-sensor manner have been thoroughly evaluated, taking into account the energy expenditure necessary for the model parameter computation. To this end, different wireless transmission protocols that are commonly adopted in the IoT framework have been considered. It has been demonstrated that SysId is more advantageous with respect to CS-driven and compression-free scenarios even in the most adverse network configurations (i.e., for very long payload sizes), thus ensuring a longer-lasting monitoring system.

Besides, a new approach for the reconstruction of global modal parameters from multiple local estimates has been proposed: the SysId2FDD+DP method, that combines the advantages of centralized processing granted by standard FDD with the superior spectral resolution ensured by SysId. Validated on real-field data from a high-rise laboratory infrastructure, the novel method proved reliable results also in presence of anomalous structural configurations, hence supporting SysId as a cost-effective and reliable method for full-scale assessment.



## ABSTRACT

*Exploiting the encouraging performances of the data compression techniques delved into the previous analyses, the scope of this Chapter is to further extend their reliability towards damage detection in combination with the most recent solutions promoted by the artificial intelligence field. Moreover, as an alternative to standard ML-driven scenarios, where the inference process is usually performed in a centralized, bulky manner, the unique TinyML paradigm is investigated for vibration-based assessment at the edge. To this end, inference models were successfully coded in a resource-constrained device, proving high accuracy for the timeliness retrieval of the structural bulletin.*

The content of this Chapter is based upon the research work [P12]:

"Machine Learning Meets Compressed Sensing in Vibration-based Structural Health Monitoring" by Zonzini F., Carbone, A., Romano, F., Zauli, M. and De Marchi L. (2021). *Submitted to Sensors, 2022.*

from which part of the text is drawn.

## 6.1 INTRODUCTION

Damage detection has a pivotal role in SHM systems as a fundamental means to implement on-condition maintenance. In particular, many novel damage detection procedures are gaining momentum thanks to the recent developments in the ML field [46]. AI applied to SHM proved considerable advantages in the accuracy and quality of the estimated structural integrity and, as discussed in Section 2.3, plenty of literature has been published in these regards in the last decades.

As far as classification is concerned, ML architectures targeting the identification of structural damages have been extensively investigated (see [158] and [159]). In such scenario, the primary aim of classification networks is to determine whether degrading phenomena are occurring or not and to notify alerts in a timely manner, a task which is usually referred to as One Class Classification (OCC) [160]. The objective of OCC is, therefore, to find which specific class a given input object belongs to by selecting either the *target* (i.e., 'normal') or *outlier* (i.e., 'anomalous') class. OCC solutions based on standard Neural Network (NN) models were shown to achieve good classification scores in numerous application scenarios, such as the monitoring of civil infrastructures (e.g., bridges [161]), industrial plants (e.g., mechanical rotors [162], wind farms [163], [164]) and avionics or automotive structures [165], [166].

Nevertheless, several issues still need to be tackled in the SHM field, which extended the monitoring process beyond the mere data analytics and structural assessment goal. Among them, the problem of potential network congestion implied by the transmission

of voluminous raw datasets has been extensively discussed in Chapters 4 and 5, and possible solutions to cope with it have been proposed. The performance of compression approaches is usually evaluated by computing the mean square error between the recovered and the originally acquired signals [104], or by analysing the degradation in the modal parameter estimation [101], [167], while only minor attention has been paid to assess how compression affects the damage classification performance. Furthermore, condition monitoring data are typically affected by EOP disturbances, whose effect on modal parameters can be even more pronounced to the one due to pure structural degradation [42]. Thus, EOPs need to be properly modeled and taken into consideration to avoid false alarms.

Beyond these aspects, another important challenge is the reduction in the computational complexity of the designed ML models, which are - up-to-date - typically demanded to huge data centers. Nonetheless, this procedural manner is not compatible with real-time structural inference. Therefore, a large demand for hardware-oriented ML solutions has become of the utmost importance for the next generation of monitoring systems.

In such scenario, this Chapter proposes a comprehensive framework for vibration-based diagnostics. As will be extensively described, data compression techniques are firstly introduced as a means to shrink the dimension of the data to be managed through the system. Then, NN models solving binary classification problems are encompassed for the sake of damage detection, by taking into consideration both the influence of environmental factors and the one of instrumental noise while. Finally, the devised models will be coded on an edge device by following the Tiny Machine Learning (TinyML) precepts.

## 6.2 FROM RAW DATA TO ANOMALY DETECTION

The ML-enabled monitoring framework proposed in this work is organized around three successive steps (Fig. 40): (i) the *data compression and recovery* phase, which is aimed at retrieving the original time waveform from compressed acquisitions; (ii) the *modal identification* step, returning the structural features of interests, and (iii) the final *classification* stage, which leverages ML techniques as enabling tools for structural integrity assessment.

Hereinafter, each processing phase is detailed.

### 6.2.1 Structural identification

For the sake of brevity, and without any loss of generality, the particular scenario leveraging CS as a means for network load reduction is considered. Nevertheless, any of the previously discussed techniques, compatible with the retrieval of modal parameters of interest, could be employed.

#### 6.2.1.1 Data compression and recovery

Noise corruption, data missing and outlier deviations are among the most frequent sources of inaccuracies hidden within acquired data. Therefore, data cleansing procedures, such as trend removal and filtering, are usually performed to account for these issues and format data in a convenient manner for the following modal investigation task [48]. At this point, compression operations are performed by peripheral sensors installed on the structure [168] and, subsequently, compressed data are transmitted to a central ag-

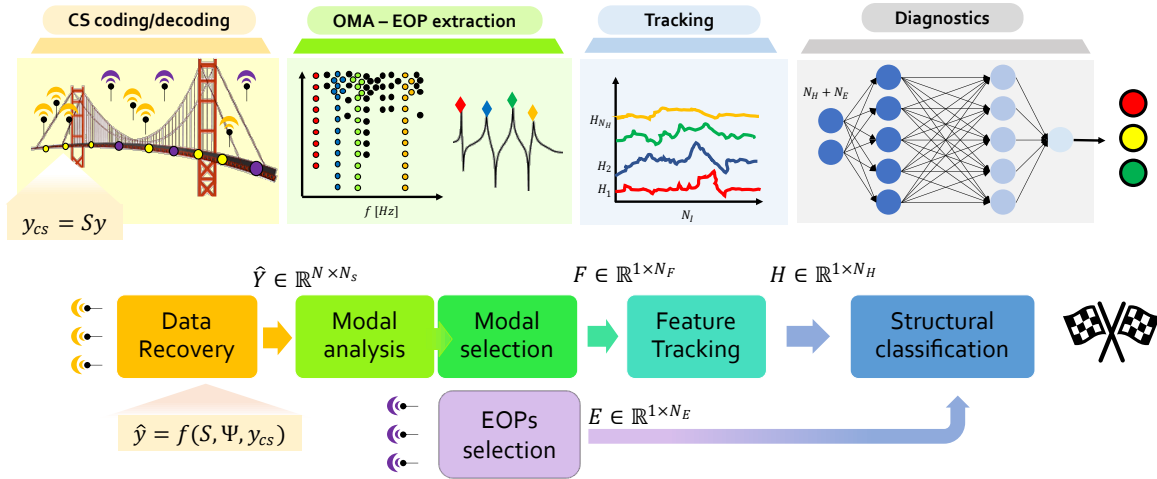


Figure 40: Proposed framework for structural assessment: from left to right, data compression and recovery, modal feature extraction and selection with the final structural assessment block. The matrix  $\hat{Y}$  is used to indicate the ensemble of CS-reconstructed signals from all the different acquisition points, as it is required by OMA algorithms to provide a global understanding of the structure under analysis.

gregating unit where the original time series is recovered following the CS decompression procedure explained in Section 4.2.2.

#### 6.2.1.2 Modal parameter extraction

Once the vector ensemble of vibration data has been estimated, the modal identification task can be entered. To expedite the monitoring process, fully automated modal identification methods would be preferable, since the retrieved outputs can be directly plugged as input for AI tools, without the need for intermediate steps aided by manual intervention of the experts. To this merit, particular attention deserves the SSI algorithm introduced in Section 2.2.2.2, the principal advantage of which over conventional spectral alternatives relying upon its completely unsupervised nature.

The crucial point of SSI is the selection of the most appropriate model order which dictates the number of identifiable modal components. It is worth noting that the model order also depends on the influence of EOP parameters which might give birth to spurious components, or induce significant changes in the spectral content distribution: therefore, such parameter must be selected in an adaptive manner.

To tackle this issue, the so-called stabilisation diagram [169], i.e., a point chart representing how the location of the identified modal frequency values may vary as a function of increasing order number  $N_p < N_F$ , can be employed.  $N_F$  represents the maximum model order deemed sufficient for the considered structure. In more detail, by sweeping in a sufficiently wide order range (let's suppose  $N_p \in [1; N_F]$ ), the vector ensemble  $F = \bigcup_{N_p=1}^{N_F} F_{N_p}, F_{N_p}^{-1} \in \mathbb{R}^{1 \times N_p}$  is created, which gathers the estimated frequency components for increasing model order. Hence, *physical* over artifact modal components can be visually evidenced as those vertical lines (i.e., modal contributions) with higher density points; in these terms, modes are labeled as *stables* if their modal contribution is evident

<sup>1</sup> A one-to-one correspondence exists between the number of structural modes and the given model order.

since low model orders. A very schematic representation of a stabilisation diagram is drawn in the green box of Fig. 40 under the label "OMA - EOP extraction": in this representative case, true modes coincide with the colored dotted vertical lines. When paired with clustering procedures, this tool provides valuable information about the frequency vector  $F$  containing the  $N_F$  stable modes, in a totally unsupervised manner.

### 6.2.1.3 Feature tracking

Once modal frequencies have been estimated via any of the clustering procedures, their evolution over time can be tracked with Gaussian moving average filters. This further step is essential for three main motivations: (i) keeping trace of slow variations induced by environmental effects, (ii) filtering out spurious components which are not consistent across successive measurements and (iii) shrinking the dimensions of the feature space to  $N_H \leq N_F$  components of interests. The latter aspect, in particular, is fundamental to ensure consistency between subsequent acquisitions (indicated as  $N_I$ ). Indeed, the number of centroids to be identified at the end of the modal feature selection step can be much higher than the total amount of meaningful vibration modes; thus, it is necessary to prevent outlier points from altering the true frequency distribution. The filter is designed to update the  $h$ -th frequency component  $f_h^{(i)}$  at iteration  $N_i$  with the mean value of the previous frequency points falling into a band of  $\pm 3\sigma$  with respect to the mean value estimated for the preceding structural instance. In the following, it is assumed that all the tracked frequency components are organized in the matrix  $H \in \mathbb{R}^{N_I \times N_H}$ .

### 6.2.1.4 Environmental Analysis

As widely discussed in the manuscript, modal parameters are extremely sensitive to environmental factors, since they are constitutive elements determining the stiffness and damping property of the structure [128]. The conventional approach to cope with them is to resort to regression methods [170]. Dynamic regression analysis and PCA are just a few of the reference approaches already investigated in the field [170]. All these methodologies aim at finding non-linear dependencies between the measured environmental factors and the identified structural parameters, which are then compensated by means of standard fitting models.

Conversely, the approach presented in this work tackles this problem from a pure data-driven perspective, by including  $N_E$  EOP parameters (grouped into the  $N_E$ -dimensional vector  $E$ ) as additional input features of the AI block. In this manner, the neural network is instructed to autonomously learn this frequency vs EOP relationship, without requiring any further processing steps to be performed aside.

## 6.2.2 Neural Network design

The real ML machine can be entered as soon as modal features are available. In their basic form, OCCs can be seen as standard neural networks trained with samples acquired for the pristine structure, since no training data is usually available for damaged conditions (i.e., the so called *adversarial population*). In these cases, a possible alternative consists in generating artificially these adversarial points. Among the OCC implementations presented in literature, the very recent One Class Classification Neural Network (OCCNN) proposed in [48] and the Autoassociative Neural Network (AENN) are taken as reference solutions.

### 6.2.2.1 OCCNN

OCCNN [161] is a ML technique aiming at finding either linear or non-linear boundaries between healthy and defective conditions in the parameter space. In these terms, it serves the goal of anomaly detection in low feature space by predicting whether an input feature vector falls into a normal or abnormal region of the total feature space. Let's suppose that  $N_T$  measurements are used in the training phase (quantities H and E in Fig. 40). The neural network topology consists of three main elements (see grey box "Structural assessment" in Fig. 42). The former is a point density estimator (step 4.1), in charge of identifying the scattering distribution of the feature values identified at the end of the tracking phase; the second one is the Adversarial Point Generator (APG) block (step 4.2), which randomly generates data  $\chi \in \mathbb{R}^{N_\chi \times (N_H + N_E)}$  of the defective class in the damaged space identified at a given iteration of the algorithm, where  $N_\chi$  can be selected as detailed in [48]. These adversarial data, together with healthy instances, are plugged as inputs to the last AI component (step 4.3), that is a two-layer fully connected NN with  $N_N$  neurons in each hidden layer, whose weights provide an exact estimate of the sought boundaries  $\Omega$  between the healthy (yellow) and unhealthy (dark violet) point distribution.

The number of cycles of the adversarial point generator is iterated until the desired level of fitting with respect to the training data distribution is reached. The higher this number, the higher the resolution of the boundary contours will become. It follows that two key variables might significantly affect the classification performance of OCCNN, which are the number  $N_{cy}$  of APG iterations retained sufficient for a robust system realization, and the number of neurons per layer.

The performances of OCCNN were firstly tested in [161], with a reported accuracy of 96% and a precision of 98%. However, the quality of the results provided in that work is strongly influenced by the training set point distribution. This means that a long data collection phase, usually performed on a yearly or at least seasonal scale, has to be conducted to create a set of baseline values comprehensive of all the possible structural-to-EOP dependencies; in turn, this mandatory step slows down the actual system deployment process. Differently from that, the framework discussed in this manuscript automates this learning task in a purely ML manner.

### 6.2.2.2 Autoassociative Neural Network

In essence, an AENN [171] (Fig. 41) represents a feed-forward multilayer NN whose goal is to reconstruct data as they appear at the input layer (a condition which implies an identical number of neurons in the input and output layer). The processing chain involves a compression stage, in which the dimensions are reduced by means of a mapping function with progressively lower neurons per layer, followed by a reconstruction step, also known as demapping layer. The role of the mapping layer (with  $N_A$  neurons) is to project the input data into a lower dimensional space, that is used as a bottleneck layer thanks to a number of neurons  $N_B$  lesser than the dimensions of the feature space; an opposite function is conversely fulfilled by the demapping counterpart. Anomaly detection is achieved by searching for abrupt variations in the residual (i.e., reconstruction error) between the input and the currently predicted output values.

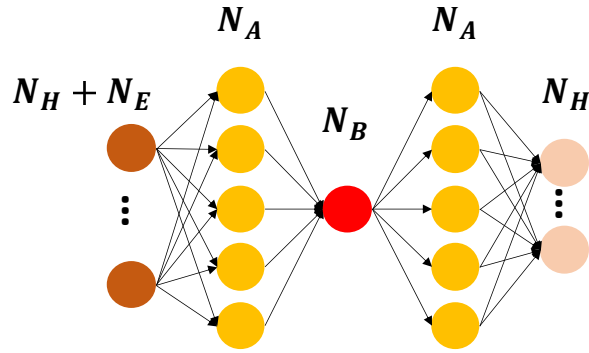


Figure 41: General scheme of an AENN architecture.

### 6.3 EXPERIMENTAL VALIDATION: THE Z24 BRIDGE CASE STUDY

The openly available dataset related to the Z24 bridge [118] provides unique features for the assessment of SHM algorithms. The Z24 bridge was monitored for more than one year by means of a permanently installed monitoring network consisting of 11 uni-axial accelerometers and multiple environmental sensors (humidity, temperature, wind). Two different experimental campaigns were performed: a long term continuous test, during which the structure was subjected to operational excitation, and a progressive damage test, consisting of purposely induced deterioration processes.

The monitoring system was programmed to acquire, on a hourly basis and from all the installed accelerometers, 65536 acceleration values at a sample rate of 100 Hz, corresponding to observation windows of 11 min. Unfortunately, some measurements were lost due to sensor failures, such that only 55.6% of the total data are now available. Among the total  $N_I = 5651$  observations, 4922 instances belong to the *normal class*, which are acquired in healthy structural conditions, while the remaining 729 instances are collected in *damaged* configurations.

A dataset preparation phase was necessary, too. Since the NN models adopted in this work only need data from the normal class during training, 70% of these data from the normal class was randomly sampled to favor diversity in terms of environmental conditions. This subset was further subdivided: 70% of it was used for training and the leftover 30% allocated to validation. Conversely, the remaining 30% of the normal class, together with all the data acquired in damaged conditions, have been employed for testing purposes. For the sake of clarity, a revised version of the workflow depicted in Fig. 40 is here included (see Fig. 42) and specialized to the Z24 use-case assuming OCCNN as neural network driver.

#### 6.3.1 From CS to feature tracking

##### 6.3.1.1 Data compression and recovery

The MRak-CS technique presented in Section 4.3.1 was considered for data compression and recovery, thanks to its peculiar adaptation to the second order statistics, i.e., to the signal energy distribution, of the processed data. The sensing matrix was designed as illustrated in Section 4.3.1.2 for  $N = 512$  long segments; a compression level equal to 6 was selected to emulate feasible compression parameters compatible with on-sensor implementations,

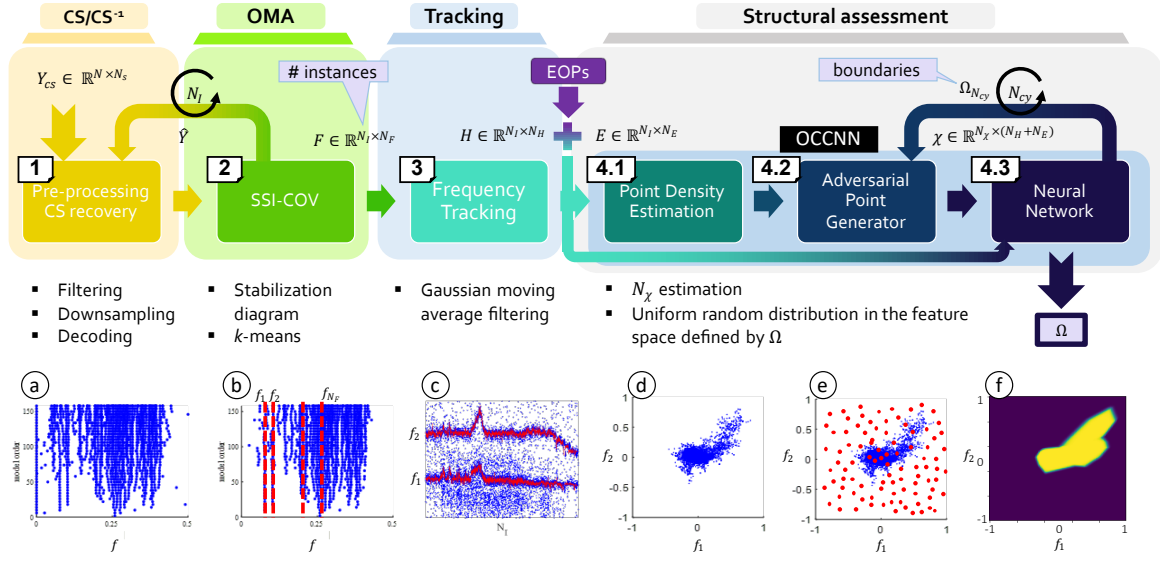


Figure 42: General scheme of the OCCNN-driven monitoring framework adopted for the structural assessment of the Z24 bridge. A graphical description of OCCNN is provided at step 4 under the label "Structural assessment".

whilst the DCT was assumed as sparsifying basis. Setting this compression factor can be regarded to as a critical scenario compared to the average compression factors discussed before while adopting CS-based solutions. Finally, the OMP algorithm was employed for the recovery of the sparse coefficients in view of edge-oriented architectures (step 1 in Fig. 42).

### 6.3.1.2 Modal identification

At step 2, SSI-COV [130] was adopted to estimate the main vibration components of the bridge. More specifically, the structural identification process was divided into three steps. Firstly, the stabilisation diagram was computed for a model order ranging from  $N_F = 1$  to  $N_F = 160$ ; then, by fixing the number of centroids to 15, the  $k$ -means algorithm [172] was run to create a batch of candidate modal frequencies. Thirdly, only the first bending and lateral modes were retained for the following analysis (i.e.,  $N_H = 2$ ) due to their high energy content and, consequently, better identification capability. The Gaussian moving average filter was finally applied to track their evolution over subsequent instances.

### 6.3.1.3 EOP selection

The environmental monitoring system deployed on the bridge mostly constituted of temperature and humidity sensors, which were deployed in a redundant configuration (more than 53 different measurement positions) over the whole structure, so as to precisely keep trace of EOP effects on the vibration signature. As already proven in previous works for the Z24 use-case [173], very high correlation was found between the frequency shifts induced by thermal excursion and the temperature variation at the top deck of the structure. Worthy to be underlined, thanks to the relatively high thermal inertia of the structure, just one temperature value per acceleration series has to be stored ( $N_E = 1$ ). Trends in modal frequencies induced by temperature fluctuations are depicted in Fig. 43 for the first (43a) and second (43b) vibration component.

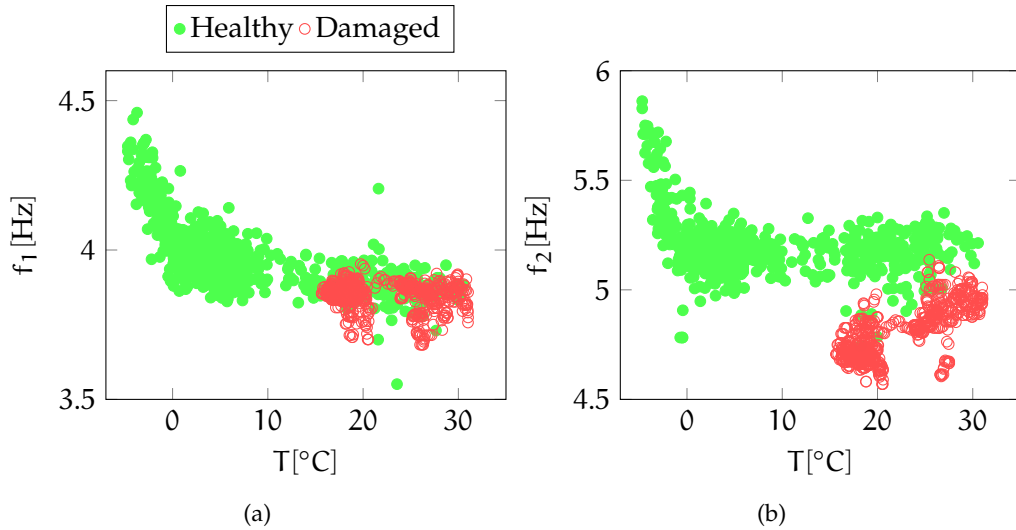


Figure 43: First (a) and second (b) frequency component vs temperature.

### 6.3.2 Neural network models

The details of the explored NN models are presented in this subsection. For the sake of brevity and from this point onward, the acronym OCCNN and AENN will be denoted as O and A. The basic OCCNN implementation, i.e., the one was proposed in [48] consisting of two hidden layers with  $N_N = 50$  neurons each, is referred to as model A ( $O_A$ ); conversely, subscripts  $B$ ,  $C$  and  $D$  will be used to indicate its distilled versions with 32, 16 and 8 neurons per layer, respectively. Besides, the number of adversarial points was generated as detailed in [48]. For the AENN case,  $N_A = 64$  neurons were selected in the mapping and demapping layer, whereas one single neuron was used for the bottleneck layer in both cases.

When the networks are fed with CS data, they will be indicated with superscript  $CS$ , while the ones complemented with temperature values are named after with prefix T (e.g.  $TO_A$ ,  $TA_1$ ). Rectified Linear Unit (ReLU) was chosen as activation function for the input and hidden layers, while softmax was considered in the output layer for all the investigated NN models. The number of training epochs was set equal to 5000 with a learning rate of the stochastic gradient descent equal to 0.05. Cross-validation with  $k$ -fold = 5 was also considered to avoid biases in the designed classification models.

### 6.3.3 Noise density in MEMS accelerometers

As anticipated in Section 4.5.3, signals acquired by MEMS accelerometers are affected by relatively higher intrinsic noise density values, which thus need to be properly accounted for in the signal processing chain to assess the actual performances of the implemented algorithms. To this end, further analyses were performed, in which the original data were degraded by adding the residual noise floor inherent in two different kinds of digital accelerometers. In more detail, the mechanical characteristics in Table 15 were assumed: as can be noticed, MEMS accelerometer type MA ( $N_o = 25 \mu\text{g}/\sqrt{\text{Hz}}$ ) refers to commercial off-the-shelf devices exhibiting the lowest noise density levels, while type MB ( $N_o = 80 \mu\text{g}/\sqrt{\text{Hz}}$ ) is representative of medium-class but extremely low-cost devices.



Table 15: Mechanical features of the considered MEMS accelerometers types.

Feature	Unity of measure	MA	MB
Sensitivity @ $\pm 2$ g	$\mu\text{g}/\text{LSB}$	61.0	3.9
Zero-g level offset	mg	40	25
Noise ( $N_o$ )	$\mu\text{g}/\sqrt{\text{Hz}}$	80	25
Zero-g change vs temperature	mg/C	$\pm 0.1$	$\pm 0.1$
Sensitivity change vs temperature	[%/C]	$\pm 0.01$	$\pm 0.01$

Coherently, the newly obtained waveforms were then processed encompassing the same operations used in presence of noise-free data while maintaining unaltered all the remaining parameters.

For the sake of NN validation, noise-corrupted data can be treated as novel datasets and, for this reason, they were taken as inputs to the previously trained  $\text{TO}_D$  model (the one with noise-free data). This verification procedure has been preferred over the generation of new models for each of the new datasets, since it represents a more severe test to be passed. At the same time, it is also appropriate in view of practical implementations, in which the variability and the uncertainties hidden in the acquired data cannot be predicted *a priori*.

#### 6.3.4 Results

Four main objectives were pursued within the experimental validation phase: (i) assess the improvement brought by the introduction of temperature values as additional input features of the AI block; (ii) evaluate the effect of the compression/recovery stages on the classification performance of the designed SHM framework; (iii) reduce the complexity (i.e., number of hyperparameters) of the NN models to be compatible with embedded processors without impinging on the accuracy of the classification; (iv) evaluate the effect of MEMS noise floor on classification performances to cope with real issues. To quantify the performance of the classifiers, four classical classification metrics [46], i.e., accuracy, precision, F1 and recall, were computed.

##### 6.3.4.1 Effect of temperature data

As can be observed in the bar chart depicted in Fig. 44, adding temperature values as additional input features to the NNs provides invaluable insight for OCCNN, which reports an average increase of 4.5 point percentages while moving from the basic  $\text{O}_A$  model to the  $\text{TO}_A$  one corrected with temperature data.

Conversely, in the AENN implementation, no consistent gain in the quality of the classification process is obtained by inputting temperatures. A possible explanation is related to the compression step given by the bottleneck layer, which acts as a filtering operator removing noise and minor details from the input signals [174]. This condition also applies to the framework analysed in this work, where the detection of structural anomalies is performed on the reconstructed frequency features at the output layer while disregarding the additional temperature data used in the input stage. Basing on these observations, only temperature-added OCCNN realizations will be investigated hereinafter.

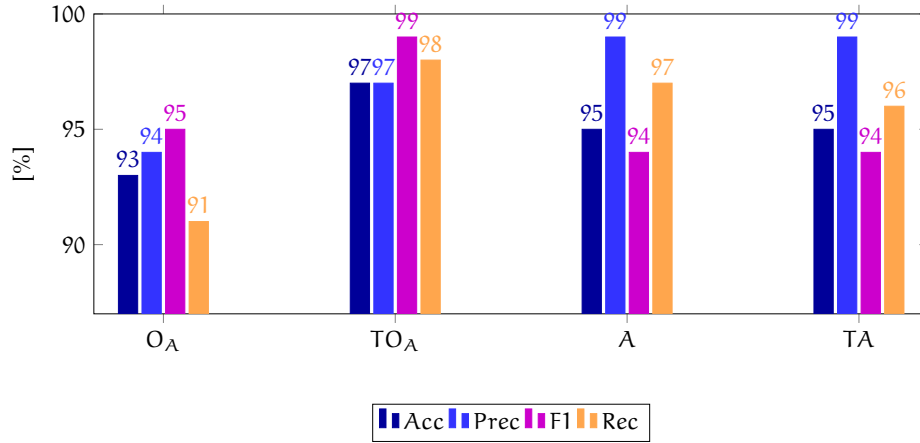


Figure 44: Performances of OCCNN and AENN reference models with ( $TO, TA$ ) and without ( $O_A, A_1$ ) temperature input values, for compression-free configurations.

Moreover, it is important to pinpoint that classification scores attained by  $TO_A$  are highly competitive to the ones presented in [161], which explores a combined AENN–OCCNN architecture to account for biases in the training point density estimation. In the AENN–OCCNN case, an AENN is employed in the first step of the classification chain and used to generate adversarial points rather than resorting to a first cycle of OCCNN to derive a rough estimation of the feature boundaries, while totally neglecting the exogenous contribution of EOPs on modal features. Despite its remarkable accuracy (96% of accuracy and 98% of precision), the AENN–OCCNN solution is poorly compatible with the inclusion of temperature values and CS compression/decompression stages due to the filtering effect at the basis of AENN.

When the current results are compared with the ones presented in [175], where PCA is employed to decouple the impact of EOPs and structural damages, the  $TO_A$  solution here proposed performs satisfactorily well, allowing to discern between healthy and deficient configurations without depending on specific principal components, the proper selection of which affects the robustness of PCA-driven solutions.

#### 6.3.4.2 Effect of data compression

The primary impact of compression/decompression stages can be observed in the larger superposition between healthy and damaged data in the feature space distribution depicted in Fig. 45. Coherently, a reduction in the performance of the CS-driven versions can be seen in the first column of Table 16 for OCCNN ( $TO_A^{CS}$ ) with respect to the results illustrated in the previous Section. Similarly as before, the inclusion of temperature in the pool of NN inputs is particularly effective even in this case, since it returns classification results comparable to those pertaining to the basic  $O_A$  alternative. Indeed, despite a minor reduction in the precision, the accuracy is almost equivalent and F1 and Recall undergo a significant improvement.

#### 6.3.5 Effect of NN distillation

Finally, the computational cost, here intended as the number of NN hyperparameters, was reduced to make the NN model compatible with the constrained resources of embedded

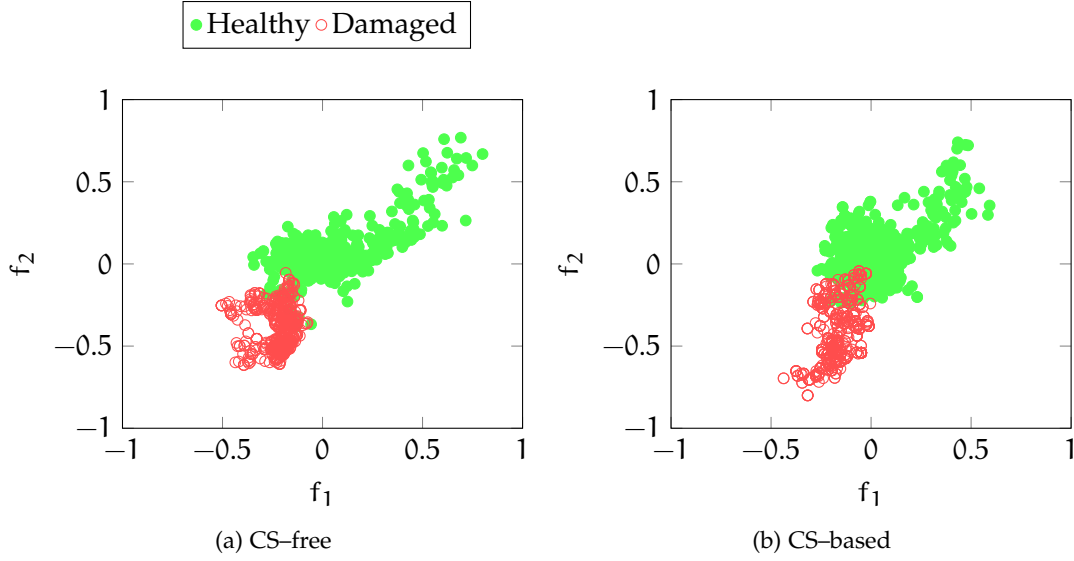


Figure 45: Feature space distribution with compression-free (a) and CS-based (b) processing framework.

Table 16: Performance metrics of OCCNN models A, B, C, D with temperature input values and CS-processed configurations: beside the classical classification scores, the number of hyperparameters is enclosed.

$N_N$	$TO_A^{CS}$	$TO_B^{CS}$	$TO_C^{CS}$	$\infty$	$TO_D^{CS}$	
					MA	MB
Hyperparameters	2852	1250	370		122	
Accuracy [%]	95.73	96.98	96.04	97.16	93.49	90.12
Precision [%]	94.12	95.78	94.59	96.25	92.65	89.25
Recall [%]	99.93	99.93	99.87	99.67	99.37	100
F1 [%]	96.94	97.81	97.16	97.93	96.18	94.04

devices, and the effect on the classification accuracy was, thus, evaluated. To this end, starting from the network with  $N_{N,A} = 50$ , the number of neurons per layer in the OCCNN architecture was then reduced to 32, 16, down to 8, corresponding to a shrinkage of model parameters to  $N_{N,D} = 122$ , with intermediate values of  $N_{N,B} = 1250$  and  $N_{N,C} = 370$ . In Table 16, the reported classification scores are included together with the number of hyperparameters, the latter decreasing at a large extent by halving the number of neurons per layer.

Remarkably, model D with only 8 neurons attains high classification performances, which are absolutely competitive with the ones associated with the most redundant configuration (model A). Moreover, it performs even better than alternative solutions with much higher parameters (see model B and C).

### 6.3.5.1 Effect of intrinsic noise density in MEMS accelerometers

The impact of non negligible noise floors in MEMS accelerometers can be quantified by observing the last three columns in Table 16 (header MA and MB). As can be noticed, the primary effect acts as a loss of up to 7 points percentage in the accuracy of the classified instances while moving from noise free (header  $\infty$ ) to MB MEMS-type. A similar

trend is evidenced for precision and F1; despite this, good performance values are globally attained, which are always very close or consistently above 90%. Recall demonstrates to be less sensitive to such noise levels, being nearly constant. On the other hand, MEMS typology MA, which features a less significant noise level, only undergoes a limited reduction in both accuracy and precision (which show, respectively, a loss of 3% and 4%, respectively).

The importance of this study is pivotal since it proves how the selection of the sensing unit might play a crucial role in the effectiveness of the adopted signal processing techniques and, therefore, the inherent source of instrumental limitations must be coped with while moving from theoretical analyses to real case studies.

#### 6.4 RUNNING STRUCTURAL INFERENCE AT THE EXTREME EDGE: A TINYML APPROACH

The framework presented in Section 6.2 tries to provide a response to two key issues affecting state-of-the-art monitoring solutions empowered by AI, that are (i) the necessity to reduce the complexity of the models and (ii) to lower the data-to-user latency time. However, to further enhance the responsiveness and the resilience of the monitoring architecture beyond the mere processing task, a final edge computing step is still lacking. To this end, the emerging field of TinyML made the near-sensor data inference a tangible, low-cost and computationally efficient complement fulfilling this specific goal.

The content of this Chapter is based upon the research work [P13]:

"Enhancing Vibration-Based Structural Health Monitoring via Edge Computing: A Tiny Machine Learning Perspective" by Zonzini, F., Romano, F., Carbone, A., Zauli, M. and De Marchi L. In *Proceedings of the ASME 2021 48th Annual Review of Progress in Quantitative Nondestructive Evaluation QNDE*, vol. 85529, 2021 (pp 1-5).

from which part of the text is drawn.

##### 6.4.1 TinyML for vibration diagnostics

TinyML is one of the most promising findings promoted by the recent advancements of the electronic and information engineering community, as witnessed by the constantly increasing interest in many application fields. Owing to its tight optimization level between the hardware and software components, it disclosed previously unforeseen, yet completely outstanding, opportunities for AI. More precisely, the TinyML computing paradigm refers to the implementation of very thin and low-power neural networks capable of running on edge devices, i.e., at the boundary between the physical and digital world<sup>2</sup>. Hence, TinyML could bring a radical shift of perspective, moving from cloud-based data analytics, which is usually performed on remote servers in a time- and energy-consuming manner, to near-sensor data inference, empowered to smart sensors in charge of processing information in a streaming fashion. Accordingly, the advantage of TinyML in the SHM context is to bring the artificial intelligence itself in strict proximity where structural information is actually sensed, so as to expedite the inference time and, in turn, the diagnostic process.

<sup>2</sup> <https://www.tinyml.org/>

TinyML was successfully applied in several domains, such as the biomedical [176], the environmental [177], [178] and the image processing field [179], to name a few. Nevertheless, its application to vibration diagnostic frameworks is still an open field of research, for which only a handful of works can be found in the literature [180]. In line with this observation, the research effort presented herein specifically attempts at filling this gap in the context of vibration monitoring.

To this end, among the multiple tasks involved in the SHM-chain, TinyML finds its natural application to damage detection and classification. Hereby, the main contribution of this Section is to present the practical embodiment of a TinyML architecture, in this case the four OCCNN models validated in Sections 6.3.2-6.2.2.1, on the Arduino Nano BLE SENSE board serving as prototyping edge device; preliminary results were presented in [P14] for the AENN counterparts.

#### 6.4.2 Experimental validation

##### 6.4.2.1 Arduino Nano 33 BLE sense board

The Arduino Nano 33 BLE Sense board <sup>3</sup> was used as target platform for the validation of the explored TinyML architectures. It is characterised by the tiniest form factor within the family of AI-empowered Arduino solutions. The MCU, which is the low-power nRF52840 component by Nordic Semiconductor, features 256 kB of serial RAM and 1 MB of FLASH memory with advanced digital signal processing functionalities enabled by a single-precision FPU. The device embeds several peripherals, such as an inertial measurement unit, a microphone, a temperature/humidity sensing element and a gesture/proximity sensor, which make it a versatile architecture for general purpose applications requiring low-power and smart sensing functionalities in a compact board.

##### 6.4.2.2 Porting the model: from cloud-server running to Arduino

In Fig. 46, the three steps that can be followed to transform a standard NN model running on remote stations into MCU-compliant models, are depicted. Once the classification architecture has been trained and validated offline in the standard Tensorflow (TF) programming environment, a quantized variant is obtained by resorting to the Tensorflow Lite (TFLite) extension, which converts the NN model and casts data types into an MCU-like format, allowing it to be run directly on the edge sensor. Since the monitoring system of the Z24 is no more active and it is actually impossible to process signals seamlessly, the edge-running and real-time functionalities of the Arduino board were simulated by pre-loading the modal features extracted at the end of the feature tracking step into the non-volatile memory of the device. Such a framework is conceived to meet the typical procedure applied in the SHM context, in which an initial and offline phase of structural characterization is executed to derive a baseline, then followed by online structural diagnostics and prognostics. In the analysed case, they correspond to the training/validation and testing of the TinyML deployment process, respectively.

---

<sup>3</sup> <https://store.arduino.cc/arduino-nano-33-ble-sense>



Figure 46: Sequence of steps to be implemented to transform a generic NN architectures from cloud/server-based Tensorflow programming to MCU-compliant ML models passing through Tensorflow Lite quantization.

### 6.4.2.3 Results

Results for the implementation on the Arduino board are summarized in Table 17, in which the standard classification scores considered before have been computed together with other remarkable performance metrics, such as the execution time, the model size and the number of hyperparameters. Noteworthy, the TinyML approach proves to be highly robust with respect to rounding effects, data cast and quantization, that were necessarily implied by the TFLite converter. As can be observed, a negligible impact on the classification metrics is exhibited while moving from TF to Arduino, with a maximum decrease of less than one point percentage for all the four metrics: these remains consistently above 94%.

On another side, it is worth mentioning that the model complexity of the OCCNN architecture is interestingly low, showing a memory occupancy around a dozen of kB, a condition which makes its embodiment on the selected prototyping device feasible. Similarly, the worst execution time of 1525 ms for a total of 1561 testing instances (measured for the  $TO_A^{CS}$  with 50 neurons per layer) led to an single inference time of less than 1 ms, hence being compliant with typical duty-cycles of the prospective applications.

In these terms, the exponential decrease in both the occupied memory and running time of the algorithms as  $N_N$  halves can be clearly observed, the combined action of which could lead, in turn, to a consistent contraction of the associated power consumption. Indeed, the model size shrinks more than 95% with a time gain above 75% while  $N_N$  moves from 50 to 8 neurons.

## 6.5 CONCLUSIONS

In this Chapter, a comprehensive framework for vibration-based diagnostics has been presented and thoroughly validated with experimental data from the Z24 bridge use case, proving that the amalgam of data compression, TinyML architectures and environmental information allows to attain high classification scores, i.e., accuracy and precision greater than 96% and 95%, respectively.

Finally, the designed NN architectures have been embedded in a resource-constrained device (i.e., the Arduino Nano 33 BLE sense board) serving as edge computing unit. Running inference model on this device reported promising classification results, corroborated by scores always above 94%, corresponding to a loss of less than 2 points percentage with

Table 17: Performance metrics of OCCNN model while moving from cloud-based TF to Arduino: beside the classical classification scores, the overall complexity in terms of memory consumption, number of hyperparameters and execution time, are enclosed.

$N_N$		$TO_A^{CS}$	$TO_B^{CS}$	$TO_C^{CS}$	$TO_D^{CS}$
Model size [kB]		13.232	6.824	3.304	2.312
Hyperparameters		2852	1250	370	122
Execution time [ms]		1525	865	481	367
Accuracy [%]					
	TensorFlow	95.73	96.98	96.04	97.16
	TensorFlow Lite	95.95	96.49	96.66	96.76
	Arduino 33 BLE Sense	96.60	96.49	96.67	96.76
Precision [%]					
	TensorFlow	94.12	95.78	94.59	96.25
	TensorFlow Lite	94.36	95.35	95.30	98.67
	Arduino 33 BLE Sense	95.18	95.35	95.30	98.67
Recall [%]					
	TensorFlow	99.93	99.93	99.87	99.67
	TensorFlow Lite	100	99.67	100	96.52
	Arduino 33 BLE Sense	100	99.67	100	96.52
F1 [%]					
	TensorFlow	96.94	97.81	97.16	97.93
	TensorFlow Lite	97.10	97.46	97.60	97.58
	Arduino 33 BLE Sense	97.53	97.46	97.60	97.58
FLASH usage [kB]		293.896	287.488	283.968	282.976
RAM usage [kB]		185.760			

respect to the TF counterpart. The overall solution paves the way to the design of an efficient and reliable diagnostic framework driven by TinyML.





## ABSTRACT

*This Chapter deals with the issues of scalability, versatility and technological limitation affecting accelerometer-only monitoring networks. All these problems are approached from an edge computing perspective, via the implementation of a tilt sensor node capable of estimating, in real-time and in a near-sensor manner, structural inclinations from the fusion of linear and rotational vibration signals. Alongside, a heterogeneous approach to OMA is proposed, which combines, both at the hardware and signal processing level, standard accelerometers with low-cost piezoelectric transducers; such solution discloses new potential for a cost-effective and minimally invasive piezoelectric-based modal analysis.*

## 7.1 INTRODUCTION

Data fusion algorithms are supported by the widely shared opinion that single-measurement systems cannot ensure satisfactory resilience, responsiveness and long-term functionalities, which though represent primary requirements of every SHM process [181], [182]. The problem in deploying homogeneous networks for vibration inspection is twofold. First of all, since every sensing technology works in limited frequency bands, mono-type measurements prevent the monitoring process to perform a multi-scale spectral analysis, capable of capturing both the static and the dynamic structural footprint. The second reason is that the geometrical shape of the structure may be such that, depending on the selected measurement technology, some sensing positions could be totally or partially blind with respect to the sought structural parameters. To this end, compensation and auto-calibration obtained by a complementary and integrated approach, in which multi-type measurements are exploited and aggregated together, allow the inspection phase to be strengthened by seizing multiple aspects of the same deterioration process [183].

A key challenge for vibration-based diagnostics of large-scale structures is, for example, achieving the capability to distinguish between global (e.g., changing load paths, loss in global stiffness) and local (e.g., crack propagation, corrosion) fault conditions [184]. In these structures, the integrity may be compromised by rather different aging phenomena, whose effect in terms of spectral content might interest broad and/or very distant bands. For this reason, the development of new strategies exploiting multiple sensor signals is really promising to implicitly reduce the uncertainty of single-source sensing architectures. Such a multi-sensing paradigm leads, in addition, to cost-benefit optimization [185], by promoting a more flexible definition of the density, type, and positioning of the sensors to be deployed.

In conventional OMA-based SHM systems, a multitude of MEMS accelerometers can be used to monitor the structural health status. Nevertheless, these devices are not suitable to perform a wide-band spectral analysis, primarily due to frequency range limitations, since these devices are usually meant to be effective in the low frequency regions [P15].

The necessity to pair this sensing strategy with alternative sensors, capable of operating in different spectral bands, is of the utmost importance; for example, this can happen when the meaningful frequency bandwidth exceeds tens of kHz, e.g., in rotating machines.

The list of sensing technologies complementary to conventional vibration sensors includes, but it is not limited to, acoustic sensors, piezoelectric sensors, strain gauges, inclinometers, magnetometers, fiber-optics, and other application-dependent sensing units, all of them providing useful information for structural characterization. Among case-studies where two or more of these technologies are employed, the work in [186] can be listed, in which the authors developed a SHM monitoring system for condition assessment, using both accelerometers and strain sensors. Similarly, Ferrari *et al.* [187] installed a hybrid sensor network on the historical Brivio bridge in Bergamo, acquiring acceleration and dynamic displacement responses, then merged via data fusion algorithms. An approach based on the coupled exploitation of inertial and acoustic sensors was also adopted in [188], demonstrating how the design of a heterogeneous sensor platform permits the monitoring process to capture the vibration response with more accuracy.

In compliance with this scenario, the scope of this Chapter is to discuss the benefits delivered by the adoption of a multi-sensing monitoring network in conjunction with the integration of data fusion algorithms for the accurate retrieval of modal features from the combination of different vibration quantities. Two main scenarios will be investigated. The first one involves the exploitation of linear and rotational data for the on-board estimation of tilt values. The second one involves, instead, a mechanism to retrieve strictly synchronized modal parameters from the combination of MEMS accelerometers and cost-effective piezoelectric devices, paving the way to a more affordable monitoring system, eventually based on a piezoelectric-driven modal analysis.

## 7.2 PROTOTYPING A TILT SENSOR NODE EMBEDDING A DATA-FUSION ALGORITHM

In this Section, the practical embodiment of a real-time data fusion algorithm based on Complementary Filters (CF) for the near-sensor extraction of tilt angles recovered from the combination of linear and angular vibration responses is presented.

The content is based upon the research work [P15]:

"A tilt sensor node embedding a data-fusion algorithm for vibration-based SHM" by Tesoni, N., Zonzini F., Marzani, A., Scarponi, V., and De Marchi, L.  
In *Electronics*, vol. 8, no. 1, p. 45, Jan. 2019.

from which part of the text is drawn.

The possibility to combine accelerations and angular velocities at the extreme edge and in a real-time manner is granted by the combination of MEMS technology with multi-degree of freedom Inertial Measurement Unit (IMU)s, consisting of the multi-axes measurement of inertial quantities (e.g., the ones provided by accelerometers or gyroscopes) by means of a miniaturized system-in-package. Thus, IMUs offer the ideal platform for the estimation of the position of an object in the space in a very compact and cost-effective manner.

The concurrent usage of accelerometers and gyroscopes provides a set of complementary quantities which can compensate for each other while estimating tilt values. The

reason is that accelerometers perform well at low frequencies: in fact, even if dynamic features suffer from crosstalk, this undesired effect is filtered out by the acceleration transfer function. Conversely, gyroscopes work optimally at higher spectral bands; however, they suffer from drifts induced by the integration procedure used to transform angular velocities into tilt values. Research works combining these techniques have been conducted for high-rise buildings [189], showing that the joined exploitation of acceleration and rotation sensors conveys a more precise understanding of the structural tilt at higher frequencies. Similarly, coupling linear and rotational data proved superior performance in monitoring wind-induced vibrations in tall infrastructures, as discussed in [190]–[193]. Furthermore, diagnostic systems for bridge monitoring have been implemented through sensor networks comprising gyroscopes and accelerometers for the purpose of damage localization [194], [195].

### 7.2.1 Combining accelerations and angular velocities via CF

Among the possible data fusion techniques for inertial data, the one based on CF, i.e., built on the low-pass filtering of linear accelerations and high-pass filtering of angular velocities, is convenient both from an algorithmic and structural point of view. From one side, its bank filtering nature readily implementable through FIR filters provides low-complexity procedures and is, therefore, inherently suitable for the implementation in extreme edge devices with limited processing functionalities. Moreover, as a primary byproduct, it minimizes phase and magnitude distortion around the cutoff frequency. On the other hand, being the CF transfer function constant over the whole spectrum [196], its design is compatible with wide-band sensing.

#### 7.2.1.1 Algorithm definition

The time-dependent acceleration-based and angular-based tilt values, addressed in the following as  $\theta_A$  and  $\theta_G$ , characterize the modal behavior of structures undergoing vibrations.

Let's suppose, for practical convenience, that devices are installed on the top surface of a structure. Under this condition, Fig. 47 schematically depicts the problem of estimating tilt values from a geometric point of view. In detail, the sensor node laying on the  $xy$ -plane is programmed to estimate inclinations of the vertical plane: consequently, the tilt is intended as a positive value around the  $z$  axis.

Acceleration vectors constitute of three components  $a_x$ ,  $a_y$ ,  $a_z$  recorded along the three directions, whereas angular rates  $\omega_x$ ,  $\omega_y$ ,  $\omega_z$  correspond to rotational spins projected on the same axes. Radial acceleration  $a_r = a_z$  and tangential acceleration  $a_t = \sqrt{a_x^2 + a_y^2}$  are fused together to extract the tilt values  $\hat{\theta}_A$  defined as:

$$\tan \hat{\theta}_A = \frac{a_t}{a_r} = \frac{\sqrt{a_x^2 + a_y^2} + \xi_c + \xi_a}{a_z + \xi_c + \xi_a} \quad (33)$$

In the expression above,  $\xi_c$  and  $\xi_a$  indicate, in order, the crosstalk noise and the accelerometer intrinsic noise affecting the collected data, their contribute becoming evident at higher frequencies. Such disturbances must be filtered out by an appropriate low-pass transfer function: as such, accelerations provide an accurate tilt estimation only for pseudo-static behavior.

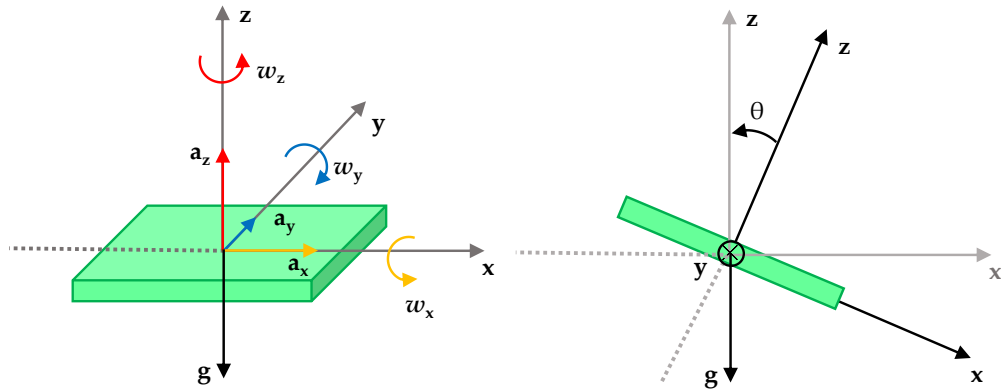


Figure 47: Geometric relationship between tilt angles  $\theta$  and accelerations along the  $z$ -direction for a device installed on the top of a structure.

Angles described by rotation around predefined directions can be numerically computed by integrating the absolute angular velocities

$$\hat{\omega}_G = \sqrt{\omega_x^2 + \omega_y^2 + \omega_z^2} + \xi_b + \xi_g \quad (34)$$

in which drift errors caused by inherently biased and noisy measurements, indicated as  $\xi_b$  and  $\xi_g$ , respectively, typically impact on pseudo-static measurements. The robustness of integration with respect to high-pass filtering leads to precise gyroscope-driven tilt estimations only in the dynamic regime.

According to the CF technique, by taking the Fourier transform of Eq. (33) and (34), the estimated  $\hat{\theta}_A(f)$  and  $\hat{\omega}_G(f)$  can be fused to obtain a unique tilt value  $\hat{\theta}(f)$  according with:

$$\hat{\theta}(f) = H_L(f) \hat{\theta}_A(f) - j \frac{H_H(f)}{2\pi f} \hat{\omega}_G(f) \quad (35)$$

This is accomplished by applying, in parallel, two second order filters ( $2q_1$  being the filter order):  $H_L(f)\hat{\theta}_A(f)$  is the low-pass filtered version of data coming from the accelerometer, whereas angular signals are high-pass filtered. The two quantities  $H_L(f)$  and  $H_H(f)$  designate the following low-pass and high-pass filter transfer functions:

$$H_L(f) = \frac{1}{1 + \left(\frac{f}{f_\beta}\right)^{2q_1}} \quad H_H(f) = \frac{1}{1 + \left(\frac{f_\beta}{f}\right)^{2q_1}} \quad H_L(f) + H_H(f) = 1 \quad (36)$$

where  $f_\beta$  indicates the cut-off frequency of the filters. Inclination values are then transformed back in the time domain by applying the inverse Fourier transform of the output provided by expression (35).

### 7.2.2 Embedding tilt estimation on edge devices

In order to keep as low as possible the memory and computational resources of the algorithm, the processing flow presented in Fig. 48 has been designed. Since operations in the Fourier domain are more computationally convenient for the implementation of filter

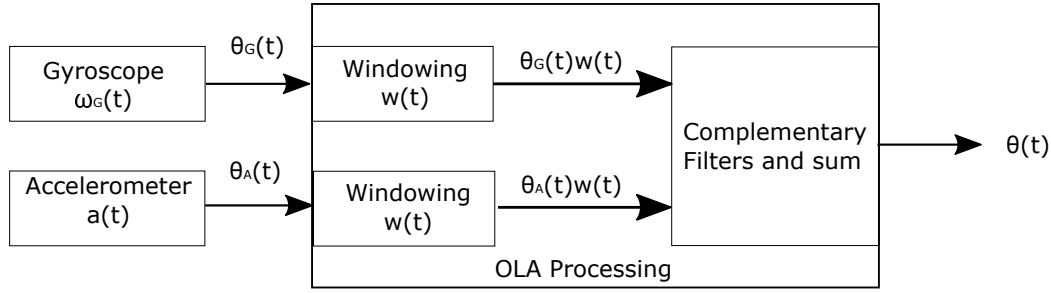


Figure 48: Schematic representation of signal processing method necessary to estimate tilt values from accelerations and angular velocities.

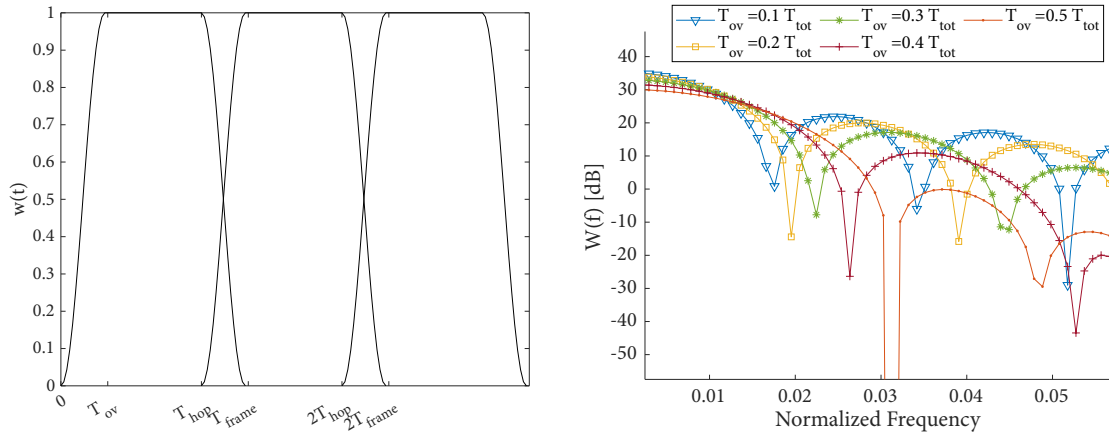


Figure 49: Adopted OLA window necessary to shrink the computational burden of the data fusion algorithm while running on sensor: (a) Time-domain working principle of the OLA mechanism and (b) window spectral properties for overlapping fraction spanning in the interval  $[0.1;0.5]$ .

banks in a digital manner, data fusion can be performed directly in the frequency domain by adopting the Overlap-Add (OLA) method [197].

In the OLA paradigm [198], data are windowed by setting the window size  $N_t$  (in the time domain) at least one order of magnitude smaller than the entire time-series  $N$ . A convenient choice of the filter mask is the one based on raised sine/cosine functions, since they allow for a constant magnitude of the filter transfer function while sliding operations are entailed. Accordingly, the mask adopted in this study is displayed in Figure 49a and can be mathematically described as:

$$w(t) = \begin{cases} \sin^2\left(\frac{\pi}{2} \frac{t}{T_{ov}}\right) & 0 \leq t < T_{ov} \\ 1 & T_{ov} \leq t < T_{hop} \\ \cos^2\left(\frac{\pi}{2} \frac{t-T_{hop}}{T_{ov}}\right) & T_{hop} \leq t < T_{frame} \end{cases} \quad (37)$$

where  $T_{frame}$  is  $\frac{N_t}{F_s}$ ,  $T_{ov}$  is the time interval in which two consecutive windows are overlapped, and  $T_{hop} = T_{frame} - T_{ov}$  is the hop size. Windowed data are then Fourier-transformed and filtered, and the estimated tilt values can be finally concatenated.

### 7.2.2.1 Selecting the OLA parameters

The selection of the optimal cutoff frequency of the complementary filters is highly dependent on the sensor technology, as well as on the specific application case. In the experiments related to static tilt conditions, a recommended procedure for the selection of such parameter is the inclusion of a calibration step aimed at minimizing the mean square error between a reference angle and the mean value of the angle extracted from an initial batch of data.

For the global accuracy, the selection of the window length  $N_t$  is also very relevant, since this parameter directly affects the quality of the filter approximation based on the discrete Fourier transform. This implies that the ratio between the frequency resolution of the windowed and non-windowed processing ( $\Delta_{ft} = \frac{F_s}{N}$  and  $\Delta_{fw} = \frac{F_s}{N_t}$ , respectively) should be lower bounded:

$$\frac{\Delta_{ft}}{\Delta_{fw}} = \frac{N_t}{N} \geq \alpha \quad \rightarrow \quad N_t \geq \alpha N \quad (38)$$

where  $\alpha$  is a predefined accuracy threshold.

It is worth noting that, since the rising and falling edge respectively obey to a  $\sin^2(t)$  and a  $\cos^2(t)$  trend, the mask of this window is shaped to satisfy the Constant-Overlap-Add (COLA) constraint stated in equation (39):

$$\sum_{k=0}^{N_w-1} w(t - k T_{hop}) = 1, \quad \forall t \quad (39)$$

being  $N_w = \frac{T_{tot}}{T_{hop}}$  the total number of iterations. This necessary and sufficient condition allows for the correct reconstruction of the signals split into successive windowed frames. COLA implies that the spectral values of the window functions must be zero at all harmonics of the hop rate  $F_{hop} = \frac{1}{T_{hop}}$ ; consequently, it must be ensured that

$$W(k F_{hop}) = 0, \quad \forall k = 1, \dots, N_w - 1 \quad (40)$$

Taking the Fourier transform of the window described in (37) and introducing the overlap fraction  $N_o = \frac{T_{ov}}{T_{frame}}$ , it follows that

$$W(f) = -\frac{(2f N_o T_{frame})^2}{1 - (2f N_o T_{frame})^2} T_{hop} \cos(\pi f N_o T_{frame}) \text{sinc}(f T_{hop}) e^{-j\pi f T_{frame}} \quad (41)$$

shows zero values for  $f = k F_{hop}$  and it is then compliant with (40), independently from both the duration of the window and the number of samples to be overlapped.

A narrow amplitude of the first lobe of the spectrum of the window, together with a highly attenuated second lobe, would be desirable. However, the spectrum obtained by processing windows with increasing values of  $T_{ov}$  (see Figure 49b) clearly demonstrates that a wider first lobe corresponds to a deeper attenuation of secondary lobes. As a result, in order to reach the best performance, the final choice must be properly balanced among these two opposite behaviors.

Besides accuracy, the computational cost to perform OLA processing is strongly affected by the selection of  $T_{ov}$  and  $N_t$ . As well known, executing FFT has a complexity  $O(N_t \log_2 N_t)$ , implying a logarithmic decrease when  $N_t$  is reduced. Therefore, the computational effort (Cost) paid to process a generic sequence of  $N$  elements divided into  $N_w$  frames results in:

$$\text{Cost} = N_w N_t \log_2(N_t) \quad (42)$$

Specifically, the contribution associated with the number of overlapped samples is upper bounded to  $2N$  whenever the maximum allowable  $T_{ov}$  is chosen. On the contrary, the logarithmic relationship from the window size leads to a consistent reduction of the cost as  $N_t$  downsizes. Consequently, following what has been anticipated in (38), there is a clear trade-off between the computational cost and the filter approximation accuracy.

### 7.2.3 Prototyping and Experimental validation

The ISSLab vibration sensor nodes were exploited for prototyping purposes thanks to their DSP functionalities. To fully exploit the versatility of this circuitry, all the parameters necessary to process data on-board were stored in registers programmable at run-time: the sampling frequency, the total number of samples to be acquired, the overlap fraction and the output data rate.

The reliability of the developed hardware and software architecture was assessed after window parameters have been quantified. The accuracy in tilt estimation was finally examined via experimental data, firstly gathered in almost static conditions to serve as a ground truth for algorithmic validation and, then, in dynamic regime for modal analysis.

#### 7.2.3.1 System Validation in static condition

The Newport IG Breadboard anti-vibration table shown in Fig. 51 was used to filter out unwanted surrounding vibrations, while one ISSLab sensor node was statically tilted to a fixed angle. At this stage, the cutoff frequency of the complementary filters was computed.

The sampling frequency was set to 1250 Hz. Since the maximum available storage capability is 30 kB (10 kB are reserved to the main program and to the firmware necessary to sample/exchange/process data) and each sensor acquires simultaneously two data bytes for each one of the six inertial Degree of Freedom (DoF), the available number of samples on each channel could not exceed 2500. Since working with data segments amounting to power of two is computationally more efficient in DSP, and assuming also a resolution ratio  $\alpha = 0.02$ , 64 samples shifted with an overlapping ratio equal to 0.25 were selected. This ensured an optimal compromise among the spectral design of the corresponding window frame and the computational complexity.

Experimental data were processed with  $f_\beta$  values varying from 80 Hz to 180 Hz at an increasing step of 1.5 Hz. The optimal cutoff frequency was obtained by that minimizing the square error in the estimated vs reference angle, reaching a minimum for 153.5 Hz. Figure 50 shows that the selection of the most appropriate cutoff frequency effectively captures the actual tilt value, while a wrong selection may cause periodic artifacts, the periodicity of them being related to the window size.

In the following, first and second order statistics have been used to establish the accuracy of the measured inclinations in stationary conditions, with the sensor node fixed at three different inclinations:  $30^\circ$ ,  $45^\circ$ ,  $60^\circ$ . Table 18 points out the distribution of the mean value and standard deviation for each configuration: relative error  $\varepsilon_r$  lower than 0.7% and  $\sigma_r$  always less than two-tenths of a degree prove that results are highly precise.

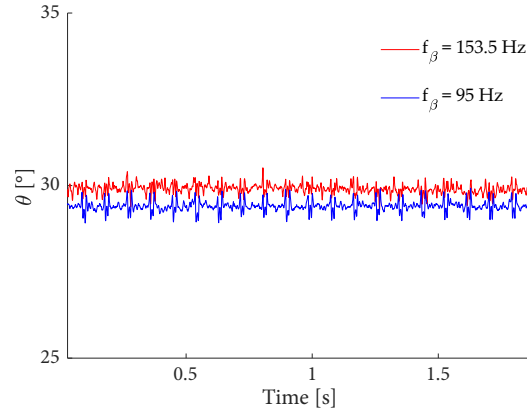


Figure 50: Effect of proper cutoff frequency selection for OLA-based sensor data fusion (actual tilt value: 30°).

Table 18: Statistics obtained for tilt values in different pseudo-static configurations: mean value, relative error and standard deviation.

Reference Tilt [°]	Measured Tilt [°]	$\varepsilon_r$ [%]	$\sigma$ [°]
30	30.1832	0.611	0.1399
45	45.0024	0.005	0.1523
60	60.3116	0.519	0.1985

It is worth pointing out that the variance slightly rises for increasing inclination values, showing an almost linear trend. This evidence paves the way to future works, which should be aimed at including an auto-calibration procedure performed directly at the sensor level: once a finer-scale training would be executed, biased measurements could be internally corrected after inferring the proper compensation curve.

### 7.2.3.2 Vibration Analysis

The steel beam already used in the previous Sections was instrumented with a network of seven ISSLab nodes connected in a daisy-chain. Sensors were placed at a step of 220 mm starting from the first node, whose distance from the fixed left edge of the beam was 135 mm.

An explicit relationship exists between acceleration and inclination. In more detail, by resorting to trigonometric relationships for the scheme introduced in Figure 47, the time-spatial dependent angle  $\theta$ , described by rotations of the sensor, can be geometrically interpreted as the derivative of vertical position displacements along the longitudinal direction.

In mathematical terms, the governing equation of a thin rod undergoing transverse motion is modelled as ([128]):

$$z(x, t) = \sum_{p=1}^{\infty} (A_p \cos(\omega_p t) + C_p \sin(\omega_p t)) \sin(\beta_p x) \quad (43)$$



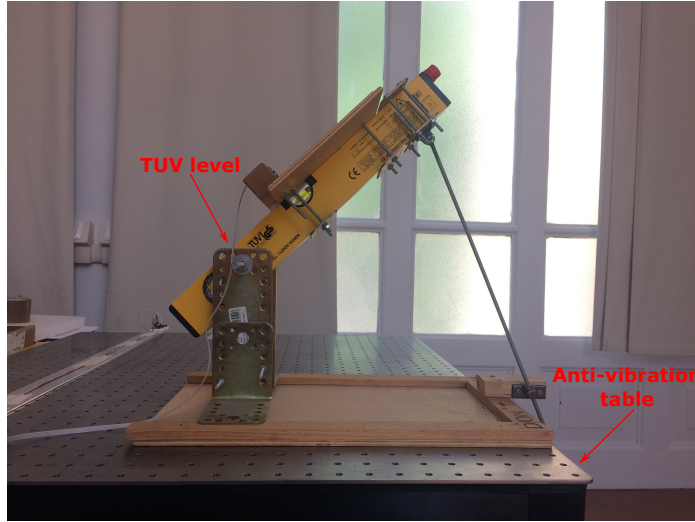


Figure 51: Experimental setup in pseudo-static conditions: anti-vibration table equipped with TUV level.

where appearing quantities  $A_p$ ,  $C_p$  are constants deriving from boundary conditions,  $\omega_p = 2\pi f_p$  correspond to the  $p$ th-angular frequency and  $\beta_p$  models the space dependency. Algebraic manipulation of (43) yields to the more compact form:

$$z(x, t) = \sum_{p=1}^{\infty} R_p \sin(\omega_p t + \alpha_p) \sin(\beta_p x), \quad R_p = \sqrt{A_p^2 + C_p^2}; \quad \alpha_p = \arctan \frac{A_p}{C_p} \quad (44)$$

on which a derivative operation can be performed providing the final result stated in Eq. (45).

$$\theta(x, t) = \frac{\partial z(x, t)}{\partial x} = \sum_{p=1}^{\infty} \beta_p R_p \sin(\omega_p t + \alpha_p) \cos(\beta_p x) \quad (45)$$

In practical scenarios,  $P < \infty$  is set.

Comparing (43) to (45), it can be inferred that the spectral content of  $z(x, t)$  and  $\theta(x, t)$  is localized at the same angular frequency  $\omega_p$ . As a consequence, frequency analysis accomplished on tilt angles or acceleration signals allows to identify the same modes of vibration. For this reason, the validation process in dynamic regime passed through the analysis of similarities between the frequency spectrum computed on acceleration data and the one estimated at the end of the data fusion procedure.

In this phase, data were acquired at a sampling frequency  $F_s = 1250$  Hz, which is compliant with the dominant modes of the structure. The beam was excited at the two-thirds of the span by means of impulse excitation, thus allowing it to oscillate in a condition of free vibrations. Since the dynamic operative conditions substantially differ from static measurements, a new calibration phase was necessary to be executed.

The most appropriate cutoff frequency was selected according to the spectral range of interest. More explicitly, the analysis included the characterization of the first and second harmonic, corresponding to  $f_1 = 6.195$  Hz and  $f_2 = 24.778$  Hz. Thereafter, a value of  $f_\beta = 27$  Hz was adopted to properly balance accelerometers and gyroscopes performance. Window size equal to 128 samples was chosen in order to provide high-resolution data,

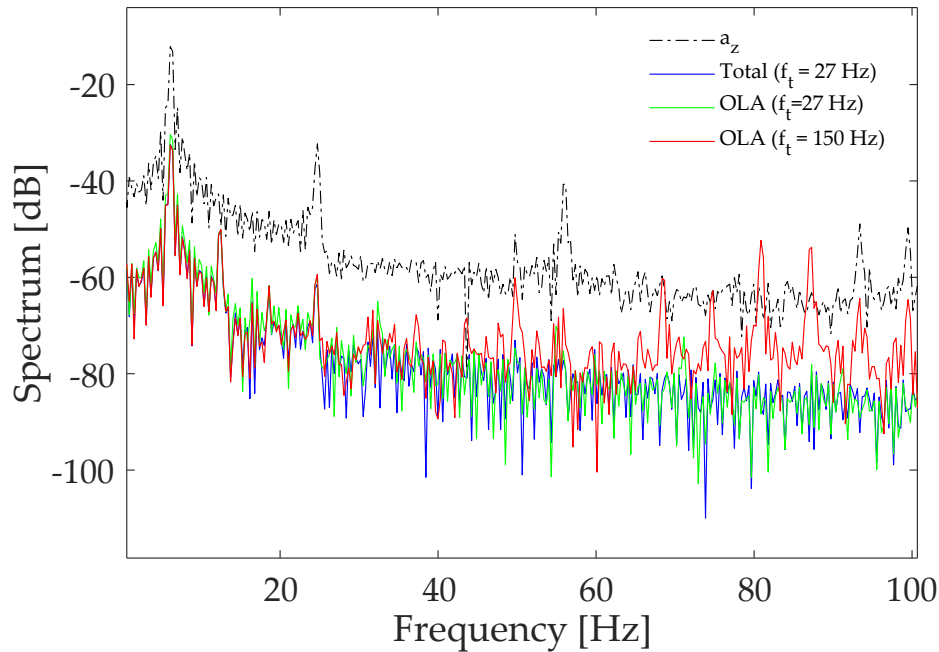


Figure 52: Comparison of spectra (obtained with FFT) resulting from the windowed and non-windowed approach with respect to the spectral content of radial acceleration.

and an overlap factor  $N_o = 0.4$  enabled to smooth the envelope of the window transition bands.

In order to assess the reliability of the proposed multi-type sensor framework, PSD results obtained for windowed and non-windowed processing were compared to the performance obtained applying the aforementioned techniques to the same dataset used for tilt angle estimation.

Improvements in the quality of the vibration analysis can be inferred from Figure 52. Basing on data extracted from a single sensor node installed on the top surface of the beam, the introduction of the right cutoff frequency intensely attenuates spurious peaks. Furthermore, the spectral trend estimated through the windowing strategy is almost perfectly superimposed to the one extracted by processing the whole dataset at one time (and it is also coherent with numerical predictions). The same outcome can be found in the panels of Fig. 53a, from which the filtering effect of the CF-based data fusion algorithm and the gain in the spectral insight obtained by the aggregation of both angular and linear vibrations can be observed.

In modal terms, Fig. 53b shows the seven spectra obtained from the sensors installed on the beam: not only the peaks corresponding to the different vibrating harmonics are distinctly resolved over the whole band with a satisfactory PSNR of about 15 dB, but a good level of coherence between them is also evident. Moreover, from the same plot, it can be observed that both the pinned-pinned frequencies (triangular marked peaks) and the free-free flexural modal components<sup>1</sup> of the structure (red circles) can be detected via the implemented near-sensor data fusion algorithm. As a result, optimized real-time algorithms embedded into the electronic equipment permit to capture detailed snapshots of the rotational properties characterizing vibrating structures.

<sup>1</sup> Probably a consequence of imperfect anchoring offered by the supports.

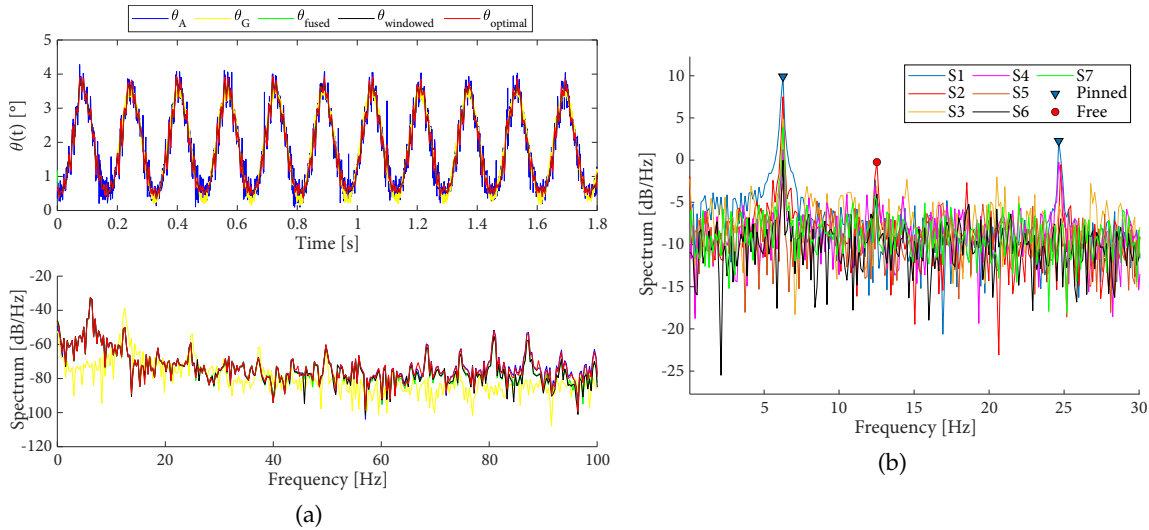


Figure 53: (a) Effect of signal fusion in time and frequency domain and (b) Comparison of PSD profiles for tilt signals estimated by nodes located at different positions of the beam.

### 7.3 HETEROGENEOUS SENSOR NETWORK FOR PZT-DRIVEN MODAL ANALYSIS

In the present Section, the ISSLab sensor network is exploited as a heterogeneous monitoring architecture basing on both low-cost PZT transducers and tri-axial MEMS accelerometers to prove that a combination of these two technologies is beneficial for continuous SHM applications in the low frequency regime.

The final objective is to demonstrate how the parallel advancements empowered by sensor networks, low-power circuits, communications and signal processing might help in tackling the lack of scalability of conventional sensing solutions, leading to sensor networks able to monitor structures with very large and complex geometries and provide the users with a thorough insight about the current health status.

The content of this Section is based upon the research works [P16], [P17]:

"Vibration-based SHM with up-scalable and low-cost sensor networks." by Zonzini, F., Malatesta, M. M., Bogomolov, D., Testoni, N., Marzani, A., and De Marchi, L. (2020). In *IEEE Transactions on Instrumentation and Measurement*, vol. 69, no. 10, pp. 7990-7998, Oct. 2020. ©2020 IEEE

"Heterogeneous sensor network for vibration-based SHM" by Zonzini, F., Malatesta, M. M., Bogomolov, D., Testoni, N., Marzani, A., and De Marchi, L. (2019). In *2019 IEEE International Symposium on Measurements & Networking (M&N)*, 2019, pp. 1-5. ©2019 IEEE

from which part of the text is drawn.

#### 7.3.1 Piezoelectric technology for modal analysis

Piezoelectric transducer technology based on piezoceramic (PZT) transducer discs [199], [200] permits operation in the range of hundreds of kHz and more and, prior than for modal analysis [201]–[203], is most commonly applied for other monitoring tasks, such

as ultrasonic inspection and acoustic emission testing [204]. In these cases, commercial systems characterized by expensive, space-, weight-, and power-demanding solutions are typically employed, leading to static and not versatile solutions.

Modal analysis inspection exploiting piezoelectricity can be applied in the high-frequency range, up to and in excess of 10 kHz [202]. Conversely, in the low-frequency range, down to and lower than 10 Hz, PZT discs are scarcely employed, since in this frequency band conventional accelerometers are classically understood to be more reliable.

An interesting byproduct of using PZT discs is the possibility to simultaneously perform OMA and AE testing [205]. This evaluation strategy is of primary importance in the integrity assessment of metallic or composite structures, either intended for civil and residential buildings (e.g., bridges, towers, buildings) [188] or industrial applications (e.g., rotating motors and hydraulic pumps [206], wind turbines [207], [208]), where the nominal vibration behaviour co-exists with important acoustic phenomena occurring as a consequence of structural deterioration (delamination, soldering, etc) and external agents (corrosion, etc). In these contexts, there is a high demand in designing compact, cost-effective and highly integrated sensor networks, while the systems presented in the literature [201] are based on bulky monolithic instrumentation, incompatible with heterogeneous measurements.

Differently, the design of the ISSLab piezoelectric sensor nodes described in Appendix A specifically aims at overwhelming this lack of versatility thanks to a very compact, minimally invasive circuitry, which can be easily interfaced even with very low-cost (< 2 \$) disc-shaped piezoceramic patches (or discs, as they will be referred in the following).

### 7.3.2 MEMS and low-cost PZT discs for modal analysis: a physical relationship

In this sub-Section, a simple test-bed consisting of an aluminum cantilever beam is exploited to derive a physical relationship between acceleration-driven and piezoelectric-driven vibration data and, therefore, to justify the employment of the latter as a viable companion technology for modal analysis.

#### 7.3.2.1 The case study: multi-type OMA of a cantilever beam

As a representative case study, a light-weight aluminum beam pinned at one end was employed in an experimental campaign comprising one piezoelectric sensor cluster (label PZT) with three closely-located active areas, and one tri-axial MEMS accelerometer (label ACC), vertically aligned on the opposite faces of the structure. The beam is  $L = 420$  mm long, with cross-section area  $b \times h$ ,  $b = 40$  mm depth and  $h = 1.98$  mm height. As depicted in Fig. 54, an additive hexagonal mass  $m_a = 100$  g has been attached in the proximity of the free edge, hence allowing the beam to naturally oscillate. The center of gravity of the additional mass has been chosen to be exactly aligned at the mid-depth,  $x_A = 15$  mm distant from the longitudinal border. A material density of  $2700 \text{ kg/m}^3$  and a Young's modulus of 70 GPa are other important physical properties, determining the stiffness and the elasticity of the beam.

Assuming the structural configuration described before, together with the intrinsic geometric and physical properties of the beam, a numerical model has been purposely developed in order to predict the theoretical modes of vibration. More specifically, by following an approach similar to [209], the effects induced by the presence of the addi-

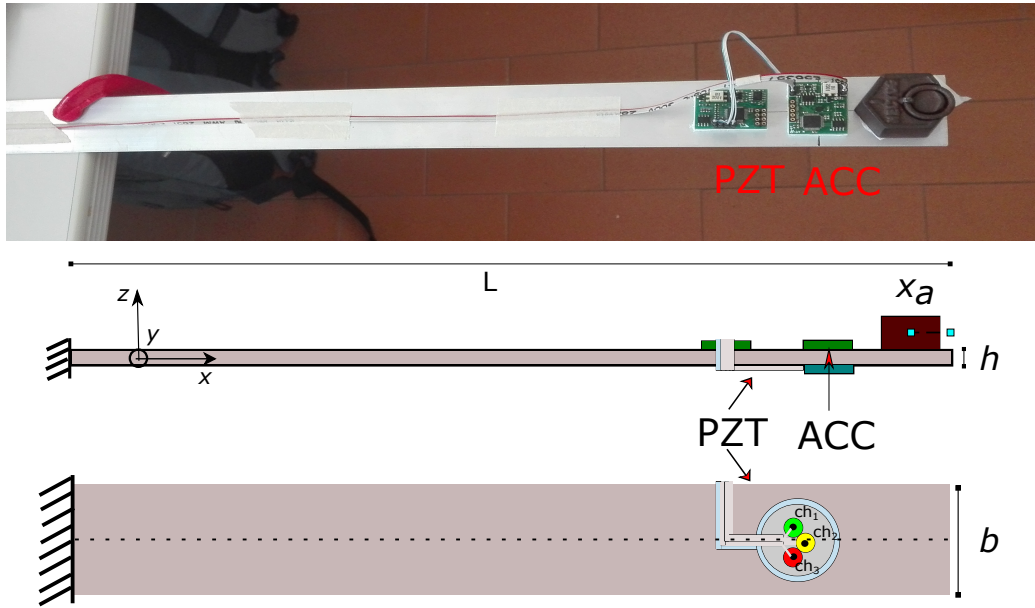


Figure 54: Experimental setup comprising one piezoelectric transducer connected to a piezoelectric sensor node (PZT) and a tri-axial MEMS accelerometer (ACC) installed on a cantilever beam. [©2019 IEEE]

tional mass have also been accounted for, providing a set of numerical frequencies equal to  $f_1 = 3.85$  Hz,  $f_2 = 36.50$  Hz,  $f_3 = 107.75$  Hz,  $f_4 = 204.93$  Hz. A sampling frequency  $F_s = 1000$  Hz has been selected for both the devices to ensure enough spectral band. Signals have been acquired for 5 s: the PZT sensor node was programmed to work with the maximum available gain of 27.3 dB, whereas an acceleration range equal to  $\pm 2g$  was retained compliant with the dynamic excursion experienced by the beam.

### 7.3.2.2 Validation: time analysis

The structural response in the dynamic regime is represented in Fig. 55, which outlines the three traces acquired by mutual PZT discs, one for each channel (lower graph) of the PZT cluster, side-by-side the accelerations measured by the MEMS along the three coordinate axes (upper plot). Measurements coming from the PZT sensor node<sup>2</sup> consist of extremely in-phase samples, clearly showing tightly consistent sinusoidal patterns, the difference among them being a matter of amplification factors. Non-idealities, such as manufacturing process, could be a reasonable explanation for this little variation.

An almost perfect superimposition between theoretical and experimental data can be inferred from acceleration envelopes, according to the fact that the beam is constrained to vibrate in a cantilever configuration as the clamp does fix its left cross section. As such, for the considered experimental test-bed, the most significant acceleration measured by the sensor is the vertical component ( $a_z$ ) fluctuating around nominal 1 g, followed, in order, by the horizontal ( $a_x$ ) and lateral ( $a_y$ ) ones, the latter being negligible compared to the other two. As a consequence of previous observations, only data recorded on PZT channels together with vertical accelerations  $a_z$  will be used for further characterization.

<sup>2</sup> For the sake of correctness, the acronym PZT refers to the material with which piezoelectric transducers are typically fabricated. In this manuscript, the same acronym will also be used as a pure linguistic license to indicate the ISSLab nodes supporting such technology.

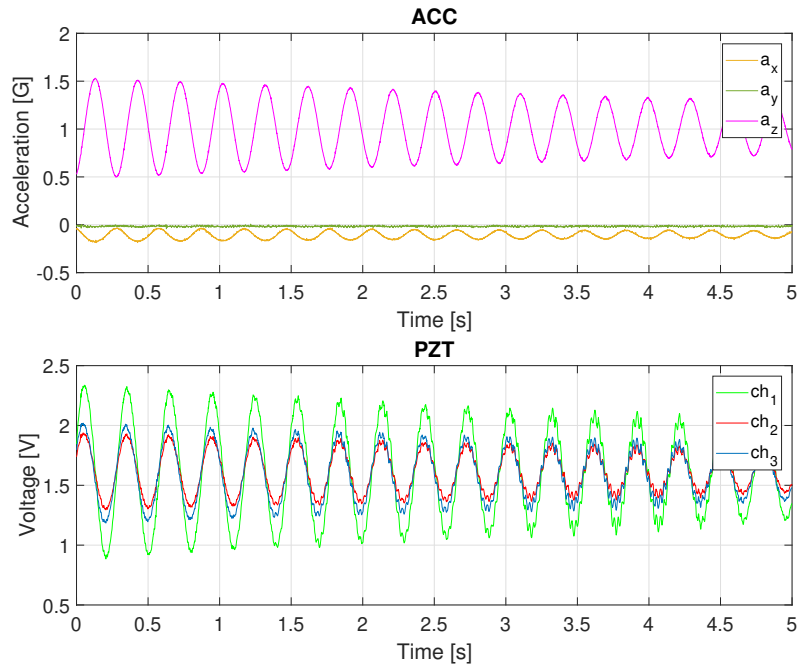


Figure 55: Dynamic response of a cantilever beam induced by an additive mass. Signals acquired in time domain on each channel of a piezoelectric sensor node and a MEMS accelerometer (top) placed in the same position. [©2019 IEEE]

In addition, a comparative study of the normalized and averaged data is provided in the upper plot of Fig. 56, highlighting how a derivative relationship exists between ACC and PZT data. In fact, since in a beam in bending the strain along the beam axis is proportional to the second order derivative of the displacement orthogonal to the beam axis, namely the deflection, and accelerations are the second order derivative of the displacements, the strain and the acceleration measured by the ACC nodes are linearly related. Moreover, the macroscopic radial deformations of the transducer caused by the deformations of the beam induce a charge redistribution in the PZT material which is related linearly to the strain perceived by the transducer and to the piezoelectric potential  $V_q$ .

At low-frequency, this voltage does not directly correspond to the actual quantity measured by the PTZ nodes. Specifically, by adopting the first order electrical model of a generic PZT transducer sketched in Fig. 57, where  $C_p$  corresponds to the piezoelectric capacitance,  $V_{out}$  quantifies the measured voltage at the output stage across a loading capacitor  $C_L$  in parallel to a load resistor  $R_L$ . Basic circuit manipulation in Laplace domain yields to the input-output voltage transfer function formalized in expression (46):

$$H(s) = \frac{V_{out}(s)}{V_q(s)} = \frac{sR_L C_p}{1 + sR_L(C_L + C_p)} \quad (46)$$

which, under the assumption  $\omega \ll 1/[R_L(C_L + C_p)]$ , with  $\omega$  being the angular vibration frequency, can be further simplified into Eq. (47), which acts as a derivative block on  $V_q$ :

$$H(s) = sR_L C_p \quad (47)$$

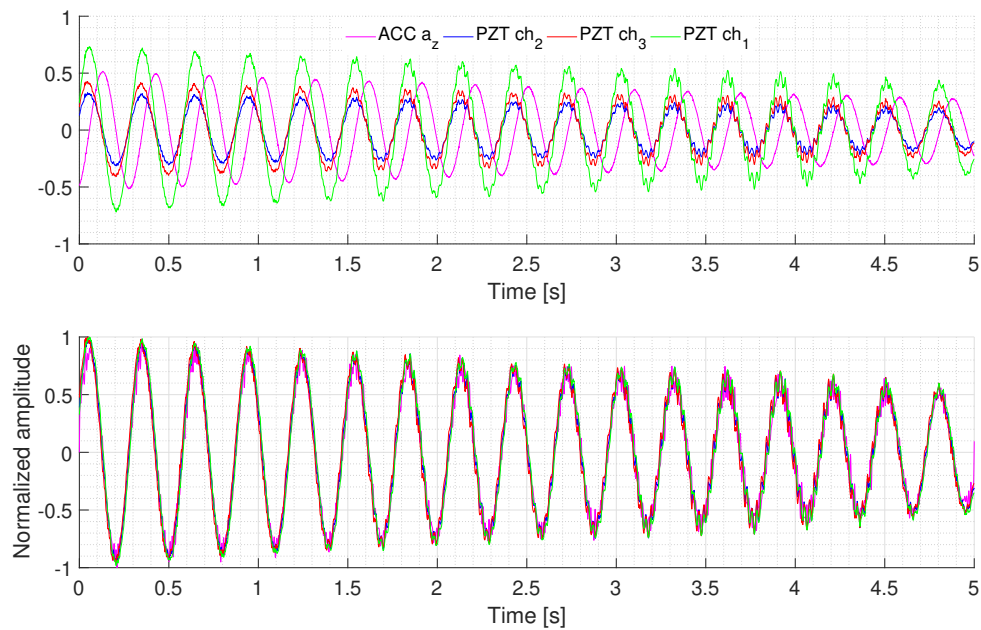


Figure 56: Comparison between PZT and ACC averaged envelopes: original signals (top) and normalized acceleration time-derivative superimposed to normalized PZT signals (bottom). [©2019 IEEE]

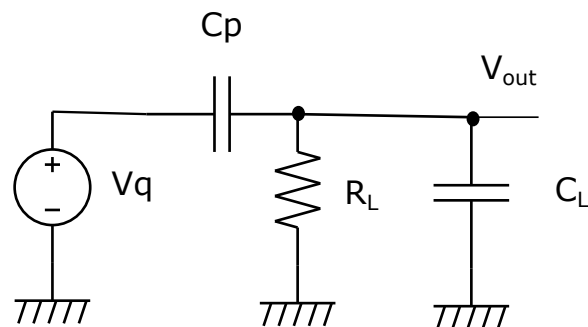


Figure 57: First order electrical model of a PZT sensor. ©2019 IEEE

Consequently, in the low-frequency range, the signal measured by the PZT nodes is the first derivative of the the strain, hence the first derivative of the signal measured by the ACC nodes.

This theoretical expectations is validated by the experimental waveforms presented in the bottom plot of Fig. 56, which superimposes all the three channel responses measured by the PZT device with the derivative of the vertical acceleration  $a_z$ : the good agreement of the signals generated by the two different sources enforces the empirical evidence that these devices register different physical quantities relative to the same vibration behavior.

### 7.3.2.3 Validation: frequency analysis

As far as natural frequency extraction is concerned, PSD was estimated through different processing techniques, yielding to the spectra drawn in Fig. 58. It is worth noticing how spectral peaks estimated from PZT and ACC acquisitions (dash-dotted vertical lines) are

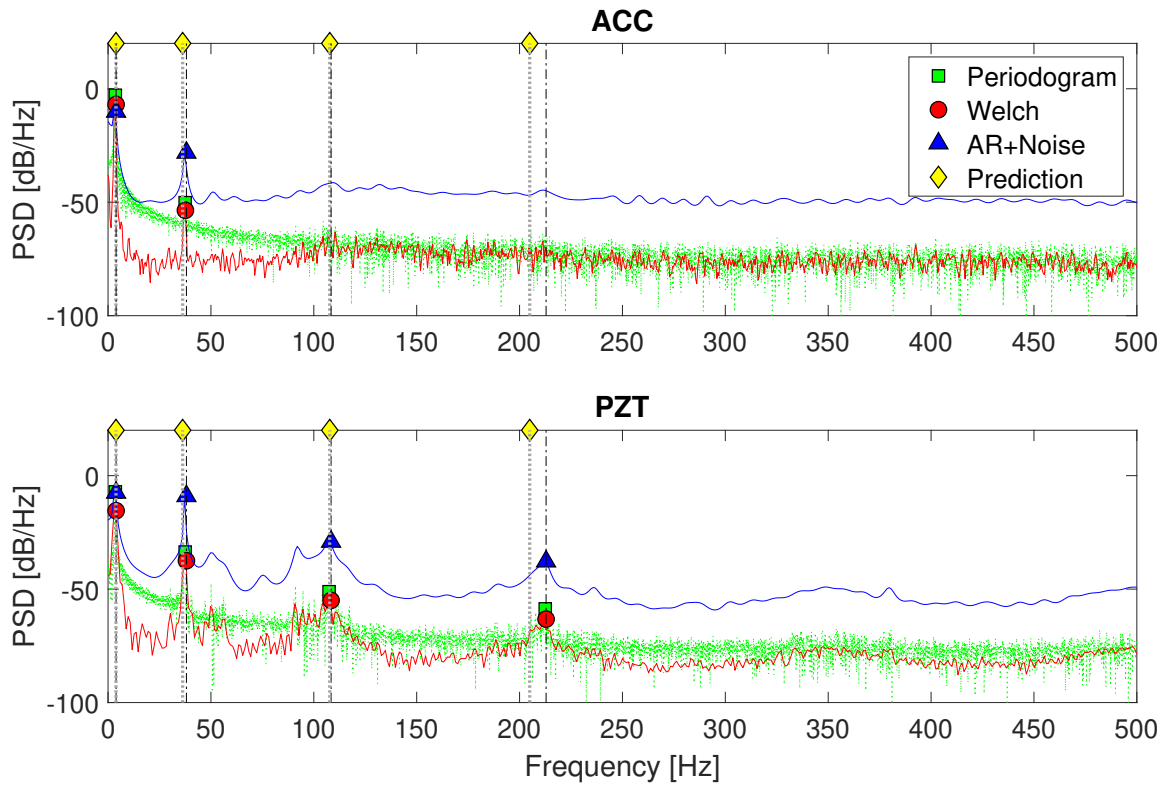


Figure 58: Comparison between spectral trend of  $a_z$  acceleration signal (top) and  $ch_1$  PZT sensor (bottom) computed with different processing techniques. [©2019 IEEE]

consistently aligned nearby the same values. From one side, this fundamental outcome demonstrates the effectiveness of custom piezoelectric devices in capturing the dynamic properties of vibrating structures, even at frequencies below a few tens of Hertz. At the same time, it can be argued that the performance of PZT devices is even superior, their spectral content being significant at higher frequencies beyond 100 Hz. Indeed, the third and fourth frequencies are visible in all the PZT spectral signatures obtained with the selected PSD estimators (periodogram, Welch's method, AR+Noise). Conversely, only the AR+Noise method is capable of identifying two faint peaks corresponding to these frequencies in the ACC curves: the other two methods are inadequate of such feat due to the poor SNR which is globally associated to the two sinusoids in the acceleration spectrum.

The PSNR has been considered as the main metric to qualify the spectral insight extracted with the two sensing technologies. The most important outcome concerns the higher PSNR characterizing the PZT-driven response around the two highest natural frequencies, independently from the adopted PSD estimator. In detail, the PSNR value around the third and fourth modes nearly drops from 15 dB and 10 dB, respectively, to 0 dB while moving from the PZT to the ACC spectral trends. Conversely, a negligible deviation can be observed for the first and second modal component, since their correspondent magnitudes are almost equally resolved with respect to the noise floor (i.e., PSNR = 25 dB).

The spectral analysis reveals that the dominant modes are centered at the following frequencies:  $f_1 = 2.93$  Hz,  $f_2 = 37.11$  Hz,  $f_3 = 104.49$  Hz,  $f_4 = 208.98$  Hz. These values express the mean average among all the experimentally calculated peaks by means of the AR+Noise estimator. Comparing these outcomes to numerical expectations, the highest



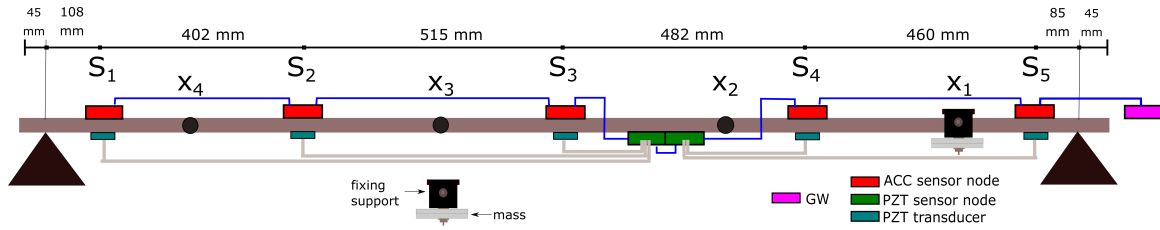


Figure 59: Experimental setup deployed on a simply supported steel beam, with one gateway (GW, in magenta), five MEMS accelerometers (ACC red devices) and akin PZT transducers (blue ones) connected to two PZT sensor nodes (green ones). The light-grey wiring lines identify the PZT transducer-to-sensor connections, whereas the blue ones refer to the sensor-to-sensor communication cables. Four different positions  $x_1$ ,  $x_2$ ,  $x_3$ ,  $x_4$  were considered to simulate the presence of crack-like faults by means of hanged masses. [©2019 IEEE]

deviation can be noticed around the first vibration mode. Alongside, a relative error averagely inferior to 5% proves the suitability of the proposed hybrid network to cope with modal frequency estimation purposes in a more consistent manner than acceleration-only alternatives.

### 7.3.3 PZT-driven modal analysis for damage detection

The objective of this sub-Section is to prove experimentally the defect capability of piezoelectric-driven modal analysis and, thus, to stress its reliability as a complementary/competitive tool for vibration-based SHM applications.

#### 7.3.3.1 The case-study: a simply supported steel beam

The structure in Section 4.4.1.1 was sensorized with a double chain of five PZT transducers and as many accelerometers (Fig. 59). The devices were almost equally spaced, for a total amount of ten passive sensing elements installed at a time. Sensors were fixed in correspondence of the same vertical position but on opposite surfaces. Each piezoelectric disc, which weights less than 190 mg, presents an external and internal diameter respectively equal to 6 mm and 4 mm. The total weight of the network so far deployed amounts to 53.1 g, which corresponds to less than 0.54% of the beam mass (9.70 kg), also comprising the extra load due to the purposely designed lodging case. Such a modest weight increment is uniformly distributed over the whole beam span, then it can be argued that its effects on the dynamic response of the structure are negligible. It is worthy to notice that only two PZT sensor nodes were necessary to acquire five transducers' signals, thanks to the featured multi-channel acquisition capability of the ISSLab PZT node.

Faulty conditions were simulated by laterally hanging additional masses on the beam at four different positions. In detail, two masses  $m_A = 988$  g and  $m_B = 1754$  g were employed (referred to as case A and B, respectively, in figures and tables), whereas the positions of the mass were  $x_4 = 335$  mm,  $x_3 = 820$  mm,  $x_2 = 1353$  mm and  $x_1 = 1854$  mm distant from the left edge of the beam. Hence, an asymmetric mass distribution was induced, causing a decrease in natural frequencies dependent on both the amount and placement of the weight itself. A schematic representation of the final monitoring net-

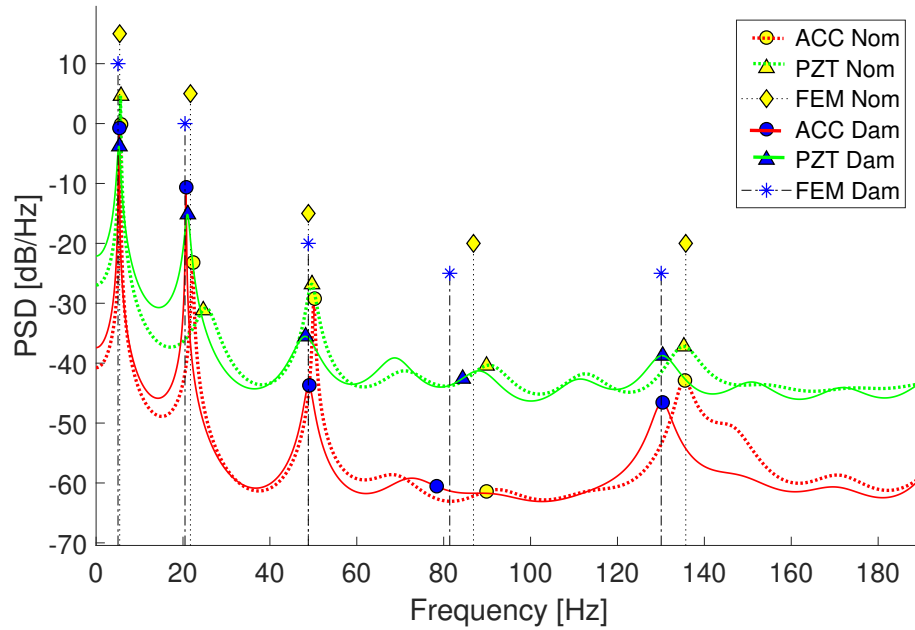


Figure 60: A comparison of spectral trends resulting from ACC (red lines, circle markers) and PZT (green lines, triangle markers) signals in nominal (dotted lines, blue markers) and altered (solid lines, yellow markers) conditions. Data were acquired in correspondence of the mid-span. [©2020 IEEE]

work is depicted in Fig. 59, from which it is clear that the selected sensing positions are proximal to the nodal and antinodal values of the first two modes of vibration.

After a preliminary characterization in nominal conditions, eight configurations with simulated damage were tested stimulating the beam in a free position of the span by means of an impact hammer. In all the experiments, 5000 samples were acquired at  $F_s = 1$  kHz. In such way, not only the effectiveness of the sensor network to extract modal parameters was validated, but also the possibility to detect a defective condition.

### 7.3.3.2 Frequency-based assessment

The spectral characterization of the beam was conducted through the AR+Noise estimator ( $N_p = 60$ ), given the necessity to efficiently handle the higher complexity of the considered scenario. The locally estimated PSD curves are finally averaged, thus obtaining a cumulative evaluation. The suitability of this heterogeneous sensor network to track damages, meant as frequency variations in the spectral content, is evidenced in Fig. 60. The computed spectra are obtained from ACC and PZT signals, recorded in healthy and altered conditions, from the halfway sensor node.

The panel proves the high accuracy of the instrumentation in identifying the high-order and most damage-sensitive modes. Moreover, it should be mentioned that the performances related to high-order even harmonics in the spectra are coherent with the reported sensing position, representing the mid-span a nodal point for the chosen bending conditions. More importantly, the vertical alignment between PZT and ACC peaks is clearly evidenced, supporting the suitability of low-cost and customized piezoelectric devices to cope with classical OMA-based SHM. Finally, a good match with the numerical

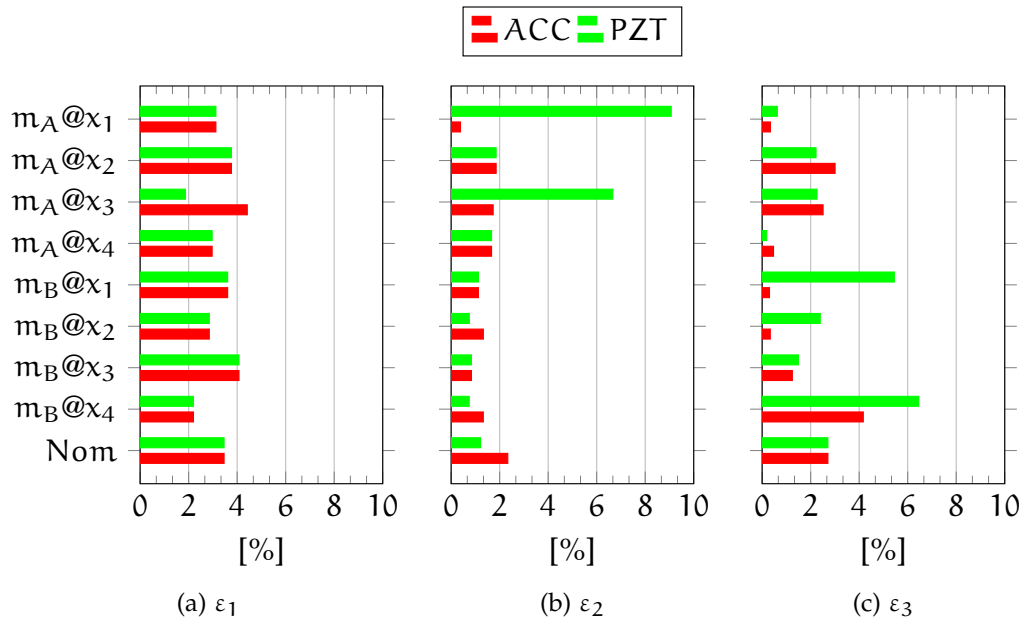


Figure 61: Relative error  $\varepsilon_p$  between AR+Noise-driven experimental estimation and numerical prediction obtained in nominal and damaged conditions; from left to right: first, second, and third natural frequency of vibration. [Adapted from ©2020 IEEE]

predictions (generated with closed analytic formulae as in Section 4.4.2.2) additionally corroborates the quality of the obtained results.

A quantitative evaluation is reported in Fig. 61, which describes, for every  $p$ -th vibration component, the absolute relative error  $\varepsilon_p = |1 - f_p/f_p^{ref}|$ , in percentage, between the first three experimentally extracted ( $f_p$ ) and numerically predicted modal frequencies ( $f_p^{ref}$ ). The non-uniform distribution of the error among the different acceleration components follows the same pattern in both the adopted sensing technologies. A noticeable fluctuation can be observed in the extraction of the third mode, independently from the specific position or entity of the hanged mass. Such effect can be attributed to the low energy content of this modal component.

From the comparative analysis, it can be concluded that the performance of the PZT devices is competitive over their MEMS counterparts, showing approximately equivalent percentage values in correspondence of the lowest frequencies. Despite some isolated peaks, concentrated around the most severe perturbation (e.g. more than 6% error for the second natural frequency when  $m_B$  is in position  $x_2$  and  $x_4$ ), the precision of the PZT transducers in detecting the most energetic and low-frequency harmonics outperforms the one obtained from acceleration data. More specifically, the efficiency of the adopted PZT-driven solution is confirmed by the related errors, averagely below 3.10% and 2.66%, for the first and second mode, respectively. Such percentages have to be compared to 3.38% and 1.40%, i.e., the relative errors achieved by processing the MEMS signals.

It is worth noting that the computed relative errors are affected by the minimum spectral resolution imposed by the sampling frequency. This resolution is equal to 0.2 Hz in the considered setup, corresponding to a theoretical worst-case variation associated to the first component of almost 3.70%.

### 7.3.3.3 Mode shape-based assessment

Finally, the extraction of mode shapes from PZT signals was precisely investigated, following the processing scheme sketched in Fig. 62. The aim is to reconstruct the first three mode shapes for each tested configuration. In performing this task, the signal amplitude recorded by every sensing unit plays a crucial role. This requirement does not apply to the natural frequencies extraction process, which explores relative differences in spectral peaks' alignment rather than in the mutual PSD magnitude. A proper mode shape *tuning* procedure (also referred to as *scaling*) was performed to counteract unavoidable differences in the transducers' amplitude response due to intrinsic non-idealities in the sensors' fabrication, wiring and coupling mechanism. Such a tuning is performed when the structure is in pristine (zero-time) conditions (superscript N) and, subsequently, evaluated for on-condition damage assessment in presence of defective configurations (superscript D).

In the zero-time testing,  $U_A$  acquisitions from ACC and PZT sensor nodes were repeated under nominal dynamic behaviour<sup>3</sup>. For each ACC and PZT acquisition, the first three raw mode shape vectors ( $\Phi_{ACC}^{(p,uN)} = [\Phi_{1,ACC}^{(p,uN)} \dots \Phi_{N_s,ACC}^{(p,uN)}]$  and  $\Phi_{PZT}^{(p,uN)} = [\Phi_{1,PZT}^{(p,uN)} \dots \Phi_{N_s,PZT}^{(p,uN)}]$ ,  $u = 1 \dots 3$  respectively) were extracted on the basis of the FDD algorithm (step 1). Then, the actual tuning procedure to determine a set of scaling factors for the PZT sensors is performed (step 2). The developed procedure is based on an iterative leave-one-out strategy, according to which  $U_A - 1$  time series were employed for the tuning of the PZT scaling factor and the remaining one for the validation.

Let us denote with  $k$  the excluded data-set at each iteration; the scaling coefficient  $\alpha_{i,PZT}^{(p,kN)}$  for the  $p$ -th PZT modal coordinate at the individual sampling position  $i$  was computed as:

$$\alpha_{i,PZT}^{(p,kN)} = \frac{1}{U_A - 1} \sum_{u=1, u \neq k}^{U_A} \frac{\Phi_{i,ACC}^{(p,uN)}}{\Phi_{i,PZT}^{(p,uN)}} \quad (48)$$

The scaling factors were then used to assemble the estimated mode shape coordinates  $\hat{\Phi}_{PZT}^{(p,kN)}$  (step 2.a):

$$\hat{\Phi}_{i,PZT}^{(p,kN)} = \alpha_{i,PZT}^{(p,kN)} \Phi_{i,PZT}^{(p,kN)} \quad (49)$$

In the experiments,  $U_A = 5$  time series from  $N_s = 5$  acceleration and as many piezoelectric transducers were acquired on the structure in pristine conditions. Thereby, 5 different sets of tuning factors were derived, the cardinality of each set being equal to the number of extracted modes.

The validity of such tuning procedure was assessed by computing MAC values (step 2.b) to measure the level of coherence between numerically predicted mode shapes  $\Phi_{ref}^{(p,N)}$  and experimentally scaled PZT mode shapes  $\Phi_{PZT}^{(p,kN)}$  coming from the  $k$ -th data-set.

As reported in the first row of Table 19, the MAC percentages obtained by averaging MAC values achieved for the five different sets of tuning factors are consistently above 90% when the structure is in the pristine (nominal) conditions. The smallest MAC value

<sup>3</sup> For the sake of clarity, the notation adopted in this Section has been changed slightly with respect to the one adopted until this point to indicate mode shapes as well as a different meaning to the quantity N has been assigned.

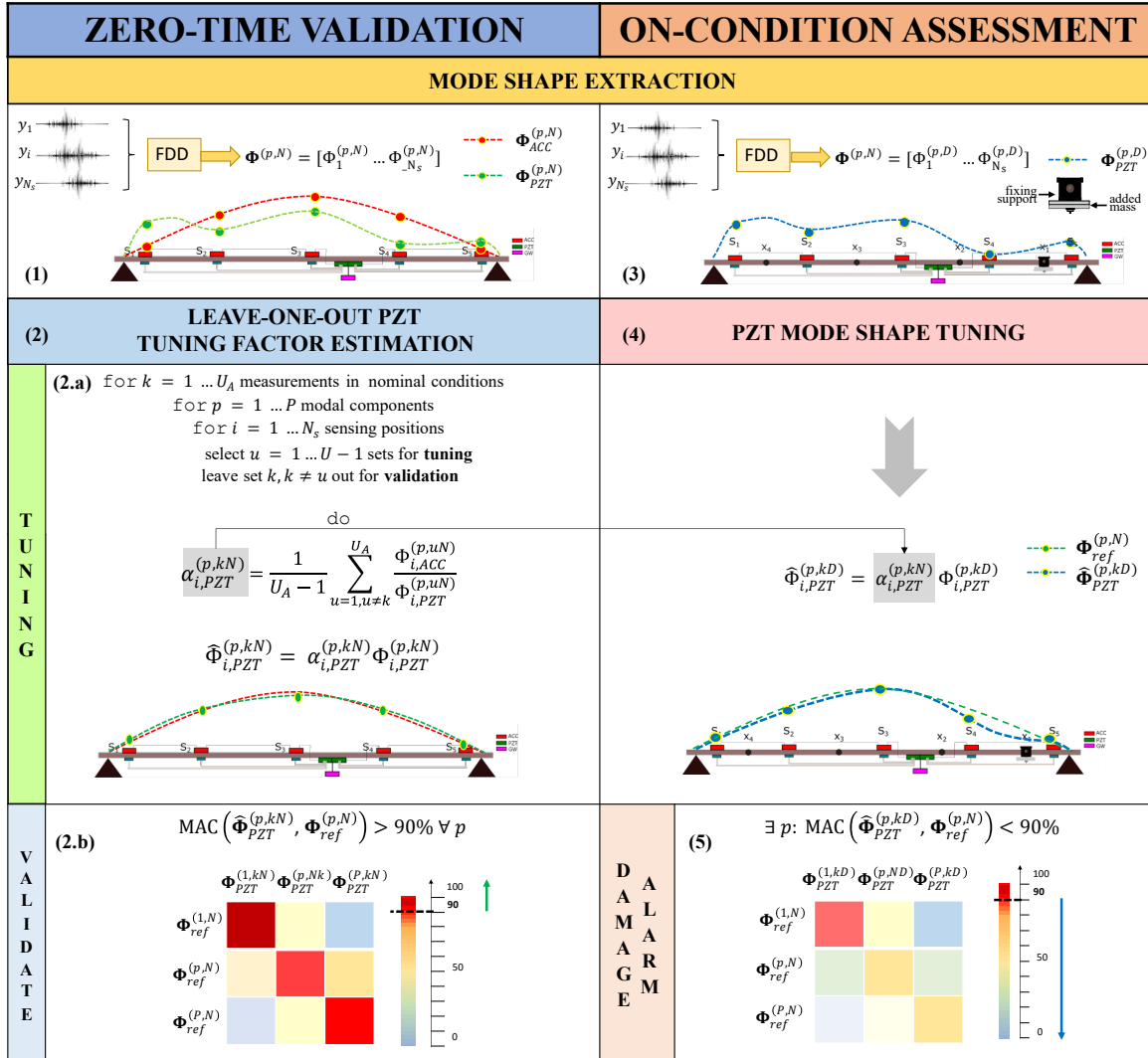


Figure 62: Processing flow adopted for PZT-based damage detection purposes. In the left column, the zero-time validation in nominal conditions comprising (1) the extraction of both the ACC and PZT raw mode shapes, (2) the PZT mode shape scaling factors estimation built on a (2.a) leave-one-out tuning procedure and (2.b) a final structural validation of the reconstructed PZT mode shapes. Procedures in the right column refer to the on-condition assessment in damaged configurations, where the previously estimated tuning factors (step 2.a) are employed to re-scale (step 4) the currently obtained raw PZT mode shapes (step 3); the comparison with reference values (step 5) is performed to notify damage alarms in case of occurrence.

Table 19: Mean values  $\mu$  and associated standard deviations  $\sigma$  of MAC values obtained in nominal condition validation and damage detection assessment after applying the proposed PZT mode shapes tuning procedure.

	$\Phi^{(1)}$		$\Phi^{(2)}$		$\Phi^{(3)}$	
	$\mu_1$	$\sigma_1$	$\mu_2$	$\sigma_2$	$\mu_3$	$\sigma_3$
Nominal	96.75	1.33	96.56	2.71	94.40	1.57
A @ $x_1$	91.23	2.06	76.07	3.60	41.38	3.24
A @ $x_2$	90.03	2.34	67.78	4.16	73.57	3.28
A @ $x_3$	83.32	2.60	78.44	2.60	72.24	3.17
A @ $x_4$	88.14	2.09	66.42	4.10	38.64	11.24
B @ $x_1$	95.24	0.93	51.32	3.79	49.44	20.72
B @ $x_2$	75.65	1.89	49.94	1.94	13.96	6.24
B @ $x_3$	96.49	0.21	54.64	3.08	96.09	1.01
B @ $x_4$	71.65	2.79	52.04	2.06	90.26	1.92

is obtained for the third mode. This is due to the fact that higher modal components only comprise a minimal part of the total mechanical energy of the structure, [201]. Alongside, it is important to underline the robustness of the scaling technique for the PZT signals, supported by the minimal standard deviations.

The capability to identify damaged conditions by monitoring mode shapes extracted from PZT acquisitions was then tested under the previously described perturbed configurations (steps 3-5 in Fig. 62). For a specific defective status indicated by the superscript D, the native modal coordinates estimated from the PZT acquisitions ( $\Phi_{\text{PZT}}^{(p,D)} = [\Phi_{1,\text{PZT}}^{(p,D)} \dots \Phi_{N_s,\text{PZT}}^{(p,D)}]$ ) were calculated with the FDD algorithm (step 3), and tuning factors  $\alpha_{i,\text{PZT}}^{(p,kN)}$  computed in step 2.a were successively applied to scale the currently extracted mode shapes (step 4). In Fig. 62, this concept is magnified by a noticeable shift in the modal pattern (blue dashed curve) occurring in the proximity of the simulated defect position, with respect to the baseline curve (green one) extracted in nominal conditions. Finally, by estimating MAC indexes with respect to reference modal coordinates (step 5), the damage detection capability of the system was verified.

Table 19 reports the mean values  $\mu_p$  and the associated standard deviations  $\sigma_p$  of the MAC related to each set of five modal correlation percentages for the considered defective conditions. For each case, it is possible to identify at least one mode with MAC correlation degrading beneath 90%. Finally, it must be acknowledged that, notwithstanding two isolated outliers related to the third mode shapes, the standard deviation of MAC values is on average less than 4 %.

#### 7.4 CONCLUSIONS

This Chapter has presented data fusion techniques, eventually running on extreme edge devices, as a viable solution to partially alleviate the technological limitations of individual sensing principles and, consequently, permit the development of up-scalable, versatile and non-invasive alternatives for the long-term monitoring of structures in dynamic regime.

Tilt values, extracted via a simple yet robust sensor data fusion algorithm, which is supported by an optimized on-board signal processing scheme, have been estimated in a near-sensor manner accomplishing significant accuracy both in pseudo-static and dy-

dynamic conditions. Besides, a physical interpretation of the relationship between vibration responses acquired by piezoceramic transducers and standard accelerometers disclosed new possibilities for piezoelectric-driven modal analysis, even in the low-frequency regions: it has been demonstrated that low-cost PZT sensors might be used alongside traditional MEMS accelerometers to efficiently estimate modal parameters of structures undergoing flexural vibrations while reducing the cost and the weight of the monitoring instrumentation.

Therefore, the procedures explored in this Chapter offer a twofold means for sensor network optimization: from one side, they extend the structural insight via complementary measurements, thus increasing the accuracy of the data analytics layer; on the other hand, they allow for a better exploitation of the available sensing and processing capabilities of the network, eventually promoting a more affordable and edge-enabled monitoring approach.





Part II

GUIDED WAVES-BASED DATA COMMUNICATION SYSTEMS



## ABSTRACT

*In this Chapter, the basic concepts of guided waves (GWs) as a powerful means to performing punctual inspection of large structures are reviewed. Then, the discussion is focused on the usage of piezoelectric transducers for GWs-based digital data communication systems, in which the transmitted signals can be used at the same time for probing the inspected structures and for communicating, wirelessly, the results of the inspection itself.*

## 8.1 INTRODUCTION

Vibration diagnostics is a non-destructive evaluation technique suitable for global damage characterization, due to the fact that vibrations reflect the structural behavior at a macroscopic scale. This means that each part of the structure oscillates at the same time without propagation of the mechanical energy [128]. Nonetheless, when local inspection is required to identify, localize and classify inner flaws or subtle phenomena occurring in the internal regions of the structure, vibration analysis might be ineffective.

Conversely, ultrasonic testing based on Guided Waves (GW) offers the opportunity to perform a punctual inspection of wide areas by leveraging the peculiar capability of guided elastic waves to be scattered by damages [210] while being confined by the boundaries of the mechanical medium in which they propagate [211]. Typically applied for elongated structures, GW testing is more generally used as a tool for monitoring thin-walled components, i.e., those structures in which the thickness is comparable-to or greater-than the wavelength of the GW itself.

Conventional GW-based SHM systems commonly comprise a distributed array of transducers which can be permanently installed on the inspected structure. These devices can be used either for actively generating or passively sensing the elastic waves: in the former case, they are connected to external signal generators, whereas the latter functionality requires data amplification and acquisition systems. Once collected, waveforms are forwarded to central processing units for further elaboration, during which a set of damage sensitive features is extracted with the final aim of providing the sought structural bulletin. However, the dimensions, costs, and weight of the commercial electronic equipments that are needed to perform the monitoring are typically not compliant with long-term functionalities and permanent installation.

To address these issues, and similarly to what has been done in the vibration diagnostics field, the design of a new generation of embedded microsystems suitable for near-sensor GW signal processing has recently been fostered. These new smart devices are characterised by unobtrusive miniaturized circuits integrating all the electronics to perform digital signal processing and custom actuation. The same devices are also capable of exchanging data without the need of additional cables, radio-frequency modules and/or external bulky instrumentation because the mechanical waveguide itself acts as the communication channel, while GWs are exploited as information carriers. In this perspective,

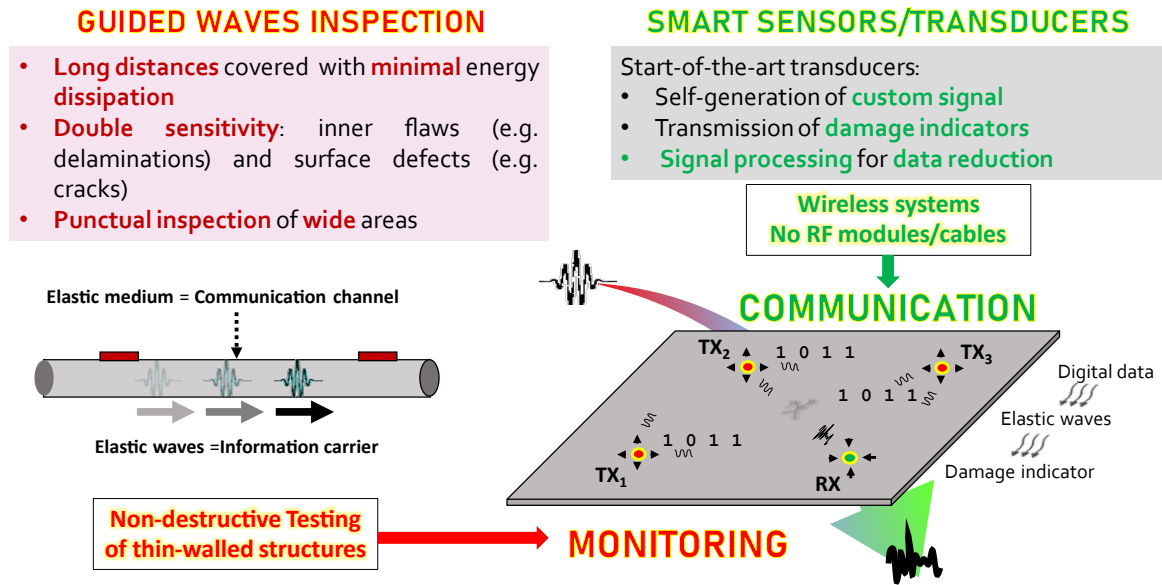


Figure 63: Exemplary description of the principles enabling GW-based wireless data transfer in SHM applications. Beside the punctual structural inspection capabilities peculiar to GWs, the complementary ability of smart sensors/transducers to on-board process and generate signals can be exploited for cable-free data sharing among the players of the SHM network itself.

the transmitted signals, to be readily generated in form of digital pulses corresponding to mutual digital messages, allow for the pursuit of a twofold purpose: (i) probing the inspected structures and, after local elaboration executed directly by the sensor board, (ii) communicating the results of the inspection. Fig. 63 symbolically schematizes these concepts for a representative case consisting of three actuating nodes (TX) and one receiving node (RX) deployed on a square plate.

This complementary and communication-oriented feature might be crucial when cabled or conventional wireless electromagnetic communication is not viable, too expensive or prone to fail, for example in underground or underwater applications. It is worth mentioning that, whenever possible, it is preferable to transmit only near-sensor processed information, rather than long time series such as the raw data. In fact, in GW inspections, pre-processed information may consist of a few scalar values representing damage indicators. In this sense, the GWs-based solutions illustrated in this dissertation pursue a local/global system optimization effort which has some analogies with what discussed for vibration-based monitoring systems in Sections 4 and 5.

In the following, the basic properties of one special class of GWs, i.e., Lamb waves<sup>1</sup>, will be analysed to provide a consistent description of their peculiar propagation behavior. This theoretical understanding deserves primary importance for the design of the most adequate transmission scheme.

<sup>1</sup> This is the specific class of GWs exploited for the sake of communication. Henceforth, to simplify the notation, the acronym GW will be used as a metonymy to indicate such waves.

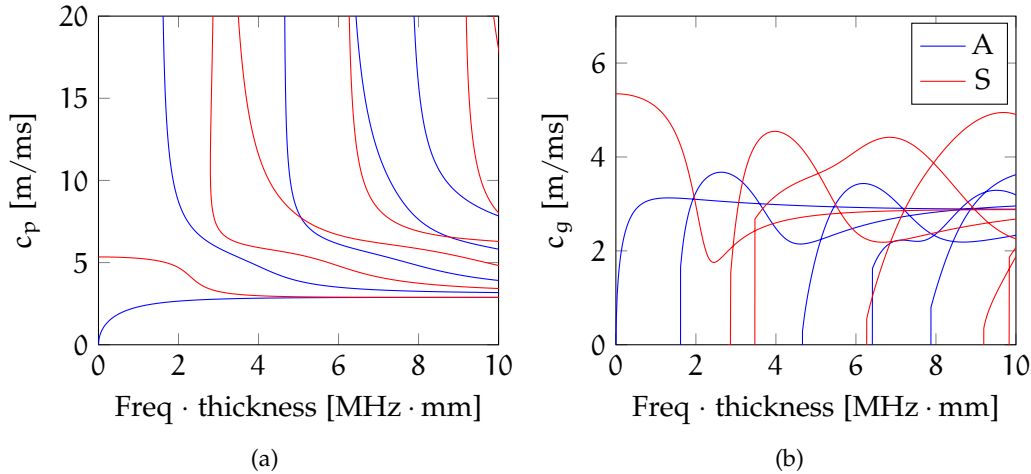


Figure 64: Dispersion curves for an aluminum square plate with 1 mm thickness: (a) phase velocity and (b) group velocity.

## 8.2 FUNDAMENTALS OF LAMB WAVES

GWs can have different nature, depending on the boundary conditions of the structure in which they propagate. Firstly studied by Sir Horace Lamb, Lamb waves are the particular form of guided waves which propagate in plates. Two main properties contributed to their diffusion in the SHM field, namely (i) their inherent capability to travel long distances with low attenuation and (ii) the concurrent sensitivity to both inner (e.g., delaminations, disbondings) and surface defects (e.g., corrosion, cracks, impacts) [212].

Nevertheless, albeit showing long-range propagation and sensitivity with respect to distinct classes of damage, it is paramount to emphasize that Lamb waves can exhibit complex behavior during propagation, primarily due to their multi-modal nature. In the GW context, *multi-modality* means that multiple modes are actuated at the same time and co-exist in the same frequency interval. For planar structures, these modes are of two different types: symmetric (S), if the particles show more radial in-plane displacement, or anti-symmetric (A), if the average motion displacement is out-of-plane, along the transverse direction. Despite being theoretically infinite, the actual number and nature of the generated modes vary with the frequency–thickness product: such concept implies that, since the thickness is prescribed by the chosen structural geometry, it is possible to adapt the frequency content of the actuated signal such that all high-order modes, apart from the first symmetric (S<sub>0</sub>) and anti-symmetric (A<sub>0</sub>) ones, that exist for all frequency bands, are cut off. Beside multi-modality, two other factors characterize Lamb waves propagation: (i) *dispersion*, i.e., the wave speed is not constant with frequency; (ii) *mode conversion*, i.e., symmetric modes may be converted into anti-symmetric ones and vice versa, especially when the waveguide has some irregularities (e.g. thickness variation).

A useful graphical representation of this propagation pattern is given by the so-called dispersion curve diagrams in Fig. 64, i.e., plots showing the profile of the phase  $c_p$  (Fig. 64a) and group  $c_g$  (Fig. 64b) velocity of the waves as a function of the frequency–thickness product.  $c_p$  is the rate at which the individual phase of the wave propagates, whereas  $c_g$  represents the propagation rate of the entire wave envelope [213]. In these figures, which are taken from an aluminum beam with 1 mm thickness, multi-modality stems from the

simultaneous presence of the red and blue curves referred to the symmetric and anti-symmetric modes, respectively, while dispersion is proven by the non constant trend of the single curve while moving from lower to higher actuation frequencies<sup>2</sup>.

In practical cases, where it is necessary to deal with a finite propagation medium, there are three other forms of complexity: the first concerns the physical interaction of GWs with the mechanical boundaries, which is responsible for reflections and reverberations, a phenomenon also known as multi-path interference; the second pertains, instead, to the mutual interferences in case of multiple active transducers. Finally, the effects of environmental changes, such as temperature fluctuations, could also alter the propagation behaviour to a substantial level.

Therefore, the successful implementation of GW-based communication mechanisms must cope with all the above mentioned detrimental effects. Appropriate encoding strategies are consequently needed to achieve robust and accurate transmission of digital information through the mechanical waveguide.

### 8.3 OVERVIEW OF GWS-BASED DATA COMMUNICATION SYSTEMS

The different GWS-based system realizations for digital data transfer can be categorized on the basis of the adopted modulation mechanism. *Modulation* is the procedure which allows to incorporate the information conveyed by a digital message or stream of bits in one or multiple carrier signals of adequate frequency. It is worth noting that, despite the different nature of the channel, modulation methods conventionally used for radio communications can be easily mapped to the GWS-based counterpart. In the literature, successful data transfer via GWS has been presented across several structures, and the achieved bit rates lie between tens of bps to hundreds of kbps, reaching a few Mbps for very short propagation distances. This transmission speed is deemed sufficient for the prospective application scenarios, where the data payload is given in form of a batch of damage indicators.

Among the large variety of communication strategies, the scope of this Section is to offer a systematic overview of state-of-the-art solutions for GW-based communication, extending what has already been provided in [P18] and [P19]. A selection of already published works is offered in Table 20, in which details concerning the attained data rate per transmission distances are explicitly reported in order to perform a thorough analysis of their performances. For a theoretical analysis of the different modulation techniques, readers are referred to [214], while the specific modulation schemes investigated in the following of the manuscript will be detailed in the next Sections.

Considered as one of the most effective modulation techniques, On-off keying (OOK) represents an efficient solution for data communication across solid planar media (e.g., plates), allowing digital messages to be delivered through the structure with considerable rate (in excess of 100 kbps) after travelling distances in the order of 50 cm. There are two main reasons enabling the success of this method: (i) its simple bit encoding/decoding mechanism, according with which a digital one is represented by the transmission of a pulse signal while omitting it encodes a binary zero, and (ii) its easy realization via low-power and low-cost electronics for GW inspection. Therefore, it is usually applied in combination with frequency multiplexing techniques to allow concurrent transmissions

<sup>2</sup> Considering that the thickness is constant, an increase in frequency-thickness product actually corresponds to an increment in the central frequency of the actuation signal

from multiple users operating in different, well-separated bands of the spectrum. For example, in [216], the impact of structural damage on the communication quality employing OOK in presence of multi-modal Lamb waves has been studied numerically as well as experimentally. In [217], successful transmission of digital data by using the same OOK scheme has also been demonstrated for two spatially separated planar waveguides. A correlation-based OOK approach has further been tested in rather complex technical components, such as a composite helicopter rotor blade and a sandwich panel [218]. In [219], wireless delivery of encoded information through a glass-fiber reinforced polymer planar waveguide has been studied by a combination of time-domain OOK and FDM schemes. A recent research work also includes a medical application: in [250], the transmission of fracture-related information is discussed, where data from a transducer fixed to the surface of a bone is sent to an acoustic receiver located externally on the skin surface. In [251], OOK and its variants have been tested utilizing a variety of solid channels, including blocks, plates, and pipes.

Moreover, a low-rate communication approach using chirped OOK has also been investigated for communicating digital data across a cylindrical structure [223]. In this case, chirp signals are employed in place of pure sinusoidal bursts to increase the SNR in the acquired signal and, thus, maximize the probability of bit recovery at the receiving side.

Despite the promising results, the frequency multiplexing strategies reported above are not advantageous in terms of spectral efficiency, since they might require large guard bands between the different modulation frequencies, necessary to minimize the probability of mutual interference. As such, researchers started to investigate Orthogonal Frequency Division Multiplexing (OFDM), a technique that can achieve higher data rates thanks to the exploitation of densely arranged and closely orthogonal sub-carriers. Typically applied for data transmission through thin walls, bit-rates up and in excess of 1 M achieved via OFDM are really promising for GW-based digital data transfer. However, it is important to underline that these high-rate performances are largely due to the very short communication distances involved in the application scenario (see [226]–[228]), a quantity which amounts to less than 10 cm. Proof is the fact that, when tested on longer propagation channels, bit-rates comparable to the ones scored by standard frequency multiplexing have been measured [225], [229].

Relevant research concerns the combination of Pulse Position Modulation, where the time delay between pulses bears information, and time reversal processing [237], which is able to compensate for dispersion and multiple wave modes. Such approach has been deployed for ultrasonic information transmission through one-dimensional waveguides [235], [252] consisting of multi-wire cables, steel pipes and bars, reaching a satisfying performance in the order of 500 bps for 4 m communication distance.

More recently, novel investigations have been conducted aiming at overcoming one of the most critical issues in presence of multi-actuating/receiving nodes, namely crosstalks between active transducers. To this end, node-to-node communication across a metallic plate has been simulated numerically in [240], where single-mode Lamb waves have been employed for parallel transmission of encoded information from multiple piezoceramic transducers by combining phase modulation (i.e., Code Division Multiplexing) with software codeword-based multiplexing. To counteract the detrimental dispersive behavior, dispersion compensation techniques have been applied to the measured signals before decoding the transmitted information. Additional calculations have been performed to investigate the aforementioned communication scheme in a tapered waveguide [239] and

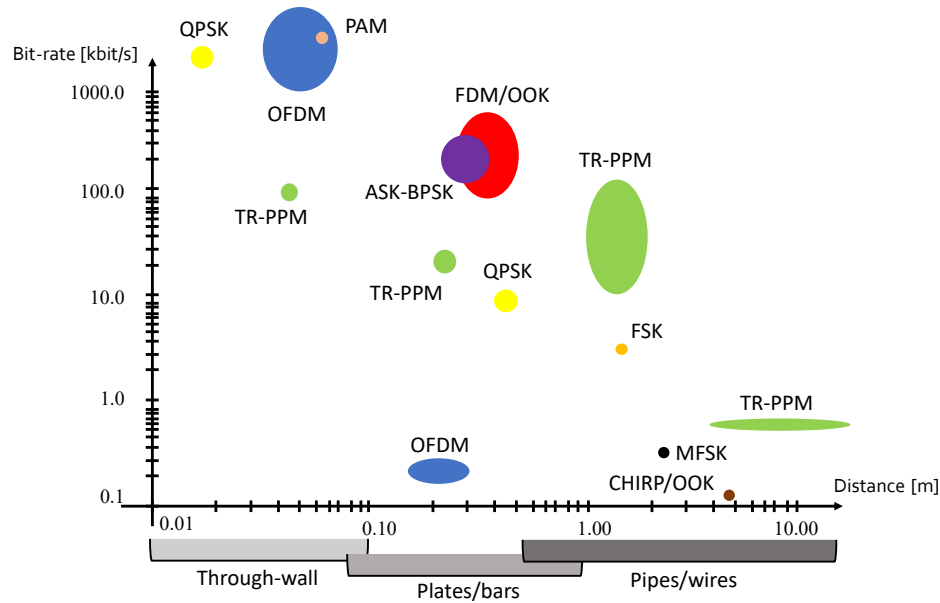


Figure 65: Performance comparison of GWs-based communications systems

proof-of-principle (PoP) experiments with/without dispersion compensation have been carried out for an aluminum plate in [253]. Noteworthy, validation of digital communications based on code multiplexing with real-field data is still missing and, thus, it represents an open field of research.

The list of explored techniques also comprises Pulse Amplitude Modulation (PAM) [242], in which the digital message is encoded in the amplitude of the transmitted pulses, and Frequency Shift Keying (FSK) or multitone FSK [243], [244], the latter making use of one or multiple frequency tones alternated, in time, depending on the binary information to be transmitted. Furthermore, particular attention deserves the application of amplitude (Amplitude Shift Keying (ASK)) or phase modulations, the latter being either Binary Phase Shift Keying (BPSK) or Quadrature Phase Shift Keying (QPSK), which offer a simple means for bit encoding via progressive shifts in the phase of the modulation signal. The reported transmission rates range from dozens to hundreds of kbps, depending on the travelled distance.

For the sake of global evaluation and aiming at offering an immediate graphical understanding about the performances of the currently available solutions for GW-based data communication, the distance/rate performance plot displayed in Fig. 65 has been extracted from Table 20. As can be observed, performances scales with the communication distance and, consequently, with the dimensions of the structure to be monitored. More specifically, it is worth noticing that, even if OFDM is very effective for through-wall communication, i.e. for distances below 10 cm, the trivial OOK or its amplitude/phase variants are more competitive when moving to planar waveguides characterized by communication distances below 1 m. Alongside, the focusing effect of time reversal demonstrated to be a robust and performative strategy for longer transmission channels (even more than 10 m) that are demanded in case of pipes or industrial cables and, thus, are inherently affected by a more pronounced dispersive behavior.



Table 20: State-of-the-art of the most significant techniques employed for GWS-based digital data communication with highlighted characteristics and reported performances (column "C" indicates whether compensation procedures are encompassed).

Technique	Characteristics	Tested setup & performance				
		C	Scenario	Dist	Bit-rate [kbps]	Ref
FDM/OOK	<ul style="list-style-type: none"> <li>- Impulse response estimation: tone-burst excitation from TX to RX</li> <li>- Bit encoding: 1 → pulse transmission, 0 → pulse omission</li> <li>- Matched filter: cross-correlation between received signal and impulse response</li> <li>- Bit decoding: cross-correlation thresholding and PP: 1 ← value above threshold, 1 ← value below threshold</li> </ul>	✗	Exp: aluminum plate	0.5 m	100	[215]
		✗	Exp: aluminum plate	0.25 m	120	[216]
		✗	Exp: two bridged aluminum plates	0.5 m	60	[217]
		✗	Exp: helicopter blade segment, small-scale grouted joint of wind plant, sandwich structure	0.3 m	158.3	[218]
		✗	Exp: CFRP plate	0.4 m	112	[219]
		✗	Exp: aluminum plate	0.6 m	100	[220]
		✗	Exp: glass plate	1 m	1.5	[221]
Chirp/OOK	Analogous to FDM/OOK, but employing chirp signals in actuation	✗	Exp: cylindrical bridge	53 m	-	[222]
		✗	Exp: cylindrical pipe	4.8 m	0.1	[223], [224]
OFDM	Discrete multi-carrier modulation to counteract multi-path fading	✗	Exp: drill string	0.3 m	0.2	[225]
		✓	Exp: steel barrier	0.04 m	1 M	[226]
		✗	Exp: steel wall	0.06 m	17.37 M	[227]
		✗	Exp: naval bulkhead	0.06 m	14 M	[228]
		✗	Exp: aluminum bar	0.32 m	200	[229]
TR-PPM	<ul style="list-style-type: none"> <li>- Impulse response estimation: tone-burst excitation from TX to RX</li> <li>- Bit encoding via time-reversed channel response: 1 → transmission of time reversed signal delayed in time, 0 → transmission of time reversed signal without delay in time</li> <li>- Matched filter between received signal and impulse response</li> <li>- Bit decoding: non coherent energy detector</li> </ul>	✗	Exp: multi-conductor cable	30 m	0.47	[230]
		✓	Exp: carbon steel pipe, stainless steel pipe	0.04 m	100	[231]-[233]
		✗	Exp: galvanized steel pipe	3 m	0.067	[234]
		✗	Exp: multi-wire cable	4 m	0.5	[235], [236]
		✗	Exp: carbon steel pipe specimen	1.5 m	100	[237]
		✗	Exp: flat aluminum bar	0.3 m	20	[238]
CDM	<ul style="list-style-type: none"> <li>- Sender-specific codeword</li> <li>- Multiple transmitters at the same time without interference</li> </ul>	✓	PoP: tapered steel rod	2 m	-	[239]
		✓	PoP: aluminum plate	0.3 m	-	[240]
		✓	Exp: aluminum plate	0.5 m	-	[241]
PAM	Pre-distortion filter to suppress echoes and destructive interferences at the receiver	✓	Exp: steel pipe	0.64 m	5 M	[242]
FSK,MFSK	Different combinations of multiple carrier frequencies to exploit full bandwidth	✓	Exp: shipping container	2.16 m	0.36	[243]
		✓	Exp: gas pipe	1.1 m	-	[244]
ASK, BPSK, QPSK	Simple modulation approach	✗	Exp: aluminum plate	0.3 m	100	[245], [246]
		✗	Exp: aluminum bar	0.5 m	12.5	[247]
		✗	Exp: aluminum plate	0.3 m	181.82	[248]
		✗	Exp: stainless steel plate	0.02 m	1 M	[249]



## FREQUENCY DIVISION MULTIPLEXING FOR LOW-POWER MIMO COMMUNICATION AT THE EDGE

---

### ABSTRACT

*This Chapter demonstrates the use of GWs for multiple-in and multiple-out (MIMO) data communications basing on an edge implementation of the Frequency Division Multiplexing technique combined with square-wave excitation. The proposed solution enables the parallel emission from multiple, low-voltage, distributed nodes without interference thanks to a spectrum-based encoding procedure. Wireless exchange of encoded information across a metallic plate and a stiffened carbon-fiber reinforced plastics structure is investigated to verify the attainable transmission rates.*

The content of this Chapter is based upon the research works [P18]–[P20]:

"Low-Power MIMO Guided-Wave Communication" by Kexel, C., Testoni, N., Zonzini F., Moll, J., and De Marchi L. In *IEEE Access*, vol. 8, pp. 217425-217436, 2020. ©2020 IEEE

"Guided-wave MIMO communication on a composite panel for SHM applications", by Zonzini, F., De Marchi, L., Testoni, N., Kexel, C. and Moll, J. In *Proc. SPIE 11381, Health Monitoring of Structural and Biological Systems IX*, 1138136 (8 May 2020).

"A Structural-Aware Frequency Division Multiplexing Technique for Acoustic Data Communication in SHM Applications", by Zonzini, F., De Marchi, L., Testoni, N., Kexel, C. and Moll, J. In *Rizzo P., Milazzo A. (eds) European Workshop on Structural Health Monitoring. EWSHM 2020, Lecture Notes in Civil Engineering*, vol 127. Springer, Cham.<sup>1</sup>

from which part of the text is drawn.

### 9.1 INTRODUCTION

Multiple-In Multiple-Out (MIMO) systems are adopted when multiple users are active at the same time and communicate to several nodes in listening mode. MIMO is beneficial to increase the reliability/robustness of the communication with multiple links. Secondly, it enables increasing the amount of information that can be delivered in each time interval by using simultaneous transmission. To achieve such task while avoiding - or, at least, minimizing - unavoidable mutual disturbances between adjacent transmitters, either time division or frequency division multiplexing techniques are required.

The first scenario divides the time axis in different slots, one per transmitting node, allowing only one sensor at a time to take full control of the channel bandwidth. Despite its simplicity, this multiplexing scheme is inapplicable in dense sensor networks, since the

---

<sup>1</sup> Adapted by permission from Springer Nature Customer Service Centre GmbH: Springer Nature, Lecture Notes in Civil Engineering, A Structural-aware Frequency Division Multiplexing Technique for Acoustic Data Communication in SHM Applications, ©2021.

implied latency might become incompatible with the admissible duty-cycles. Conversely, the rationale behind Frequency Division Multiplexing (FDM) is to allocate a specific frequency band to each emitter of the network for communicating, in parallel, at multiple carrier frequencies. In this case, all the nodes of the network are active simultaneously and, thus, specific policies need to be put in place to counteract operative interferences and regulate access to the shared communication channel.

## 9.2 PHYSICS-INFORMED CARRIER FREQUENCY SELECTION

The explored FDM approach assumes carrier-related information to be sent in the form of rectangular digital pulses, actuated as square-wave excitation sequences. This actuation mechanism has been preferred over more sophisticated techniques to be compatible with the self-generation functionalities of custom signals that are available in embedded low-cost transducers.

Driven by this paradigm, a novel on-off keying modulation mechanism has firstly been proposed in [P20] by assigning to every device in transmission a unique set of carrier frequencies, each of them in a one-to-one correspondence with one delivered bit. As such, transmitting at a certain frequency encodes the binary value '1', while omitting transmission at this frequency represents the binary value '0'. Therefore, the entire message that a single node can transmit derives from the linear superposition of several single carrier excitations. Correspondingly, the decoding procedure at the receiving node can be simply accomplished by probing for the absence or presence of a particular carrier frequency within the spectral content of the acquired signals. If the intensity in the surrounding of the carrier is higher than the noise level, then the value '1' is considered, otherwise the binary value '0' is assumed. The aforementioned superposition can either be realized mathematically when a single actuator emits the already-completed superposition, or it can be realized physically by a multi-channel actuator that is fed independently by multiple single-carrier signals.

To summarize, the complete FDM-based communication system so far designed includes the following three phases: (1) *actuation*, performed by TX nodes which send a specific digital message encapsulated in form of elastic waves, (2) *propagation*, i.e., the excited GWs travel along the mechanical waveguide and (3) *decoding*, charged to the RX nodes which passively collect and analyse the input signals by sensing its spectral content.

To maximize the probability of correct reconstruction and ease the decoding process at the receiving side, the selection of the optimal carriers plays a crucial role. As far as GWs-based digital communication systems are considered, this step becomes even more crucial since elastic waves are inherently subjected to a dispersive propagation pattern. Hence, a carrier frequency selection procedure has been specifically suggested in [P19] to maximize the energetic content of each transducer-related message.

In case of GW-based communication system, a reasonable means to address all these issues is to exploit the physical bandwidth of the mechanical waveguide itself, namely its eigenmodes, since the associated frequency bands represent the topmost energetic channels and, thus, suffer from minor dissipation while propagating. In this sense, the selection procedure is *physics-informed*. Noteworthy, this choice has the additional and non-negligible benefit of reducing the power consumption of the electronics since less energy is required in actuation to travel the same distance.

Two different approaches were found to be compatible with energy efficient data communication, which will be referred to as *model-assisted* and *empirical* approach, respectively:

- *Model-assisted* approach: this carrier selection method encompasses the exploitation of numerical or analytical models to predict the eigenmodes of the mechanical waveguides of the structure. This solution is applicable whenever the structural, mechanical, and geometrical properties are very well known and easy to be modeled via software.
- *Empirical* approach: this strategy requires empirical data gathered at the network start up, during a preliminary calibration phase, to estimate the carriers experimentally. In this case, a couple of TX–RX nodes equipped with embedded signal processing functionalities is sufficient. More specifically, the method consists in transmitting, repeatedly, pseudo–random digital sequences from the active TX node to the passive RX transducer: since the spectral profile of a pseudo–random signal, namely the injected signals in this case, is approximately white in the frequency band of interest, this means that the spectral content of the received signals tends to coincide with the transfer function of the structure itself. The most energetic peak–related frequencies appearing in this spectrum can be taken as proxies of the structural eigenmodes.

### 9.2.1 Joint optimization of the square–wave excitation–sequence length

The switching actuation is computationally advantageous but responsible for the generation of odd–numbered harmonics besides the fundamental one, the presence of which must be considered by tackling both their vicinity to the carrier and their spectral intensity, since they might constitute an additional source of interference.

To cope with this issue, the highest carrier frequency must lie below the second harmonic of the lowest carrier and it is, in turn, completely determined by the square–wave excitation–sequence length. Thus, an appropriate tuning of this parameter is of the utmost importance to limit the effect of the spurious components: the optimization procedure presented in [P20] specifically tries to solve this problem and can be summarized as follows.

Let's assume  $K$  transmission channels are active, each  $k$ -th communication link is characterized by a sequence length  $L_k$  defined by the number of times one rectangular pulse of duration  $t_k$  and dubbed pulse width is repeated. Hence,  $L_k$  coincides with the number of excitation cycles of a conventional tone–burst if sinusoidal actuation would have been considered. Assuming that waveforms are produced with a constant duty cycle of 50%, the total excitation–sequence duration is  $T_k = 2t_k \cdot L_k$ .

Two fundamental hypotheses can then be introduced, namely:

1. two distinct sequences  $L_h, L_k$  possess identical duration  $T^2$ , a crucial condition to be guaranteed for communication scenarios where a global clock or synchronization mechanism is desired;
2. the distance between two successive carrier frequencies is constant, which is necessary to prevent the optimization problem to be overdetermined.

<sup>2</sup> Since  $T_h = T_k \forall h, k$ , the index is dropped and the time duration is simply referred to as  $T$ .

Hence,  $f_k = \frac{F_s}{T} L_k$  holds, where  $F_s$  is the sample rate. Since  $F_s$  and  $T$  are constant quantities common to all the communication links, it can be deduced that the  $k$ -th carrier frequency is uniquely derived once  $L_k$  is determined. To this end, the optimal set of excitation–sequence length can be estimated as those values corresponding to the minimum sequence duration  $T$  concurrently allowing for the minimization of the maximal sequence length  $L_k$  related to the highest harmonic.

Among the multiple sets of excitation–sequence lengths satisfying this condition, the one allowing the associated carrier frequencies to be proximal to the numerically estimated or experimentally retrieved eigenmodes can be finally selected.

### 9.3 EXPERIMENTAL VALIDATION

Hereinafter, the experimental results obtained for the near–sensor implementation of the investigated FDM technique are presented, pursuing the following three objectives:

1. Assess how the selection of the proper set of carrier frequencies may impact on the quality of the received signals, while exploring different mechanical waveguides. According with the spectrum–driven reconstruction procedure, rigorous quantification of this aspect has been achieved by computing the inactive/inactive ratio

$$r_k = \frac{S_k^{IA}}{S_k^A}, \quad k \in 1, \dots, K \quad (50)$$

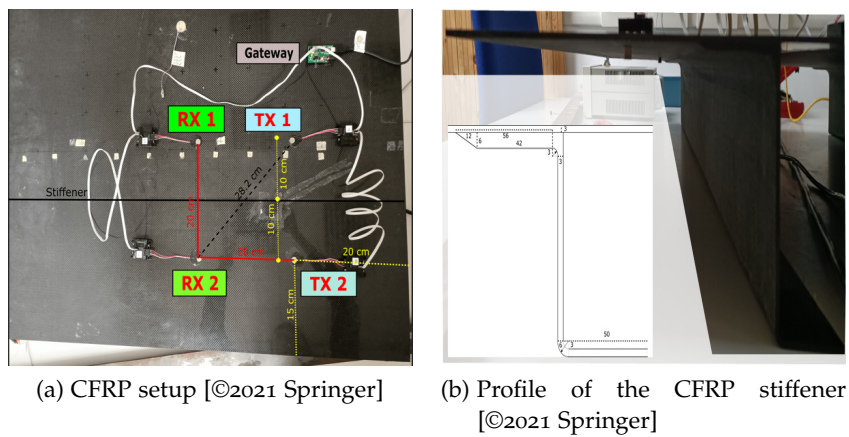
which evaluates the ratio between the spectral intensities at the carrier peak values when the  $k$ -th channel is inactive ( $S_k^{IA}$ ) over the ones measured in active ( $S_k^A$ ) configuration. The lower the  $r_k$ , the higher the carrier identification capability becomes and, thus, the quality of the reconstructed bit value. The rationale for exploiting this metric is that, when the optimal set of structural–driven carriers is selected, the spectral efficiency increases and a lower value of the spectral ratio should be computed.

2. Investigate the bit reconstruction performance as a function of the excitation–sequence length. The Bit–error rate (BER)

$$\text{BER} = \frac{N_{\text{Err}}}{N_{\text{bit}}} = \frac{\sum_{i=1}^{N_{\text{bit}}} b_i \oplus \hat{b}_i}{N_{\text{bit}}} \quad (51)$$

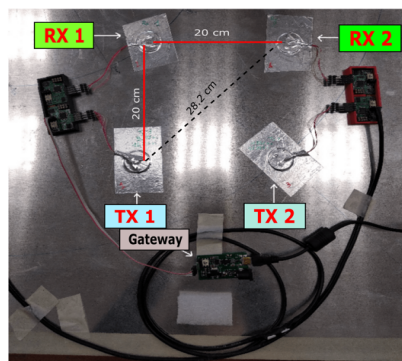
has been taken as figure–of–merit to quantify the bit recovery accuracy between the total number of transmitted ( $N_{\text{bit}}$ ) and mis–classified ( $N_{\text{err}}$ ) bits for a generic channel;  $\oplus$  represents the bit–wise xor operator. For the implemented FDM scheme, a proper spectral threshold is required to discriminate between the logic value ‘1’ and ‘0’ and, thus, to count falsely classified bits.

3. Evaluate the robustness of the bit–reconstruction method with respect to structural complexities and/or irregular designs, where anisotropy, strong attenuation and mode conversion might play a crucial role.



(a) CFRP setup [©2021 Springer]

(b) Profile of the CFRP stiffener [©2021 Springer]



(c) Aluminum plate setup [©2020 IEEE]

Figure 66: Experimental setup and relative communication distances: top (a) and (b) lateral view of the CFRP with highlighted stiffener geometry; top view of the aluminum plate.

### 9.3.1 Materials and methods

Two geometrically equal square plates (1000 mm wide and 3 mm thick), one is a metallic component made of aluminum (Al, Fig. 66c) and the other one a stiffened Carbon-fiber reinforced plastics (CFRP) (Fig. 66a), were instrumented with a small MIMO communication network of ISSLab piezoelectric sensor nodes. While the geometry of the metallic plate is regular, two stiffener elements are placed in longitudinal direction in the CFRP structure, at a distance of 150 mm from the left and right border, respectively (see Fig. 66b).

The network comprises a couple of ISSLab transmitter nodes (TX1 and TX2) and two receiver nodes (RX1 and RX2) arranged in a 20 cm squared configuration. Indeed, owing to the three-channel connectivity offered by a single sensor board and the presence of all the circuitry necessary for the low-voltage excitation and acquisition of the electric signals, these devices served as ideal prototyping boards for MIMO scenarios in a compact and energy efficient manner. To fully exploit the multi-drop capabilities of these sensors, a custom sensing unit consisting of a single multi-channel PZT disc with three active regions [254], as the one introduced in Section 7.3.2.1, was connected to the three different connectors of the sensor node.

The sensor nodes were configured as follows. Two channels for each transmitter node were used to excite as many different carrier frequencies by means of rectangular digital

pulses, while receiver nodes were programmed to simultaneously acquire 3000 samples at a sample rate of 500 kHz (i.e., acquisition window of 6 ms).

### 9.3.2 Carrier frequency selection

In this experiment, linear superposition of effects was leveraged to inject in the structures up to four different signals at a time, spanning  $2^4 = 16$  different bit combinations (i.e., 16 possible damage-related messages). Each test was repeated 10 times to assess the robustness against noise and jitter. The burst excitation-sequence length were, instead, estimated by solving the combinatorial problem in [P20], yielding to  $L_k = \{10, 12, 15, 18\}$  as candidate set of optimal excitation-sequence lengths.

As a general outcome, by exploiting the amplification stage embedded into the ISSLab receiver nodes and carefully choosing the transmitted carrier frequencies, a peak-to-peak voltage of 387 mV was measured in the received signal in correspondence of an actuation peak-to-peak voltage of 3.3 V. The amplitude of the excited pulses exactly corresponds to the aforementioned voltage value. In the absence of any transmitted signal, the maximum peak-to-peak voltage of the received signals was 6.03 mV.

#### 9.3.2.1 Aluminum plate

The isotropic nature of the aluminum material made the development of a numerical model an affordable task. Therefore, a model-assisted approach implemented via the COMSOL® software package was employed for the computation of the eigenmodes of the plate. This simulation returned  $\lambda_1 = 9.8$  kHz,  $\lambda_2 = 14.3$  kHz,  $\lambda_3 = 18.1$  kHz as the first three mechanical wavemodes. Knowing this, the approach described in Section 9.2.1 led to these four carrier frequencies:  $f_{1,1}^A = 9.89$  kHz,  $f_{1,2}^A = 14.82$  kHz,  $f_{2,1}^A = 11.85$  kHz,  $f_{2,2}^A = 17.78$  kHz. In the above notation, the subscript  $n,k$  stands for transmitting node  $n \in \{TX1, TX2\}$  and channel number  $k$ , respectively.

#### 9.3.2.2 CFRP structure

Since the inherent complexity of the CFRP structure makes the numerical study of the eigenmodes a challenging and time-consuming task, an empirical approach was conversely followed in this case. More specifically, exploiting the advantageous capability of the developed circuitry to generate custom signals, pseudo-random digital sequences were repeatedly transmitted by means of an active transducer operating at a symbol rate  $F_{sym} = 200$  kHz and recorded by a passive transducer operating at a sampling frequency  $F_s = 2$  MHz. The latter value was chosen to be sufficiently flat in the frequency band of 0-100 kHz, ensuring an oversampling factor of ten compliant with a Nyquist spectral window of 1 MHz. Assuming the same burst-excitation lengths mentioned before, the average spectrum obtained from 99 pseudo-random noise repetitions revealed the best suitable set of carrier frequencies to be located at  $f_{1,1}^C = 10.70$  kHz,  $f_{1,2}^C = 12.84$  kHz,  $f_{2,1}^C = 16.00$  kHz,  $f_{2,2}^C = 19.25$  kHz.

To demonstrate how communication performances may deteriorate as a consequence of non adequate transmission channels, additional tests were performed for the CFRP component, in which the sensors in actuation were configured via the same set of carrier frequencies estimated for the aluminum setup. For the sake of clarity, the labels 'Non Opt'



Table 21: Comparison of normalized spectral intensity [ $V^2/\text{Hz}$ ] that is accumulated in a bin (width 2 kHz) around the carrier frequencies at both receivers. Besides the metallic (Al) plate, two sets of communication channels are considered for the CFRP element, one for the optimal (Opt) and one for the non optimal (Non Opt) set of carrier frequencies. [©2021 Springer]

	Al				CFRP Non Opt				CFRP Opt			
	$f_{1,1}$	$f_{2,1}$	$f_{1,2}$	$f_{2,2}$	$f_{1,1}$	$f_{2,1}$	$f_{1,2}$	$f_{2,2}$	$f_{1,1}$	$f_{2,1}$	$f_{1,2}$	$f_{2,2}$
$S_k^A$	0.09	0.08	0.12	0.07	0.04	0.05	0.08	0.23	0.01	0.02	0.03	0.01
$S_k^A$	0.63	0.55	0.43	1.00	0.07	0.06	0.14	0.52	0.06	0.16	0.41	0.21
$r_k$	0.14	0.15	0.29	0.07	0.52	0.76	0.57	0.43	0.17	0.02	0.07	0.05

and ‘Opt’ will be employed in the following result section to indicate the two distinct cases.

### 9.3.2.3 Results

Obtained  $r_k$  values are reported in Table 21, which compares the spectral intensity accumulated in a frequency bin of 2 kHz around each carrier at both receivers [P19].

As a general remark, the analysis illustrates that sharp discrimination can be achieved between active and inactive channels only if a physics-informed set of carrier frequencies is selected. This is demonstrated by very well pronounced spectral amplitudes characterized by a low inactive-active ratio below 0.5 for both the Al plate and the CFRP configured on their relative set of best carriers. Conversely, the same condition does not apply for the CFRP when a bad choice of the carriers is assumed, as proven by  $r_k$  values consistently above or in the proximity of 0.5.

For the sake of a comparative analysis between the two different structures, Fig. 67 depicts exemplary spectra of the normalized intensity of the GWs arriving at the receiving nodes (the intensity recorded at RX1 and RX2 are summed to provide a cumulative understanding) for a complementary set of messages: 1011 in the first row and 0100 in the second one. As can be noticed, the intensity received in the CFRP case is reduced as compared to the aluminum plate due to the stronger attenuation in the waveguide.

Even though the received intensity is lessened in the CFRP panel (as justified by a comparison of the spectral magnitudes of Fig. 67d-67b opposed to those of Fig. 67a-67c, the bit reconstruction (in terms of a lower inactive-active ratio in Table 21) can nevertheless be sharper than in the aluminum plate for certain carrier frequencies (i.e.,  $f_{1,2}$ ).

### 9.3.3 Impact of structural irregularity

The effects of the stiffening elements on the TX-RX communication link have been appraised for the CFRP test-bed. To this end, besides the sensor setup shown in Fig. 66a (Conf A), where one receiving and one transmitting node per side are placed with respect to the stiffener element, an alternative sensor configuration (Conf B) was tested, in which the devices TX2 and RX1 were exchanged. In this setup, the actuators and receiver positions’ are decoupled with respect to the stiffening element itself such that all the communication paths encounter the same structural discontinuity. Noteworthy, this

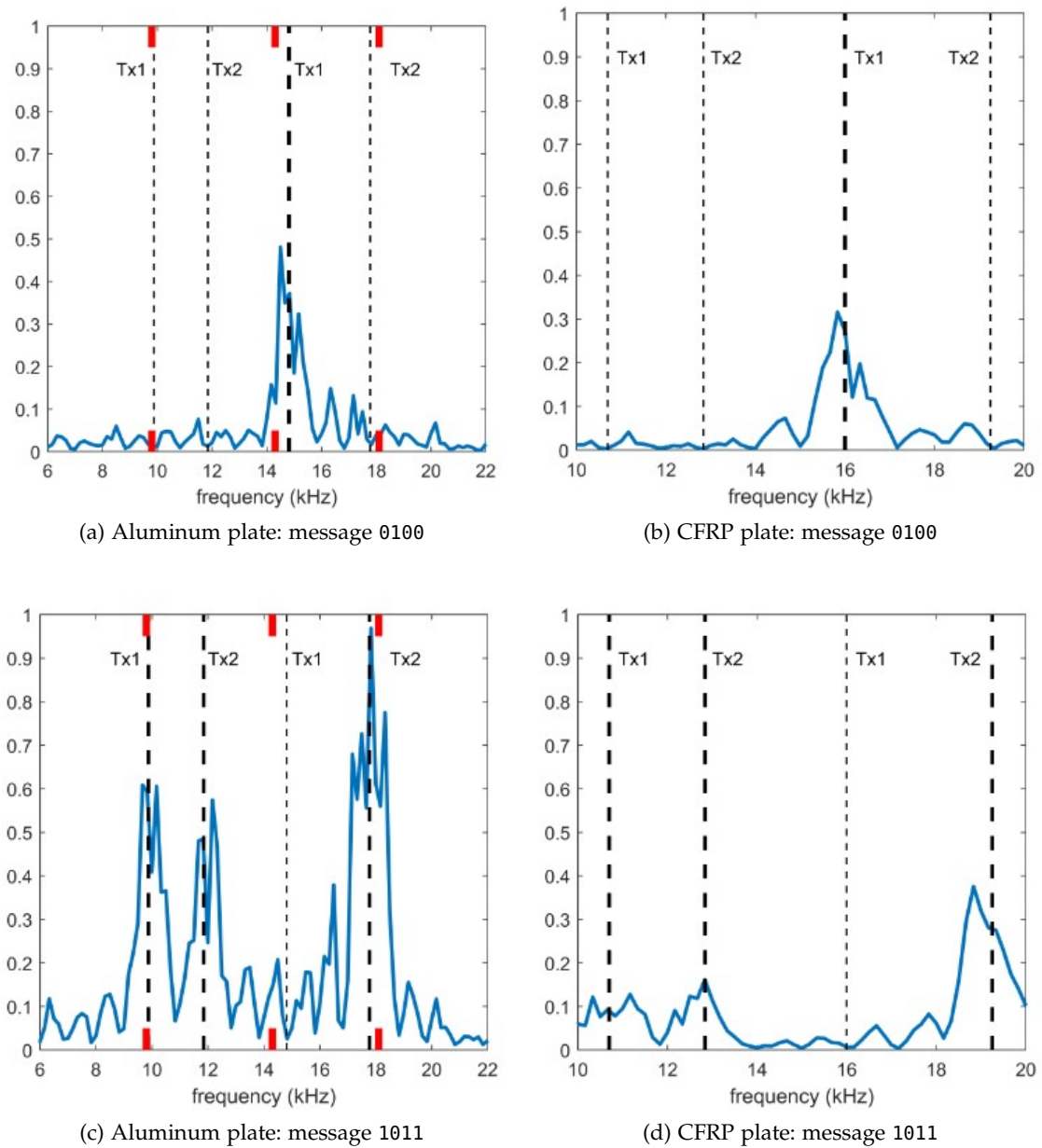


Figure 67: Spectra of the cumulative normalized intensity (arbitrary unit in the vertical axis) in the received signals and magnification with bold vertical lines indicating the selected frequency carriers. The transmission of two complementary messages is shown: 0100 and 1011 in the first and second line, respectively, while the column on the left is for the metallic plate and the one on the right pertains to the CFRP element. [©2020 IEEE]

architectural modification maintains unaltered the mutual communication distances and also permits the same set of previously estimated carrier frequencies to be reused<sup>3</sup>.

Results in terms of inactive/active ratio are given in Table 22. In the second case (Conf B), the cumulative average spectrum between the two receivers was considered, since the

<sup>3</sup> Note that the frequency transfer function of the mechanical structure does not depend on the sensor arrangement. Moreover, Conf A already takes into account the presence of obstructed communication channels, i.e., RX<sub>1</sub>-TX<sub>2</sub>, RX<sub>2</sub>-TX<sub>1</sub>.

Table 22: Comparison of normalized spectral intensity [ $V^2/\text{Hz}$ ] that is accumulated in a bin (width 2 kHz) around the carrier frequencies at both receivers for the CFRP plate in two different configurations: setup A with receivers attached on two opposite sides with respect to the stiffener; setup B for receivers on the same side. [©2021 Springer]

	Conf B				Conf A: RX1				Conf A: RX2			
	$f_{1,1}$	$f_{2,1}$	$f_{1,2}$	$f_{2,2}$	$f_{1,1}$	$f_{2,1}$	$f_{1,2}$	$f_{2,2}$	$f_{1,1}$	$f_{2,1}$	$f_{1,2}$	$f_{2,2}$
$S_k^A$	0.06	0.02	0.04	0.03	0.02	0.05	0.02	0.01	0.01	0.02	0.03	0.01
$S_k^A$	0.12	0.14	0.29	0.40	0.03	0.64	0.06	0.31	0.06	0.16	0.41	0.21
$r_k$	0.50	0.14	0.14	0.08	0.69	0.09	0.33	0.03	0.17	0.02	0.07	0.05

position of the transmitter nodes is identical with respect to the stiffener. Conversely, the first sensor arrangement (Conf A) required the analysis to be performed independently to properly evaluate critical communication channels disturbed by the stiffener element.

As a general remark, the reported performance values corroborate the digital communication capability of the system, as witnessed by inactive–active ratio always below 0.5 apart from the isolated case of frequency  $f_{1,1}$ . Two additional considerations are necessary. The first concerns the impact of the geometrical discontinuity, which hampers the direct communication path. Prove is the fact that an order of magnitude in the ratio exists among line–of–sight and obstructed communication distances. Secondly, the attenuation is not uniformly distributed between the chosen carriers; this result may be reasonably addressed to their different energy content as a consequence of higher proximity to the real eigenmodes of the structures.

#### 9.3.4 Impact of excitation–sequence length on the bit reconstruction accuracy

Bit reconstruction, namely the discrimination between a communication link that is on versus a link that is off, is another crucial functionality to be assessed also against varying length of the square-wave excitation signal [P20]. To investigate these aspect, an entire signal length of 6 ms was initially assumed: this duration corresponds to a data rate  $F_g$  of 0.17 kbps per frequency, if one follows the approach to encode a bit in the time domain through temporal activation or deactivation of a certain carrier. This means that, if a carrier frequency of 9.88 kHz is chosen and the excitation length is 6, the actuation of one bit solely spans 0.607 ms. Increasing the data rate by reducing the processed signal duration, accordingly deteriorates bit reconstruction, because each bit is contaminated with the signal intensity stemming from the late signal content of the previous bits.

In the computational analysis of the BER versus the excitation–sequence length, the processed signal duration was reduced to 1 ms, 2 ms and 3 ms and the spectral intensity around each carrier was contaminated artificially with the late signal content of the preceding bits. For each receiving node, each of its channels and also each carrier, a subset of 3200 combinations of preceding bits was sampled randomly from the available experimental data which contain all possible active/inactive channel combinations.

In Fig. 68a, an average BER calculated from the four measured carriers is given as a function of the sequence length (horizontal axis) and data rate per frequency (3 different curves; see legend). It can be observed that, especially for the higher data rates, the BER increases as the excitation length increases, because the prolonged excitation creates an additional overlapping contribution into subsequent bits. Nevertheless, the graph shows

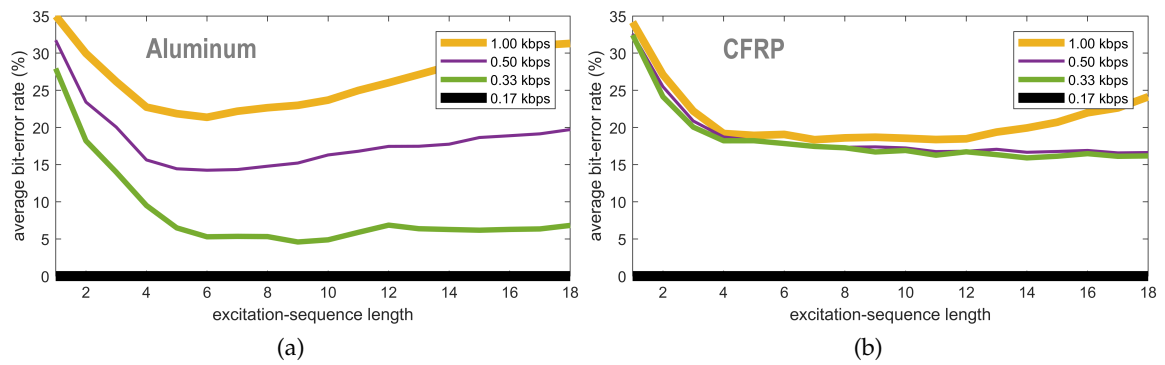


Figure 68: Average BER as a function of excitation–sequence length and data rate per frequency for the (a) aluminum and (b) CFRP structure. [©2020 IEEE]

that, in both structures, error–free communication is possible at a data rate of 0.17 kbps per carrier.

Basing on the empirically determined set of carriers, the length–dependent BER analysis was carried out also for the CFRP structure (see Fig. 68b). Above a data rate of 0.17 kbps, the BER increases abruptly for all excitation lengths. When compared to the aluminum case, the BER does not exhibit such a significant dependence on the data rate, because those upper three curves lie rather close to one another. Despite its complexity, for the highest and second highest data rate (1.00 kbps and 0.17 kbps), the CFRP performs similarly or sometimes better than the isotropic metal plate.

To summarize, for the considered frameworks, the implemented FDM technique can be efficiently used for digital communication up to a data rate of 0.17 kbps, which is compliant with the considered SHM scenario, where the transmitting nodes should exchange only small piece of information, i.e., numerical values or damage indicators. Moreover, it is worth considering that such a data rate was achieved with a minimal power consumption of 224 mV, which is a considerable gain with respect to the common energy drawn by electromagnetic–based data communication systems. As a final comment, it is worth stressing that the indicated data rates represent data rates per frequency, which means that the actual data rates may be escalated by increasing the number of utilized carrier frequencies.

#### 9.4 CONCLUSIONS

The parallel transmission of information across structural components using FDM is discussed in this Chapter, allowing for communication of multiple transmitting nodes with a satisfying data rate of 0.17 kbps. The presented approach relies on the transmission of digital messages actuated in form of square–wave sequences, since these can be readily realized with energy–aware hardware. A specific procedure for the estimation of the optimal excitation–sequence length was proposed to ensure reliable communication and avoid interferences. Finally, the importance of adopting a physics–informed methodology for the selection of the proper carrier frequencies, as well as the possible presence of mechanical irregularities in the propagation path, were also investigated.

## DIRECT SPREAD SPECTRUM MODULATION AND DISPERSION COMPENSATION FOR GWS-BASED COMMUNICATION

---

### ABSTRACT

*The objective of this Chapter is to overcome the mutual interference between active transmitters by resorting to Code Division Multiplexing (CDM) techniques which grant the best compromise between channel availability while transmitting and defect resolution while performing structural inspection. Moreover, a simple yet effective dispersion compensation algorithm is also encompassed in order to counteract the detrimental effects due to multi-path fading and those associated to dispersion and multi-modal propagation. A preliminary experimental campaign conducted on a slender aluminum beam validates the feasibility of the approach.*

The content of this Chapter is based upon the research work [P21]:

"Direct Spread Spectrum Modulation and Dispersion Compensation for Guided Wave-based Communication Systems" by Zonzini F., De Marchi L., Testoni, N. and Marzani, A. In *2019 IEEE International Ultrasonics Symposium (IUS)*, 2019, pp. 2500-2503. ©2019 IEEE

from which part of the text is drawn.

### 10.1 INTRODUCTION

An effective GW-based communication system should tackle two main challenge: the former involves the requirement of advanced multiplexing strategies to limit crosstalk, the latter aims at compensating the intrinsic dispersive nature of elastic waves. As discussed in Section 9.1, the majority of the works demonstrating successful application of GWS-based communication systems substantially deals with time or frequency-division multiplexing schemes, which intrinsically imply a trade-off between the channel availability and the desired defect resolution. Alternatively, a recent and ready-to-be-investigated research direction concerns the adoption of Code Division Multiplexing (CDM) modulation schemes [241], [255], [256], whose main benefits stem from the full bandwidth allocated to each actuator throughout time. This is achieved via software by encapsulating each transmitter-related message via a unique coding sequence, or codeword, which ensures, in principle, perfect reconstruction after the decoding phase.,

An additional important aspect in GWS-based systems is related to the complicated propagation pattern experienced by the elastic waves. Indeed, it is worth recalling that Lamb waves are characterized by a multi-modal propagation profile, additionally subjected to beam spreading and dispersive phenomena exhibited as changes in group and phase velocity. These variations primarily derive from physical and in-operation working conditions even if the boundaries of the interrogated component may also induce multiple reflections in the recorded signals. Therefore, suitable mechanism capable of compensat-

ing such drifts are required for the efficient transmission of the encoded packets beyond the mere advantages of the modulation technique.

In this Chapter, the advantages of a CDM encoding mechanism for GWS-based digital communications are exploited, in conjunction with a spectrum-driven dispersion compensation algorithm to be applied in the post-processing phase, at the receiving side, to partially alleviate propagation-related drawbacks.

## 10.2 DEDICATED PROCESSING FLOW FOR CDM-BASED AND DISPERSION COMPENSATED TRANSMISSION WITH GWS

The dedicated processing flow necessary to implement the proposed CDM-based and dispersion-compensated communication system are introduced is schematized in Fig. 69.

### 10.2.1 Direct Spread Spectrum pulse coding

The adoption of ad-hoc encoding procedures is fundamental to preserve orthogonality between active transducers and consequently reduce their mutual interference. On top of that, a suitable CDM solution is provided by Direct Spread Spectrum (DSS) modulation.

As detailed in the yellow box of Fig. 69, given a sender-specific binary stream  $b_n$  generated at a data rate  $F_g$  (step 1), DSS encodes each bit with a sequence of  $L$  pseudo-noise (PN) chips produced at a chipping frequency  $F_{ch} = LF_g$  [257] (step 2.b). The sequences are generated such that the orthogonality property is preserved, i.e., the cross-correlation between two different PN code is null. Thereby, the modulating effect of the PN code spreads the energy of the transmitted signal over a substantially wider spectral band (step 2.a), increasing the equivalent bit-rate proportionally to the spreading factor  $L$  [258]. The resulting signal  $s_n$  to be transmitted consists of a phase-modulated sequence of bits actuated as an elastic wave. At the receiving node, after a mixture signal is acquired and purposely processed to compensate dispersion (step 3), the demodulation step can be performed by means of a matched filter [256].

In more detail, the received signal is firstly demodulated via correlation with a harmonic component tuned at the bit rate (step 4). Then, chip-wise integration (step 5) is necessary to transform the continuous signal in a digital stream of bits  $\tilde{s}_n^{(i)}$ . Once bits are converted, DSS demodulation takes place (step 6) by multiplication with the sender-specific chipping sequence; the demodulated stream is then passed to a sign detector block (step 7) to evaluate the polarity of the corresponding bits and the complete bit stream  $\hat{b}_n$  can finally be recovered.

Consequently, choosing the proper noise-like carrier code plays a crucial role to achieve ideally zero disturbance among different transmitting users. A general rule-of-thumb should prefer the adoption of highly uncorrelated sequences. In these cases, guarantees exist that, after de-spreading, the structural information sent by each actuator is protected [259] and can be correctly reconstructed. As demonstrated for classical CDM-oriented wireless communication systems, Gold, Kasami or Walsh codes are among the most effective strategies [260] to satisfy this requirement.

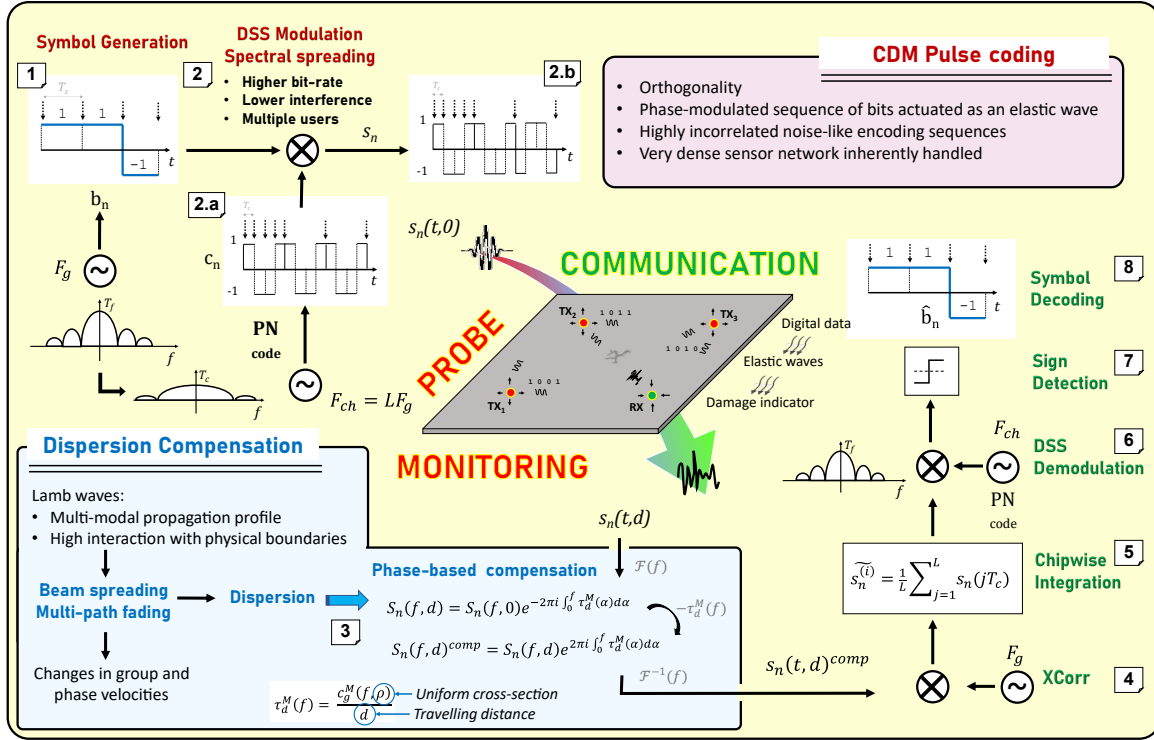


Figure 69: Overview of the processing flow adopted for CDM-oriented communication systems exploiting elastic waves. Beside modulation and demodulation steps which are performed according to classical DSS modulation principles, a compensation procedure is inserted to account for the detrimental effects of dispersion.

### 10.2.2 Dispersion compensation

Let  $s_n(t, 0)$  and  $s_n(t, d)$  describe, respectively, the coded waveform exciting the  $n$ -th piezoelectric transducer and the undamped  $M$  wave mode received at a distance  $d$ , traveling in a waveguide with uniform cross-section  $\rho$  and characterized by a wave group dispersion curve  $c_g^M(f, \rho)$ . The relation in the frequency domain between the two signals is:

$$S_n(f, d) = S_n(f, 0) e^{-i2\pi \int \tau_d^M(\alpha) d\alpha} \quad (52)$$

with  $\tau_d^M(f) = \frac{d}{c_g^M(f, \rho)}$  indicating the group delay.

The detrimental effects of the scattering phenomena act as a non-linear frequency term in equation (52), hindering the efficacy of the demodulating process independently from the adopted communication scheme. Accordingly, post-multiplying the phase spectrum of the received signal by an opposite term  $-\tau_d^M(f)$ , namely

$$S_n(f, d)^{comp} = S_n(f, d) e^{i2\pi \int \tau_d^M(\alpha) d\alpha} \quad (53)$$

might be considered as a simple, though effective counteracting solution.

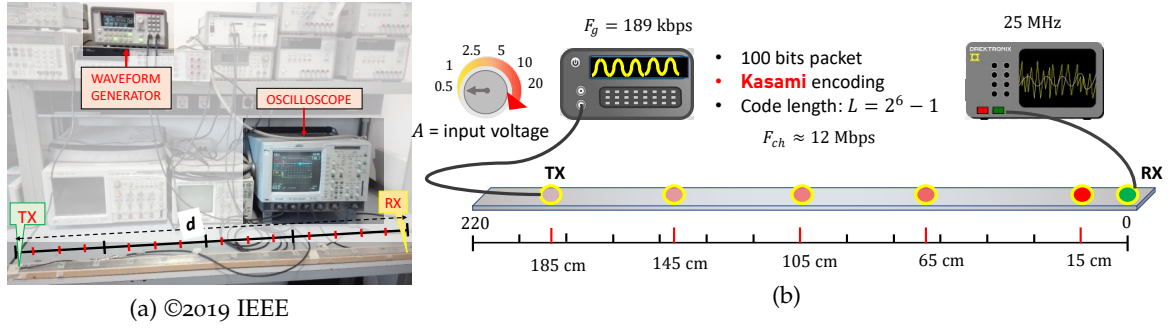


Figure 70: Experimental setup for CDM communication tests over a slender aluminum beam. Five different inter-communicating distances were considered, whereas the amplitude of the actuated signal was regulated by means of a waveform generator.

### 10.3 EXPERIMENTAL VALIDATION

An experimental proof-of-concept of the joint CDM-based and dispersion-compensated GWS-based communication system is discussed in this Section for the representative case of a slender aluminum beam.

#### 10.3.1 Materials and methods

The validation was performed on a 2000x35x2 mm thin aluminum beam instrumented with two commercial sensors (P-876 DuraAct Patch Transducers) glued on its surface and deployed in a transmitter-receiver (TX-RX) configuration. As shown in Fig. 70, the electronic equipment also comprised a waveform generator connected to the actuator node and operating at a data rate  $F_g = 189$  kbps. This carrier frequency for the ultrasound wave was experimentally determined during a preliminary analysis, in which successive sinusoidal signals, tuned on different frequency tones, were sent through the mechanical waveguide. In compliance with the Lissajous method [261], the frequency to be selected belongs to the configuration revealing the best input-output linear relationship, that is the frequency which carries most of the energy of the structure. Consequently, this choice minimizes the intrinsic wave attenuation.

The communication tests were instead executed by transmitting random packets of 100 spreaded bits encoded by Kasami sequences of length  $L = 2^6 - 1$ , thus ensuring good cross-correlation properties. Hence, modulated signals were sent according to an equivalent chipping rate  $F_{ch} \approx 12$  Mbps and finally sampled by means of an oscilloscope operating at 25 MHz. Demodulation was achieved by matched filtering the received data compensated for dispersion, once wave group dispersion curves were computed with the Semi-Analytical Finite Element method [262].

In detail, two main issues were addressed during the experimental campaign, analyzing how the energy of the actuated pulses and the inter-communication distances might affect the quality of the delivered information; BER was employed as a quantitative measure of these performances. To achieve this purpose, the transmission range was almost uniformly moved from 15 cm to 185 cm, while fixing the position of the RX device at one edge of the beam. Simultaneously, the amplitude of the pulsed signal was gradually increased from



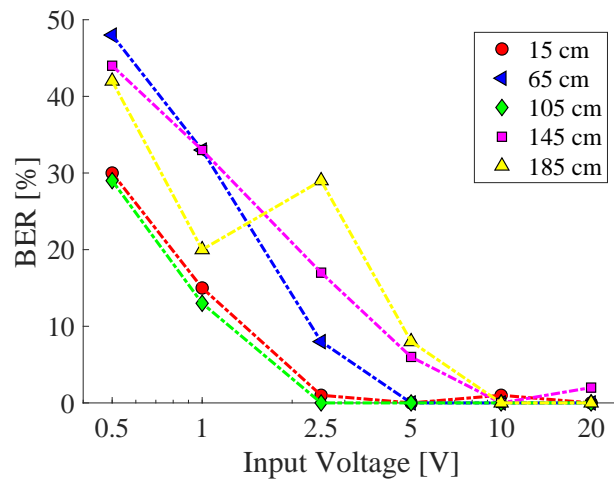


Figure 71: BER trends for the CDM-based and dispersion compensated communication scenario as functions of input voltages and distances. [©2019 IEEE]

0.5 V to 20.0 V, nearly doubling the level of the provided input at each step. To summarize, a total amount of five distances and six different voltages were globally investigated.

### 10.3.2 Results

Coherently with the kind of experiments, the first instance to be considered concerns the influence of the transmission range on the quality of the decoded signals. Results depicted in Fig. 71 pinpoint an almost linear dependency between BER percentages and communication distances. On the other hand, it is worth noticing that the error in signal reconstruction is extremely sensitive to the amplitude of the actuated pulses, BER values obeying to a nearly inverse proportionality as input energy drops below a minimum spatially-dependent threshold.

Performing a cumulative evaluation, the coherence of the obtained outcomes is theoretically supported by the linear dependency, in spectral domain, between the amplitude of the acquired signal and the energy of the transmitted one (see Equation (52)). As such, it is reasonable to witness an exponential deterioration in the performances of the system as the supplied voltage decreases. Fig. 72a confirms this experimental evidence being the SNR noticeably lower for low-level amplitude signals; hence, detecting the incident wave front becomes more difficult and, accordingly, it becomes more complicated to discern among meaningful information and noise.

Conversely, the exponential decay appearing in Equation (52) relates the spatial term to the amplitude of the wave mode via a non-linear operator, meaning that it is not possible to analytically derive or predict the correspondent effect on the quality of the digital communication. Moreover, the scenario in which communication quality worsens the longer the transmitting range does not hold for every inspected distance, as proven by reading the graph at constantly generated pulse magnitude.

For the sake of clarity, Fig. 72b reveals that, for 1 V input signals, a transmission range of 65 cm is not suitable due to the reduced SNR, which justifies the corresponding out-of-order BER. A feasible explanation for this evidence may be found in the detrimental interaction of the guided wave with the physical boundaries. Such interfering sources

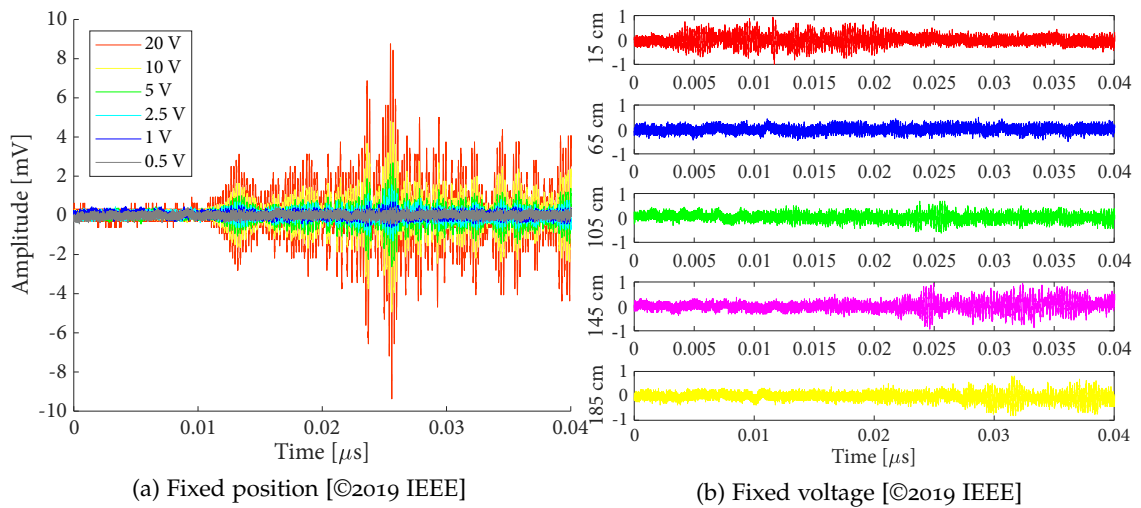


Figure 72: Received signals related to the transmission of a CDM-modulated single bit while (a) decreasing the amplitude of the actuated pulses with fixed communication distance of 105 cm and (b) increasing the inter-communication distance at a constant supplied voltage of 1 V.

can cause reflections and consequent destructive signal superimposition, which might be non negligible especially for a thin and tight structure like that considered. Therefore, certain TX-RX positions are intrinsically more favorable with respect to the mechanical and dispersion characteristics of the structure under test. It follows that, if the best system configuration is chosen, wider communication ranges can be covered with a lower input energy, without impinging upon the accuracy of the delivered information.

#### 10.4 CONCLUSIONS

This Chapter presented the mapping of the classical CDM modulating technique to GWS-based communication systems, precisely exploiting a spectral spreading technique which is beneficial in presence of multiple actuating nodes, since it reduces the mutual spectral interference among them. Additionally, in order to counteract the detrimental impact of dispersion resulting from beam spreading and reflections, a compensation procedure was encompassed before demodulating the received signals. An experimental validation of the proposed modulating scheme has been presented for a slender aluminum beam. Results proved that, when the proper network configurations are selected, even low-voltage power supply could be applied to travel long distances.

## LOW-DEPTH TIME REVERSAL AND PULSE POSITION MODULATION TECHNIQUE FOR ULTRASONIC COMMUNICATION

---

### ABSTRACT

*A strategy based on the the Time Reversal (TR) method is investigated in this Chapter to counterbalance the effects of reverberations and multi-path fading inherent to the dispersive nature of GWs, simultaneously compensating the operative interference between active transducers. This communication scheme is implemented in an original fashion to be compatible with the low—depth synthesis capabilities of low-cost switching amplifiers. An experimental investigation conducted for a simulated metallic plate suggested that a data rate up to tenth of kbps can be reached even by exploiting highly digitized waveforms without losing the original information content.*

The content of this Chapter is based upon the research works [P22]:

"Low Depth Time Reversal Modulation Technique for Ultrasonic Guided Waves-based Communications" by Zonzini F., Testoni, N., Marzani, A. and De Marchi L. In *2020 IEEE International Ultrasonics Symposium (IUS)*, 2020, pp. 1-4. ©2020 IEEE

from which part of the text is drawn.

### 11.1 INTRODUCTION

As already discussed, the physical and operative shortcomings related to the peculiar propagation behavior of Lamb waves have to be properly evaluated. Strategies which try to tackle this task substantially set the compensation procedure aside from the practical communication mechanism, since they are commonly performed in a post-processing phase via advanced signal processing, such as [263], [264] to cite seminal works in the field. These techniques usually require the communication channel to be precisely modeled, a condition which is difficult to met for practical use cases, where the structural parameters are not known *a-priori* and/or need to be estimated from the retrieved data. Conversely, the Time reversal (TR) alternative [265] is considered in this Chapter, due to its intrinsically combined transmission-compensation approach. This latter method takes advantage of the channel time-invariance to concurrently suppress both the detrimental effects of dispersion and the non-coherent disturbances among active transducers. Whenever the channel reciprocity condition applies, namely the time reversal operation is invariant with respect to the physical processes at the basis of GWs propagation, the forward and successive backward transmission of a broadband ultrasonic signal travelling along the same acoustic channel can be received at the original source location in a highly focused manner [266].

Additionally, it is important to underline that, in their basic definition, communication systems built on the TR method are not suited for MIMO scenarios, but rather require a Multiple-In Single-Out (MISO) sensor configuration, i.e., a multiple-output sensor array

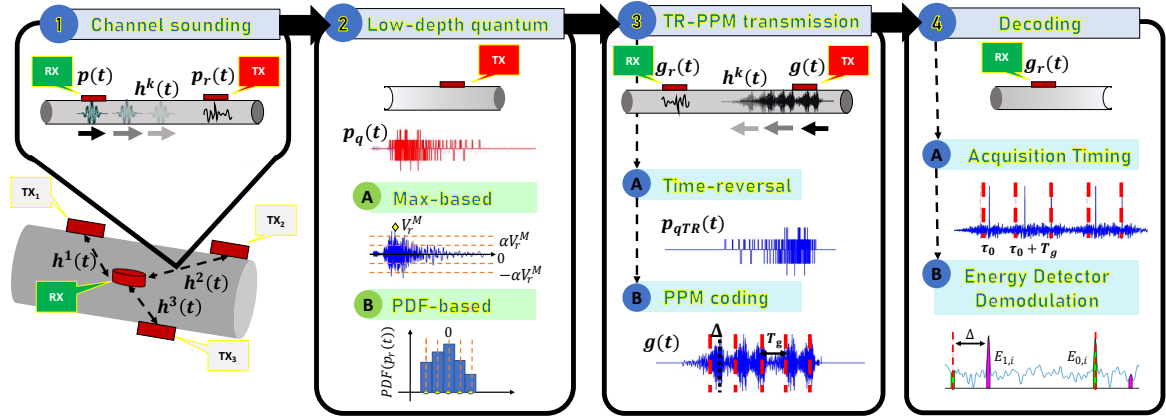


Figure 73: Proposed four stages low-depth TR-PPM scheme. [©2020 IEEE]

**Algorithm 2** Max-based quantization algorithm

---

**Input:**  $p_r^k(t)$ ,  $N_{lev}$ ,  $\alpha$

- 1:  $V_r^{k,M} = \max\{|p_r^k(t)|\}$
- 2:  $\Delta V^k = 2\alpha \frac{V_r^{k,M}}{N_{lev} - 1}$
- 3:
- 4: **for all**  $i \in [0, \dots, N_{lev} - 1]$  **do**
- 5:      $V_{th}^k(i) = V_r^{k,M} - i\Delta V^k$
- 6: **end for**
- 7: **for all**  $n \in [0, \dots, N]$  **do**
- 8:      $i_{n,th} = \min_i \{p_r^k(t) - V_{th}^k(i)\}$
- 9:      $p_q^k(t_n) = V_{th}^k(i_{n,th})$
- 10: **end for**

**Output:**  $p_q^k(t)$

---

communicates with one intended receiver sensor; in these terms, TR implicitly requires transceiver nodes, capable of both receiving or transmitting data.

The approach proposed in this manuscript is original with respect to alternative solutions presented in the literature [267], [268], because it is built on a novel low-depth synthesis of the time-reversed waveforms. Such perspective favors implementations of the methods on low-cost switching amplifiers, as those typically embedded in extreme edge devices for GWS-driven inspection.

## 11.2 DETAILING THE LOW-DEPTH TR-PULSE POSITION MODULATION SCHEME

A four stage and low-depth TR technique for hardware-oriented TR has firstly been proposed in [P22] to cope with the typical computing and power resources available in cost-effective smart transducers. The overall processing flow is schematically depicted in Fig. 73.

Let's assume that an array of  $K$  transmitting nodes  $TX_k$  is used to transmit the same digital message (e.g., a damage indicator) to a common receiving node RX; the communication scheme involves the subsequent phases, which are organized in the two-way handshake mechanism in Fig. 74:

1. Step 1: *Channel sounding* ( $RX \rightarrow TX_k$ ): a probe signal  $p(t)$  of duration  $T_p$  is broadcasted from the intended RX device to every  $TX_k$  node to probe for the corresponding  $k$ -th communication channel  $h^k(t)$  (from point 1 to point 2.A in Fig. 74). Among the traditionally employed pivot signals, Gaussian pulses, chirp signals, rectangular or saw-tooth waves can be listed.
2. Step 2: *Low-depth quantization* ( $TX_k$ ): locally performed by each transmitting node, a thresholding procedure is applied to the channel-operated signal  $p_r^k(t) = p(t) * h^k(t)$  in compliance with the low-level pulse generation capabilities of embedded ultrasound transmitters. Two different algorithms are proposed to tackle this task, yielding the quantized signal  $p_q^{(k)}(t)$ . The first one, named *Max-based* (step 2.A), is shown in Algorithm 2: it requires as inputs  $p_r^k(t)$ , the number of desired quantization levels  $N_{lev}$ , and the scaling factor  $\alpha$ , i.e., a parameter introduced to adapt the thresholding function to the maximum registered input voltage. The second one is named after as *PDF-based* (step 2.B), and simply computes the Probability Density Function (PDF) of  $p_r^k(t)$ , binning it according to the prescribed number of levels.
3. Step 3: *Retransmission* ( $TX_k \rightarrow RX$ ): this phase is composed of two successive steps. Once the time-reversed version of the signal  $p_{qTR}^k(t) = p_q^k(-t)$  is computed (step 3.A), the Pulse Position Modulation (PPM) technique (step 3.B) [269] is applied for the actual transmission of the digital information content (from point 2.D to point 3.A in Fig. 74). PPM is a modulation procedure in which a specific bit  $b_i^1$  is encoded as a sequence of  $N_g$  pulses, eventually delayed by a quantity  $\Delta$  depending on whether  $b_i = 1$  or  $b_i = 0$  has to be transmitted ( $\Delta \geq T_p$  has to be satisfied to ensure a correct bit reconstruction [268]). In case the complete message constitute of  $i = \{1, \dots, N_{bit}\}$  symbols to be sent at a data rate  $F_g = 1/T_g$  ( $T_g$  being the symbol time), the Low-depth Time Reversal (LDTR)-PPM signal is formalized as:

$$g^k(t) = \sum_{i=1}^{N_{bit}} \gamma^k p_{qTR}^k(t - iT_g N_g - b_i \Delta) \quad (54)$$

where  $\gamma^k = \sqrt{\frac{\int_{-\infty}^{+\infty} |p(t)|^2 dt}{\int_{-\infty}^{+\infty} |p_{qTR}^k(t)|^2 dt}}$  indicates an energy normalization coefficient en-

suring that every bit carries the same energy [268] and can be easily computed at the TX side since the energy of  $p^k(t)$  is a deterministic quantity. This quantity is known in advanced after the probe signal and its duration have been defined.

Worthy to be observed, this is the actual point where the benefits of a multi-user TR process come to play. Indeed, it has been thoroughly demonstrated that TR acts as a focusing operator that converts each bit-related LDTR-PPM waveform into a compressed impulsive signal with a prominent peak located at the center of the aggregated channel impulse response [266]. As a result, the energies hidden in several TX-RX communication paths add coherently and, as an immediate byproduct, inter-transmitter interference is automatically filtered out.

<sup>1</sup> Differently from the previous Chapters in which  $b_n$  was used to indicate an entire sequence of bits related to one specific actuator/channel, here the quantity  $b_i$  is used to indicate in a more general form to indicate one out of the total  $N_{bit}$  inside each  $b_n$  stream of bit.

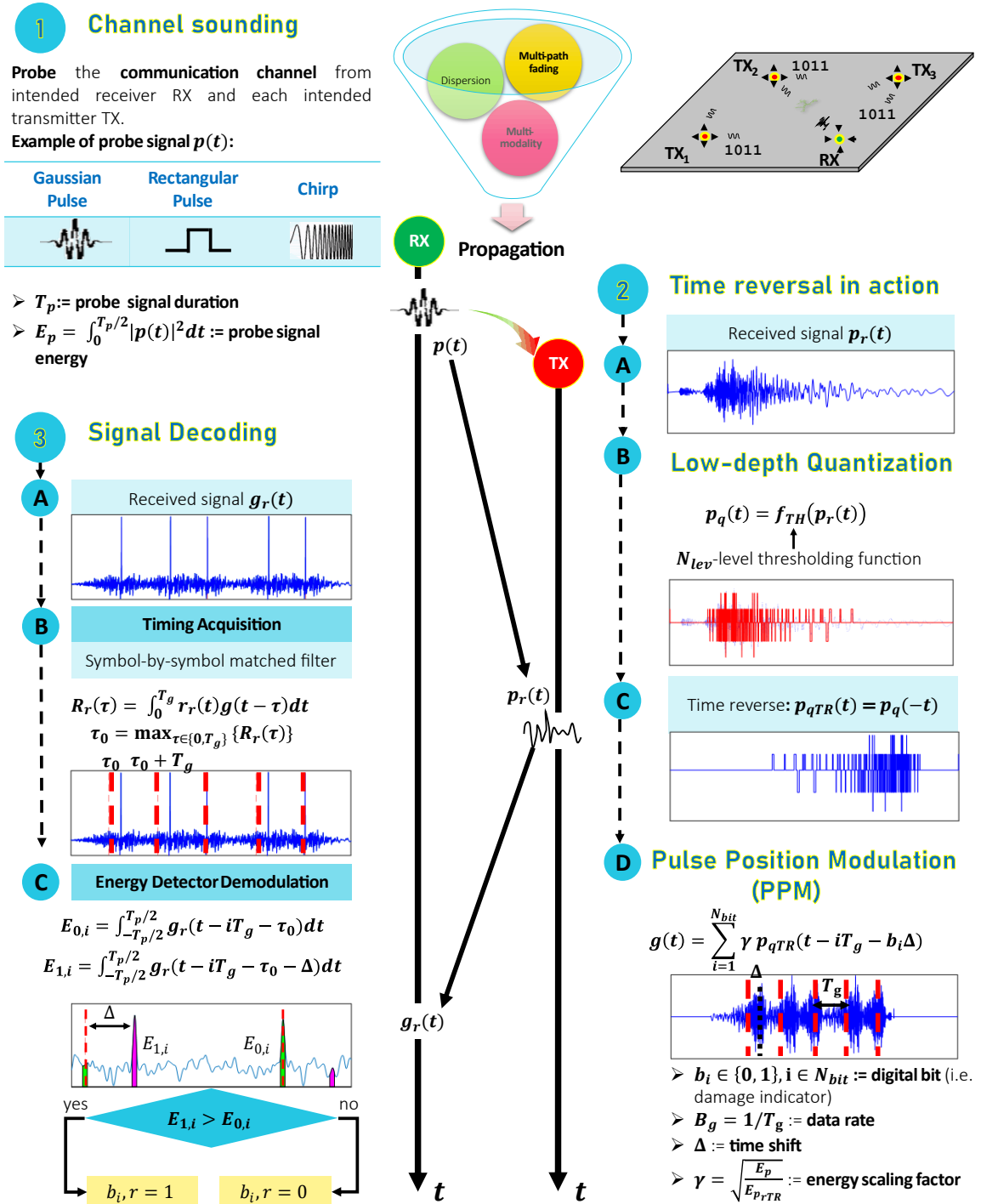


Figure 74: Details of the two-way handshake LDTR-PPM communication scheme extending the description provided in Fig. 73. The channel index is dropped to simplify notation.

4. Step 4: *Decoding (RX)*: the starting time  $\tau_0$  for demodulation coincides with the temporal position of the peak value produced as output of a symbol-by-symbol sliding correlation filter. Hence, the received signal  $g_r(t) = \sum_{k=1}^K g^k(t) * h^k(t)$  is obtained by combining all the elements of the TX array and then by matching it with a pre-selected template  $r_r(t) = p_{qTR}(t)$ , namely

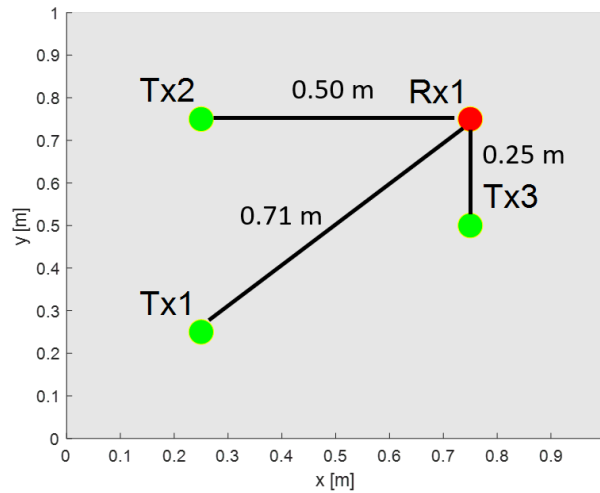


Figure 75: LDTR-PPM communication: simulated experimental setup with underlined communication distances.

$$\tau_0 = \max_{\tau \in \{0, T_g\}} \left\{ R_r(\tau) = \int_0^{T_g} r_r(\tau) g_r(t - \tau) d\tau \right\} \quad (55)$$

Finally, a non-coherent energy detector is encompassed for the purpose of bit reconstruction. Each initial bit  $\hat{b}_i$  can be straightforwardly reconstructed by comparing the two energy quantities  $E_{0,i} = \int_{-T_p/2}^{T_p/2} g_r^2(t - \tau_0 - iT_g) dt$  and  $E_{1,i} = \int_{-T_p/2}^{T_p/2} g_r^2(t - \tau_0 - iT_g - \Delta) dt$ : in case  $E_{0,i} \geq E_{1,i}$ ,  $b_i = 0$  is detected; otherwise the corresponding bit is assumed equal to 1.

### 11.3 EXPERIMENTAL VALIDATION

In view of future ISSLab advancements in which the design of a new generation of integrated receiver-transmitter sensor nodes will be pursued, a preliminary estimation of the communication performances of the devised low-depth solution is performed via synthetic signals generated in MATLAB® environment. A purposely coded ray-tracing algorithm has been exploited, which is capable of (i) taking into consideration the reflections, up to the fourth order, due to interference with the boundaries of the physical medium and (ii) modelling the dispersion and multi-modal propagation behavior of the actuated Lamb waves via analytical formulae.

#### 11.3.1 Materials and Methods

The validation of the proposed LDTR-PPM communication strategy was simulated on a 1000x1000x3 mm 1050A aluminum square plate in which a network of  $K = 3$  transmitting nodes and one RX device is arranged as schematically depicted in Fig. 75. This structure was selected to be the numerical companion of the laboratory metallic structure described in Section 9.3.

The well-known Gaussian modulated pulse  $p(t) = Ae^{-\left(\frac{t-t_0}{T_p}\right)^2} \cos(2\pi F_c t)$ ,  $F_c$  being the modulating tone, was considered as the reference signal for channel probing, whose parameters  $A = 3.3$  V,  $F_c = 250$  kHz,  $T_p = 1/F_c$  and  $t_0 = T_p/2$  were assumed to mimic real-world system implementations [266]. As far as the TR-PPM scheme is pertained,  $N_{\text{bit}} = 1000$  independent and identically distributed random bits were supposed to be sent through the mechanical wave-guide, each of them consisting of  $N_g = 1$  pulse. Moreover, the transmission rate  $F_g$  was varied in the interval [10, 20, 30] kbps, whereas the time shift for PPM was chosen to be  $\Delta = T_g/4$ . Finally, all signals were acquired at an equivalent sampling frequency of 2 MHz.

Moving to the quantization phase, a number of output voltage levels  $N_{\text{lev}} = 5$  was chosen to replicate the typical analog-to-digital synthesis capabilities of commercial off-the-shelf low-cost ultrasonic emitters (e.g. [270], [271]). A return-to-zero logic is assumed during quantization, which clamps the intermediate output threshold voltage at zero. Furthermore, in the particular case of the Max-based procedure, three values for the scaling factor  $\alpha$  were tested, i.e.,  $\alpha_1 = 0.4$ ,  $\alpha_2 = 0.7$  and  $\alpha_3 = 1$ . In that way, it was possible to quantify the distortion effects introduced by the mere low-level signal synthesis.

### 11.3.2 Results

In the result session, both the impact of the quantization procedure and the range of admissible bit rates compatible with a satisfying BER were appraised.

#### 11.3.2.1 Low-depth quantization

Different low-depth versions of the probe signal received at node TX<sub>1</sub> are displayed in Fig. 76, superimposed to the quantization-free waveform  $p_r(t)$ .

By analysing the shape of the produced signals it is possible to state that, the higher the  $\alpha$  value of the Max-based algorithm, the lower the level of resemblance between the two initial (red curve) and quantized data (coloured curves). More in detail, the highest divergences affect the first signal arrivals (i.e., line-of-sight communication links), which are more concentrated in time but less energetic and, hence, tend to be masked by the high-order components caused by the physical interaction with the boundaries of the interrogated structure.

#### 11.3.2.2 Bit recovery performance

The signal reconstruction capability was assessed via computation of the average BER obtained from five different transmission tests (see Fig. 77).

A global trend common to all the considered scenarios is observed, corresponding to an abrupt increase in BER percentages as  $F_g$  reaches 30 kbps. Another fundamental result is worthy of consideration, that is the good level of superimposition in BER curves between quantization-free and low-depth synthesized signal waveforms. Indeed, for transmission rates up to 20 kbps, the error introduced by the quantization process worsens by less than 2.1 percentage points with respect to the same implementation in case the original signals would have been transmitted. Comparing the effect of the thresholding functions, the highest fitting characterizes the Max-based strategy with  $\alpha_1 = 0.4$ . Such an outcome is reasonable given the capability of the corresponding output voltage thresholds to preserve



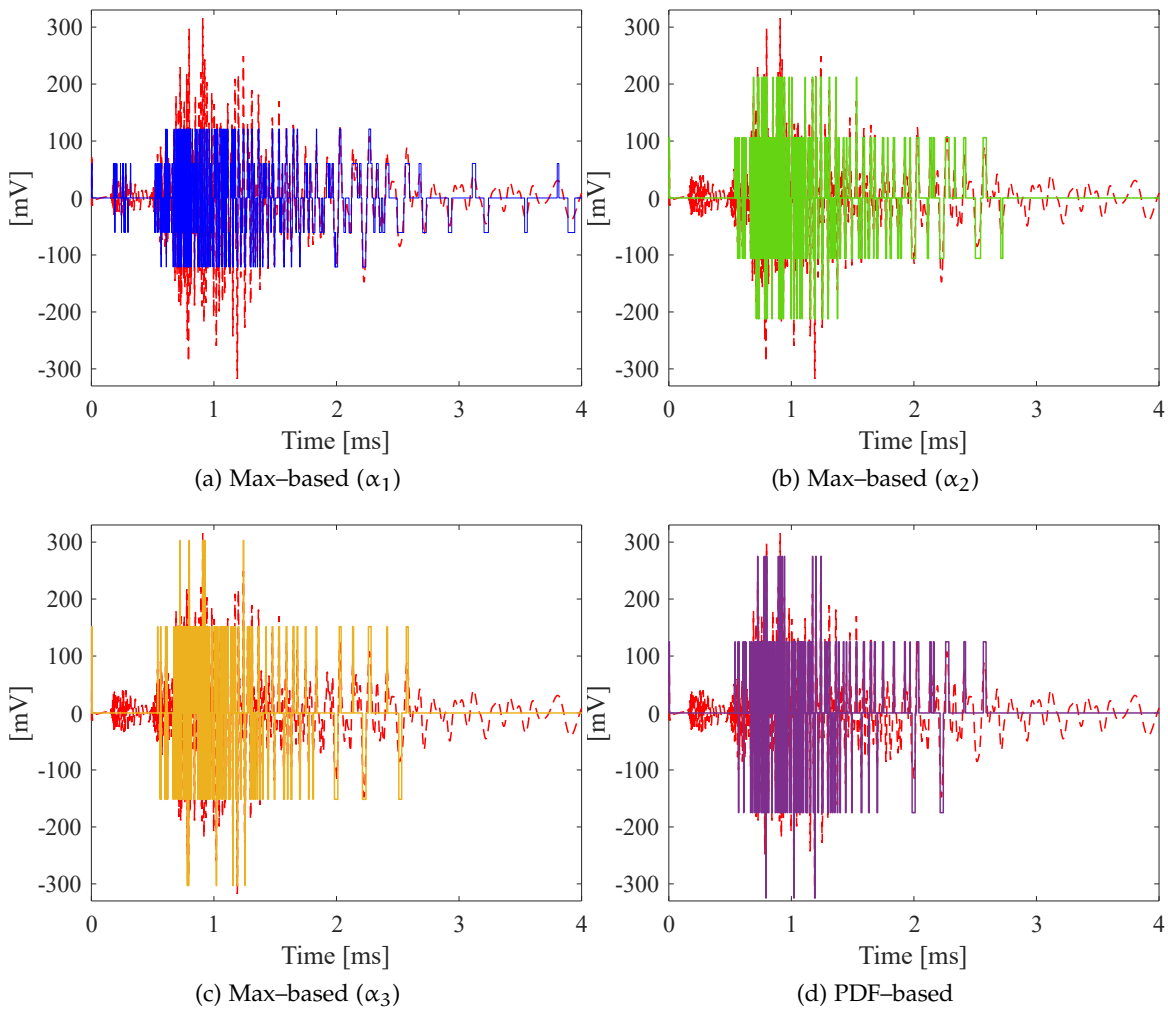


Figure 76: TR-PPM. Low-depth thresholded version of the received Gaussian probe signal  $p_r(t)$  travelling along the communication link TX<sub>3</sub>-RX for different quantization functions. [©2020 IEEE]

the signal content hidden within the first signal arrival (see Fig. 76a). Therefore, it is numerically shown that, in case a proper quantization strategy is selected, the LDTR-PPM communication performances are very competitive to those obtained via the classical TR-PPM implementation, even for significant symbol rates.

### 11.3.2.3 Bit recovery vs probe signal

To better corroborate the feasibility of the proposed LDTR-PPM technique, further communication scenarios were evaluated taking into account the effect of various probe signals on the quality of the recovered stream of bits. To this purpose, three additional finite-length pulses, with duration identical to one chosen for the Gaussian probe, were considered: the rectangular pulse, whose two-level nature is inherently apt at being implemented in hardware with minimal complexity and does not require any additional quantization step; two triangular-shaped pulses, i.e., the standard triangular pulse and the saw-tooth pulse. The two latter are continuous signals whose amplitude increases linearly: as such, a PDF-based quantization procedure could be the preferential choice.

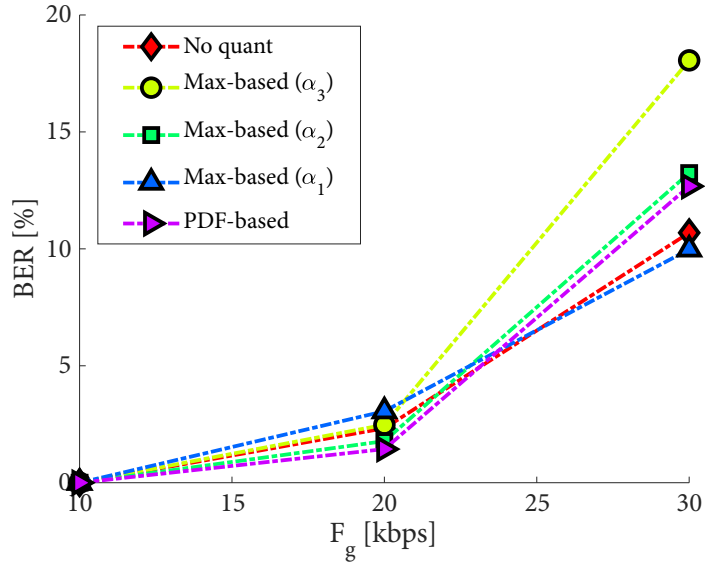


Figure 77: LDTR-PPM. Average BER for increasing bit rate and varying thresholding procedures with Gaussian probe signal. [©2020 IEEE]

Moreover, non-impulsive chirp signals were deemed worthy of investigation for their capability to convey higher energy to the receiving point. This property comes from the fact that a chirp signal consists of a sequence of burst waves whose frequency content varies in time. Thus, it is capable of injecting in the structure a higher spectral content due to the prolonged interval of actuation time. Two different variants were taken into consideration: the linear up-chirp, in which the phase of the bursts increments linearly and it is quantized via the PDF-based algorithm, and the pseudo-chirp, which corresponds to the digitized version of the former due to the fact that the output values can assume only two values (and, analogously to the rectangular pulse, does not require quantization). The interval swept by the frequency content of the chirp signals has been varied between 50 kHz and 150 kHz, with a central frequency of 100 kHz, for a total probing time of 50  $\mu$ s.

Comparative results for the impulsive signals exploiting the same structural configuration introduced above are given in tabular form (see Table 23). As a primary evidence, all the considered probe signals reach perfect bit reconstruction for a data rate of 10 kbps: this outcome highlights the potential of the investigated methodology, whose performance is at least two orders of magnitude (in the simulated setting) higher than the one obtained for the FDM alternative. Secondly, the computed bit recovery capability presents a uniform distribution, i.e., percentage errors below 3% for 20 kbps and an abrupt increment at 30 kbps, irrespective of the probing signal and the quantization procedure. Finally, it is worth pinpointing that the discrepancy between non quantized and quantized signal synthesis is very narrow, the highly digitized versions working even better in some cases.

On the other hand, for the chirp-like signals, different values of the bit-rate were tested. In fact, in order the LDTR-PPM method to be applicable,  $\Delta = \frac{T_g}{D_\Delta} \geq T_p$  holds, imposing  $F_g \leq \frac{1}{D_\Delta T_p}$ . By selecting  $D_\Delta = 2, 3, 4$ , namely  $F_g = \{5, 6.7, 10\}$  kbps, the BER percentages in Table 24 were estimated. In this case, the condition of null error for the bit rate of

Table 23: LDTR-PPM technique vs varying impulsive probe signals: BER percentages are included for increasing bit-rate.

Probe signal	Quantization	Symbol rate		
		10 kbps	20 kbps	30 kbps
Gaussian	No quantization	0.0	1.2	11.1
	Max-based ( $\alpha_1$ )	0.0	0.8	12.5
	Max-based ( $\alpha_2$ )	0.0	1.7	11.7
	Max-based ( $\alpha_3$ )	0.0	3.1	14.3
	PDF-based	0.0	2.0	13.0
Rectangular	-	0.0	2.3	11.7
Saw-tooth	No quantization	0.0	2.7	12.2
	PDF-based	0.0	3.0	13.4
Triangular	No quantization	0.0	1.9	13.0
	PDF-based	0.0	2.8	14.7

Table 24: LDTR-PPM technique vs chirp-like probe signals: BER percentages are included for increasing bit-rate.

Probe signal	Quantization	Symbol rate		
		5 kbps	6.7 kbps	10 kbps
Linear chirp	No quantization	0.0	0.0	0.3
	PDF-based	0.0	0.0	0.2
Pseudo-chirp	-	0.0	0.0	0.3

10 kbps is no longer satisfied, even if the BER, for both signals and independently from the quantization stage, remains stably beneath 0.3%.

#### 11.4 CONCLUSIONS

This Chapter focused on the implementation of a low-depth synthesis of the TR-PPM communication method, which is beneficial in that it allows for a concurrent transmission-compensation functionality. Experimental simulation performed by simulating the communication behavior over a metallic aluminum plate demonstrated that, independently from the probe signal and the quantization algorithm, error-free signal reconstruction is achievable with a data rate up to tens of kbps; hence, the obtained results support the possibility to apply this technique as a competitive candidate for GWs-based digital communications.



## FREQUENCY STEERABLE ACOUSTIC TRANSDUCERS AND QUADRATURE AMPLITUDE MODULATION

---

### ABSTRACT

*This Chapter is devoted to a numerical investigation of the Quadrature Amplitude Modulation (QAM) technique for GWs-based communication. Differently from the standard software/digital implementation of this scheme, multiplexing is achieved via the spatial multiplexing capability of frequency steerable acoustic transducers.*

The content of this Chapter is based upon the research work [P23]:

"Quadrature Amplitude Modulation for Acoustic Data Communication in Ultrasonic Structural Health Monitoring Systems" by Reyes, M.O., Moll, J., Zonzini, F., Mohammadgholiha, M. and De Marchi L. In *Proceedings of the ASME 2021 48th Annual Review of Progress in Quantitative Nondestructive Evaluation QNDE*, vol. 85529, 2021 (pp 1-7).

from which part of the text is drawn.

### 12.1 INTRODUCTION

In GW systems, simple hardware solutions can be achieved by using shaped transducers featuring inherent directional capabilities. A noticeable example of this kind of devices is provided by the so-called Frequency steerable acoustic transducers (FSAT)s: they are based on a spatial filtering effect which is dependent on the angle of propagation of the generated and sensed elastic waves, so that the beam-steering is controlled by the spectral content of the transmitted and acquired signals [272]. The frequency-related directivity of the FSATs can be fruitfully applied in GWs-based communications to implement a spatial multiplexing strategy, similar to the solutions which are currently investigated in 5G communications [273].

Besides the promising communication-related functionalities of the sensing layer, a proper modulation scheme is still necessary to codify the content of the transmitted message. A compelling alternative to the previously discussed methodologies is provided by Quadrature Amplitude Modulation (QAM), i.e., a modulation technique that offers efficient usage of the channel bandwidth combining together two amplitude signals into a single stream of bits. QAM presents a second, interesting benefit, which is a better capability to tolerate poor noise levels [274].

The contribution of this Chapter is to pair the conventional QAM scheme with the built-in spatial multiplexing capabilities of FSAT device to realize, in hardware, the sought frequency directivity. The combination of QAM and FSAT technology paves the way to future sensor network realizations in which autonomous transceivers [275], suitable to be integrated directly on the structure, can perform damage inspection and digital data communication in a very compact and efficient manner.

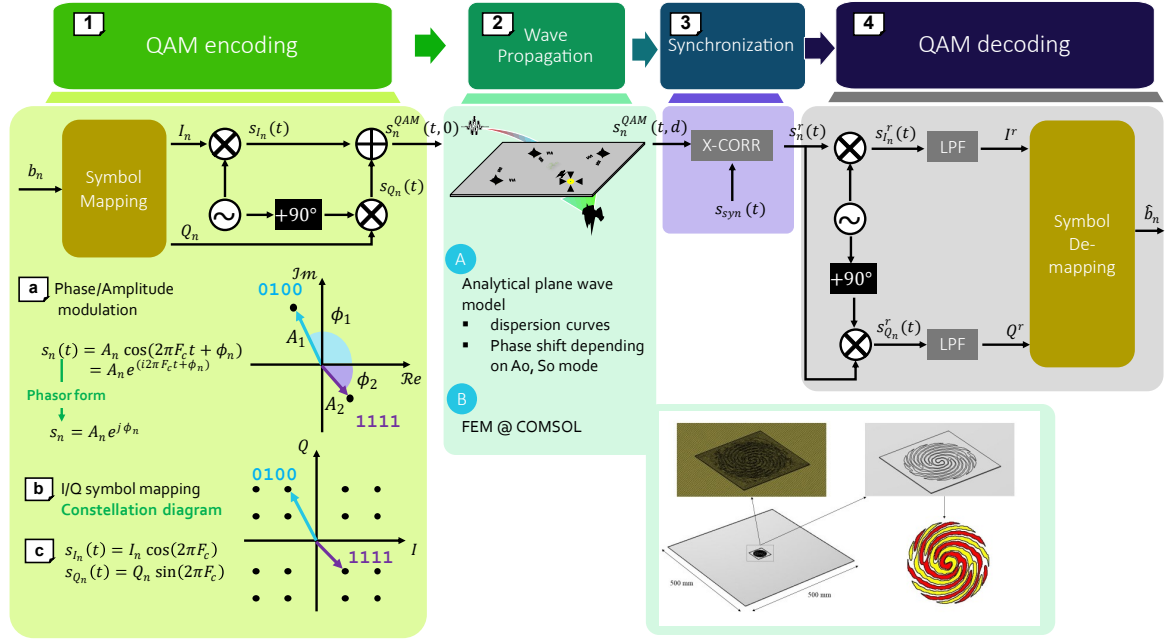


Figure 78: Block diagram of the adopted QAM-based communication framework, specifically modelling the effects of wave dispersion. A schematic representation of the FEM model used to validate the frequency directivity of FSATs is also enclosed.

12.2 QAM SIGNAL PROCESSING FOR GWS PROPAGATION IN ISOTROPIC PLATES

QAM is a modulation mechanism that modifies both the amplitude and the phase of the signal to be transmitted, while holding the same frequency throughout time. This technique exploits sinusoidal tones as modulating waveforms; as such, the first step in the direction of implementing a QAM-based communication scheme is the selection of the carrier frequency  $F_c$ . Note that a proper choice of this parameter is of the utmost importance for GWs propagation, since numerous modes may be excited [276] depending on the operative frequency range (see Section 8).

Notwithstanding the methodological aspects of the QAM technique itself, which replicate the conventional electromagnetic-based implementation, a dedicated signal processing flow has been required, in this case, to efficiently manipulate the dispersive behavior of Lamb waves and investigate the spatial multiplexing capabilities of FSATs when combined with this modulation technique.

The adopted workflow is clarified in Fig. 78 and is based upon the four-step procedure described hereinafter:

1. Step 1: QAM coding and transmission:

In the first stage, QAM is used to map the digital sequence of bits into a number of symbols  $N_{sym}$  dictated by the selected number of binary digits, e.g., 16-QAM indicates that up to 16 different symbols can be generated if  $\log_2(16) = 4$  bits are used to represent a single piece of information.

Every symbols is converted into a sinusoidal signal of identical frequency content but characterized by a specific amplitude  $A_n$  and phase  $\phi_n$  (step 1.a). In mathematical terms, one symbol reads as:

$$s_n(t) = A_n \cos(2\pi F_c t + \phi_n) = A_n e^{i(2\pi F_c t + \phi_n)} \quad (56)$$

which can be rewritten in an equivalent phasor form, yielding  $s_n = A_n e^{i\phi_n}$ . Both two formulations admit a geometrical interpretation in the complex plane, uniquely determined by two components (step 1.b): the in-phase component  $I_n$  lying on the real axis, and the in-quadrature component  $Q_n$  along the imaginary axis, with a phase shift of  $90^\circ$  between them. Such representation is also referred to as *constellation diagram*, [277] owing to the fact that it represents all the possible complex-valued pair of coordinates that a symbol can assume, i.e., it corresponds to the alphabet of binary values dictated by the selected number of digits per symbol. QAM could be easily escalated to a higher-order constellation using more symbols: from one side, this allows for the transmission of more bits per symbol; on the other hand, it complicates the propagation environment since, by adding more points in the same area, the symbols will be closer together and, therefore, they will be more susceptible to disturbances. In the representative case depicted in Fig. 78, an 8-bit word 0100111 is considered: with 16-QAM, it is mapped into two symbols of four bits each (i.e., 0100 and 1111), corresponding to two different points of the constellation diagram.

After separation in its I/Q components, the symbol is ready to be “mounted” over the carrier by means of a sinusoidal signal (step 1.c): a cosine waveform for the in-phase component, namely  $s_{I_n}(t) = I_n \cos(2\pi F_c t)$ , and a sine waveform for the quadrature companion component, i.e.,  $s_{Q_n}(t) = Q_n \sin(2\pi F_c t)$ . These signals are then mixed together in a train of symbols  $s_n^{\text{QAM}}(t) = s_{I_n}(t) + s_{Q_n}(t)$ . After modulation, multiple modulated symbols can be combined in sequence and dispatched through the same channel by means of a piezoelectric transceiver converting the electric signal into mechanical displacements. Let’s call with  $s_n^{\text{QAM}}(t, 0)$  the actuated signal.

## 2. Step 2: Wave propagation modelling:

GWs travel a communication distance  $d$  prior than reaching the receiver node. While propagating, they undergo well-known detrimental phenomena which need to be properly modeled for the effective evaluation of the investigated communication scheme. Prior than pairing QAM with the spatial multiplexing capability of FSATs, a preliminary proof-of-concept has been encompassed by means of an analytical wave propagation model: the objective of this phase is to probe for the actual suitability of QAM itself for GWS-based communications. To this end, a first numerical model, indicated with label A in Fig. 78, was designed: it exploits the same spectrum-based procedure already presented in Section 10.2 and simulates the dispersive GWs propagation behavior by resorting to a numerical derivation of the dispersion curves characteristics; indeed, by knowing them, Eq. (52) can be applied to retrieve the spectrum of the received message yielding the propagated and dispersed QAM signal  $s_n^{\text{QAM}}(t, d)$ . After this first numerical verification via a plane wave model, a second numerical model was built (case B), in which the sought spatial multiplexing capability of FSATs to cope with the same goal were specifically investigated in view of future hardware prototyping phases.

In this case, a FEM designed with the COMSOL® libraries was employed, since this software provides a very powerful tool for the simulation of the mechanical and

electrical response of piezoelectric–transducers. As displayed in the bottom right part of Fig. 78, the latter coincides with the dual–color spiral shaped FSAT printed on a piezoelectric layer, while an aluminum plate with dimensions of 500 mm × 500 mm and thickness of 1 mm has been considered as propagation medium. In this case, the GW–operated signal was retrieved from the out–of–plane displacement generated by the FSAT when  $s_n^{\text{QAM}}(t, 0)$  is provided as input to the FEM.

3. Step 3: *Reception and synchronization:*

Prior than entering the true demodulation procedure, the exact instant for demodulation needs to be retrieved. This can be easily achieved by cross–correlating the received message with a synchronization sequence  $s_{\text{syn}}(t)$  agreed in advance by the transmitter and the receiver.  $s_n^r(t)$  is used in step 3 of Fig. 78 to indicate the synchronized version of the received signal.

4. Step 4: *QAM decoding:*

The synchronized message is then demodulated, again by resorting to the same sinusoidal signals in quadrature used at the encoding side, to separate the imaginary and real components  $s_{I_n}^r(t)$  and  $s_{Q_n}^r(t)$ . The high frequency content of the signal needs also to be removed, and this can be achieved with help of a low pass filter (LPF), returning the sought  $I^r$  and  $Q^r$ . These two latter quantities are plugged as input to the demapping block (performing the opposite operations entailed by the mapping block) and a reconstructed version of the bit chain,  $\hat{b}_n$ , is finally returned.

## 12.3 EXPERIMENTAL VALIDATION

### 12.3.1 *Materials and Methods*

The aluminum isotropic plate already mentioned in Section 12.2 was considered for validation purposes by imposing a plate thickness of 1 mm to be consistent between the two numerical models. The communication distance was set equal to  $d = 200$  mm.

A 64–QAM modulation scheme (i.e.,  $\log_2 64 = 6$  bits per symbol) was selected and a message consisting of a stream of 48 bits packed into  $N_{\text{sym}} = 48/6 = 8$  symbols was generated at a symbol rate of 8 ksym/s, corresponding to a bit–rate of 48 kbps. An oversampling factor of 50x was assumed for the sampling frequency to ease the synchronization process and be compliant with the Nyquist’s band.

The configuration of the QAM parameters was completed by selecting two different carrier frequencies:  $F_{c,1} = 130$  kHz and  $F_{c,2} = 150$  kHz. These values were deemed compliant with the analysed test–bed, for which the bandwidth 50–500 kHz represents a suitable choice for actuation: indeed, within this interval, only the first symmetric and anti–symmetric modes  $S_0$  and  $A_0$  are excited. This band was determined by analysis of the corresponding dispersion curves.

As far as the model simulating the FSAT is concerned, the radiation patterns for these two carriers (when the corresponding QAM–modulated signals are provided as input to the model) are displayed in the left hand side of Fig. 79. To create these plots, the out–of–plane displacement fields were generated and extracted over a circle with a radius  $d$  around the transducer. The preferential radiation directions are clearly visible in Fig. 79, in both representations and for both actuation frequencies.



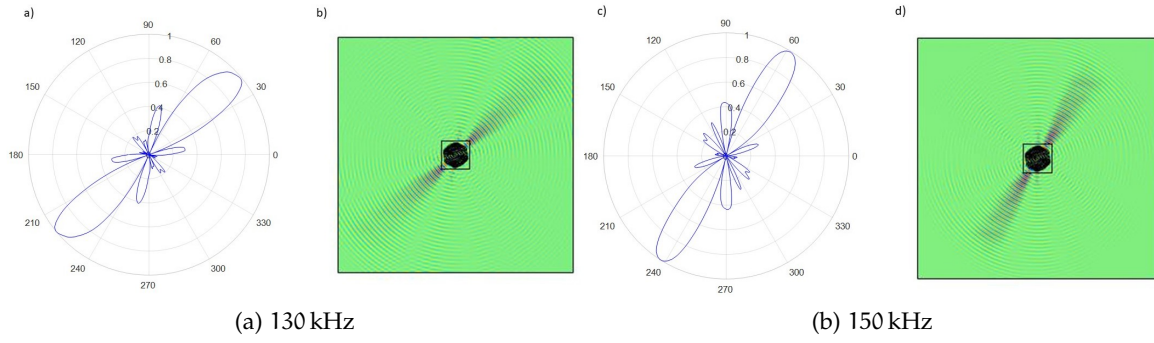


Figure 79: Radiation pattern and wavefield snapshot for (a) 130 kHz and (b) 150 kHz carrier frequency obtained with FEM simulation of the FSAT.

The quality of the results was judged both qualitatively and quantitatively: firstly, by visually analyzing the level of superposition between the original and the reconstructed constellation diagram, and then by computing the corresponding Root Mean Square Error (RMSE):

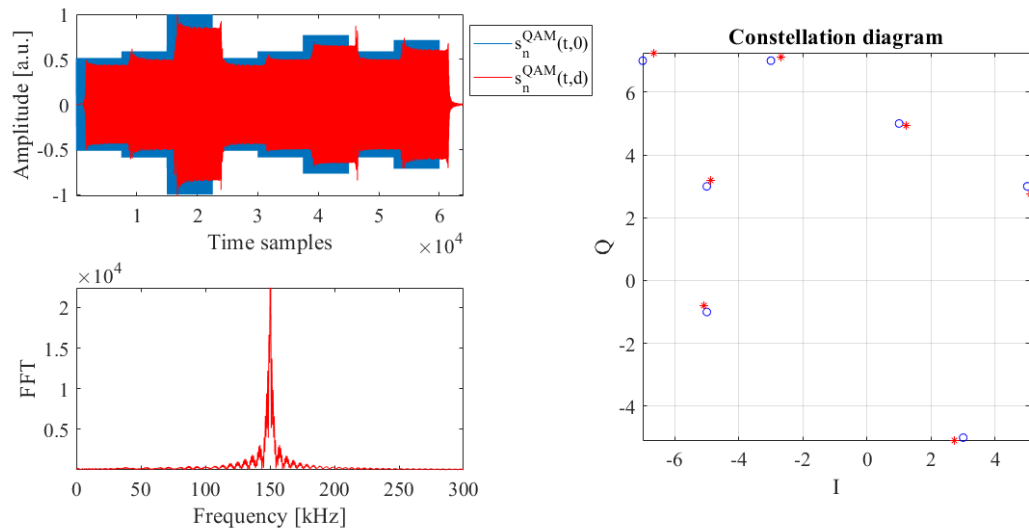
$$\text{RMSE} = \sqrt{\frac{\sum_{n=1}^{N_{\text{sym}}} [(I_n - I_n^r)^2 + (Q_n - Q_n^r)^2]}{N_{\text{sym}}}} \quad (57)$$

### 12.3.2 Results

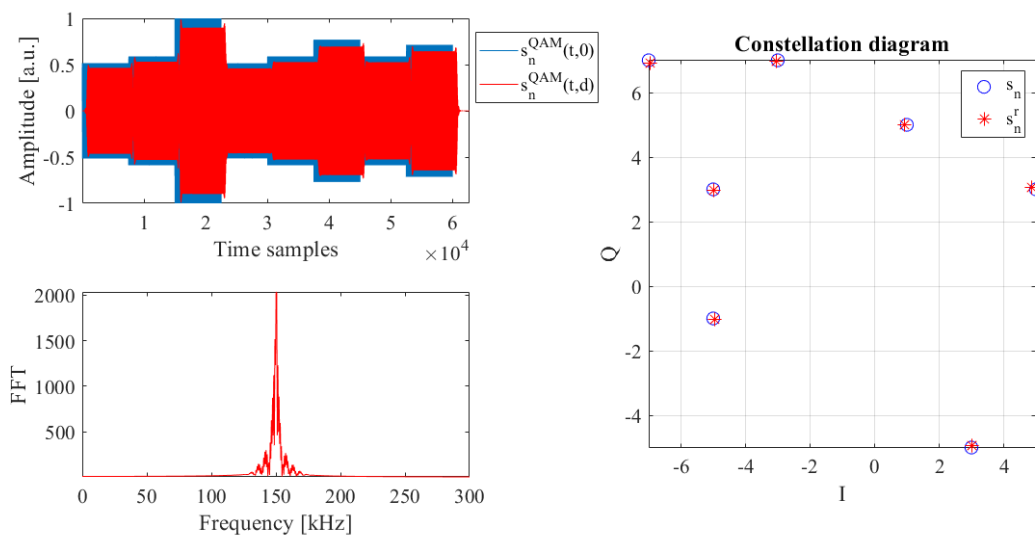
The effectiveness of the explored communication framework was tested both in ideal propagation environments where the only source of non-ideality is the one associated to the GW behavior, and secondly, by adding the effects of external noise sources.

#### 12.3.2.1 Bit reconstruction in noise free conditions

In Figure 80a and Figure 80b, the results of the analytical plane wave model and the ones related to the simulated FSAT are presented, respectively, imposing a carrier frequency equal to  $F_{c,2}$ . In the top left panel, the actuation signal (blue) and the received signal prior than synchronization (red), are illustrated. From the chart related to the plane wave model, it is possible to identify some "glitches" generated at every phase/symbol change, while similar disturbances are considerably reduced for the FEM case. This is due to the spatial filtering effect of the FSAT that cancels out most of these undesired effects on the signal. In the bottom left charts, instead, the spectrum of the received signal is computed, in which a sharp peak arises at the selected carrier frequency with both modelling strategies. On the right hand side of the same figure, the recovered symbols are plotted in form of a constellation diagram: as can be observed, the error affecting FSAT-driven results is noticeably lower to the one associated with the analytical counterpart. This evidence is corroborated by a better level of agreement between the numerical QAM constellation and the one reconstructed after FEM simulations, and further proven by RMSE values of 0.2743 and 0.0751, respectively, for the two models. Noteworthy, these results are independent from the selection of the specific carrier frequency, as proven by very similar performances



(a) Analytical model



(b) FEM FSAT

Figure 80: Simulation results for QAM with 150 kHz carrier frequency. Top left: normalized transmitted (blue) and received (red) signals for 8 bit symbols. Bottom left: FFT of the received signal. Right: original (blue circular markers) and demapped (red star) symbol constellation.

Table 25: RMSE values as a function of decreasing SNRs for QAM data communication (carrier frequency equal to 130 kHz (first column block) and 150 kHz (second column block)).

SNR	130 kHz		150 kHz	
	Analytical model	FEM - FSAT	Analytical model	FEM - FSAT
$\infty$	0.2320	0.2150	0.2743	0.0751
13.98 dB	0.2466	0.2284	0.2793	0.0838
7.96 dB	0.2613	0.3112	0.2789	0.1500
4.44 dB	0.3448	0.2626	0.3099	0.2108
1.94 dB	0.3174	0.3170	0.2981	0.1969
0 dB	0.3838	0.3604	0.3149	0.2270

obtained for the selection of  $F_{c,1} = 130$  kHz (Fig. 81a and 81b): in this case, the RMSE value amounts to 0.2320 and 0.2150 for the analytical and FEM simulation, respectively.

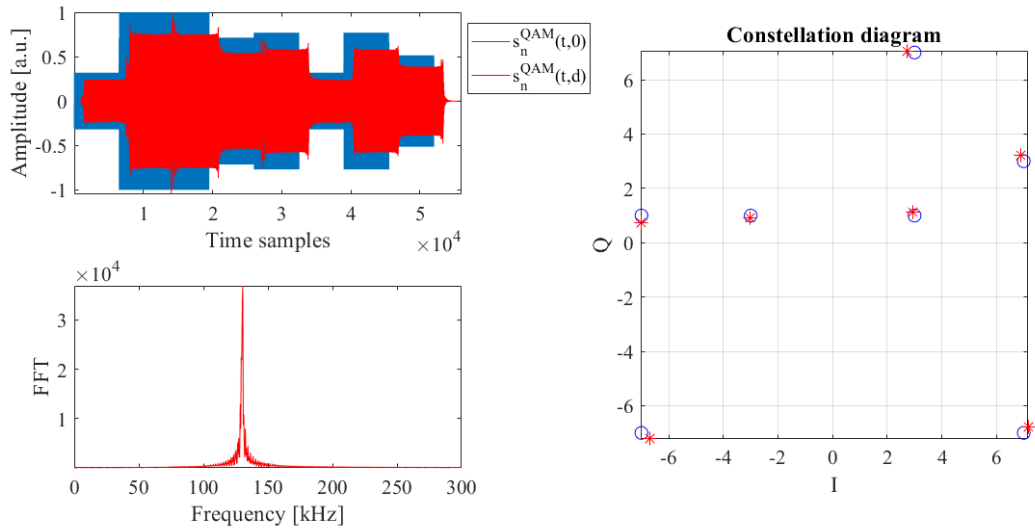
The reported results not only prove the suitability of QAM as modulation strategy for GWs-based digital communications, which is corroborated by the good level of agreement returned by the analytical simulation: more importantly, they demonstrate how QAM could be realized with custom hardware solutions as the one provided by FSATs directly attached to the structure, performing even better than the expected analytical predictions.

#### 12.3.2.2 Bit reconstruction in noisy conditions

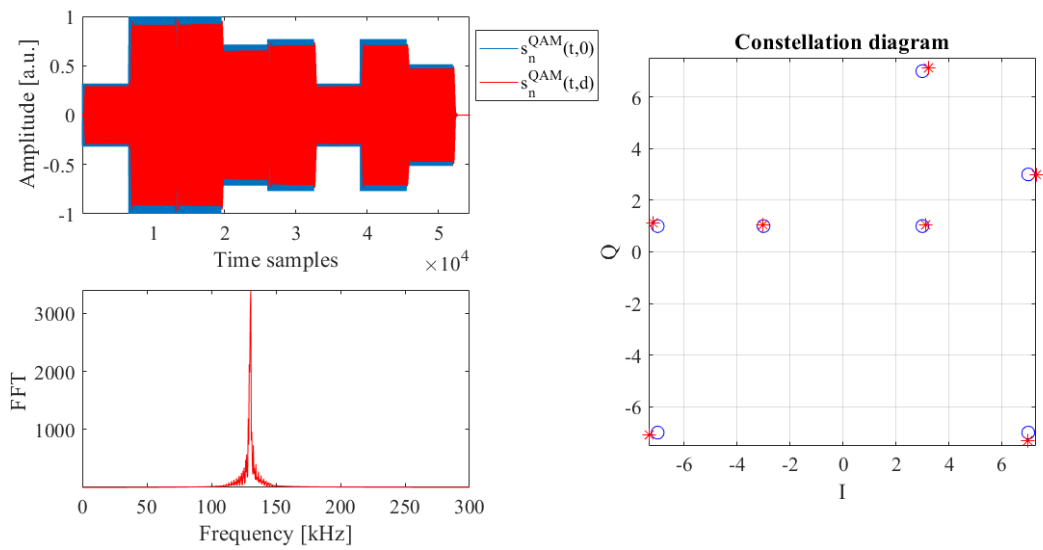
Besides the analysis of the GW propagation behavior, the perturbations due to noisy channels were evaluated by adding a weighted amount of noise to the received signal (prior than synchronization), proportional to the maximum recorded amplitude. To this end, simulations were repeated starting from the noise-free configurations discussed before ( $\text{SNR} = \infty$ ) and continually increasing the percentage of noise level down to  $\text{SNR} = 0$  dB; the remaining system parameters were left unchanged. More specifically, the corresponding percentage of noise was progressively increased from 0% to 100% at integer steps of 20 points per time.

Results for the 0 dB case are depicted in Fig. 82, where, in the time domain, it is no longer possible to identify any symbol or visible shape of the original signal. Nevertheless, the QAM-based communication system is capable of successfully recovering the transmitted payload with a minor increase in the RMSE, both in the analytical and in the FEM wave propagation models; this outcome is proven by values reported in Table 25.

Focusing on the 150 kHz carrier (second column block), the reported error slightly increases while reaching more unfavourable propagation settings. However, such increment is not equally effecting both models. Indeed, if the analytical simulation shows a maximum deviation around 0.04 points, in the FEM analysis the difference is fourfold (i.e., 0.0751 vs 0.2270). Despite this loss of accuracy, it should be specified that the point-wise constellation superposition always achieves a significant level of accuracy, the FEM model being always more performative than the analytical solution, even under the most significant noise levels. A similar error distribution can be noticed also for the 130 kHz carrier component (first column block). In this case, the deviation is averagely higher for both models, showing minor differences among them.

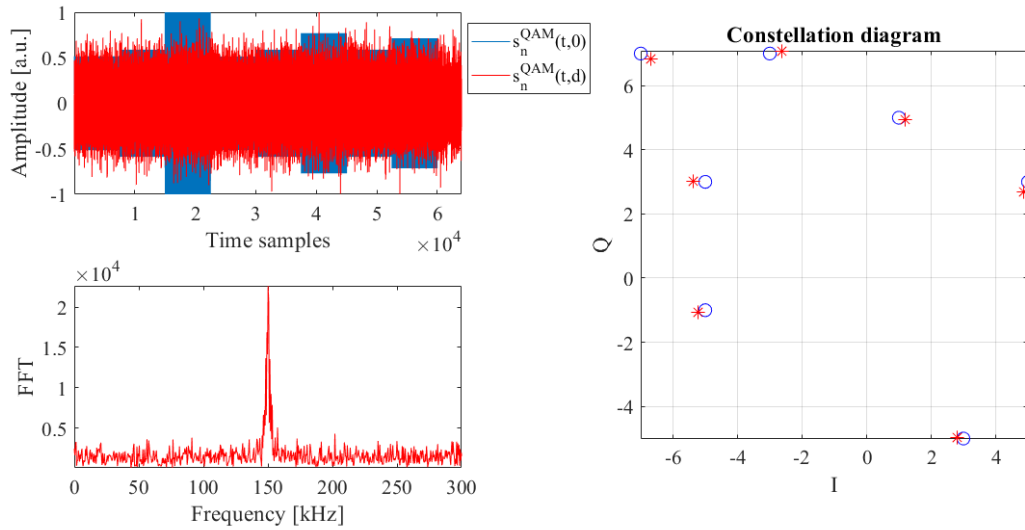


(a) Analytical model

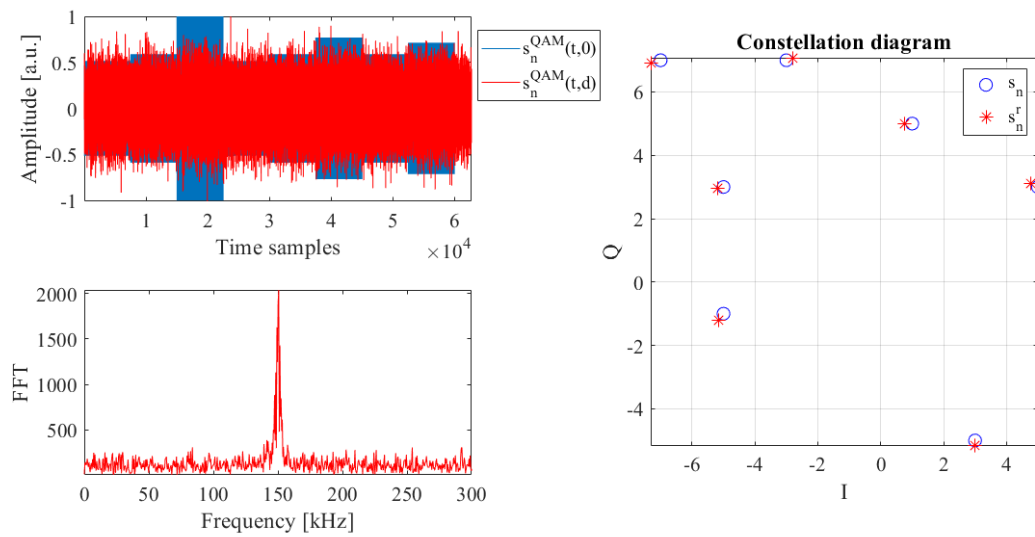


(b) FEM FSAT

Figure 81: Simulation results for QAM with 130 kHz carrier frequency. Top left: normalized transmitted (blue) and received (red) signals for 8 bit symbols. Bottom left: FFT of the received signal. Right: original (blue circular markers) and demapped (red star) symbol constellation.



(a) Analytical model



(b) FEM FSAT

Figure 82: Simulation results for QAM with 150 kHz carrier frequency and SNR = 0 dB. Top left: normalized transmitted (blue) and received (red) signals for 8 bit symbols. Bottom left: FFT of the received signal. Right: original (blue circular markers) and demapped (red star) symbol constellation.

## 12.4 CONCLUSIONS

In this Chapter, the effectiveness of QAM for ultrasonic data communication has been examined, with particular emphasis on its implementation in hardware enabled by the spatial multiplexing capability of FSATs. Numerical simulations aided by purposely developed wave dispersion models, one purely analytical and the other one emulating the actual FSAT behavior, were performed and framed within a QAM-based communication scenario driven by GWs. A good superposition between the expected and the retrieved constellation diagrams was reported, even in very noisy communication scenarios. The obtained results demonstrate that the inherent frequency directivity of FSATs combined with the robust communication scheme offered by QAM could represent a valuable step forward towards the design of a next generation of autonomous systems for SHM.

Part III

ENHANCING ACOUSTIC EMISSION-BASED MONITORING  
VIA DEEP LEARNING





## ARTIFICIAL INTELLIGENCE ALGORITHMS FOR TIME OF ARRIVAL ESTIMATION IN ACOUSTIC EMISSION SIGNALS

---

### ABSTRACT

*Estimating the time of arrival in acoustic signals is an essential step in diagnostic techniques based on acoustic emissions. To address this task while overcoming the limitations of reference statistical methods classically applied in the field, the current Chapter tries to offer a solution based on AI. Two Deep Learning models will be presented: one is built on a standard Convolutional Neural Network, while the second one implements a Capsule Neural Network architecture, which is an emerging model capable of preserving the hierarchical relationships between features. Experimental results will be conducted in the framework of a metallic square plate.*

The content of this Chapter is based upon the research work [P24]:

"Deep Learning Approaches for Robust Time of Arrival Estimation in Acoustic Emission Monitoring" by Zonzini, F., Bogomolov, D., Dhamija, T., Testoni, N., De Marchi, L. and Marzani, A. In *Sensors*, vol. 22, no. 3, pp. 1-22, January 2022.

from which part of the text is drawn.

### 13.1 INTRODUCTION

Among the non-destructive testing techniques for SHM systems, the method based on AE is one of the most effective for the structural assessment of civil and industrial plants, enabling for the identification of weaknesses in structures such as pipelines and heat exchangers, vessels and storage tanks, columns and reactors, etc. AE monitoring is based on the control of the acoustic activity of the target structure [278], primarily the one provoked by the growth of cracking phenomena. Indeed, it is well known that, when an acoustic event occurs as a consequence of cracks, disbondings or delaminations induced by inner and/or external flaws, acoustic waves are generated, which propagates in the physical medium. One of the main advantages of AE relies on the possibility to localize such sources by passively capturing the induced acoustic response of the structure. It is, therefore, from the extraction of a batch of representative acoustic features, typically defined on a time domain basis, and their evolution over time, that potential dangerous defects can be detected at an early stage of degradation and preventive alarms can be issued [279].

One of the most important parameters to be extracted from an acoustic signal consists of the Time of Arrival ( $T_{oA}$ ), also known as onset time, namely the time taken by the induced wave to travel from its origin to the acquisition point.  $T_{oA}$ , when estimated on multiple sensing positions, inherently provides a simple, yet effective means for signal source location. The literature about these localization methods is quite vast and comprehends, among the others, approaches based on geometrical or angular relationships, such as the ones built on the angle of arrival or the Difference Time of Arrival ( $DT_{oA}$ ) [280].

Alternative methods are based on the estimation of the signal energy [281], but this parameter is typically very sensitive to environmental and operational factors (e.g., imperfect coupling between the AE transducers and the structure) which hamper their exploitation for long-term integrity evaluation.

AE testing is typically implemented with long inspection intervals by purposely increasing the mechanical load applied to the structure [282]<sup>1</sup>. However, more recently, a new approach has emerged, in which AE monitoring is performed in real time, via the permanent placement of AE equipment on the monitored structure and by detecting the emissions generated during the normal load cycles. Despite the advantages in terms of responsiveness and preventive detection, the adoption of the latter approach is challenged by the difficulty in accurately identifying weak AE events in noisy environments, particularly at the early stages of defect growth [283]. Indeed, permanently installed AE systems must counteract the corruption of noise generated by operational processes, such as vibrations of rotating machinery (e.g., a pump unit or an engine), responsible for extra disturbances [284], and of unpredictable noise sources, such as electromagnetic interference and ambient noise in the vicinity of the monitoring system [285], [286].

The less favorable SNRs, which characterize real-time monitoring acquisitions, may prevent the accurate tracking of AE features, and in particular of the ToA. Statistical algorithms for onset time determination have proven their effectiveness even at high SNRs, but the noise factors mentioned above significantly affect the reproducibility and accuracy of ToA estimation results. Consequently, the implementation of reliable methods for signal detection, moreover robust to noise, is still an open research field.

### 13.1.1 The problem of ToA estimation: from statistical methods to machine learning

By computing the similarity between two signals, Cross-Correlation (X-Corr) can be used as a powerful tool for the estimation of the time disalignment of two time series. In practical AE scenarios, where the monitoring network constitutes of a passive mesh of transducers and the true excitation source is unknown, X-Corr offers a means for DToA quantification among pair of receivers rather than a measure of the actual ToA, and proved its effectiveness for the characterization of AE signals in multiple environments [287]. However, X-Corr is highly susceptible to minor perturbations in the statistical properties of the input signals (e.g., residual noise sources superposed to the actual information content).

Striving to cope with these issues, Akaike Information Criterion (AIC) approaches the task of ToA identification as a pure statistical problem based on the second order statistics of the input signal. In essence, AIC leverages the concept of signal entropy to probe for the presence of abrupt changes in the statistical distribution of the observed signal. For a discrete signal with N samples, this is achieved by computing, for each sample [k], the quantity:

$$\text{AIC}[k] = k \log \sigma_{y[1:k]}^2 + (N - k - 1) \log \sigma_{y[k+1:N]}^2 \quad (58)$$

which is a logarithmic measure of the cumulative variance of the preceding ( $y[1 : k]$ ) and successive ( $y[k + 1 : N]$ ) signal window with respect to the current sample index k. In other

<sup>1</sup> <https://eur-lex.europa.eu/legal-content/IT/TXT/?uri=celex:32014L0068>, <https://ec.europa.eu/docsroom/documents/41641>

words, AIC splits the full waveform into a  $k$  dimensional and  $N - k$  dimensional smaller vectors, respectively spanned by the first  $N$  and the last  $N - k$  samples, and describes the level of similarity between them. The rationale is that, in correspondence of a sharp change in the signal profile, such as the one associated with the arrival of the incoming wave-front generated by the acoustic source, the divergence between the pre and post signal variances increases to a large extent, generating a minimum in the overall AIC function. The instant of time aligned with this minimum is the sought  $T_{oA}$ .

Notably, this method can provide reliable outcomes when the processed signal presents two clearly distinct regions, e.g., an high-entropy portion where dominates uncorrelated noise, and a low-entropy segment where the acoustic signal is present [288]. Nevertheless, as discussed in [289], this might not be the case for AE monitoring scenarios, in which the mere attenuation due to signal propagation, which is responsible for low-amplitude received waveforms, is further hindered by additive operative noise, demanding for more advanced data processing solutions.

Led by the constantly increasing success of AI in learning complex patterns hidden within signals, interesting AI solutions to tackle  $T_{oA}$  estimation were proposed, with particular emphasis on the seismology field. Indeed, in geology,  $T_{oA}$  of pressure waves travelling through the Earth's crust is of crucial importance, because it permits the thorough characterization of incipient earthquakes or micro-seismic events and, consequently, to predict their time, magnitude and location. Hence, a close analogy exists between the two application domains and, by virtue of this similarity, solutions tested in seismology can be adopted also for AE signal processing.

Literature works about AI in seismic analysis is very recent and includes, among the seminal examples, a template-based artificial neural network for earthquake phase detection [290], while [291] proposed an unsupervised fuzzy clustering logic for  $T_{oA}$  recognition in micro-seismic waves. Another example worthy of attention was examined in the work by Zachary E. Ross [292], where the  $T_{oA}$  of pressure waves in seismograms was considered as a pattern recognition problem on top of which a DL model was trained. The importance of this work is that it is based on a fully agnostic approach, in which time picking is turned into a pure black-box model by processing data directly in the time domain without any additional pre-processing. Considered among the most powerful architectures for deep and ultra-deep learning, PhaseNet and UNet [293] were also investigated as alternative methods for seismic arrival time picking, reporting outstanding results. A comprehensive list of the most recent trends in this direction can be found in [294].

Therefore, the objective of the novel methods proposed henceforth is (i) to build accurate AI models capable of handling highly perturbed AE signal properties and (ii) to test them in operative SHM frameworks, such as acoustic source localization purposes.

## 13.2 DL MODELS FOR TOA ESTIMATION

Two different NN models were implemented for the purpose of  $T_{oA}$  estimation.

### 13.2.1 Convolutional Neural Network

Convolutional Neural Network (CNN) is a class of artificial neural networks that can extract relevant information from raw data and retains it in the form of weights and biases of the corresponding layers: the learnt parameters are then used to make classification

and/or predictions as soon as new signal instances are available. A general CNN architecture consists of two main stages, i.e., *feature extraction* and *classification*, which are completely described by the following architectural blocks:

- *Convolutional layers*: these elements are in charge of feature extraction from input data, which are passed in a tensor form of dimensions  $N_{in}$ . A convolutional layer runs dot products between the input data and a specific set of weights (or mask), which are stored as taps of a corresponding filter, also known as *kernel*. This filter is recursively applied to subsequent portions, or patches, of the input data by means of a sliding filter mask which is shifted by a constant quantity called stride ( $N_{stride}$ ). To do so, the dimension of the kernel,  $N_{ks}$ , has to be considerably lower than the length of the original input signal.

To increase the learning capability of the network, more than one filter is employed in a single convolutional layer: if  $N_{filter}$  is the number of total different kernels per layer,  $N_{filter}$  different maps of the the same input data are provided in output via a proper activation function. A convolutional layer is, thus, completely determined by the tuple of values:  $(N_{in}, N_{filter}, N_{ks}, N_{stride})$ .

Multiple convolutional layers are usually stacked one after the other, and this enables each layer of the network to identify different properties of the input in a comprehensive manner. Low-level features are captured at the end of the first set of convolution operations, while the remaining high-level features can be inferred from the subsequent convolutional layers. The typology of the convolutional layer is dictated, in turn, by the dimensions of the manipulated data. In the case of ToA estimation, where the problem is intrinsically mono-dimensional and thought to be performed on a sensor-wise basis, 1D convolutional (Conv1D) layers are necessary.

- *Pooling layers*: "to pool" means merge; and this is what the pooling layer is actually in charge of. Indeed, not only the number of points in each feature map returned at the end of a single convolutional block might be extremely huge, but also many of them only capture minor details about the pattern hidden within data; thus, they can be neglected. Therefore, in order to shrink the computational complexity and the spatial size of the convolved features, the benefit of the pooling layer is to provide a distilled version of each feature map. Different pooling strategies have been proposed for the sake of dimension reduction: max pooling (MaxPool), which only preserves the maximum value in a specific patch of the feature map; average pooling (AvgPool), which extracts a single scalar as the average of the points falling in the same feature patch.
- *Dense layers*: once manifold representations of the input have been processed via a combination of convolutional operations, the sought pattern hidden within the computed feature maps finally remains to be learned. This is achieved by means of dense fully-connected (FC) layers, i.e., feed-forward layers with neurons that have full connections to all activations delivered by the previous layer.

Firstly, the feature maps provided by the last pooling layer are flattened, namely unrolled in a uni-dimensional vector of appropriate dimension; then, the associated values are used as input of a standard artificial neural network, which acts either as a classifier or a regressor depending on the desired task. For the ToA estimation

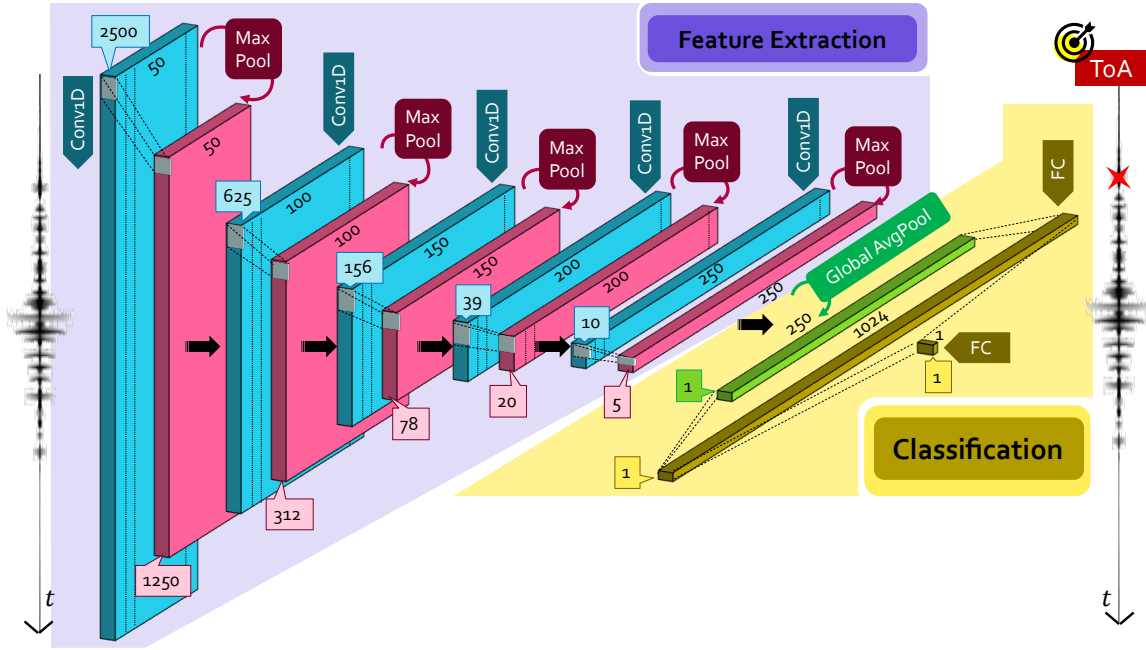


Figure 83: Proposed small CNN for ToA estimation from 5000-long time series. The quantities reported in the blue and pink boxes indicate the dimensions of the output features of the corresponding layer.

problem at hand, in which we are interested in predicting one single value coincident with the sought onset time, a regressor form has been chosen by forcing one single neuron in the output layer of the last fully-connected block.

#### 13.2.1.1 Large CNN model

The first CNN architecture considered in this work is schematically represented in Figure 83 and is devised for ToA retrieval from 5000-long time series. As can be seen, five  $(5000/2^{2l}, N_{\text{filter}}, 10, 2)$  Conv1D layers ( $l \in \{0, \dots, 4\}$  being the layer index), with  $N_{\text{filter}} \in \{50, 100, 150, 200, 250\}$  and ReLU activation function, are stacked in cascade and followed by a MaxPool layer with compression factor equal to 2. A global average pooling layer (Global AvgPool) has also been included at the end of the convolutional block to force the regressor behavior of the network: Global AvgPool yields one single feature map out of the 250 different representations at the end of the last AvgPool layer. This single map is then passed to a first FC layer having 1024 neurons activated by ReLU; ToA can finally be retrieved from the output layer consisting of a  $1 \times 1$  FC layer with one neuron and linear activation. It is worth saying that the so far designed CNN model is characterized by 1,259,299 parameters requiring a minimum memory space of at least 1.5 MB even in quantized form: the Adam optimizer [295] with learning rate of 0.001 and loss weight equal to 1 has been used for training such parameters, while the model was trained for 15 epochs.

#### 13.2.1.2 Small CNN model

It must be emphasized the fact that, in order to be applicable in real edge/extreme edge computing scenarios, the devised algorithmic solutions must cope with the limited pro-

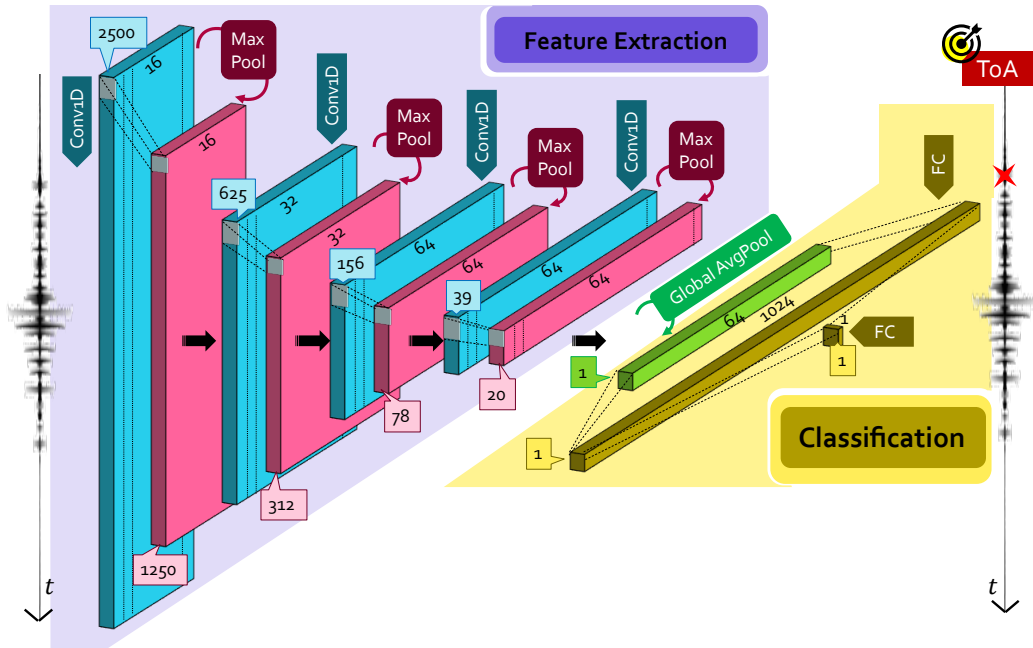


Figure 84: Proposed small CNN for ToA estimation. The quantities reported in the blue and pink boxes indicate the dimensions of the output features of the corresponding layer.

cessing capabilities of resource-constrained devices. However, converting the previously described CNN model into a TinyML format is not practicable due to the excessive amount of memory (and, in turn, of computational power) it requires. For this reason, a distilled version of the preceding model has been derived as displayed in Fig. 84, in which the five convolutional layers have been substituted with four smaller size Conv1D+MaxPool layers with 16, 32, 64 and 64 filters while leaving unaltered all the remaining parameters. The dimensions of the GlobalAvg layer were changed accordingly. In this lighter version, only 134,481 parameters need to be learned, for a total memory occupancy of nearly 150 kB after conversion to embedded programming format, which leads to a complexity reduction of more than 10x, while making the model compatible with the above-mentioned memory constraints of edge devices. Hereinafter, to differentiate the two models, this smaller one will be called as "small CNN".

Notably, the model reduction of both the number of convolutional layers and filters per layer has been preferred over other pruning strategy, given its proven advantages in terms of algorithmic complexity and memory footprint, as well as for its robustness against model over-parametrization [296] and better generalization to out-of-distribution data.

### 13.2.2 Capsule Neural Network

Despite their outstanding performances, CNNs might be ineffective under the following circumstances [297]: (i) the observed data pattern presents shifts/rotations, since CNNs are phase and shift invariant; (ii) the spatial relationship between the feature maps is an important indicator of the data distribution, since CNNs do not exploit spatial dependencies; (iii) the loss of information introduced by the pooling layers is unacceptable, especially for very deep model where pooling is mandatory.

Very recently released in the field of AI [298], Capsule Neural Network (CapsNet) represent a powerful competitor to convolutional architectures for classification tasks. Three main reasons can be mentioned. Firstly, CapsNet transforms basic feature maps in correlated feature maps via the novel concept of capsule unit: this correlation-based approach implies preservation of spatial dependencies between data. Secondly, albeit disregarding the pooling layer, it is capable of correct prediction even when trained on fewer data. Thirdly, its vector-based output allows for robust classification performances by making use of simpler network architectures. This latter aspect deserves particular attention in view of TinyML implementations, owing to the fact that CapsNet actually offers a first means for knowledge distillation, which is performed directly at an architectural level via novel machine learning operators, rather than being executed at a coding/firmware level, where most of the effort is usually spent.

Successful application of CapsNet for micro-seismic phase picking were accounted in [297], showing great performances for earthquake signal characterization. Inspired by this first attempt, an AE-oriented variant of CapsNet is proposed in this manuscript to cope with ToA prediction.

In its general form, the block diagram of a CapsNet architecture nests a capsule representation in cascade to standard convolutional without pooling between them, to learn, in a lossless way, novel representations from the generated feature maps. More formally, it consists of the following two elements:

- *Primary capsule*: this layer performs convolution aggregation via the so-called *capsule unit*  $u_i$  ( $i \in \{1, \dots, N_{PC}\}$  being the capsule index), corresponding to multiple combinations of the feature maps retrieved at the end of the convolution process. In their working principles, primary capsules provide an alternative form of convolutional layers: the main difference is that, in this case, a vector-based output is computed rather than working with unitary depth. As such, a convolution-based processing is performed by each capsule, which is driven by an appropriate set of kernels and relative stride.
- *Digit capsule*: at this point, the agreement among different capsules has to be estimated so that it is possible to preserve the spatial dependency between those block representations with highest relevance. This concept is mathematically encoded via the weight opinion matrix  $W_{ij}$ , with  $j \in \{1, \dots, N_{class}\}$  being the number of classes, each with vector-based output of dimension  $N_{DC}$ . Hence, every capsule is judged by means of  $N_{class}$  opinions  $u_{j|i}$ , also called local digit capsules, to be computed as:

$$u_{j|i} = W_{ij}u_i \quad (59)$$

From these local representations, a further level of feature combination is added in a spatially-dependent manner, by following the routing-by-agreement protocol [299]. This procedure, also called dynamic routing, introduces the concept of agreement, i.e., how much the individual digit capsules agree with the combined one. The level of agreement is numerically quantified by the weight routing matrix  $R_{ij}$  via the coupling coefficient

$$c_{ij} = \frac{e^{R_{ij}}}{\sum_{c=1}^{N_{\text{class}}} e^{R_{ic}}} \quad (60)$$

As such, the final digit capsule  $s_j$  is given by  $s_j = \sum_i c_{ij} u_{j|i}$ . As in traditional convolutional layer, activation is required to ensure that digit capsules with low opinions shrunk to zero, since they do not convey meaningful information. However, the vector-based output of the capsules requires ad-hoc functions to fulfill this task: the squashing function

$$v_j = \frac{\|s_j\|^2}{1 + \|s_j\|^2} \frac{s_j}{\|s_j\|^2} \quad (61)$$

was purposely proposed in [298] to address this task, where  $s_j$  and  $v_j$  are the input and output of the  $j$ -th convolutionally-operated capsule. The quantity  $u_{j|i} \cdot v_j$  finally yields the actual measure of agreement, i.e., the higher this product, the more preference is awarded to the corresponding primary capsule  $u_i$ . At this point, an iterative algorithm can be called to update the routing matrix, until the desired level of agreement is reached and the sought  $N_{\text{class}} \times N_{\text{DC}}$  digit capsule block can be derived, which serves as output layer for the entire neural network. Finally, it is sufficient to calculate the  $\ell_2$  norm of each of the  $N_{\text{class}}$  rows to obtain a corresponding value of the output probability associated to each single class.

For AE-related problems, just two classes can be considered, i.e., noise and AE signals: in this case, an high value of the output probability  $p_{\text{AE}}$  for class "AE signal" indicates that the input instance is most likely to contain a true AE event, whereas low values can be seen as indicators of noisy input.

An overview of the proposed CapsNet architecture for AE signal processing has been graphically summarized in the left hand side of Fig. 85. The initial convolutional block consists of two Conv1D layers without pooling, activated by ReLU and with dimensions (500,64,9,2) and (250,128,9,2), respectively. At the output of the convolutional layer, 128 feature maps of 125 samples each are computed: these feature maps are passed to the primary capsule layer. Here, 78 primary capsules of 8 feature maps each are created, and then processed via capsule-oriented convolution operations via kernels of size 9 and stride equal to 3. Dynamic routing is then performed, yielding to  $N_{\text{class}}$  different digit capsules with vector size equal to 8. A last stage in which the  $\ell_2$  norm is applied to each row of the the digit capsule block returns the two desired class probabilities (noise and AE).

In terms of model complexity, the proposed CapsNet architecture requires 301,952 parameters and allocates a memory space of 375 kB, a quantity which is 4.2x lower and 2.25x bigger to the ones estimated for the original and small CNN, respectively. Once again, Adam optimizer (with a learning rate of 0.001) was used for training the model for 15 epochs.

### 13.2.2.1 ToA retrieval from CapsNet

Determining ToA with CapsNet is a two-step process. Indeed, in its definition, CapsNet acts a classifier for the input batch of data, meaning that it can only predict whether the



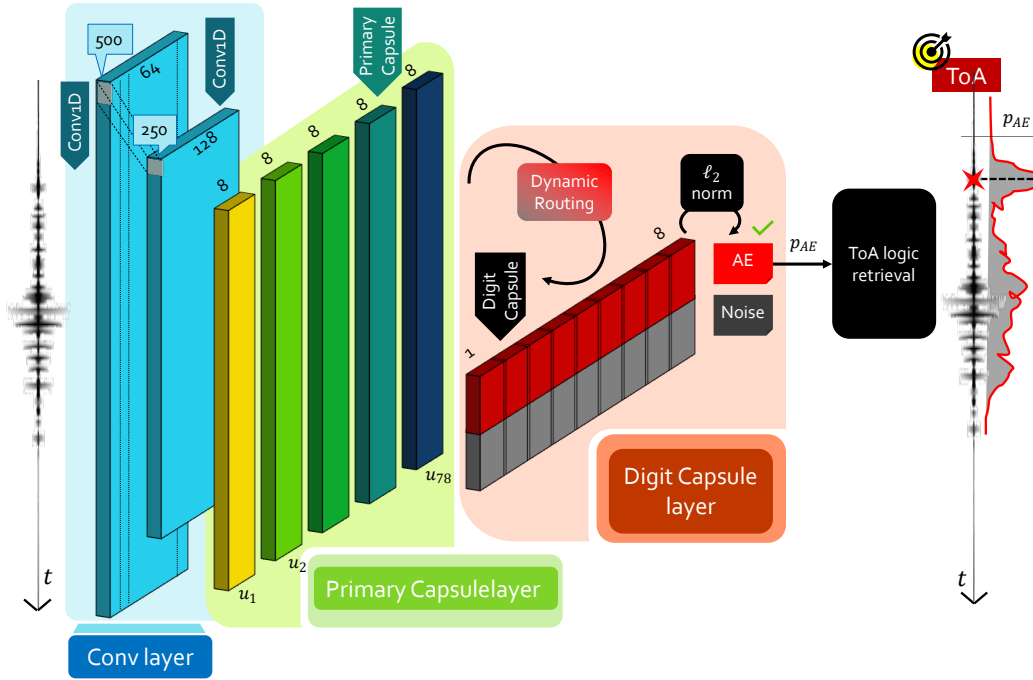


Figure 85: Proposed CapsNetToA architecture for ToA estimation.

current instance is most likely to contain low-entropy signal content (high probability) or rather noisy data (low probability). Therefore, a dedicated logic has been implemented to extract one single time value out of the class probability distribution. Hereinafter, the entire processing flow, encompassing both CapsNet and the time retrieval logic, will be named after as CapsNet-driven ToA estimator (CapsNetToA).

To this end, an approach similar to the one suggested in [297] is adopted. The idea is to split the entire waveform of 5000 samples into smaller and overlapped windows, each of them identified by a unique time stamp taken as the central value of the corresponding time span. For every segment, a probability value is returned; the cumulative trend in the probability distribution can be easily obtained by concatenating, in time, the predictions related to subsequent windows.

The rationale is that the probability curve is expected to assume low value until the signal statistics do not change. Then, when the first window containing the wave arrival is processed, the curve increases progressively, reaching its maximum (in the ideal case, unitary probability) for the exact window centered on the actual  $T_{oA}$ .

On a first attempt, one may resort to statistical tools such as PP or thresholding functions to retrieve  $T_{oA}$  as the first peak probability value. However, such simple approach might suffer from several drawbacks, which can be listed as follows: it presents poor generalization capabilities, in the sense that the selection of a threshold or benchmark value is strictly application- and environmental-dependent; as such, it badly conjugates with the critical variability of AE scenarios. The second reason relates to the impossibility of accurately retrieving very early onset times, i.e., the ones below or almost equal to the window length, for which the true peak probability value is unavoidably missed. In this case, in fact, all the initial windows will output nearly unitary value and, thus, a criterion based on the leading peak selection will unavoidably estimate  $T_{oA}$  from secondary signal arrivals.

Conversely, ML solutions can inherently handle all these sources of complexities in a very efficient and user-transparent way. For this reason, a second NN block has been stacked in cascade to CapsNet to retrieve ToA from the output probability history yielded at the end of the capsule processing. It is worth observing that, in ToA terms, the problem is exactly analogous to the one faced to estimate ToA via CNN when working directly with time series data. The main difference between the two processing frameworks is that, for this second scenario aided by CapsNet, probability functions are available as inputs. Coherently, in the novel approach proposed in this manuscript and which is novel with respect to the one in [297], it is suggested to employ the same small CNN as "ToA logical retrieval" block (see Fig. 85) in a completely agnostic and general-purpose manner.

The parameters of CapsNetToA were configured as follows. Assuming an operative sampling frequency of 2 MHz, the selection of a window size of 500 samples with stride equal to 10 imposed a lower bound of 5  $\mu$ s to the ToA resolution. These values are compliant with the time resolution admitted for the prospective applications, where ToA usually settles around hundreds of microseconds.

### 13.3 EXPERIMENTAL VALIDATION: A NUMERICAL FRAMEWORK

The effectiveness of the designed models was tested within the framework of the metallic plate already exploited in the previous Chapters for GWs communications. Firstly, a preliminary phase of dataset generation was performed to train the models, whose accuracy in prediction was then assessed by comparison with ground truth labels. This preliminary validation is of critical importance to validate the robustness of the NN solutions in comparison with reference statistical methods, especially to observe how performances can scale with respect to noise levels.

#### 13.3.1 Dataset generation

As is widely recognized, DL models requires a large amount of data to be trained on to avoid erroneous predictions. Moreover, since we are dealing with prediction problems, the same data need to be labelled. However, labeling a massive amount of experimental data is, unfortunately, practically unfeasible. Alternatively, analytical simulations could be adopted to rapidly generate the labelled dataset. In particular, a consistent yet representative dataset was created via the ray-tracing algorithm introduced in Section 10.3 under the fundamental hypothesis that acoustic emissions travel along the mechanical medium in form of GWs, for which the propagation pattern through the mechanical medium is well known, and a numerical simulator can be efficiently adopted. As far as the target structure is considered, the square aluminum plate of Section 11.3 was taken as reference, while a Gaussian modulated pulse with central frequency of 250 kHz was assumed to simulate the effect of acoustic sources: in this frequency range, only the Ao and So modes characterize the propagation behavior, a condition which is desired to minimize the detrimental effect of multi-modality.

Every time series constituted of 5000 samples acquired at a theoretical sampling frequency of 2 MHz: these quantities were chosen to be compatible with commercial off-the-shelf sensors for AE monitoring. More in detail, the signal generation procedure followed the subsequent steps:

1. **Travelling distance selection:** theoretically, the number of possible propagation distances between the AE location and the receiving point is infinite. However, by exploiting the symmetrical design of the structure ensured by its isotropic nature, the number of useful configurations can be reduced to a large extent. A square area of  $5 \times 5$  positions circumscribed to the top east corner of the plate was allocated to AE receivers, while a total amount of  $10 \times 5$  AE actuation points were uniformly distributed in the left half of the plate. For a wave speed  $c_g$  of 5371 m/s retrieved from the dispersion curve diagrams of this plate, the chosen sampling grid imposes a maximum and minimum theoretical onset time of 185 ms (i.e., 370 time samples) and  $4.68 \mu\text{s}$  (i.e., 9 time samples) for the farthest and shortest distance, respectively.
2. **Noise level variation:** since the primary objective of the proposed NN alternatives is to surpass the poor estimation capabilities of reference statistical methods in presence of noise, this aspect deserved particular attention. To cope with it, a Gaussian noise signal of increasing magnitude was progressively added to the acoustic wave, by sweeping the SNR from 30 dB down to 0 dB in steps of 1 dB. Despite the fact that the nature of the background noise of real AE signals can indeed differ [300], additive white stationary noise (such as the one generated by electronic components) can be considered as the main source of SNR degradation and, consequently, was used to simulate noisy AE scenarios in this study.
3. **Pre-trigger window variation:** in real AE equipment, the starting time for data logging is triggered by the incoming wave, e.g., once it exceeds a predefined energy threshold. However, being capable of acquiring also the moments leading up to the acoustic event is of vital importance for appropriate AE signal characterization. As such, sensors are generally programmed to preserve memory of the pre-trigger signal history by reserving it a specific portion of the data buffer. This quantity, known as pre-trigger window, might vary largely from hundreds to thousands of samples, depending on both the application scenario and the employed electronics.

Although representing a deterministic parameter that does not strictly depend on the physical phenomenon at the basis of acoustic wave propagation, the pre-trigger time actually plays a crucial role during the learning stage. This observation means that, theoretically, a one-to-one correspondence should exist between one model and one pre-trigger window. This aspect not only requires time and extra computing effort, due to the fact that a new training phase must be entailed whenever a change in the network configuration occurs, but it is also not viable in practical scenarios. Therefore, a data augmentation procedure has been encompassed to favor the generalization capability of the neural network models.

To this end, acoustic signals were initially generated with a fixed pre-trigger window of 500 samples, that represents a reasonable choice for typical scenarios. Then, one time-lagged version of each signal was derived by adding randomly from 500 to 2000 samples to the initial pre-trigger window. Since the total number of samples in the time history is limited to 5000, these forward shifts required additional  $N_{\text{pre}}$  samples to be concatenated with the initial portion of the signal, while disregarding the final  $N - N_{\text{pre}}$  ones: to avoid both discontinuities and alterations in the statistical properties, the extra portion of the signal to be added was generated in form of a white noise term drawn from a Gaussian distribution, whose variance was taken

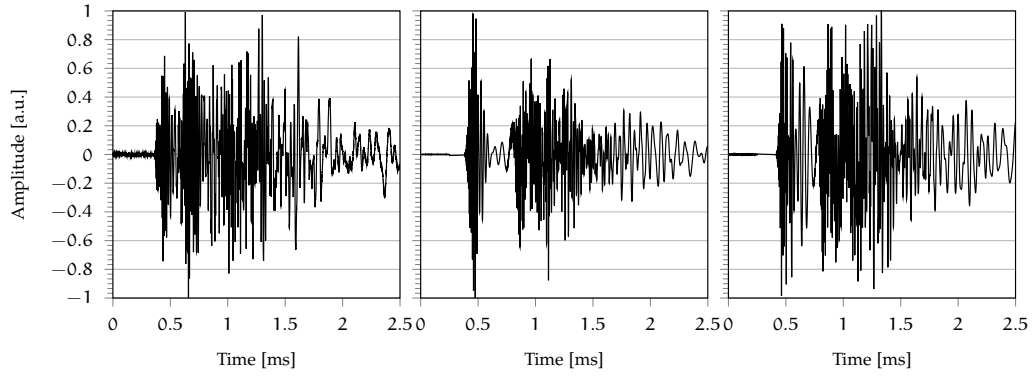


Figure 86: Example of synthetic signals generated with the ray-tracing algorithm.

to be coincident with the one estimated for the first 400 samples in the original pre-trigger window. Another batch of data was also generated, comprising signals with an increased pre-trigger time beyond 2500 samples, and was entirely used during the testing phase in order to probe how the neural networks could behave with respect to unforeseen delays in the signal.

4. **Label generation:** when Lamb waves are to be characterized, it is difficult to give an unambiguous definition of their ToA due to dispersion and multi-modality. For this reason, rather than adopting a labeling approach based on the propagation theory, a different strategy was undertaken in this work. In particular, we exploited the fact that AIC inherently provides very accurate ToA estimations when the SNR is high. As such, the label attached to each time series was taken from the output yielded by AIC when applied to noise-free signals.

A total amount of  $N_{inst} = 60000$  signals was generated via exhaustive combination of all the possible configurations between propagation distance, noise level and pre-trigger window: 80% of them were used for training, 10% for validation, and the remaining 10% for testing. Each time series has then been normalized and mean-removed. Some exemplary signals collected at the end of the dataset generation phase are plotted in Figure 86.

### 13.3.2 Performance metrics

Since "true" labels are available, the simplest methodology to assess the accuracy of the models is to quantify the error between the predicted and the actual ToAs. This strategy is efficient since it allows also to probe the accuracy of AIC in noisy scenarios: indeed, once applied to noise-corrupted variants of the same data, AIC predictions might deteriorate proportionally to the level of added perturbations.

Therefore, the RMSE was computed as accuracy indicator. Differently from the definition provided in Eq. (57) which has been specialized there to deal with complex values, its canonical expression:

$$\text{RMSE} = \sqrt{\frac{\sum_{i=1}^{N_{\text{test}}} (\text{ToA}_i - \hat{\text{ToA}}_i)^2}{N_{\text{test}}}} \quad (62)$$

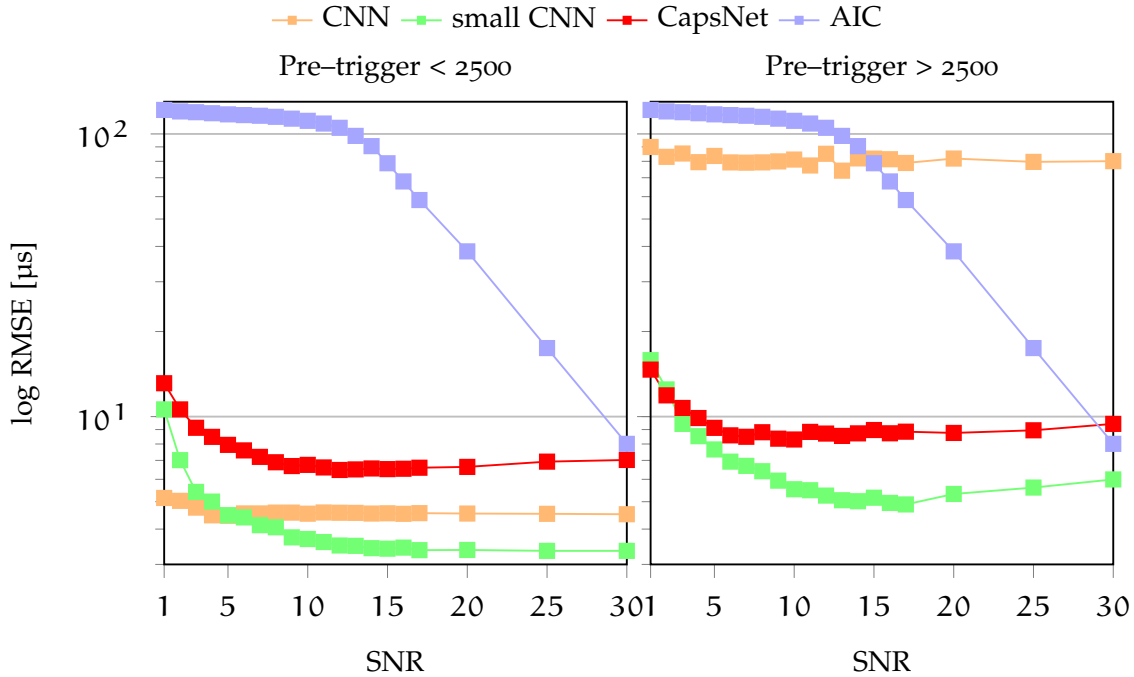


Figure 87: RMSE error for ToA estimation on synthetic test dataset for varying SNRs. (left) Pre-trigger window used for training (i.e., pre-trigger window lower than 2500 samples) and (right) Increased pre-trigger window.

was resorted to for ToA characterization:  $ToA_i$  is the true value,  $\hat{ToA}_i$  is the current prediction and  $N_{test}$  is the number of instances used during testing.

### 13.3.3 Results

ToA estimation results for test data with pre-trigger window below 2500 (i.e., the one used for training) are displayed in the left panel of Fig. 87: they are given in terms of RMSE (log scale) as a function of increasing SNR. From this figure, two different trends in the reported errors are evident: indeed, if the NN models present a maximum deviation below 11  $\mu\text{s}$ , the error profile of AIC is inversely proportional to the noise level affecting the signal; moreover, AIC is characterized by a slowly decaying trend with smoother profile. The performances of the four approaches are in the same order of magnitude only for a SNR equal to 30 dB, i.e., as discussed before, in those conditions in which the signal statistics are well defined and easy to be identified even via conventional processing tools.

Secondly, in the comparison between the AI approaches, the original CNN shows an almost stable error around 4.5  $\mu\text{s}$ , irrespective from the specific SNR apart from a negligible increment in case of very unfavorable noise levels. It is worth noting that the distillation operation (small CNN) is less performative for SNR below 5 dB but very effective for all the remaining SNRs. Finally, the curve error of CapsNetToA is similar to the one discussed for small CNN, with slightly higher errors at high SNRs.

A graphical depiction of the output collected from the different approaches is displayed in Fig. 88, which shows a zoom in the 0.1-0.4 ms window with drawn star markers indicating the predictions obtained from AIC (blue), CNN (orange), CapsNetToA (red) and small CNN (green), superimposed to the true label (yellow diamond). As can be observed, the

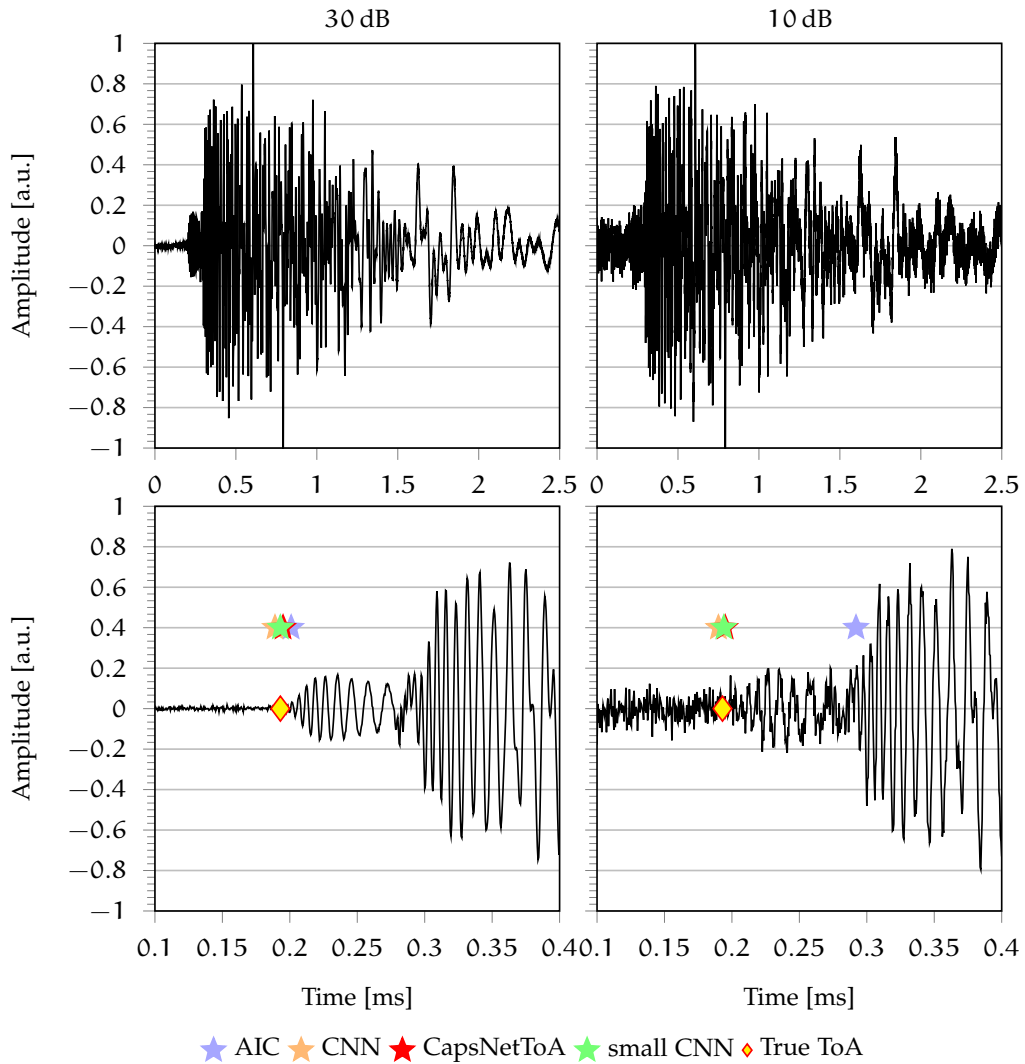


Figure 88: ToA predictions for AIC (blue), CNN (orange), CapsNetToA (red) and small CNN (green) with synthetic dataset: (left column) SNR = 30 dB and (right column) SNR = 10 dB, with second row depicting a magnified region of the time interval where ToA is located.

estimates are considerably accurate in the left panel (SNR = 30 dB) for all the methods, while AIC completely fails in the case of important noise levels (same signal, but SNR = 10 dB) depicted in the right-hand side.

The performance achieved by varying the pre-trigger windows are reported in the right hand side of Figure 87. As can be seen, no change is observable for AIC, owing to its time invariance. Conversely, an abrupt loss of accuracy affects the biggest CNN model, whose RMSE error maintains the same profile at the expenses of a 20x increase in the magnitude. Such behavior can be attributed to over-parametrization problems as well as to poor generalization capabilities of the CNN due to the huge amount of parameters to be learned with respect to the actual amount of instances used in the training phase and the complexity of the problem at hand. In more detail, this is due to the fact that the number of learnable parameters largely exceeds the total amount of training instances. Besides, a second reason for such difference in CNN performances consists in potential overfitting,

i.e., over-adaptation to the training dataset leading to a lack of capability to generalize during testing. Consequently, the biggest CNN model may not adequately capture the ToA information.

Conversely, as shown in Fig. 87, the smallest CNN model is not prone to overfitting and over-parametrization, thanks to its more appropriate balancing between the number of trainable parameters and available data. Therefore, the distilled model is capable of generalizing from the trend hidden within training data, which is actually the expected goal of the neural network, rather than memorizing the training data itself, as happens with the largest CNN. Proof is the fact that the small CNN model is still capable of providing coherent results, once again showing the best results among all the considered methods. For these reasons, only the small CNN model and CapsNetToA will be taken into consideration in the following analyses, due to their better performances in terms of memory footprint, accuracy and generalization with respect to the length of the pre-trigger window.

Finally, the computational complexity of the designed NN models has also been evaluated in terms on execution time in order to assess their actual portability on edge devices. To this end, when tested on a 1.8 GHz dual core Intel® core i-5 processor, the average inference time for a single signal has been measured equal to 8.63 ms, 4.79 ms and 39.61 ms for CNN, small CNN and CapsNetToA (comprehensive, in this case, of both CapsNet and the time retrieval logic), respectively. As can be observed, the computational time nearly halves while moving from the biggest to the smallest CNN, while CapsNetToA shows the longest execution time. This is due to the fact that this architecture requires the ToA output probability curve to be reconstructed from several overlapped windows of the input signal, an operation which imposes CapsNet to be executed multiple times. For the specific CapsNet design considered in this work, 1200 sliding windows need to be processed, each of them asking for nearly 30  $\mu$ s. Note that such amount of time can be reduced either by reducing the number of windows or by changing the length of the window itself. In line with these results, it is worth saying that, even if the performance might scale when the same algorithms are deployed on embedded devices depending on the frequency clock of the featured processor, the above reported execution times are compatible with the near-sensor implementation of the investigated models.

#### 13.4 EXPERIMENTAL VALIDATION: TOA FOR ACOUSTIC SOURCE LOCALIZATION

In this Section, experimental data for a laboratory aluminum plate are exploited to assess the suitability of the trained models to cope with acoustic source localization problems.

##### 13.4.1 *Materials*

The exploited numerical simulator implicitly models the mechanical behavior of the companion laboratory plate presented in Section 9.3. Therefore, the trained models returned at the end of the preliminary validation phase were employed for localization purposes with real-field data.

It is worth recalling that, for the considered scenario, acoustic waves are actuated in form of guided elastic waves via a tone burst of 2 cycles, central frequency of 250 kHz and nominal amplitude of 0.6 Vpp by means of an arbitrary waveform generator Agilent 33220A: its output was passed through a gated power amplifier RITEC GA-2500A (100x signal magnification) and then connected to an actuator, a Murata piezoelectric ceramic

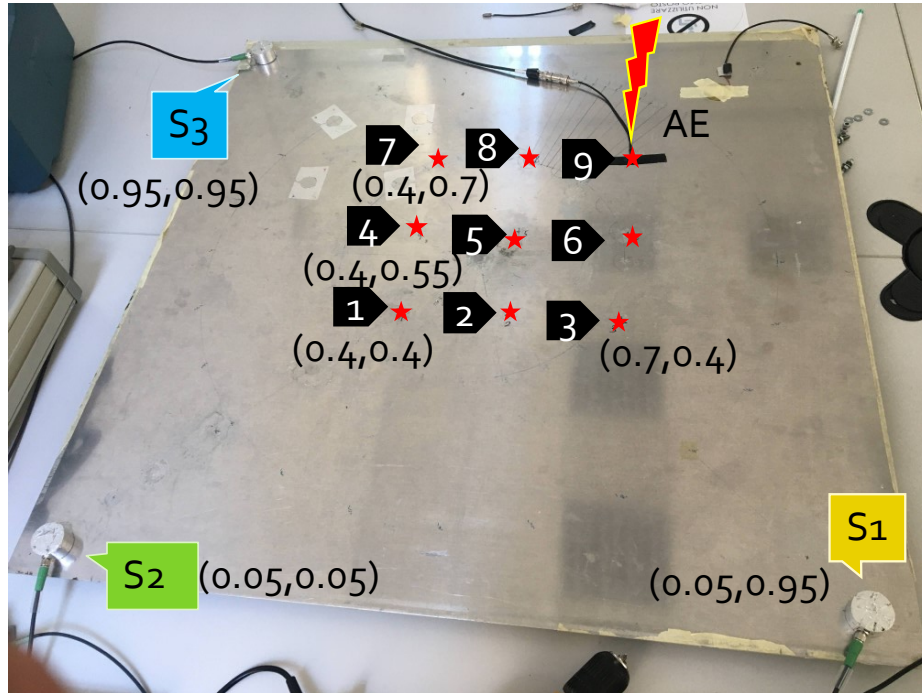


Figure 89: Sensor deployment on a metallic laboratory plate for the sake of AE source localization.

disc. As schematically drawn in Fig. 89, three of these discs ( $S_1$ ,  $S_2$ ,  $S_3$ ) were installed at three different corners of the plate and connected to one ISSLab piezoelectric sensor node, which is in charge of data collection.

### 13.4.2 Methods

#### 13.4.2.1 Objectives and testing procedures

Three different kinds of experiments were performed, pursuing two main objectives: (i) assess the time picking performance against operative disturbances responsible for important noise levels; (ii) evaluate the suitability of the devised neural network architectures to deal with source localization. Three different experiments were conducted:

1. *Drill experiments*: to mimic the effect of noisy environments, a power drill was intentionally activated in the proximity of the structure while collecting signals generated by impact excitation in correspondence of point 5. In order to perform a consistent statistical characterization, experiments were repeated 30 times by progressively increasing the pre-trigger window from 1000 to 1500 at integer steps of 50 samples.
2. *Additive white Gaussian noise experiments (AWGN)*: these tests share the same logic of the drill experiments, but a different source of noise was used in this case. In particular, an arbitrary white noise waveform actuated via a second piezoelectric transducer located in the upper right part the plate has been considered for better reproducibility. As before, experiments were repeated 30 times for varying pre-trigger windows, keeping point 5 for excitation.
3. *Localization experiments*: nine different points were selected for actuation (indicated in Fig. 89), which are uniformly spaced in a square area with length equal to 0.3 m. For



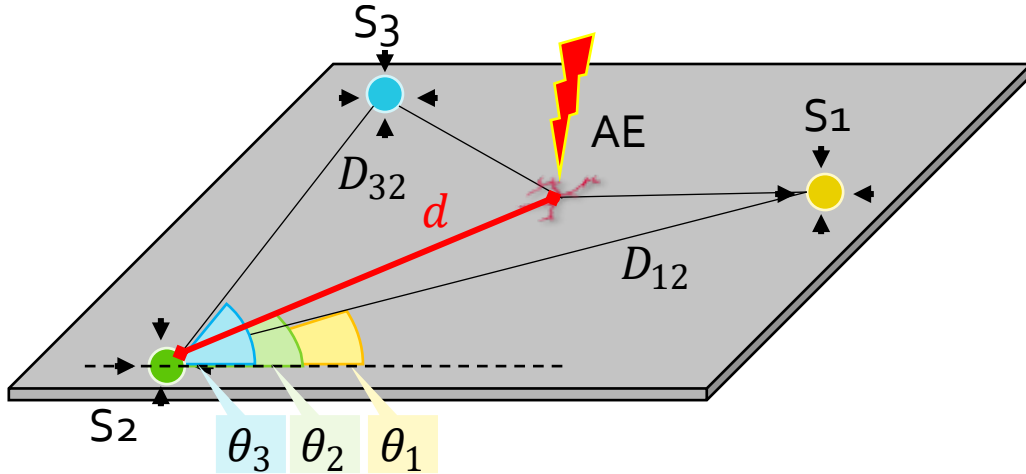


Figure 90: Geometrical representation of the adopted localization model via a three sensor array: the objective is to estimate the AE-to-sensor distance  $d$  and its relative direction  $\theta$ .

each point, experiments were repeated three times with a constant sample window of 5000 samples, pre-trigger window of 1500 samples and sample rate equal to 2 MHz.

#### 13.4.2.2 Localization algorithm

To achieve successful object localization in 2D environments, a minimum network density of three sensing elements with known position has to be deployed on the monitored structure. Among the various strategies, the triangulation method proposed in [301] has been leveraged for its geometrical simplicity, straightforward application in combination with ToA estimation and well-proven functioning for isotropic/homogeneous structures, as the one offered by the considered test-bed.

A graphical rendering of the triangulation problem is pinpointed in Fig. 90, where a toy plate is supposed to be instrumented with a network of three sensors, namely  $S_1$ ,  $S_2$  and  $S_3$ . If  $S_2$  serves as a reference sensor for the network,  $\theta_1$  and  $\theta_3$  represent the relative orientation of sensor  $S_1$  and  $S_3$  with respect to an horizontal axis passing for  $S_2$  and aligned along the longitudinal dimension of the plate; similarly,  $D_{12}$  and  $D_{32}$  indicate the spatial distance between the two pairs of sensors with respect to  $S_2$ .

Now, if an acoustic event occurs at a generic point of the structure, the triangulation algorithm aims at retrieving the set of polar coordinates  $(d, \theta)$  uniquely identifying the acoustic source in the space.  $d = d_2$  corresponds to the sought  $S_2$ -AE distance, while  $\theta_2 = \theta$  indicates which, among all the possible directions, the acoustic signal comes from. Once generated, the acoustic wave propagates in the structure and strikes the three sensors in three different instants of time due to the different AE-to-sensor distance: by application of any of the ToA estimation strategies investigated before, a guess of these onset times can be formulated. Let's denote them as  $ToA_1$ ,  $ToA_2$  and  $ToA_3$  for  $S_1$ ,  $S_2$  and  $S_3$ , respectively. Unfortunately, these quantities do not coincide with the physical time  $t_i = d_i/c_g$  taken by the wave to travel the corresponding distances  $d_i$  at a wave speed  $c_g$ ; they rather represent a cumulative sum between  $t_i$  and the event actuation time  $T_0$ , which is common to all the sensors but not known to the system.

Thus, even if geometrically well-posed, the estimation of  $d$  from the mere knowledge of  $ToA_2$  is not practicable. However, by computing the time difference of arrival out of the absolute  $ToA$  between the reference sensor  $S_2$  and the two remaining nodes, the  $T_0$ -independent quantities

$$\begin{aligned}\delta t_{32} &= ToA_3 - ToA_2 = (t_3 + T_0) - (t_2 + T_0) = t_3 - t_2 \\ \delta t_{12} &= ToA_1 - ToA_2 = (t_1 + T_0) - (t_2 + T_0) = t_1 - t_2\end{aligned}$$

can be obtained for sensor pairs  $S_2$ - $S_3$  and  $S_2$ - $S_1$ , respectively: more importantly, they coincide with the physical differences between the true wave propagation times. Analogously, the spatial difference between the travelled distances can be formulated as:

$$\begin{aligned}\delta d_{32} &= d_3 - d = c_g \delta t_{32} \\ \delta d_{12} &= d_1 - d = c_g \delta t_{12}\end{aligned}$$

The mathematical problem can thus be solved by means of the linear system:

$$\begin{cases} d_3 = d + c_g \delta t_{32} \\ d_1 = d + c_g \delta t_{12} \end{cases} \quad (63)$$

which is, in this form, not solvable since three unknowns but only two equations are available. To overcome this issue, it is sufficient to apply simple trigonometric relationships to the geometrical scheme of Fig. 90: in particular, the Carnot's theorem states that:

$$d_3^2 = d^2 + D_{32}^2 - 2dd_{32} \cos(\theta_3 - \theta) \quad (64a)$$

$$d_1^2 = d^2 + D_{12}^2 - 2dd_{12} \cos(\theta - \theta_1) \quad (64b)$$

Hence, by taking the square power of both sides of Eq. (63) and plugging Eq. (64a) and Eq. (64b) in its first and second row, respectively, the system can be rewritten only in terms of  $d$  and  $\theta$ , which are the sought output of the localization process:

$$\begin{cases} d = \frac{1}{2} \frac{D_{32}^2 - c_g^2 \delta t_{32}^2}{c_g \delta t_{32} + D_{32} \cos(\theta_3 - \theta)} \\ d = \frac{1}{2} \frac{D_{12}^2 - c_g^2 \delta t_{12}^2}{c_g \delta t_{12} + D_{12} \cos(\theta - \theta_1)} \end{cases} \quad (65)$$

Algebraic manipulation of the system in Eq. (65) yields the auxiliary solving equation for  $\cos \theta$  to coincide with:

$$r \sin(\theta + \theta_a) = K \quad (66)$$

with

$$\begin{aligned}
G &= \frac{D_{32}^2 - c_g^2 \delta t_{32}^2}{D_{12}^2 - c_g^2 \delta t_{12}^2} \\
g_1 &= GD_{12} \cos \theta_1 - D_{32} \cos \theta_3 \\
g_2 &= GD_{12} \sin \theta_1 - D_{32} \sin \theta_3 \\
K &= -c_g(G\delta t_{12} - \delta t_{32}) \\
r &= \sqrt{g_1^2 + g_2^2} \\
\theta_a &= \tan^{-1} \left( \frac{g_1}{g_2} \right)
\end{aligned}$$

Finally,  $d$  can be computed back from the system in Eq. (65). By knowing  $\theta$  and  $d$ , the estimated AE source position  $\hat{P}(\hat{x}_P; \hat{y}_P)$  can be easily derived as

$$\begin{cases} \hat{x}_P = x_{S_2} + d \cdot \cos \theta \\ \hat{y}_P = y_{S_2} + d \cdot \sin \theta \end{cases} \quad (67)$$

where  $x_{S_2}$  and  $y_{S_2}$  represents the 2D coordinates of the reference sensor  $S_2$ .

#### 13.4.2.3 Performance evaluation procedure

All the quantities appearing in Eq. (66), apart from  $\delta t_{12}$  and  $\delta t_{32}$ , are deterministic once the sensor network configuration has been defined. As such, achieving good localization capability is, inversely, a synonym of accurate onset time estimation and offers, in these terms, a powerful means to assessing the quality of the time picking activity of the devised NN models. Note that, in this operative setting where no synchronization is present between the actuation and the reception components of the monitoring network, no possibility exists to define a true ground truth due to the uncertainties implied by the experimental setting.

In the first stage of experimental verification, focused has been posed to the mere time detection capability of the devised NNs while disregarding additional sources of errors (e.g., imperfect estimation of the true wave speed) and avoid their propagation through the mathematical steps necessary to solve Eq. (66). Therefore, a preliminary analysis has been carried out to estimate the pure  $DT_{oA}$ : to this end, the predicted  $\hat{\delta t}_{12}$  and  $\hat{\delta t}_{32}$  values were compared with their theoretical expectations, given by physical relationships, and their absolute difference was computed.

Four  $ToA$  estimators were considered for this purpose: beside the three NN models trained on the synthetic data, AIC and X-Corr were also applied from the pool of conventional statistical approaches. For each of the three experiments, results were globally judged in terms of mean value  $\mu$  and standard deviation  $\sigma$  describing the statistical distribution of the absolute errors for  $DT_{oA}$  estimation coming from multiple realizations of the same test.

Finally, since the objective was to demonstrate the superior ability of NN models to cope with  $ToA$  estimation problems, for which AIC is currently recognized as a benchmark solution in the field, results were formatted in a more readable fashion by computing the mean and standard deviation ratios

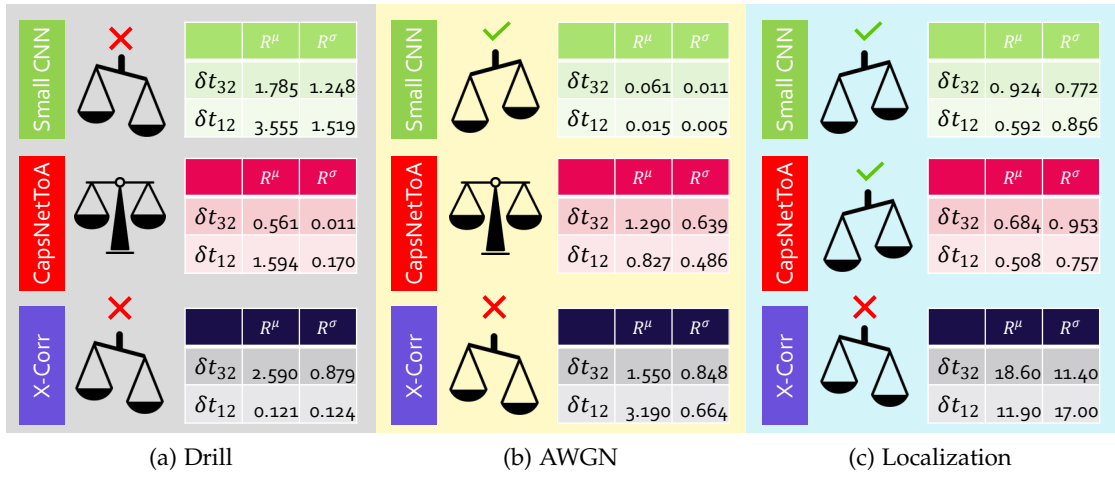


Figure 91: Ratios in the mean ( $R^\mu$ ) and standard deviation ( $R^\sigma$ ) of the absolute errors for ToA estimation in the framework of the laboratory metallic plate: (a) drill, (b) AWGN and (c) localization experiments.

$$R^\mu = \frac{\mu_x}{\mu_{AIC}} \quad (68a)$$

$$R^\sigma = \frac{\sigma_x}{\sigma_{AIC}} \quad (68b)$$

between AIC-driven scores (subscript  $AIC$ ) and the ones returned by all the remaining methods (subscript  $x$ ): a ratio higher than one indicates that AIC performs averagely better, and vice versa for ratios inferior to the unitary value.

### 13.4.3 Results

Results in terms of  $R^\mu$  and  $R^\sigma$  are displayed in Fig. 91 for each of the three different types of experiments: drill, AWGN and localization are provided in Fig. 91a, 91b and 91c, respectively. Read by row, each entry is associated, from top to the bottom, to small CNN, CapsNetToA and X-Corr.

As a primary observation, X-Corr shows the worst accuracy levels in all the different settings, especially for localization tests. On the other hand, albeit CapsNet and small CNN proving high effectiveness in some estimations, their performances are not always superior to the ones of AIC. Nevertheless, despite this aspect which is mostly related to the different effect of induced noise with respect to the Gaussian assumption adopted for dataset generation, the consistency of these models is corroborated by a lower standard deviation.

Given these preliminary analyses, the Euclidean distance  $d_p = |P - \hat{P}|$  between the true  $P(x_p; y_p)$  and estimated  $\hat{P}(\hat{x}_p; \hat{y}_p)$  AE position returned by Eq. (67) was computed in a final stage of the validation procedure to assess the accuracy in source localization task. To precisely evaluate the effect of noise, and following the testing procedure described in Section 13.3, white Gaussian noise has been added to the gathered time series by sweeping the SNR in the interval 2-20 dB at integer steps of 4 dB. In this way, it was possible to investigate how the same model could perform in remarkably harsher propagating envi-

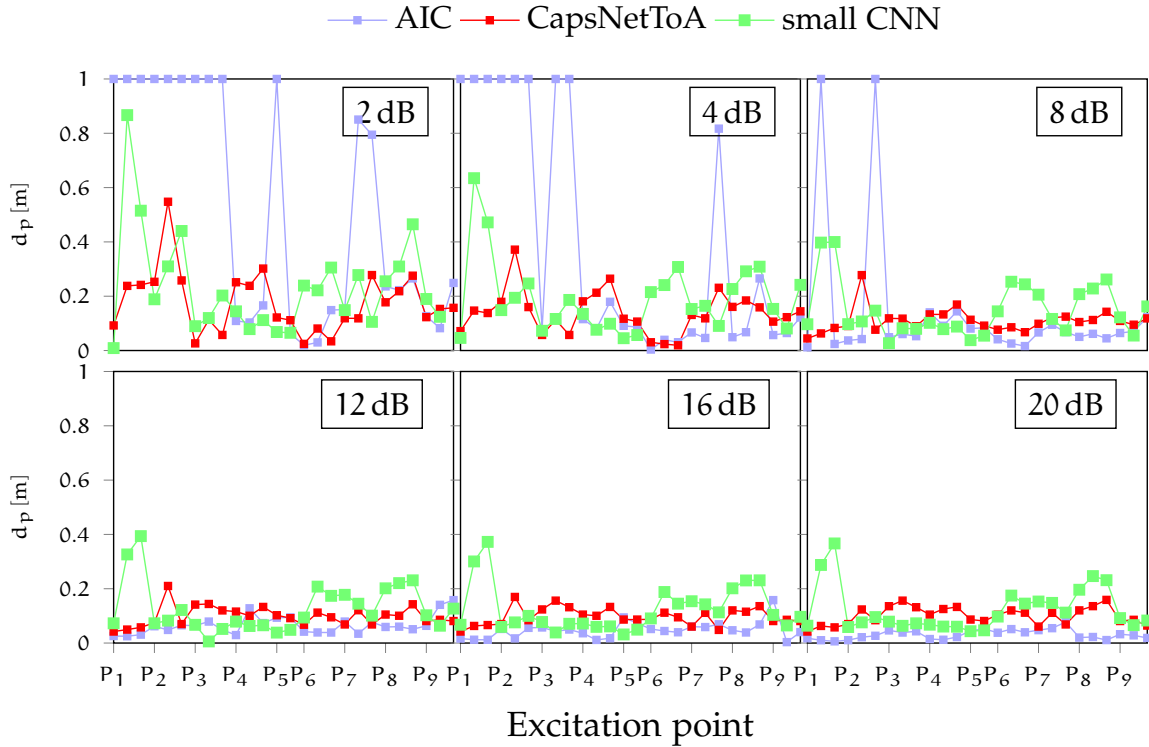


Figure 92: Absolute errors for acoustic signal localization on a laboratory metallic plate under various noise levels.

ronments, as they could appear in real AE scenarios subject to varying but not predictable noisy conditions.

Outcomes from localization experiments are drawn in Fig. 92: for each excitation point, three markers are included, corresponding to as many tests in this configuration. Additionally, it is worth specifying that points indicating a constant error of  $d_p = 1$  m have been included to identify all those cases in which the estimated coordinates are not compatible with the physical solutions for the structure at hand (i.e., negative or larger than 1.41 m distances, which is the maximum propagation length for this plate). Besides, Fig. 93 provides an example of time domain signals for excitation point 5 in two different noisy conditions: 20 dB on the left column and 8 dB on the right, with magnified ToA values in the second row.

First of all, one remark is worthy of attention, which is related to the difference in the experimental signals with respect to the synthetic ones employed for training (see comparison between Figure 86 and Figure 93). In fact, in the real setting, the effects of the sensor transfer function as well as the detrimental ones due to attenuation, multiple reflections and propagation in the physical medium might lead the envelope of the acquired signals to vary in a significant way. As such, being capable of obtaining an accurate prediction on real signals starting from a simulated dataset can be seen as a more severe test to be passed.

Going deeper into the results, the NN methods provide more consistent estimates, irrespective of the single excitation point and just showing a minor increment starting from  $\text{SNR} = 4$  dB, where the errors increase up to 30 cm for 2 dB, which represents a challenging working condition for AE equipment. Conversely,  $d_p$  reduces to a large extent in all the

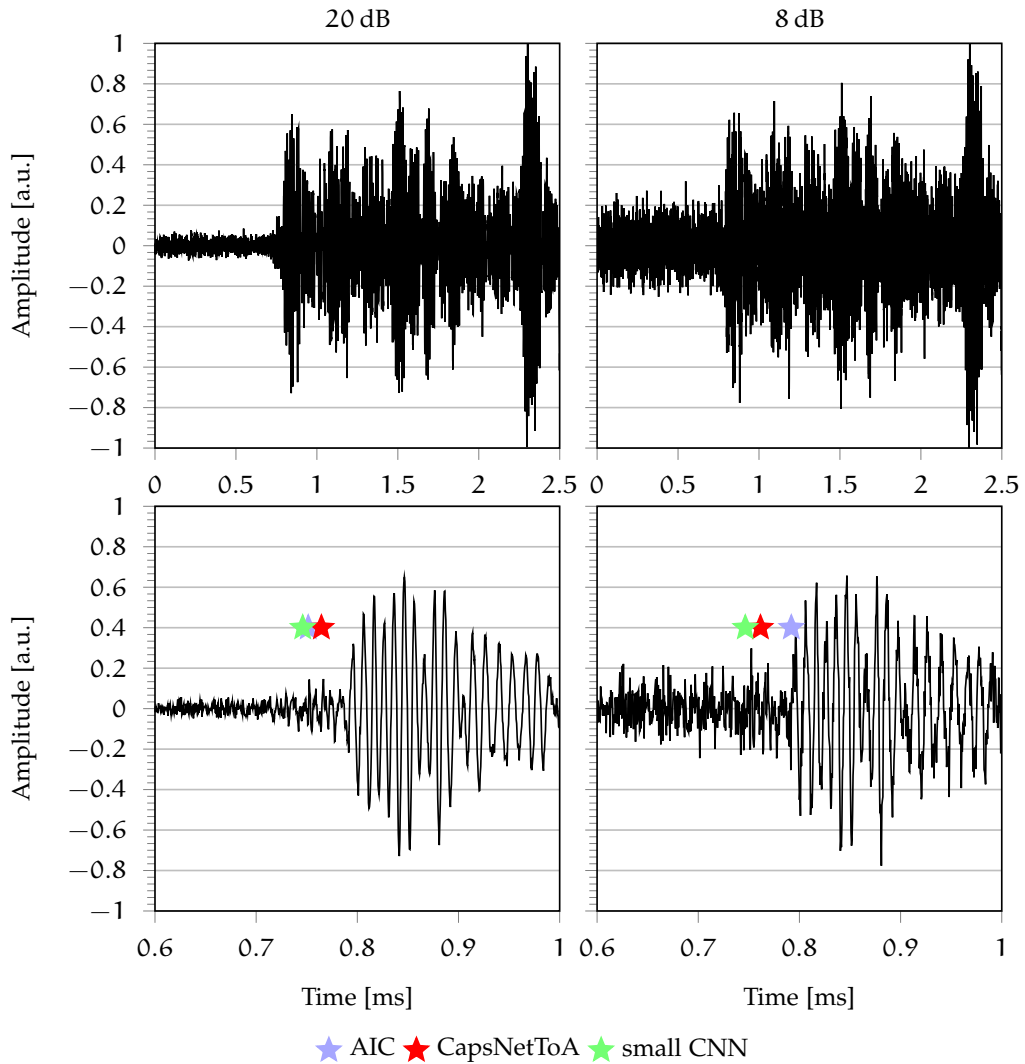


Figure 93: ToA predictions for AIC (blue), CapsNetToA (red) and small CNN (green) for excitation point 5: (left column) SNR = 20 dB and (right column) SNR = 8 dB, with second row depicting a magnified region of the time interval where ToA is located.

remaining noisy configurations, the CapsNetToA model being the most accurate estimator with an average error of 5 cm, followed by small CNN, whose average error is less than 8 cm.

Moreover, it is possible to observe that the quite similar localization pattern shown by small CNN, which tends to worsen the lower the SNR, is a consequence of the noise generation procedure, according to which the same signal, but with different additive noise, are processed. For the same reason, even if less pronounced, an analogous trend characterizes also AIC and CapsNetToA.

The slightly better performances of CapsNetToA with respect to small CNN can be attributed to the superior generalization capability of the first solution, which better handles the discrepancy between the actuated pulse and the synthetic one used during training. This generalization capability is a very desirable property in practical scenarios, where the actuated pulse is unknown.

Moreover, the same plots show that, despite AIC being highly performative in low noise conditions, as proven by a maximum deviation of 7 cm for the 20 dB configuration, the introduction of high noise levels leads AIC to completely fail ( $d_p = 1$  m) in multiple positions (e.g.,  $P_1, P_2, P_3$ ).

The above considerations confirm the trends already reported in Fig. 87, showing that AIC remains a robust and competitive strategy for AE signal characterization for relatively low noise values affecting data, whose drawbacks in dealing with poor SNRs can be overcome via AI approaches, which can still achieve a satisfactory level of precision in the identification of the acoustic source.

### 13.5 CONCLUSIONS

In this Chapter, NN models were proposed to deal with the problem of ToA estimation in AE-monitoring: two CNNs of different complexity and one CapsNetToA model combining the advantages of CNN and CapsNet. The capabilities of these DL-driven methods was measured both with synthetic and experimental data, showing an average accuracy 10x higher to the one achievable with conventional alternatives, which systematically fail in presence of significant noise levels.





In this dissertation, novel signal processing techniques have been introduced, discussed and implemented, under the cap of the edge processing paradigm as a means to optimizing the underlying sensing, communication and data management layers of SHM systems. Such research effort has been conducted by investigating both horizontal aspects common to multiple monitoring applications, and the specificities of the individual problems.

Hereinafter, the main contributions described in the three parts of this Thesis will be briefly recalled and further commented in a comprehensive manner.

#### 14.1 MAIN CONCLUSIONS OF PART I

In Part i, novel signal processing techniques aimed at solving open issues in vibration diagnostics have been proposed with the ultimate goal of pursuing a joint HW–SW optimization of the dedicated monitoring architecture. In particular, starting from the sensing up to the structural diagnostic layer, the mutually interrelated findings discussed in this Thesis can be summarized as follows:

- The sensor network implementation can be tackled with a divide–and–conquer strategy based on clustered architectures, which are the backbone of the full–scale improvement of the monitoring process, thanks to the flexible allocation of the computing and power resources. Such solution presents two additional benefits: firstly, thanks to local processing capabilities, it permits to reduce the network congestion in comparison to centralized alternatives. Secondly, the cluster–based characterization procedure offers a preliminary means for defect localization by probing for local anomalies in the estimated structural parameters.
- Clustered architectures are intrinsically compliant with the deployment of heterogeneous sensor networks, in which the advantages of individual sensing technologies can be combined. In particular, the possibility to process and merge acceleration data and angular velocities on smart sensor boards has been demonstrated for the retrieval of tilt angles. Furthermore, a cost–effective vibration analysis method has been disclosed via the the development of a processing flow fusing together inertial signals with mechanical displacements recorded by low–cost and minimally invasive piezoelectric discs.
- Graph Signal Processing may pave the way to a versatile strategy for sensor clustering on very large and complex structural geometries. This is due to the fact that GSP allows for the proper reconstruction of global structural parameters even in presence of non–overlapped clusters of sensors. This implies a more flexible sensor deployment, reduced wiring, and minimal sensor density.
- Data compression techniques running on extreme edge devices represent a viable solution to cope with both local and global sensor network optimization. Being capable of performing a near–sensor compression allows to: (i) conveniently exploit

the limited storage resources of the sensor nodes, (ii) lower the transmission time and the related power consumption and, consequently, (iii) extend sensor life-cycle.

- Among the possible compression strategies, the low computational cost of the Compressed Sensing encoder combined with a model-based adaptation approach can be used for efficient data reduction at the extreme edge of the monitoring network without affecting the quality of the reconstructed structural features.
- System Identification can be successfully applied for network load reduction. This technique achieves massive compression levels, which are at least one order of magnitude higher to the ones attainable by conventional alternatives. Moreover, it has been demonstrated how an efficient management of the available computational/memory resources, in conjunction with advanced linear algebra operators, can significantly shrink the computational cost involved by SysId and make it suitable for near-sensor embodiment. A comprehensive cost-benefit analysis has revealed that, despite the higher algorithmic cost, the proposed extreme-edge implementation of SysId is, in terms of energy, one forth less onerous than standard compression methods.
- In essence, SysId is a means to perform the features extraction task at the extreme edge. This is the fundamental difference with CS-schemes which are based on a lossy recovery of the acquired time series in central processing units, where feature extraction and inference can be run. Quite interestingly, among the features extracted with SysId, those typical of the operational modal analysis, i.e., peak frequencies and mode shapes, are included. This paves the way to future monitoring opportunities, in which even the inference process is brought at the extreme edge.
- It has been proven that a one-class classifier neural network provides an effective tool to deal with structural anomaly detection. In particular, when fed with damage sensitive features, (e.g., frequency-related parameters in the case of vibration diagnostics) and temperature data, these algorithms are suitable to monitor, in a completely automatic way, the non linear and non predictable – via standard methodologies – influence of environmental and operational factors on the nominal vibration response, providing remarkable classification performance.
- A TinyML approach for vibration-based structural inference can be adopted by leveraging the on-board digital signal processing functionalities made available by smart sensors. The possibility to perform the structural assessment at the edge between the physical and the digital world not only can accelerate the diagnostic process, but can further reduce the energy consumption and the network congestion.
- Relying on the previous results, a comprehensive framework for the structural assessment of vibrating structures has been investigated by proving the feasibility to combine all the investigated means for network optimization at the different stack of the SHM chain: from data compression up to TinyML-enabled structural inference, in conjunction with feature extraction at the extreme edge.

## 14.2 MAIN CONCLUSIONS OF PART II

In Part ii, it was shown how, by exploiting the near-sensor processing functionality of intelligent sensors, it is possible to implement efficient ultrasound communication schemes by actuating and sensing, with piezoelectric transducers, guided elastic waves that can travel across media impenetrable to electromagnetic waves. It is worth noting that the same sensor network can be used also for structural inspection by tracking anomalous echoes.

Different modulation techniques were considered to tackle the additional complexities induced by the guided propagation, such as multi-path interference, multi-modality and dispersion. More specifically, the following results have been attained:

- Frequency Division Multiplexing realized via binary excitation can be readily integrated in low-power edge devices, equipped with minimal digital signal processing functionalities, for the implementation of multiple-in multiple-out communications at the sensor level. With the proper tuning of the carrier frequency, a data rate in the order of hundreds of kbps has been achieved, even when the waveguide is highly irregular.
- Code Division Multiplexing is a viable option when a large number of piezo-transducers is simultaneously firing, as typically happens for beamforming purposes. This is due to the possibility to encode transducer-specific messages via a unique codeword by means of a SW manipulation of the generated signals. Furthermore, the standard scheme at the basis of CDM has been extended by including an additional processing step, necessary to counteract the dispersive propagation behavior of elastic waves and, in turn, enhance the quality of the decoded information. An equivalent transmission rate of hundreds of kbps turned out to be feasible with this mechanism.
- Rather than performing dispersion compensation in a post-processing phase, a low-depth variant of the Time Reversal transmission technique has been proposed. The implemented method is compatible with the limited signal synthesis capabilities of low-cost pulsers. TR is combined with pulse position modulation and, by virtue of the channel reciprocity, allows for a direct suppression of inter-sensor interferences while filtering out also the effects of reverberation and reflection. In the dissertation, it has been shown that the adoption of a dedicated quantization mechanism can speed up the communication rate to tens of kbps.
- Finally, the spatial multiplexing capability of frequency steerable acoustic transducers has been paired with Quadrature Amplitude Modulation to implement a technique similar to those explored by modern 5G communications. Such approach yields to three main advantages. Firstly, it can theoretically achieve very interesting transmission rates, exceeding tens of kbps. Secondly, it is very robust against noise corruption. Lastly, it is based on minimally invasive transducers which can be integrated on the structure.

For the sake of clarity, Table 26 provides a summary of the investigated techniques towards the implementation of GWs-based communications. A comparative analysis is offered, by examining both the advantages and shortcomings of each solution, as well

Table 26: Summary of the investigated techniques for GWs-based digital data communication with highlighted characteristics and reported performances. Column "Top" stands for the sensor network topology they require, whereas column "C" indicates whether compensation procedures were also encompassed.

Technique	Characteristic			Tested setup & performance		
	Top	Pros	Cons	C	Scenario	Bit-rate
FDM via square-wave excitation	Sync. MIMO	<ul style="list-style-type: none"> <li>– Readily implementation with low-cost and low-power hardware</li> <li>– Simple spectrum-based bit reconstruction</li> </ul>	<ul style="list-style-type: none"> <li>– Limited transmission rate</li> <li>– Square-wave excitation length needs to be estimated in advance</li> </ul>	✗	Experimental testbed: <ul style="list-style-type: none"> <li>– Aluminum plate with 2 TX and 2 RX node</li> <li>– CFRP with 2 TX and 2 RX node</li> </ul>	0.17 kbps
CDM	Async. MIMO	<ul style="list-style-type: none"> <li>– Modulation achieved via software</li> <li>– Reduced cross-talk interference thanks to spreading</li> <li>– Very dense sensor networks with very high bit-rate</li> </ul>	<ul style="list-style-type: none"> <li>– Carrier frequency selection</li> <li>– More complicated system realization</li> <li>– More prone to inter-symbol interference</li> </ul>	✓	Experimental testbed: slender aluminum beam with 1 TX and 1 RX	189 kbps
LDTR-PPM	Sync. MISO	<ul style="list-style-type: none"> <li>– GW dispersion and cross-talk inherently suppressed</li> <li>– Readily implementation with low-cost pulsers</li> </ul>	<ul style="list-style-type: none"> <li>– Extension to MIMO is required</li> <li>– Tranceivers are required</li> <li>– Longer time for communication gating</li> </ul>	✓	Simulated testbed: aluminum plate with 1 TX and 3 RX nodes	10 kbps
QAM+FSAT	Sync. MIMO	<ul style="list-style-type: none"> <li>– Spatial multiplexing realized at the hardware level</li> <li>– High robustness to significant noise levels</li> </ul>	<ul style="list-style-type: none"> <li>– More complicated system realization</li> <li>– Non ideal coupling</li> </ul>	✗	Simulated testbed: aluminum plate with 1 FSAT	48 kbps

as the reported performances during the experimental validation phases. The number of receivers and transmitters which can be handled is indicated under the column "Top" in which it is also specified whether the transmission is synchronous or asynchronous.

As a general comment, the performances in terms of available bandwidth vary largely depending on the employed modulation scheme, with three orders of magnitude in between the highest (CDM) and lowest (FDM) data rate. Moreover, it is worth discussing the ease of deployment characterizing each technique. To this end, while the procedure entailed by FDM can be readily implemented in a time and algorithmic efficient manner, the same condition does not apply also in the other cases, for which the realization of the entire coding/decoding flow is more complicated and requires ad-hoc post-processing steps.

Additionally, the importance of applying dispersion compensation procedures must be highlighted, since the complex propagation pattern experienced by GWs does influence the quality of the decoded information. In this case, LDTR-PPM deserves particular attention since it is capable of effectively counteracting both the detrimental effects due to wave propagation and the ones associated with sensor interference. Conversely, for the

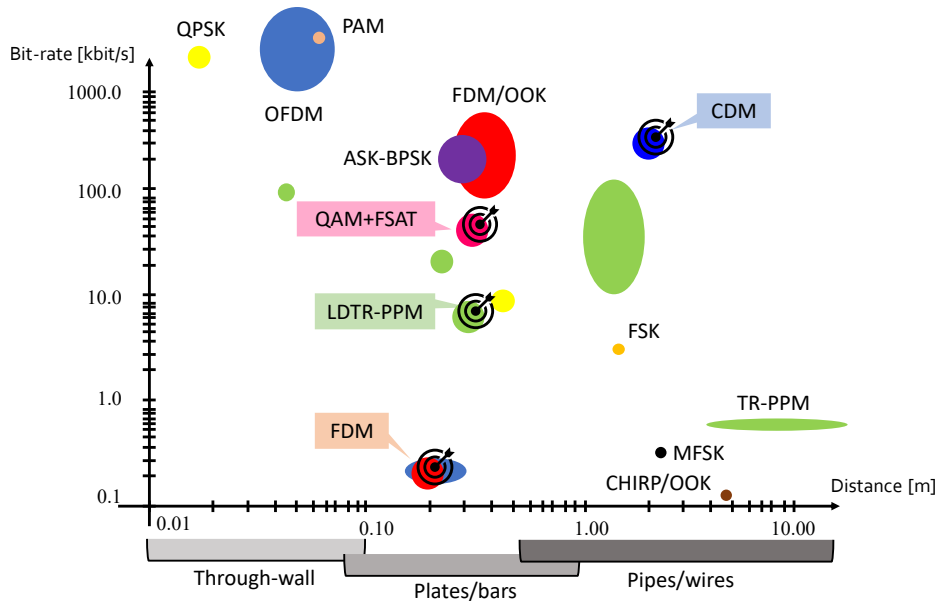


Figure 94: Comparison between the GWs-based communication strategies implemented in this work and state-of-the-art companion alternatives.

remaining techniques considered in this work, dedicated procedures to be applied in a post-processing phase are required to recover from such disturbances.

Finally, Fig. 94 extends the performance plot in Fig. 65 via superposition between the findings of this work with state-of-the-art solutions already discussed in Table 20. The following considerations are worthy of attention:

- The proposed CDM approach represents the first experimental validation of spread spectrum techniques for GW-based communication. Moreover, even if tested on a relatively simple testbed, it allows significant data rates and communication distances to be achieved.
- The performances of the deployed low-power FDM are comparable to the ones attained by OFDM for the same propagation distances. Furthermore, despite a drop or nearly three orders of magnitudes is registered with respect to previous works employing FDM, it is of paramount importance to underline that the specific GW-based communication system proposed here only exploits low-power MIMO sensor nodes, which do not require from commercial, bulky electronics.
- The combination of QAM with FSAT discloses new potentials for spatial multiplexing, a result which has been fostered by the unique frequency directivity of the novel transducers. As such, the performance of QAM+FSAT are comparatively better to the ones reported by FDM and LDTR-PPM being equal the communication distance.

### 14.3 MAIN CONCLUSIONS OF PART III

Part iii of the dissertation has been entirely devoted to the problem of onset time detection, also referred to as ToA, in acoustic emission-based monitoring. This problem is particularly complex when the signals are affected by non negligible noise sources, either

deterministic or random. Solutions inspired by the deep learning processing field were implemented, whose main features and performance are detailed in the following:

- Convolutional Neural Networks can efficiently cope with this challenge and, when properly trained on a consistent and exhaustive batch of data, they do overreach standard methods. Furthermore, it has been demonstrated how distilled models could both downsize the complexity of the model to a large extent and prevent overfitting problems affecting the quality of the results.
- Capsule Neural Networks extend the learning capabilities of CNNs by leveraging, in the learning process itself, the spatial relationships between the learned features. In addition, they are based on simpler and lighter neural networks which require much lower computational resources for accurate performance. Via CapsNet, ToA estimation is split into a two-step process: at first, the component related to the acoustic signal is discriminated from noise; then, the output is passed to a second block for proper time retrieval.
- The implemented models proved to be very competitive in terms of computational resources and source localization performances, especially in medium to highly noisy scenarios, with respect to standard methods, among which the Akaike Information Criterion has been chosen as reference.

#### 14.4 ONGOING RESEARCH ACTIVITIES

This dissertation has explored a novel paradigm in the structural health assessment of engineered structures that has been enabled by the advent of smart sensors and intelligent sensor systems, i.e., autonomous structural diagnostics running at the edge with minimal power and computational resources with respect to server-based computing.

This Section depicts a synthetic overview about the research activities which are currently in progress.

##### 14.4.1 *Objective 1: Tackling open issues*

In AE testing, ongoing research is focused on the TinyML implementation of the machine learning models proposed for ToA estimation. To this end, as anticipated, the small CNN model yields to a total model size, after conversion to the TFLite format, of nearly 150 kB with negligible loss of performances when tested on the synthetic dataset, i.e., this sensor-compliant version of the model reported a maximum RMSE of about 5  $\mu$ s, which is still more accurate than the AIC solutions for all the considered noise levels. Conversely, the original model size of CapsNetToA (taking into account both CapsNet and the time retrieval logic) has been estimated to be as large as 375 kB: a novel design flow is currently under investigation to further reduce this number and its related computational time.

In the vibration-based field, the investigation of alternative structural assessment strategies driven by SysId is of the utmost importance; in this case, the foreseen future developments are twofold. First of all, the demonstrated TinyML functionalities on the smart sensors may enable the estimation of SysId via AENN. The second possible development in SysId aims at overcoming the possible shortcomings of the local-to-global feature combination procedure and, hence, at being compatible with the retrieval of very faint spectral

peaks which are not easily identifiable via PP algorithms. To the same end, additional efforts have been spent to move standard OMA algorithms at the edge. More specifically, a recent work has focused on the edge coding of the FDD algorithm as a pivotal tool for centralized modal feature recovery [P25]. A similar perspective concerns the development of a novel version of the CS-based and TinyML-enabled framework in Fig. 40, in which the decoder block is omitted and compressed features are passed directly to a neural network block for the final diagnostic step.

Finally, in ultrasonic communications, the suitability of other modulation schemes to cope with the peculiar propagation behavior of GWs has to be investigated. Recently, further experiments have been conducted in which the working principle of the Orthogonal FDM was simulated, obtaining a transmission rate of more than 40 ksps in a squared plate sensorized with four devices. Similar experiments are currently conducted with FSAT prototypes.

#### 14.4.2 *Objective 2: Designing a custom monitoring network*

Despite serving as an effective, versatile and up-scalable platform for monitoring purposes, an improved version of the ISSLab sensor network employed in the experimental tests illustrated in this dissertation is currently under development to enhance its memory, computational and synchronization functionalities. The final aim is to design a new generation of smart sensor nodes equipped with all the electronics and circuitry necessary to efficiently collect, on-board elaborate and outsource the locally estimated features. In this sense, the design of a new generation of sensor nodes has been started with the ultimate goal of prototyping a highly optimized, yet easily re-configurable, smart device in which all the presented near-sensor algorithms can be executed.

Besides this, the possibility to implement some of the investigated algorithms in parallel low-power architectures has to be explored. This is specifically the case of the eS-TSQR-OLS procedure detailed in Fig. 33, which is inherently suitable for implementation in multi-core systems.

#### 14.4.3 *Objective 3: Testing the processing framework on real scenarios*

The validation of the investigated SHM methods in real structures affected by environmental and operative influences has an invaluable importance for the understanding of the actual robustness, resilience and effectiveness of the conceived solutions. Thanks to the research projects currently running at the University of Bologna, there will be opportunity to test the proposed strategies for the monitoring of both civil infrastructures and industrial plants. In particular, the test cases are related to the condition monitoring of the railway catenary system, and of large-size storage tanks. The former industrial case is ideal to test modal analysis solutions. In the latter case, the problem of acoustic source identification and location is crucial for corrosion monitoring.

### 14.5 FUTURE OUTLOOKS

The HW-SW co-design of sensors and systems for SHM is a process in constant development due to the stringent requirements for the real-field adoption and the parallel rapid

evolution of ICT products. As such, the promising technological advancements illustrated in this manuscript cannot be considered as final solutions, but rather must be intended as stepping stones for future, additional and more optimized solutions: most of them have already been mentioned in Section 14.4 and represent an active field of research. Without claiming to be exhaustive, some other possible improvements are worthy to be mentioned. For example, GSP could be exploited not only as a means for feature combination at the end of the characterization step, but specifically for the task of identification.

There is also plenty of room for improvements in the TinyML field. In fact, it is worth considering that, in the implementation procedure proposed in the dissertation, the training and testing phase of the NN machine are performed offline on different devices. Despite its advantages, such an approach poorly scales in time as the inference model needs to be updated. Consequently, novel frameworks involving model training at the edge should deserve primary attention in future TinyML realizations: in this direction, promising solutions are currently under investigation by leveraging the continual and reinforced learning concepts.

Beside the promising results achieved in the signal processing field, only a few research studies appraise their effective performance in presence of result or instrumentation uncertainties [302], [303], which are likely to affect the long-term assessment process. Moreover, it should be considered that such aspect becomes even more important in a near-sensor computing perspective, where the additional uncertainties due to embedded processors, such as low-depth data quantization and the need for simplified arithmetic operations, might destructively sum with the data variability induced by external factors (e.g., ambient and operational changes). Hence, the appropriate judgment of the true signal processing performance must take into consideration these potential drawbacks, since they might influence the structural bulletin at a large extent. Proof is the fact that, as stated in the roadmap to quantifying the benefit of SHM [304], the data analysis and interpretation process and, by extension, the entire monitoring technology (from sensing to data inference), are assigned maximum importance in the cost function maximizing the benefit of the SHM system itself. Therefore, future studies will be devoted to the thorough analysis of this pillar concept, by incorporating in the standard evaluation process novel models and variables tightly related to current issues in decentralized, edge-enable SHM solutions, such as result uncertainty due to low data quantization and/or sensor failure.



Part IV

APPENDIX



To be effective, a SHM architecture must rely on the optimal combination of hierarchical hardware resources (sensor nodes, gateways, edge processors) and the associated software infrastructure in charge of data management, data analytics and structural assessment. To address these issues, a low-power, light-weight and small footprint monitoring network with data-to-cloud capabilities was developed within the Intelligent Sensor System Labs of the University of Bologna [P4], [P26]. The network, referenced throughout the manuscript as ISSLab network, is designed to be, at the same time, low-cost, scalable, and easily reconfigurable to be suitable both for short-term and long-term monitoring tasks.

The architecture is composed of three elements: two compact devices, generally addressed to as *sensor nodes* — one interfacing PZT transducers and the other one hosting a 6 DoF IMU — integrating all the peripherals and circuitry necessary to autonomously collect, pre-process and manage data, and a purposely developed network interface, or *gateway*, which orchestrates the single device in a centralized manner and is extensively described in [P4].

The sensor nodes differ on the basis of the sensing element, which requires ad-hoc electronics for the proper acquisition and conditioning of the measured signal, while the network and communication layers are shared. This means that the two types of sensor nodes can be used either standalone or concurrently deployed on the same structure in case heterogeneous diagnostic approaches are required.

In the following, emphasis will be posed on the description of the technological features of sensor nodes and sensor network interface. Table 27 finally provides a synthetic overview of the ISSLab network characteristics.

#### A.0.1 *Communication layer*

The communication between all the device of the network is achieved via a multi-drop Sensor Arena Network (SAN) bus, which exploits Data-over-Power (DoP) communication based on the EIA RS-485 standard. Depending on the supplied power, up to 64 sensor nodes connected in daisy-chain can be joined simultaneously. At this prototyping stage, the selection of a wired connection was preferred over a wireless one to design lighter nodes, which did not require the presence of a battery. The communication protocol can be effectively used over long distances and in electrically noisy environments (which are common in several application fields) with an effective maximum data rate of 200 kbps. Data are transmitted sequentially, in packets, by exploiting a proprietary lossless encoding technique. The reception of each data packet must be acknowledged by the receiver before the next packet is sent by the transmitter.

During acquisition, signals are collected simultaneously by each sensor node. A unique time stamp is provided by means of an internal 32-bit high-speed hardware counter, clocked at 64 MHz; once every hour, a 32-bit low-speed software counter is updated.

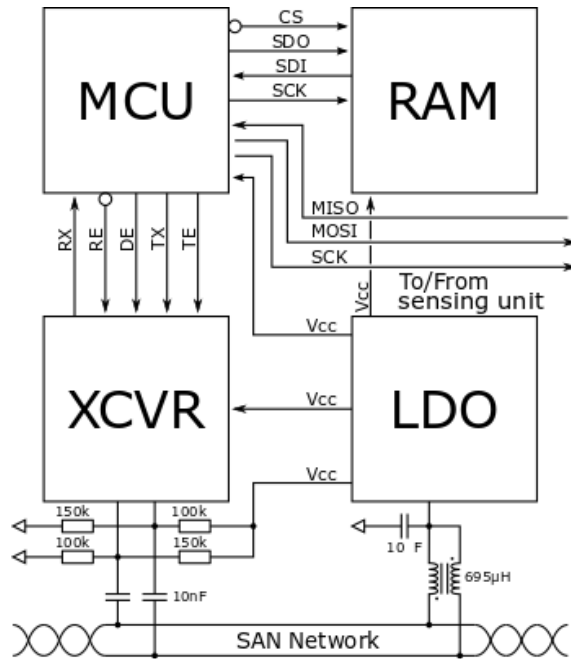


Figure 95: Generic four building block architecture of the ISSLab sensor nodes [P4].

Synchronization is another important aspect to be discussed. In the ISSLab network realization, a synchronization algorithm based on a software implementation of the classical three-way handshake adopted by the RFC 793 Transmission Control Protocol is exploited. First, the gateway sends a synchronization command addressed to a single node, then the receiving node responds with a similar command, addressed to the gateway, and, finally, the gateway sends an acknowledge message to the sensor node. The first two steps allow the gateway to compute the round trip time (RTT), whereas the last two steps allow the sensor node to compute the RTT. Several factors contribute to the RTT: the messages' encoding/decoding time, the messages' transmission time, the delays between the messages' transmission and reception at the electrical level, and the messages' processing time. The messages' transmission time is already known to the gateway and the sensor nodes since messages' length and data rate are known a priori and do not change over time; the sum of remaining terms, called residual RTT, conversely can change over time and was experimentally estimated to be largely dominated by the messages' encoding/decoding time: as such,  $RTT/2$  is considered a good approximation of the propagation delay at the software level. Thus, once each node in the network knows its own RTT ( $RTT_i$ ), the gateway issues a broadcast synchronization command containing its local time  $T_0$ ; following this last command, each sensor node in the network sets its internal counters to  $T_0 + RTT_i / 2$ . By issuing the synchronization command once per acquisition, the divergence between the sensor nodes' clocks in the proposed network over 2400 s of observations was 4.7 ms [P16] ©2011 IEEE.

#### A.o.2 Sensor node architecture

It is worth mentioning that each sensor node, irrespective of the sensing principle it exploits, is built upon the four building block architecture shown in Fig. 95:

1. **MCU:** the core element of the node is an ST Microelectronics STM32F303 MCU powered at 3.3 V that belongs to the family of low-voltage 32 bit mixed-signal processors with DSP functionalities enabled by a single precision FPU. It integrates 40 kB of RAM and 256 kB of FLASH memory, which are sufficient for data acquisition and signal pre/post processing. It contains two serial peripheral interfaces (SPI) and a universal synchronous/asynchronous receiver/transmitter (USART) together with all the clock generators, shift registers and data buffers necessary to perform input/output serial data transfers independently of device program execution.
2. **Serial RAM:** a microchip 23LC1024 128 kbit serial RAM device is used to lodge processed data samples waiting for further retrieval and expand the limited memory resources of the MCU, which might be insufficient for advanced signal processing. It features an unlimited number of read/write cycles and zero write time, allowing for data rate up to 20 Mbps in sequential access mode.
3. **Tranceiver (XCVR):** an ST Microelectronics ST3485EB 3.3 V XCVR for RS-485 and RS-422 communications is used to interface the MCU to the network bus. It guarantees 12 Mbps data rate at a very low-power consumption and it is connected to the SAN via a mesh of passive components.
4. **Low-dropout (LDO):** a Texas Instrument LM3480 LDO regulator supplies the entire node by fixing the output voltage at 3.3 V, regulated from the 5.0 V power supply required by the entire SAN bus.

### A.0.3 Sensing layer

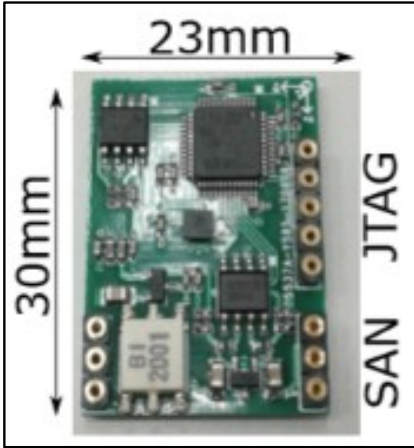
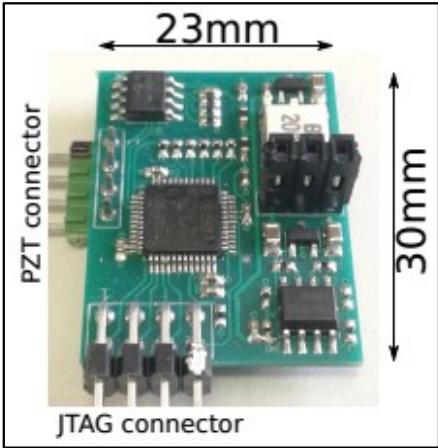
#### A.0.3.1 Inertial sensor node

A prototype of the sensor node developed for the purpose of vibration data collection is displayed in the left hand-side of Table 27. The sensing element constitutes of an ST Microelectronics LSM6DSL iNEMO IMU, namely a system-in-package device featuring a 3D digital accelerometer and a 3D digital gyroscope realized in MEMS technology.

The most important mechanical features of the linear and angular part are reported in Table 27 (label ACC and ROT). The inertial node is designed to gather highly accurate acceleration data thanks to a maximum dynamic range programmable from  $\pm 2$  to  $\pm 16$  g, coupled with a linear sensitivity of  $61 \mu\text{g}/\text{LSB}$  and a noise density of  $80 \mu\text{g}/\sqrt{\text{Hz}}$  in high-performance mode. The angular counterpart operates with a gyroscope sensitivity of  $4.375 \text{ mdps}/\text{LSB}$ , an angular velocity range varying from  $\pm 125$  to  $\pm 2000$  dps and a noise level of  $4 \text{ mdps}/\sqrt{\text{Hz}}$ . Available data rates for both the linear and angular acquisitions are comprised between 12.5 Hz and 6.664 kHz, with a flat frequency response in the whole bandwidth.

The sensor node is equipped with DSP functionalities, such as the execution of basic frequency-related operations and PP algorithms [P27], or more complex elaboration as the extraction of tilt angles from the combination of linear and rotational inertial data [P15].

Table 27: ISSLab sensor network portrait: electrical and network characteristics common to all the sensor nodes are included beside the main features of the inertial and piezoelectric sensor node.

	Inertial sensor node			Piezoelectric sensor node
				
Sensor	LSM6DSL	ACC	ROT	<ul style="list-style-type: none"> <li>- Three acquisition channels (PZT connector)</li> <li>- Embedded pre-amplifier: 9 gain levels (from x1 to x23)</li> <li>- Embedded 12 bit rail-to-rail ADC</li> <li>- Embedded coin-size pre-amplifier on PZT transducer</li> </ul>
	Full-scale	$\pm 2$ to $\pm 16$ g	$\pm 125$ to $\pm 2000$ dps	
	Data-rate	12.5 to 6664 Hz		
	Sensitivity	61 $\mu$ g/LSB	4.375 mdps/LSB	
	Noise density	80 $\mu$ g/ $\sqrt{\text{Hz}}$	4 mdps/ $\sqrt{\text{Hz}}$	
On-board DSP	STM32F303 MCU: <ul style="list-style-type: none"> <li>- Memory: 40 kB RAM, 256 kB FLASH</li> <li>- DSP: single-precision FPU for 32-bit data parallelism</li> <li>- Power: &lt; 40 mA @ 64 MHz in active mode</li> </ul> <div style="display: flex; justify-content: space-between;"> <ul style="list-style-type: none"> <li>✓ Fast Fourier Transform</li> <li>✓ Tilt angle</li> <li>✓ Peak Picking</li> </ul> <ul style="list-style-type: none"> <li>✓ Acoustic features: rise time, energy count, zero-crossing level</li> <li>✓ Self-calibration algorithm</li> </ul> </div>			
Network	<ul style="list-style-type: none"> <li>- SAN bus with multi-drop capabilities</li> <li>- Data-over-Power communication based on the EIA RS-485 standard</li> <li>- Proprietary lossless encoding technique</li> <li>- Maximum effective data-rate: 200 kbps</li> <li>- Three-way handshake synchronization protocol: software implementation of TCP</li> <li>- Synchronization error: 4.7 ms</li> </ul>			
Electrical	<ul style="list-style-type: none"> <li>- Low-power consumption: &lt; 40 mW in normal operating mode @ 5.0 V SAN</li> <li>- Up to 64 nodes connected in daisy-chain fashion</li> <li>- Industrial operative range: <math>-40^{\circ}\text{C}</math> to <math>85^{\circ}\text{C}</math></li> </ul>			

A.0.3.2 Piezoelectric sensor node

The working principle of the so-called piezoelectric sensor node, firstly described in [305], is the passive acquisition of bulk and/or guided waves originated by impacts, corrosion, or other source phenomena which travel along the sensorised structure. This sensor node features three acquisition channels (PZT connectors) connected to as many piezoelectric transducers and is equipped with all the analog signal conditioning and digital func-

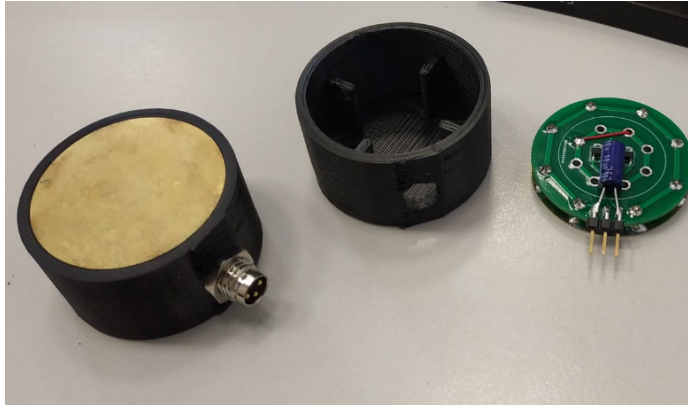


Figure 96: PZT transducer (left) with embedded pre-amplifier (right) and the lodging case (middle).

tionalities necessary for signal filtering and feature extraction. Hence, when the stress wave energy crosses a certain threshold, the sensor starts to store the signal from the PZT transducer and autonomously process data on-board. To increase the amplitude of the incoming signals, each transducer is connected to an embedded programmable gain amplifier which provides nine different gain levels, from  $\times 1$  to  $\times 23$ . Each analog signal is then sampled by an embedded 12 bit, rail-to-rail ADC with a programmable sampling frequency up to 800 kHz [P28].

PZT transducers (shown in Fig. 96) correspond to extremely low-cost PZT discs, i.e., buzzers whose cost does not exceed a couple of dollars. Each disc integrates and embeds coin-size pre-amplifier.

To fully exploit the advantages of this custom electronics and be compatible with pitch-catch monitoring configurations, an active variant of the same piezoelectric devices was designed, too. In this case, high-speed general purpose I/O drivers are used to drive the PZT transducers for data transmission purposes and make the sensor autonomous for the generation of custom signals.

#### A.o.4 *Sensor network interface*

Similarly to the sensor nodes, the SAN interface presents the four building block architecture in Fig. 97. An FTDI FT231X Universal Serial Bus (USB) to full handshake UART integrated circuit is used to provide USB 2.0 connectivity to a smart data relay device (i.e., a connected PC) with maximum data transfer rates of 3 Mbaud. It is operated by a single supply line taken directly from the USB bus and internally regulated to by integrated LDOs. A Linear Technology LTC4414 low loss PowerPath™ Controller (PPC) is used to create a near ideal diode function for power switchover and permits the interface a highly efficient management of the available power sources, namely the 5.0 V, 500 mA USB power supply line. The PPC primarily feeds a medium current LDO, which feeds an ST Microelectronic ST3485EB RS485/RS422 XCVR, used to interface the UART to the SAN network. Each interface node is roughly 48 mm  $\times$  26 mm wide, weights less than 10 g, and consumes 12 mA.

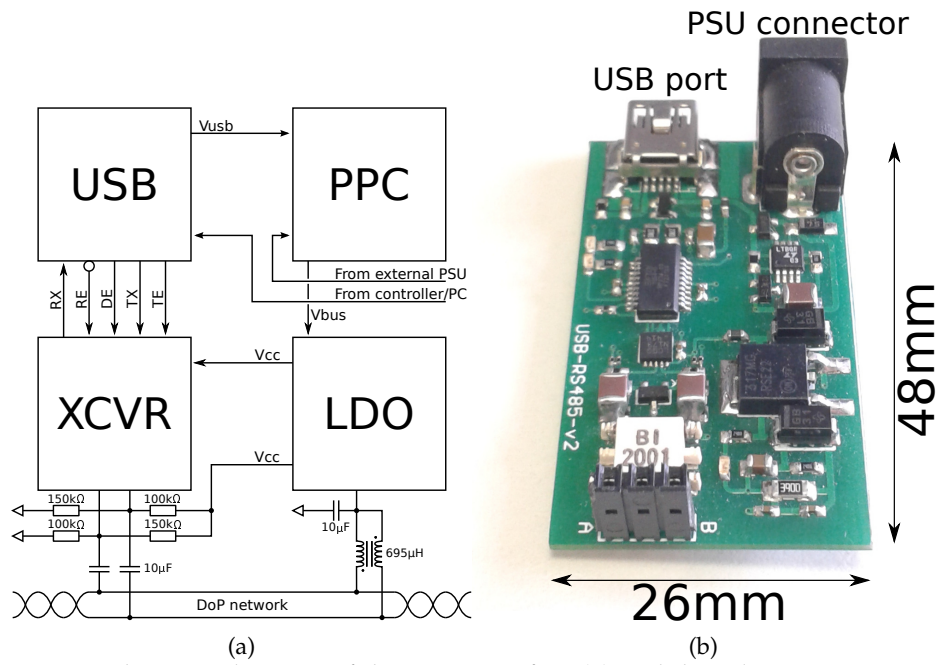


Figure 97: Schematic diagram of the SAN interface (a) and the relative prototype (b).



*Face your fear, empty yourself,  
trust your own voice, let go of control,  
have faith in outcomes, connect with a larger purpose,  
derive meaning from the struggle*

— Kano Jigoro

## ACKNOWLEDGMENTS

---

It is 7:01 in the morning of the last day of my Ph.D. when I switched on my PC and Google advertised me that today is Kano Jigoro anniversary. I do not know him, I am curious. I discover he his the guru of judo; more importantly, he dispensed several aphorisms.

One of them, in particular, attracts my attention, like the voice of an ancient mariner at the end of his trip, when he turns back to the moment in which he set sail and rewinds the film of the adventures encountered while exploring unknown seas. Today I feel like that boatswain diving into the ocean of my Ph.D. experience, during which I had to *face my fear, have faith in outcomes, connect with a larger purpose*.

Every crew needs a captain, and I have been blessed of having Prof. Luca as mentor. For his patience and never-ending support. For his search of perfectionism and scientific rigor. For his continuous stimuli and, first among all, for the trust has been deserving me since the first day. Thank you for holding the helm of my research journey and helping me finding the compass in the jungle.

Prof. Alessandro Marzani and Nicola Testoni. Your insightful suggestions, your utmost know-how and unconditioned love for research, have become a great source of inspiration. I will always be grateful to both of you for having accompanied me throughout this trip.

One special thank goes also to Prof. Eleni Chatzi and Vasilis Dertimanis, who granted me the exceptional opportunity to join their research group at ETHZ and explore new approaches to the fascinating world of SHM: your foremost expertise provided invaluable advancements to my studies.

I would like to send my sincere gratitude to Prof. Guido Masetti, the one who firstly fueled my passion for research and invited me to join his research group, that day. I would have never imagined it would have been such an amazing, thorough experience.

All the guys of the ISSLab at the University of Bologna: travelling with you in this entangled world of human and scientific research has been a great pleasure. In particular, a huge thanksgiving to Matteo: one hat, one pumpkin, the long-lasting research for the roots, all of them have been comfortable musics even in the most difficult days. I will never forget it.

All the students and the people who boarded in the same ship and I met in my path: each of you gifted me important pearls of wisdom. Marta, there is no need to mention that you are the foremost, the one who has always been supporting me in the most fruitful and critical manner I could have desired.

Finally. My family. My safe harbor. You instilled me the unconditioned passion for research, the humility and curiosity for the *other*, for the *others*, which I deem are pivotal milestones for whatever kind of *Research*. Paola. Enrico. Morena. Massimo. Didì. Worthless to say you have been my lighthouse in the night, in this roller-coaster journey of feelings, actions, silence; you have been the Dirac Delta of my daily life.

Now it is 7:20 of the last day of my Ph.D. It's time to go, with Kano's words in mind, to weigh anchor for novel, ready-to-be-discovered destinations. To be continued...

## PUBLICATIONS

---

- [P1] F. Zonzini, A. Girolami, L. De Marchi, A. Marzani, and D. Brunelli, «Cluster-based vibration analysis of structures with gsp,» *IEEE Transactions on Industrial Electronics*, vol. 68, no. 4, pp. 3465–3474, 2020.
- [P2] F. Zonzini, A. Girolami, D. Brunelli, N. Testoni, A. Marzani, and L. D. Marchi, «A graph signal processing technique for vibration analysis with clustered sensor networks,» in *International Conference on Applications in Electronics Pervading Industry, Environment and Society*, Springer, 2019, pp. 355–361.
- [P3] A. Girolami, F. Zonzini, L. De Marchi, D. Brunelli, and L. Benini, «Modal analysis of structures with low-cost embedded systems,» in *2018 IEEE International Symposium on Circuits and Systems (ISCAS)*, IEEE, 2018, pp. 1–4.
- [P4] N. Testoni, C. Aguzzi, V. Arditì, F. Zonzini, L. De Marchi, A. Marzani, and T. S. Cinotti, «A sensor network with embedded data processing and data-to-cloud capabilities for vibration-based real-time shm,» *Journal of Sensors*, vol. 2018, 2018.
- [P5] F. Zonzini, M. Zauli, M. Mangia, N. Testoni, and L. De Marchi, «Model-assisted compressed sensing for vibration-based structural health monitoring,» *IEEE Transactions on Industrial Informatics*, vol. 17, no. 11, pp. 7338–7347, 2021. DOI: [10.1109/TII.2021.3050146](https://doi.org/10.1109/TII.2021.3050146).
- [P6] F. Zonzini, M. Zauli, A. Carbone, F. Romano, N. Testoni, and L. De Marchi, «Hardware-oriented data recovery algorithms for compressed sensing-based vibration diagnostics,» in *International Conference on Applications in Electronics Pervading Industry, Environment and Society*, Springer, 2020, pp. 69–75.
- [P7] M. Zauli, F. Zonzini, N. Testoni, A. Marzani, and L. De Marchi, «Compressive sensing and on-board data recovery for vibration-based shm,» in *European Workshop on Structural Health Monitoring*, Springer, 2020, pp. 327–334.
- [P8] F. Zonzini, M. Zauli, M. Mangia, N. Testoni, and L. De Marchi, «Hw-oriented compressed sensing for operational modal analysis: The impact of noise in mems accelerometer networks,» in *2021 IEEE Sensors Applications Symposium (SAS)*, IEEE, 2021, pp. 1–5.
- [P9] F. Zonzini, V. Dertimanis, E. Chatzi, and L. De Marchi, «System identification at the extreme edge for network load reduction in vibration monitoring,» *IEEE Journal of Internet of Things*, 2021.
- [P10] F. Zonzini, C. Aguzzi, L. Gigli, L. Sciuillo, N. Testoni, L. De Marchi, M. Di Felice, T. S. Cinotti, C. Mennuti, and A. Marzani, «Structural health monitoring and prognostic of industrial plants and civil structures: A sensor to cloud architecture,» *IEEE Instrumentation & Measurement Magazine*, vol. 23, no. 9, pp. 21–27, 2020.
- [P11] C. Aguzzi, L. Gigli, L. Sciuillo, A. Trotta, F. Zonzini, L. De Marchi, M. Di Felice, A. Marzani, and T. S. Cinotti, «Modron: A scalable and interoperable web of things platform for structural health monitoring,» in *2021 IEEE 18th Annual Consumer Communications & Networking Conference (CCNC)*, IEEE, 2021, pp. 1–7.

- [P12] F. Zonzini, A. Carbone, F. Romano, M. Zauli, and L. De Marchi, «Machine learning meets compressed sensing in vibration-based structural health monitoring,» *IEEE Transactions on Instrumentation and Measurement*, 2021.
- [P13] F. Zonzini, F. Romano, A. Carbone, M. Zauli, and L. De Marchi, «Enhancing vibration-based structural health monitoring via edge computing: A tiny machine learning perspective,» in *Proceedings of the ASME 2021 48th Annual Review of Progress in Quantitative Nondestructive Evaluation QNDE 2021*, ASME, 2021, pp. 1–6.
- [P14] F. Zonzini, F. Romano, A. Carbone, M. Zauli, and D. Marchi, *Tinyml meets vibration-based structural health monitoring: Solving a binary classification problem at the edge*, <https://www.youtube.com/watch?v=RmUQzFTnGGY>, Jun. 2021.
- [P15] N. Testoni, F. Zonzini, A. Marzani, V. Scarponi, and L. De Marchi, «A tilt sensor node embedding a data-fusion algorithm for vibration-based shm,» *Electronics*, vol. 8, no. 1, pp. 1–1–4, 2019.
- [P16] F. Zonzini, M. M. Malatesta, D. Bogomolov, N. Testoni, A. Marzani, and L. De Marchi, «Vibration-based shm with up-scalable and low-cost sensor networks,» *IEEE Transactions on Instrumentation and Measurement*, vol. 69, no. 10, pp. 7990–7998, 2020.
- [P17] F. Zonzini, M. M. Malatesta, D. Bogomolov, N. Testoni, L. De Marchi, and A. Marzani, «Heterogeneous sensor-network for vibration-based shm,» in *2019 IEEE International Symposium on Measurements & Networking (M&N)*, IEEE, 2019, pp. 1–5.
- [P18] F. Zonzini, L. De Marchi, N. Testoni, C. Kexel, and J. Moll, «Guided-wave mimo communication on a composite panel for shm applications,» in *Health Monitoring of Structural and Biological Systems XIV*, International Society for Optics and Photonics, vol. 11381, 2020, p. 1 138 136.
- [P19] —, «A structural-aware frequency division multiplexing technique for acoustic data communication in shm applications,» in *European Workshop on Structural Health Monitoring*, Springer, 2020, pp. 769–778.
- [P20] C. Kexel, N. Testoni, F. Zonzini, J. Moll, and L. De Marchi, «Low-power mimo guided-wave communication,» *IEEE Access*, vol. 8, pp. 217 425–217 436, 2020.
- [P21] F. Zonzini, L. De Marchi, N. Testoni, and A. Marzani, «Direct spread spectrum modulation and dispersion compensation for guided wave-based communication systems,» in *2019 IEEE International Ultrasonics Symposium (IUS)*, IEEE, 2019, pp. 2500–2503.
- [P22] F. Zonzini, N. Testoni, A. Marzani, and L. De Marchi, «Low depth time reversal modulation technique for ultrasonic guided waves-based communications,» in *2020 IEEE International Ultrasonics Symposium (IUS)*, IEEE, 2020, pp. 1–4.
- [P23] M. Reyes, J. Moll, F. Zonzini, M. Mohammadgholiha, and L. De Marchi, «Quadrature amplitude modulation for acoustic data communication in ultrasonic structural health monitoring systems,» in *Proceedings of the ASME 2021 48th Annual Review of Progress in Quantitative Nondestructive Evaluation QNDE 2021*, ASME, 2021, pp. 1–7.

- [P24] F. Zonzini, D. Bogomolov, T. Dhamija, N. Testoni, L. De Marchi, and A. Marzani, «Deep learning approaches for robust time of arrival estimation in acoustic emission monitoring,» *Sensors*, vol. 22, no. 3, 2022, ISSN: 1424-8220. DOI: [10 . 3390 / s22031091](https://doi.org/10.3390/s22031091). [Online]. Available: <https://www.mdpi.com/1424-8220/22/3/1091>.
- [P25] F. Zonzini, F. Romano, A. Carbone, M. Zauli, and D. Marchi, «Vibration monitoring at the extreme edge via frequency domain decompositions,» in *52nd Annual Meeting Società Italiana Elettronica (SIE)*, SIE, University of Trieste, 2021.
- [P26] F. Zonzini, L. De Marchi, and N. Testoni, «A small footprint, low power, and light weight sensor node and dedicated processing for modal analysis,» in *Lecture Note in Electrical Engineering*, Springer, 2018, pp. 361–370.
- [P27] F. Zonzini, M. M. Malatesta, D. Bogomolov, N. Testoni, L. De Marchi, and A. Marzani, «A spectral peak-picking method for on-board operational modal analysis of multi-type vibration-based shm,» in *ANCRiSST 2019 Procedia*, Sapienza University of Rome, 2019.
- [P28] M. M. Malatesta, F. Zonzini, D. Bogomolov, N. Testoni, L. De Marchi, and A. Marzani, «Structural health monitoring reliability enhancement by an automated sensor tuning procedure,» in *e-proceedings of the 30th European Safety and Reliability Conference and 15th Probabilistic Safety Assessment and Management Conference, ESREL2020-PSAM15 Organizers*, 2020.



## REFERENCES

---

- [1] C. Scuro, P. F. Sciammarella, F. Lamonaca, R. S. Olivito, and D. L. Carni, «Iot for structural health monitoring,» *IEEE Instrumentation & Measurement Magazine*, vol. 21, no. 6, pp. 4–14, 2018.
- [2] M. A. Hannan, K. Hassan, and K. P. Jern, «A review on sensors and systems in structural health monitoring: Current issues and challenges,» *Smart structures and systems*, vol. 22, no. 5, pp. 509–525, 2018.
- [3] F. Ubertini, S. Laflamme, E. Chatzi, B. Glisic, and F. Magalhaes, «Dense sensor networks for mesoscale shm: Innovations in sensing technologies and signal processing,» *Measurement Science and Technology*, vol. 28, no. 4, p. 040 103, 2017.
- [4] K. Worden, E. J. Cross, N. Dervilis, E. Papatheou, and I. Antoniadou, «Structural health monitoring: From structures to systems-of-systems,» *IFAC-papersonline*, vol. 48, no. 21, pp. 1–17, 2015.
- [5] M. Z. A. Bhuiyan, J. Wu, G. Wang, and J. Cao, «Sensing and decision making in cyber-physical systems: The case of structural event monitoring,» *IEEE Transactions on Industrial Informatics*, vol. 12, no. 6, pp. 2103–2114, 2016.
- [6] G. Hackmann, W. Guo, G. Yan, Z. Sun, C. Lu, and S. Dyke, «Cyber-physical code-design of distributed structural health monitoring with wireless sensor networks,» *IEEE Transactions on Parallel and Distributed Systems*, vol. 25, no. 1, pp. 63–72, 2013.
- [7] G. Mei, N. Xu, J. Qin, B. Wang, and P. Qi, «A survey of internet of things (iot) for geohazard prevention: Applications, technologies, and challenges,» *IEEE Internet of Things Journal*, vol. 7, no. 5, pp. 4371–4386, 2019.
- [8] F. Lamonaca, C. Scuro, P. F. Sciammarella, R. S. Olivito, D. Grimaldi, and D. L. Carni, «A layered iot-based architecture for a distributed structural health monitoring system,» *Acta Imeko*, vol. 8, no. 2, pp. 45–52, 2019.
- [9] S. A. Putra, B. R. Trilaksono, M. Riyansyah, D. S. Laila, A. Harsoyo, and A. I. Kistijantoro, «Intelligent sensing in multiagent-based wireless sensor network for bridge condition monitoring system,» *IEEE Internet of Things Journal*, vol. 6, no. 3, pp. 5397–5410, 2019.
- [10] X. Dong, D. Zhu, Y. Wang, J. P. Lynch, and R. A. Swartz, «Design and validation of acceleration measurement using the martlet wireless sensing system,» in *Smart Materials, Adaptive Structures and Intelligent Systems*, American Society of Mechanical Engineers, vol. 46148, 2014, V001T05A006.
- [11] T. Srisooksai, K. Keamarungsi, P. Lamsrichan, and K. Araki, «Practical data compression in wireless sensor networks: A survey,» *Journal of network and computer applications*, vol. 35, no. 1, pp. 37–59, 2012.
- [12] J. Kim and J. P. Lynch, «Autonomous decentralized system identification by markov parameter estimation using distributed smart wireless sensor networks,» *Journal of Engineering Mechanics*, vol. 138, no. 5, pp. 478–490, 2012.

- [13] Z. Zou, Y. Bao, H. Li, B. F. Spencer, and J. Ou, «Embedding compressive sensing-based data loss recovery algorithm into wireless smart sensors for structural health monitoring,» *IEEE Sensors Journal*, vol. 15, no. 2, pp. 797–808, 2014.
- [14] R. Ferrari, F. Pioldi, E. Rizzi, C. Gentile, E. Chatzi, R. Klis, E. Serantoni, and A. Wieser, «Heterogeneous sensor fusion for reducing uncertainty in structural health monitoring,» in *1st ECCOMAS thematic conference on uncertainty quantification in computational sciences and engineering (UNCECOMP 2015)*, vol. 1, 2015, pp. 511–528.
- [15] A. Engel, B. Liebig, and A. Koch, «Energy-efficient heterogeneous reconfigurable sensor node for distributed structural health monitoring,» in *Proceedings of the 2012 Conference on Design and Architectures for Signal and Image Processing*, IEEE, 2012, pp. 1–8.
- [16] A. Kamariotis, E. Chatzi, and D. Straub, «Value of information from vibration-based structural health monitoring extracted via bayesian model updating,» *Mechanical Systems and Signal Processing*, vol. 166, p. 108465, 2022.
- [17] E. M. Dogo, A. F. Salami, C. O. Aigbavboa, and T. Nkonyana, «Taking cloud computing to the extreme edge: A review of mist computing for smart cities and industry 4.0 in africa,» *Edge computing*, pp. 107–132, 2019.
- [18] H. Wenzel, *Health monitoring of bridges*. John Wiley & Sons, 2008.
- [19] S. A. Putra, B. R. Trilaksono, M. Riyansyah, D. S. Laila, A. Harsoyo, and A. I. Kistijantoro, «Intelligent sensing in multiagent-based wireless sensor network for bridge condition monitoring system,» *IEEE Internet of Things Journal*, vol. 6, no. 3, pp. 5397–5410, 2019.
- [20] Y. Ou, K. E. Tatsis, V. K. Dertimanis, M. D. Spiridonakos, and E. N. Chatzi, «Vibration-based monitoring of a small-scale wind turbine blade under varying climate conditions. part i: An experimental benchmark,» *Structural Control and Health Monitoring*, vol. 28, no. 6, e2660, 2021.
- [21] S. Bogoevska, M. Spiridonakos, E. Chatzi, E. Dumova-Jovanoska, and R. Höffer, «A data-driven diagnostic framework for wind turbine structures: A holistic approach,» *Sensors*, vol. 17, no. 4, p. 720, 2017.
- [22] M. Vishwakarma, R. Purohit, V Harshlata, and P Rajput, «Vibration analysis & condition monitoring for rotating machines: A review,» *Materials Today: Proceedings*, vol. 4, no. 2, pp. 2659–2664, 2017.
- [23] M. P. Limongelli, E. Chatzi, M. Döhler, G. Lombaert, and E. Reynders, «Towards extraction of vibration-based damage indicators,» in *EWSHM-8th European workshop on structural health monitoring*, 2016.
- [24] C. Rainieri and G. Fabbrocino, «Operational modal analysis of civil engineering structures,» *Springer, New York*, vol. 142, p. 143, 2014.
- [25] M. Dahak, N. Touat, and M. Kharoubi, «Damage detection in beam through change in measured frequency and undamaged curvature mode shape,» *Inverse Problems in Science and Engineering*, vol. 27, no. 1, pp. 89–114, 2019.
- [26] G. Toh and J. Park, «Review of vibration-based structural health monitoring using deep learning,» *Applied Sciences*, vol. 10, no. 5, p. 1680, 2020.



- [27] H Naderpour and P Fakharian, «A synthesis of peak picking method and wavelet packet transform for structural modal identification,» *KSCE Journal of Civil Engineering*, vol. 20, no. 7, pp. 2859–2867, 2016.
- [28] R. Brincker, L. Zhang, and P. Andersen, «Modal identification of output-only systems using frequency domain decomposition,» *Smart materials and structures*, vol. 10, no. 3, p. 441, 2001.
- [29] W. Leurs, F. Deblauwe, and F. Lembregts, «Modal parameter estimation based on complex mode indicator functions,» in *Proceedings of the International Society for Optical Engineering*, Citeseer, 1993, pp. 1035–1035.
- [30] B. Peeters, H. Van der Auweraer, P. Guillaume, and J. Leuridan, «The polymax frequency-domain method: A new standard for modal parameter estimation?» *Shock and Vibration*, vol. 11, no. 3, 4, pp. 395–409, 2004.
- [31] K. Gkoktsi and A. Giaralis, «A sub-nyquist co-prime sampling music spectral approach for natural frequency identification of white-noise excited structures,» in *Proceedings of the 8th International Conference on Computational Stochastic Mechanics (CSM 8)*, Research Publishing, 2018, pp. 246–255.
- [32] H Naderpour and P Fakharian, «A synthesis of peak picking method and wavelet packet transform for structural modal identification,» *KSCE Journal of Civil Engineering*, vol. 20, no. 7, pp. 2859–2867, 2016.
- [33] E. Reynders, «System identification methods for (operational) modal analysis: Review and comparison,» *Archives of Computational Methods in Engineering*, vol. 19, no. 1, pp. 51–124, 2012.
- [34] R. Guidorzi, R. Diversi, L. Vincenzi, and V. Simioli, «Ar+ noise versus ar and arma models in shm-oriented identification,» in *2015 23rd Mediterranean Conference on Control and Automation (MED)*, IEEE, 2015, pp. 809–814.
- [35] B. Peeters and G. De Roeck, «Stochastic system identification for operational modal analysis: A review,» *J. Dyn. Sys., Meas., Control*, vol. 123, no. 4, pp. 659–667, 2001.
- [36] S. Ibrahim, «Fundamentals of time domain modal identification,» in *Modal Analysis and Testing*, Springer, 1999, pp. 241–250.
- [37] F. Poncelet, G. Kerschen, J.-C. Golinval, and D. Verhelst, «Output-only modal analysis using blind source separation techniques,» *Mechanical systems and signal processing*, vol. 21, no. 6, pp. 2335–2358, 2007.
- [38] S. Greś, M. Döhler, P. Andersen, and L. Mevel, «Kalman filter-based subspace identification for operational modal analysis under unmeasured periodic excitation,» *Mechanical Systems and Signal Processing*, vol. 146, p. 106996, 2021.
- [39] S. R. Venkatesh and M. A. Dahleh, «On system identification of complex systems from finite data,» *IEEE Transactions on Automatic Control*, vol. 46, no. 2, pp. 235–257, 2001.
- [40] C. R. Farrar and K. Worden, «An introduction to structural health monitoring,» *Philosophical Transactions of the Royal Society A: Mathematical, Physical and Engineering Sciences*, vol. 365, no. 1851, 2007, ISSN: 1364503X. DOI: [10.1098/rsta.2006.1928](https://doi.org/10.1098/rsta.2006.1928).

- [41] R. Belkeziz and Z. Jarir, «A survey on Internet of Things coordination,» *Proceedings - 2016 3rd International Conference on Systems of Collaboration, SysCo 2016*, vol. 4, no. 3, pp. 619–635, 2017. DOI: [10.1109/SYSCO.2016.7831328](https://doi.org/10.1109/SYSCO.2016.7831328).
- [42] W. Fan and P. Qiao, «Vibration-based damage identification methods: A review and comparative study,» *Structural health monitoring*, vol. 10, no. 1, pp. 83–111, 2011.
- [43] Z. Hong-Ping, H. Bo, and C. Xiao-qiang, «Detection of structural damage through changes in frequency,» *Wuhan University Journal of Natural Sciences*, vol. 10, no. 6, pp. 1069–1073, 2005.
- [44] M. Pastor, M. Binda, and T. Harčarik, «Modal assurance criterion,» *Procedia Engineering*, vol. 48, pp. 543–548, 2012.
- [45] S. Sharma, S. Sharma, and A. Athaiya, «Activation functions in neural networks,» *towards data science*, vol. 6, no. 12, pp. 310–316, 2017.
- [46] O. Avci, O. Abdeljaber, S. Kiranyaz, M. Hussein, M. Gabbouj, and D. J. Inman, «A review of vibration-based damage detection in civil structures: From traditional methods to machine learning and deep learning applications,» *Mechanical systems and signal processing*, vol. 147, p. 107 077, 2021.
- [47] R. Frans, Y. Arfiadi, and H. Parung, «Comparative study of mode shapes curvature and damage locating vector methods for damage detection of structures,» *Procedia engineering*, vol. 171, pp. 1263–1271, 2017.
- [48] E. Favarelli, E. Testi, and A. Giorgetti, «One class classifier neural network for anomaly detection in low dimensional feature spaces,» in *2019 13th International Conference on Signal Processing and Communication Systems (ICSPCS)*, IEEE, 2019, pp. 1–7.
- [49] H. Tang, G. Tang, and L. Meng, «Prediction of the bridge monitoring data based on support vector machine,» in *2015 11th International Conference on Natural Computation (ICNC)*, IEEE, 2015, pp. 781–785.
- [50] M. Vagnoli, R. Remenyte-Priscott, and J. Andrews, «A bayesian belief network method for bridge deterioration detection,» *Proceedings of the Institution of Mechanical Engineers, Part O: Journal of Risk and Reliability*, vol. 235, no. 3, pp. 338–355, 2021.
- [51] A. Verzobio, D. Bolognani, J. Quigley, and D. Zonta, «Quantifying the benefit of structural health monitoring: Can the value of information be negative?» *Structure and Infrastructure Engineering*, pp. 1–22, 2021.
- [52] K. Feng, A. González, and M. Casero, «A knn algorithm for locating and quantifying stiffness loss in a bridge from the forced vibration due to a truck crossing at low speed,» *Mechanical Systems and Signal Processing*, vol. 154, p. 107 599, 2021.
- [53] M. Arul and A. Kareem, «Data anomaly detection for structural health monitoring of bridges using shapelet transform,» *arXiv preprint arXiv:2009.00470*, 2020.
- [54] A. Diez, N. L. D. Khoa, M. M. Alamdari, Y. Wang, F. Chen, and P. Runcie, «A clustering approach for structural health monitoring on bridges,» *Journal of Civil Structural Health Monitoring*, vol. 6, no. 3, pp. 429–445, 2016.

- [55] Y. Jiao, H. Liu, P. Zhang, X. Wang, and H. Wei, «Unsupervised performance evaluation strategy for bridge superstructure based on fuzzy clustering and field data,» *The Scientific World Journal*, vol. 2013, 2013.
- [56] C.-W. Kim, T. Morita, Z. Wang, and K. Sugiura, «Long-term bridge health monitoring focusing on the mahalanobis distance of modal parameters,» in *Journal of Physics: Conference Series*, IOP Publishing, vol. 628, 2015, p. 012 055.
- [57] P. Lu, B. M. Phares, L. Greimann, and T. J. Wipf, «Bridge structural health-monitoring system using statistical control chart analysis,» *Transportation research record*, vol. 2172, no. 1, pp. 123–131, 2010.
- [58] J. C. Gertrudes, A. Zimek, J. Sander, and R. J. Campello, «A unified view of density-based methods for semi-supervised clustering and classification,» *Data mining and knowledge discovery*, vol. 33, no. 6, pp. 1894–1952, 2019.
- [59] I. Farreras-Alcover, M. K. Chryssanthopoulos, and J. E. Andersen, «Regression models for structural health monitoring of welded bridge joints based on temperature, traffic and strain measurements,» *Structural Health Monitoring*, vol. 14, no. 6, pp. 648–662, 2015.
- [60] Y. Zhang and Y. Lei, «Data anomaly detection of bridge structures using convolutional neural network based on structural vibration signals,» *Symmetry*, vol. 13, no. 7, p. 1186, 2021.
- [61] S. Jeong, M. Ferguson, R. Hou, J. P. Lynch, H. Sohn, and K. H. Law, «Sensor data reconstruction using bidirectional recurrent neural network with application to bridge monitoring,» *Advanced Engineering Informatics*, vol. 42, p. 100 991, 2019.
- [62] Z. Shang, L. Sun, Y. Xia, and W. Zhang, «Vibration-based damage detection for bridges by deep convolutional denoising autoencoder,» *Structural Health Monitoring*, p. 1 475 921 720 942 836, 2020.
- [63] R. Zhao, R. Yan, Z. Chen, K. Mao, P. Wang, and R. X. Gao, «Deep learning and its applications to machine health monitoring,» *Mechanical Systems and Signal Processing*, vol. 115, pp. 213–237, 2019.
- [64] T. Nagayama and B. F. Spencer Jr, «Structural health monitoring using smart sensors,» Newmark Structural Engineering Laboratory. University of Illinois at Urbana . . . , Tech. Rep., 2007.
- [65] V Krishnamurthy, K Fowler, and E Sazonov, «The effect of time synchronization of wireless sensors on the modal analysis of structures,» *Smart Materials and Structures*, vol. 17, no. 5, p. 055 018, 2008.
- [66] J. J. Moughty and J. R. Casas, «A state of the art review of modal-based damage detection in bridges: Development, challenges, and solutions,» *Applied Sciences*, vol. 7, no. 5, p. 510, 2017.
- [67] X. Liu, J. Cao, W.-Z. Song, P. Guo, and Z. He, «Distributed sensing for high-quality structural health monitoring using wsns,» *IEEE Transactions on Parallel and Distributed Systems*, vol. 26, no. 3, pp. 738–747, 2015.
- [68] Y.-A. Chapuis, L. Zhou, Y. Fukuta, Y. Mita, and H. Fujita, «Fpga-based decentralized control of arrayed mems for microrobotic application,» *IEEE Transactions on Industrial Electronics*, vol. 54, no. 4, pp. 1926–1936, 2007.

- [69] B. Spencer, T. Nagayama, and J. A. Rice, «Decentralized structural health monitoring using smart sensors,» in *Sensors and Smart Structures Technologies for Civil, Mechanical, and Aerospace Systems 2008*, International Society for Optics and Photonics, vol. 6932, 2008, p. 693 202.
- [70] V. Krishnamurthy, K. Fowler, and E. Sazonov, «The effect of time synchronization of wireless sensors on the modal analysis of structures,» *Smart Materials and Structures*, vol. 17, no. 5, p. 055 018, 2008.
- [71] F. Hu and Q. Hao, *Intelligent sensor networks: the integration of sensor networks, signal processing and machine learning*. CRC Press, 2012.
- [72] K. Fang, C. Liu, and J. Teng, «Cluster-based optimal wireless sensor deployment for structural health monitoring,» *Structural Health Monitoring*, vol. 17, no. 2, pp. 266–278, 2018.
- [73] X. Liu, J. Cao, S. Lai, C. Yang, H. Wu, and Y. L. Xu, «Energy efficient clustering for wsn-based structural health monitoring,» in *INFOCOM, 2011 Proceedings IEEE, IEEE*, 2011, pp. 2768–2776.
- [74] M. Abdulkarem, K. Samsudin, F. Z. Rokhani, and M. F. A. Rasid, «Wireless sensor network for structural health monitoring: A contemporary review of technologies, challenges, and future direction,» *Structural Health Monitoring*, p. 1 475 921 719 854 528, 2019.
- [75] P. K. Patil and S. Patil, «Review on structural health monitoring system using wsn for bridges,» in *2017 International conference of Electronics, Communication and Aerospace Technology (ICECA)*, IEEE, vol. 1, 2017, pp. 628–631.
- [76] A. B. Noel, A. Abdaoui, T. Elfouly, M. H. Ahmed, A. Badawy, and M. S. Shehata, «Structural health monitoring using wireless sensor networks: A comprehensive survey,» *IEEE Communications Surveys & Tutorials*, vol. 19, no. 3, pp. 1403–1423, 2017.
- [77] G. Hackmann, W. Guo, G. Yan, Z. Sun, C. Lu, and S. Dyke, «Cyber-physical code-sign of distributed structural health monitoring with wireless sensor networks,» *IEEE Transactions on Parallel and Distributed Systems*, vol. 25, no. 1, pp. 63–72, 2014.
- [78] S.-H. Sim, J. F. Carbonell-Márquez, B. Spencer Jr, and H. Jo, «Decentralized random decrement technique for efficient data aggregation and system identification in wireless smart sensor networks,» *Probabilistic Engineering Mechanics*, vol. 26, no. 1, pp. 81–91, 2011.
- [79] S. Yuan, Y. Ren, L. Qiu, and H. Mei, «A multi-response-based wireless impact monitoring network for aircraft composite structures,» *IEEE Transactions on Industrial Electronics*, vol. 63, no. 12, pp. 7712–7722, 2016.
- [80] A. T. Zimmerman, M. Shiraishi, R. A. Swartz, and J. P. Lynch, «Automated modal parameter estimation by parallel processing within wireless monitoring systems,» *Journal of Infrastructure Systems*, vol. 14, no. 1, pp. 102–113, 2008.
- [81] I. L. Dos Santos, L. Pirmez, É. T. Lemos, F. C. Delicato, L. A. V. Pinto, J. N. de Souza, and A. Y. Zomaya, «A localized algorithm for structural health monitoring using wireless sensor networks,» *Information Fusion*, vol. 15, pp. 114–129, 2014.

- [82] M. Ceriotti, L. Mottola, G. P. Picco, A. L. Murphy, S. Guna, M. Corra, M. Pozzi, D. Zonta, and P. Zanon, «Monitoring heritage buildings with wireless sensor networks: The torre aquila deployment,» in *Proceedings of the 2009 international conference on information processing in sensor networks*, IEEE Computer Society, 2009, pp. 277–288.
- [83] A. Ortega, P. Frossard, J. Kovačević, J. M. Moura, and P. Vandergheynst, «Graph signal processing: Overview, challenges, and applications,» *Proceedings of the IEEE*, vol. 106, no. 5, pp. 808–828, 2018.
- [84] I. Jabłoński, «Graph signal processing in applications to sensor networks, smart grids, and smart cities,» *IEEE Sensors Journal*, vol. 17, no. 23, pp. 7659–7666, 2017.
- [85] S. Ljubisa, M. Danilo P., D. Milos, K. Ilija, S. Ervin, and C. Anthony G., «Understanding the basis of graph signal processing via an intuitive example-driven approach [lecture notes],» *IEEE Signal Processing Magazine*, vol. 36, no. 6, pp. 133–145, Nov. 2019. DOI: [10.1109/MSP.2019.2929832](https://doi.org/10.1109/MSP.2019.2929832).
- [86] W. Contreras and S. Ziavras, «Efficient infrastructure damage detection and localization using wireless sensor networks, with cluster generation for monitoring damage progression,» in *Ubiquitous Computing, Electronics and Mobile Communication Conference (UEMCON), 2017 IEEE 8th Annual*, IEEE, 2017, pp. 173–178.
- [87] M. Döhler, E. Reynders, F. Magalhaes, L. Mevel, G. De Roeck, and A Cunha, «Pre- and post-identification merging for multi-setup oma with covariance-driven ssi,» in *Dynamics of Bridges, Volume 5*, Springer, 2011, pp. 57–70.
- [88] S.-K. Au, «Assembling mode shapes by least squares,» *Mechanical Systems and Signal Processing*, vol. 25, no. 1, pp. 163–179, 2011.
- [89] Ç. Hızal, G. Turan, E. Aktaş, and H. Ceylan, «A mode shape assembly algorithm by using two stage bayesian fast fourier transform approach,» *Mechanical Systems and Signal Processing*, vol. 134, p. 106 328, 2019.
- [90] E Parloo, P Guillaume, and B Cauberghe, «Maximum likelihood identification of non-stationary operational data,» *Journal of Sound and Vibration*, vol. 268, no. 5, pp. 971–991, 2003.
- [91] D. I. Shuman, S. K. Narang, P. Frossard, A. Ortega, and P. Vandergheynst, «The emerging field of signal processing on graphs: Extending high-dimensional data analysis to networks and other irregular domains,» *arXiv preprint arXiv:1211.0053*, 2012.
- [92] M. Daković, L. Stanković, and E. Sejdić, «Local smoothness of graph signals,» *Mathematical Problems in Engineering*, vol. 2019, 2019.
- [93] A. Girolami, F. Zonzini, L. De Marchi, D. Brunelli, and L. Benini, «Modal analysis of structures with low-cost embedded systems,» in *Circuits and Systems (ISCAS), 2018 IEEE International Symposium on*, IEEE, 2018, pp. 1–4.
- [94] Y. Bao, H. Li, X. Sun, Y. Yu, and J. Ou, «Compressive sampling-based data loss recovery for wireless sensor networks used in civil structural health monitoring,» *Structural Health Monitoring*, vol. 12, no. 1, pp. 78–95, 2013.
- [95] R. Klis and E. N. Chatzi, «Vibration monitoring via spectro-temporal compressive sensing for wireless sensor networks,» *Structure and Infrastructure Engineering*, vol. 13, no. 1, pp. 195–209, 2017.

- [96] S. M. O'Connor, J. P. Lynch, and A. C. Gilbert, «Compressed sensing embedded in an operational wireless sensor network to achieve energy efficiency in long-term monitoring applications,» *Smart Materials and Structures*, vol. 23, no. 8, 2014.
- [97] Y. Yang and S. Nagarajaiah, «Output-only modal identification by compressed sensing: Non-uniform low-rate random sampling,» *Mechanical Systems and Signal Processing*, vol. 56, pp. 15–34, 2015.
- [98] J. Y. Park, M. B. Wakin, and A. C. Gilbert, «Modal analysis with compressive measurements,» *IEEE Transactions on Signal Processing*, vol. 62, no. 7, pp. 1655–1670, 2014.
- [99] A. Burrello, A. Marchioni, D. Brunelli, S. Benatti, M. Mangia, and L. Benini, «Embedded streaming principal components analysis for network load reduction in structural health monitoring,» *IEEE Internet of Things Journal*, vol. 8, no. 6, pp. 4433–4447, 2020.
- [100] K. Gkoktsi and A. Giaralis, «A multi-sensor sub-nyquist power spectrum blind sampling approach for low-power wireless sensors in operational modal analysis applications,» *Mechanical Systems and Signal Processing*, vol. 116, pp. 879–899, 2019.
- [101] F. Zonzini, M. Zauli, M. Mangia, N. Testoni, and L. De Marchi, «Model-assisted compressed sensing for vibration-based structural health monitoring,» *IEEE Transactions on Industrial Informatics*, 2021.
- [102] E. J. Candes and Y. Plan, «A probabilistic and ripless theory of compressed sensing,» *IEEE transactions on information theory*, vol. 57, no. 11, pp. 7235–7254, 2011.
- [103] E. J. Candès, J. Romberg, and T. Tao, «Robust uncertainty principles: Exact signal reconstruction from highly incomplete frequency information,» *IEEE Transactions on information theory*, vol. 52, no. 2, pp. 489–509, 2006.
- [104] D. L. Donoho, «Compressed sensing,» *IEEE Transactions on information theory*, vol. 52, no. 4, pp. 1289–1306, 2006.
- [105] A. Burrello, A. Marchioni, D. Brunelli, and L. Benini, «Embedding principal component analysis for data reduction in structural health monitoring on low-cost iot gateways,» in *Proceedings of the 16th ACM International Conference on Computing Frontiers*, 2019, pp. 235–239.
- [106] Y. Bao, Z. Tang, and H. Li, «Compressive-sensing data reconstruction for structural health monitoring: A machine-learning approach,» *Structural Health Monitoring*, vol. 19, no. 1, pp. 293–304, 2020.
- [107] H. O. Ahmed and A. K. Nandi, «Three-stage hybrid fault diagnosis for rolling bearings with compressively sampled data and subspace learning techniques,» *IEEE Transactions on Industrial Electronics*, vol. 66, no. 7, pp. 5516–5524, 2018.
- [108] J. Yan, H. Peng, Y. Yu, and Y. Luo, «Compressive sensing of wind speed based on non-convex  $l_p$ -norm sparse regularization optimization for structural health monitoring,» *Engineering Structures*, vol. 194, pp. 346–356, 2019.
- [109] E. J. Candes and T. Tao, «Decoding by linear programming,» *IEEE transactions on information theory*, vol. 51, no. 12, pp. 4203–4215, 2005.
- [110] S. Salloum, J. Z. Huang, and Y. He, «Random sample partition: A distributed data model for big data analysis,» *IEEE Transactions on Industrial Informatics*, vol. 15, no. 11, pp. 5846–5854, 2019.

- [111] A. Marchioni, M. Mangia, F. Pareschi, R. Rovatti, and G. Setti, «Subspace energy monitoring for anomaly detection@ sensor or@ edge,» *IEEE Internet of Things Journal*, 2020.
- [112] W. Staszewski, «Wavelet based compression and feature selection for vibration analysis,» *Journal of sound and vibration*, vol. 211, no. 5, pp. 735–760, 1998.
- [113] R. A. Meyers *et al.*, *Encyclopedia of physical science and technology*. Academic Press, 1987.
- [114] M. Mangia, R. Rovatti, and G. Setti, «Rakeness in the design of analog-to-information conversion of sparse and localized signals,» *IEEE Transactions on Circuits and Systems I: Regular Papers*, vol. 59, no. 5, pp. 1001–1014, 2012.
- [115] M. Mangia, F. Pareschi, V. Cambarelli, R. Rovatti, and G. Setti, *Adapted Compressed Sensing for Effective Hardware Implementations: A Design Flow for Signal-Level Optimization of Compressed Sensing Stages*. Springer, 2017.
- [116] A. Karpatne, G. Atluri, J. H. Faghmous, M. Steinbach, A. Banerjee, A. Ganguly, S. Shekhar, N. Samatova, and V. Kumar, «Theory-guided data science: A new paradigm for scientific discovery from data,» *IEEE Transactions on Knowledge and Data Engineering*, vol. 29, no. 10, pp. 2318–2331, 2017.
- [117] M. Nielsen, «On the construction and frequency localization of finite orthogonal quadrature filters,» *Journal of Approximation Theory*, vol. 108, no. 1, pp. 36–52, 2001.
- [118] E. Reynders and G. D. Roeck, «Continuous vibration monitoring and progressive damage testing on the z 24 bridge,» *Encyclopedia of structural health monitoring*, 2009.
- [119] Z. Du, X. Chen, H. Zhang, and B. Yang, «Compressed-sensing-based periodic impulsive feature detection for wind turbine systems,» *IEEE Transactions on Industrial Informatics*, vol. 13, no. 6, pp. 2933–2945, 2017.
- [120] V. S. G. Thadikemalla and A. S. Gandhi, «A data loss recovery technique using compressive sensing for structural health monitoring applications,» *KSCE Journal of Civil Engineering*, vol. 22, no. 12, pp. 5084–5093, 2018.
- [121] Y. Bao, H. Li, X. Sun, Y. Yu, and J. Ou, «Compressive sampling-based data loss recovery for wireless sensor networks used in civil structural health monitoring,» *Structural Health Monitoring*, vol. 12, no. 1, pp. 78–95, 2013.
- [122] A. K. Nandi and H. Ahmed, *Condition Monitoring with Vibration Signals: Compressive Sampling and Learning Algorithms for Rotating Machines*. John Wiley & Sons, 2020.
- [123] Y. Li, S. Bu, Z. Liu, and C. Zhang, «Mechanical fault diagnosis of rolling bearing based on locality-constrained sparse coding,» in *2015 IEEE Conference on Prognostics and Health Management (PHM)*, IEEE, 2015, pp. 1–7.
- [124] J. Wang, W. Qiao, and L. Qu, «Wind turbine bearing fault diagnosis based on sparse representation of condition monitoring signals,» *IEEE Transactions on Industry Applications*, vol. 55, no. 2, pp. 1844–1852, 2018.
- [125] S. Nagarajaiah and B. Basu, «Output only modal identification and structural damage detection using time frequency & wavelet techniques,» *Earthquake Engineering and Engineering Vibration*, vol. 8, no. 4, pp. 583–605, 2009.
- [126] R. R. Coifman and M. V. Wickerhauser, «Entropy-based algorithms for best basis selection,» *IEEE Transactions on information theory*, vol. 38, no. 2, pp. 713–718, 1992.

- [127] J. M. Duarte-Carvajalino and G. Sapiro, «Learning to sense sparse signals: Simultaneous sensing matrix and sparsifying dictionary optimization,» *IEEE Transactions on Image Processing*, vol. 18, no. 7, pp. 1395–1408, 2009.
- [128] K. F. Graff, *Wave motion in elastic solids*. Courier Corporation, 2012.
- [129] R. A. Ibrahim, *Handbook of Structural Life Assessment*. Wiley Online Library, 2017.
- [130] C. Rainieri and G. Fabbrocino, «Operational modal analysis of civil engineering structures,» *Springer, New York*, vol. 142, p. 143, 2014.
- [131] N. Hurley and S. Rickard, «Comparing measures of sparsity,» *IEEE Transactions on Information Theory*, vol. 55, no. 10, pp. 4723–4741, 2009.
- [132] K. Tatsis, V. Dertimanis, Y. Ou, and E. Chatzi, «Gp-arx-based structural damage detection and localization under varying environmental conditions,» *Journal of Sensor and Actuator Networks*, vol. 9, no. 3, p. 41, 2020.
- [133] M. Rani, S. B. Dhok, and R. B. Deshmukh, «A systematic review of compressive sensing: Concepts, implementations and applications,» *IEEE Access*, vol. 6, pp. 4875–4894, 2018.
- [134] J. Laine and D. Mougenot, «Benefits of mems based seismic accelerometers for oil exploration,» in *TRANSDUCERS 2007-2007 International Solid-State Sensors, Actuators and Microsystems Conference*, IEEE, 2007, pp. 1473–1477.
- [135] A. Lavrenko, F. Römer, G. Del Galdo, and R. Thomä, «On the SNR variability in noisy compressed sensing,» *IEEE Signal Processing Letters*, vol. 24, no. 8, pp. 1148–1152, 2017.
- [136] X. Chaoang, T. Hesheng, and R. Yan, «Compressed sensing reconstruction for axial piston pump bearing vibration signals based on adaptive sparse dictionary model,» *Measurement and Control*, vol. 53, no. 3-4, pp. 649–661, 2020.
- [137] F. Zonzini, A. Girolami, L. De Marchi, A. Marzani, and D. Brunelli, «Cluster-based vibration analysis of structures with graph signal processing,» *IEEE Transactions on Industrial Electronics*, 2020.
- [138] M. Mangia, F. Pareschi, V. Cambareri, R. Rovatti, and G. Setti, «Rakeness-based design of low-complexity compressed sensing,» *IEEE transactions on circuits and systems I: Regular Papers*, vol. 64, no. 5, pp. 1201–1213, 2017.
- [139] Q. Huynh-Thu and M. Ghanbari, «Scope of validity of PSNR in image/video quality assessment,» *Electronics letters*, vol. 44, no. 13, pp. 800–801, 2008.
- [140] R. Brincker and C. Ventura, *Introduction to operational modal analysis*. John Wiley & Sons, 2015.
- [141] F. J. Cara, J. Juan, E. Alarcón, E. Reynders, and G. De Roeck, «Modal contribution and state space order selection in operational modal analysis,» *Mechanical Systems and Signal Processing*, vol. 38, no. 2, pp. 276–298, 2013.
- [142] P. Stoica, R. L. Moses, *et al.*, «Spectral analysis of signals,» 2005.
- [143] T. R. Pillai, S. Palaniappan, A. Abdullah, and H. M. Imran, «Predictive modeling for intrusions in communication systems using gamma and arma models,» in *2015 5th National Symposium on Information Technology: Towards New Smart World (NSITNSW)*, IEEE, 2015, pp. 1–6.



- [144] F. Merchant, T. Vatwani, A. Chattopadhyay, S. Raha, S. Nandy, and R. Narayan, «Efficient realization of householder transform through algorithm-architecture co-design for acceleration of qr factorization,» *IEEE Transactions on Parallel and Distributed Systems*, vol. 29, no. 8, pp. 1707–1720, 2018.
- [145] L. Ma, K. Dickson, J. McAllister, and J. McCanny, «Qr decomposition-based matrix inversion for high performance embedded mimo receivers,» *IEEE Transactions on Signal Processing*, vol. 59, no. 4, pp. 1858–1867, 2011.
- [146] J. Demmel, L. Grigori, M. Hoemmen, and J. Langou, «Communication-avoiding parallel and sequential qr factorizations,» *CoRR abs/0806.2159*, 2008.
- [147] *Stm32l5 nucleo-144 board (mb1361)*, UM2581, Rev 4, ST Microelectronics, Sep. 2020.
- [148] I. A. Rezek and S. J. Roberts, «Parametric model order estimation: A brief review,» 1997.
- [149] A. Mariani, A. Giorgetti, and M. Chiani, «Model order selection based on information theoretic criteria: Design of the penalty,» *IEEE Transactions on Signal Processing*, vol. 63, no. 11, pp. 2779–2789, 2015.
- [150] C. Magnant, E. Grivel, A. Giremus, L. Ratton, and B. Joseph, «Classifying autoregressive models using dissimilarity measures: A comparative study,» in *2015 23rd European Signal Processing Conference (EUSIPCO)*, IEEE, 2015, pp. 998–1002.
- [151] Y. Ou, K. E. Tatsis, V. K. Dertimanis, M. D. Spiridonakos, and E. N. Chatzi, «Vibration-based monitoring of a small-scale wind turbine blade under varying climate conditions. part i: An experimental benchmark,» *Structural Control and Health Monitoring*, vol. 28, no. 6, e2660, 2021.
- [152] E. Morin, M. Maman, R. Guizzetti, and A. Duda, «Comparison of the device lifetime in wireless networks for the internet of things,» *IEEE Access*, vol. 5, pp. 7097–7114, 2017.
- [153] *Nrf52840 product specification v 1.2*, 4413\_417 v1.2 / 2021-01-15, Nordic Semiconductor, Jan. 2021.
- [154] *Max2830 2.4ghz to 2.5ghz 802.11g/b rf transceiver, pa, and rx/tx/antenna diversity switch*, 19-0774, Rev 2; 3/11, maxim integrated, Jan. 2019.
- [155] *Sx-newah(us)*, JW205520AA, Rev 4, silex technology, Sep. 2020.
- [156] *Sx1272/73 - 860 mhz to 1020 mhz low power long range transceiver*, SX1272/73, Rev 4, semtech, 2019.
- [157] W. D'AMBROGIO and A. Fregolent, «The use of antiresonances for robust model updating,» *Journal of Sound and Vibration*, vol. 236, no. 2, pp. 227–243, 2000.
- [158] M. Azimi, A. D. Eslamlou, and G. Pekcan, «Data-driven structural health monitoring and damage detection through deep learning: State-of-the-art review,» *Sensors*, vol. 20, no. 10, p. 2778, 2020.
- [159] G. Toh and J. Park, «Review of vibration-based structural health monitoring using deep learning,» *Applied Sciences*, vol. 10, no. 5, p. 1680, 2020.
- [160] A. Agarwal, V. Gupta, *et al.*, «Performance evaluation of one-class classifiers (occ) for damage detection in structural health monitoring,» in *Machine Learning for Intelligent Multimedia Analytics*, Springer, 2021, pp. 273–305.

- [161] E. Favarelli and A. Giorgetti, «Machine learning for automatic processing of modal analysis in damage detection of bridges,» *IEEE Transactions on Instrumentation and Measurement*, 2020.
- [162] P. Luong and W. Wang, «Smart sensor-based synergistic analysis for rotor bar fault detection of induction motors,» *IEEE/ASME Transactions on Mechatronics*, vol. 25, no. 2, pp. 1067–1075, 2020.
- [163] J. Liu, F. Qu, X. Hong, and H. Zhang, «A small-sample wind turbine fault detection method with synthetic fault data using generative adversarial nets,» *IEEE Transactions on Industrial Informatics*, vol. 15, no. 7, pp. 3877–3888, 2018.
- [164] Y. Peng, W. Qiao, L. Qu, and J. Wang, «Sensor fault detection and isolation for a wireless sensor network-based remote wind turbine condition monitoring system,» *IEEE Transactions on Industry Applications*, vol. 54, no. 2, pp. 1072–1079, 2017.
- [165] R. Iqbal, T. Maniak, F. Doctor, and C. Karyotis, «Fault detection and isolation in industrial processes using deep learning approaches,» *IEEE Transactions on Industrial Informatics*, vol. 15, no. 5, pp. 3077–3084, 2019.
- [166] W. Lu, Y. Li, Y. Cheng, D. Meng, B. Liang, and P. Zhou, «Early fault detection approach with deep architectures,» *IEEE Transactions on Instrumentation and Measurement*, vol. 67, no. 7, pp. 1679–1689, 2018.
- [167] B. Xu, Z. Wu, G. Chen, and K. Yokoyama, «Direct identification of structural parameters from dynamic responses with neural networks,» *Engineering Applications of Artificial Intelligence*, vol. 17, no. 8, pp. 931–943, 2004.
- [168] R. A. Swartz, «Decentralized algorithms for shm over wireless and distributed smart sensor networks,» in *Earthquakes and Health Monitoring of Civil Structures*, Springer, 2013, pp. 109–131.
- [169] H. Shokravi, H. Shokravi, N. Bakhary, S. S. Rahimian Koloor, and M. Petru, «Health monitoring of civil infrastructures by subspace system identification method: An overview,» *Applied Sciences*, vol. 10, no. 8, p. 2786, 2020.
- [170] C. Gentile, M. Guidobaldi, and A. Saisi, «One-year dynamic monitoring of a historic tower: Damage detection under changing environment,» *Meccanica*, vol. 51, no. 11, pp. 2873–2889, 2016.
- [171] J. Gu, M. Gul, and X. Wu, «Damage detection under varying temperature using artificial neural networks,» *Structural Control and Health Monitoring*, vol. 24, no. 11, e1998, 2017.
- [172] A. Likas, N. Vlassis, and J. J. Verbeek, «The global k-means clustering algorithm,» *Pattern recognition*, vol. 36, no. 2, pp. 451–461, 2003.
- [173] B. Peeters and G. De Roeck, «One-year monitoring of the z24-bridge: Environmental effects versus damage events,» *Earthquake engineering & structural dynamics*, vol. 30, no. 2, pp. 149–171, 2001.
- [174] N. Vlahović and G. Kvaščev, «Noise reduction by using autoassociative neural networks,» in *2016 13th Symposium on Neural Networks and Applications (NEUREL)*, IEEE, 2016, pp. 1–5.

- [175] D. Sen, K. Erazo, W. Zhang, S. Nagarajaiah, and L. Sun, «On the effectiveness of principal component analysis for decoupling structural damage and environmental effects in bridge structures,» *Journal of Sound and Vibration*, vol. 457, pp. 280–298, 2019.
- [176] A. Moin, A. Zhou, A. Rahimi, A. Menon, S. Benatti, G. Alexandrov, S. Tamakloe, J. Ting, N. Yamamoto, Y. Khan, *et al.*, «A wearable biosensing system with in-sensor adaptive machine learning for hand gesture recognition,» *Nature Electronics*, vol. 4, no. 1, pp. 54–63, 2021.
- [177] F. Alongi, N. Ghielmetti, D. Pau, F. Terraneo, and W. Fornaciari, «Tiny neural networks for environmental predictions: An integrated approach with miosix,» in *2020 IEEE International Conference on Smart Computing (SMARTCOMP)*, IEEE, 2020, pp. 350–355.
- [178] A. Albanese, M. Nardello, and D. Brunelli, «Automated pest detection with dnn on the edge for precision agriculture,» *IEEE Journal on Emerging and Selected Topics in Circuits and Systems*, 2021.
- [179] L. Lamberti, M. Rusci, M. Fariselli, F. Paci, and L. Benini, «Low-power license plate detection and recognition on a risc-v multi-core mcu-based vision system,» in *2021 IEEE International Symposium on Circuits and Systems (ISCAS)*, IEEE, 2021, pp. 1–5.
- [180] F. Barchi, L. Zanatta, E. Parisi, A. Burrello, D. Brunelli, A. Bartolini, and A. Acquaviva, «Spiking neural network-based near-sensor computing for damage detection in structural health monitoring,» *Future Internet*, vol. 13, no. 8, p. 219, 2021.
- [181] B. Khaleghi, A. Khamis, F. O. Karray, and S. N. Razavi, «Multisensor data fusion: A review of the state-of-the-art,» *Information fusion*, vol. 14, no. 1, pp. 28–44, 2013.
- [182] D. Lahat, T. Adali, and C. Jutten, «Multimodal data fusion: An overview of methods, challenges, and prospects,» *Proceedings of the IEEE*, vol. 103, no. 9, pp. 1449–1477, 2015.
- [183] M. Kok, J. D. Hol, and T. B. Schön, «Using inertial sensors for position and orientation estimation,» *arXiv preprint arXiv:1704.06053*, 2017.
- [184] A. R. J. Downey, «Sensing skin for the structural health monitoring of mesoscale structures,» Ph.D. dissertation, Iowa State University, 2018.
- [185] G. Capellari, E. Chatzi, and S. Mariani, «Cost–benefit optimization of structural health monitoring sensor networks,» *Sensors*, vol. 18, no. 7, p. 2174, 2018.
- [186] M. Whelan, M. P. Fuchs, M. Gangone, and K. D. Janoyan, «Development of a wireless bridge monitoring system for condition assessment using hybrid techniques,» *Proc SPIE*, Mar. 2007. DOI: [10.1117/12.715905](https://doi.org/10.1117/12.715905).
- [187] R. Ferrari, F. Pioldi, E. Rizzi, C. Gentile, E. N. Chatzi, E. Serantoni, and A. Wieser, «Fusion of wireless and non-contact technologies for the dynamic testing of a historic rc bridge,» *Measurement Science and Technology*, vol. 27, no. 12, p. 124 014, 2016.
- [188] A. Belisario-Briceño, S. F. Zedek, T. Camps, R. François, C. Escriba, and J.-Y. Fourniols, «Shm based on modal analysis: Accelerometer and piezoelectric transducers instrumentation for civil engineering in heterogeneous structures,» in *EWSHM-7th European Workshop on Structural Health Monitoring*, 2014.

- [189] R. Hu, Y. Xu, X. Lu, C. Zhang, Q. Zhang, and J. Ding, «Integrated multi-type sensor placement and response reconstruction method for high-rise buildings under unknown seismic loading,» *The Structural Design of Tall and Special Buildings*, vol. 27, no. 6, e1453, 2018.
- [190] X Li, C Rizos, Y Tamura, L Ge, A Yoshida, and J Cranenbroeck, «Fundamental bending mode and vibration monitoring with inclinometer and accelerometer on high-rise buildings subject to wind loads,» in *5th World Conf. Structural Control and Monitoring*, 2010, pp. 1–15.
- [191] C. O. Yigit, X. Li, C. Inal, L. Ge, and M. Yetkin, «Preliminary evaluation of precise inclination sensor and gps for monitoring full-scale dynamic response of a tall reinforced concrete building,» *Journal of Applied Geodesy*, vol. 4, no. 2, pp. 103–113, 2010.
- [192] J.-Z. Su, Y. Xia, L. Chen, X. Zhao, Q.-L. Zhang, Y.-L. Xu, J.-M. Ding, H.-B. Xiong, R.-J. Ma, X.-L. Lv, *et al.*, «Long-term structural performance monitoring system for the shanghai tower,» *Journal of civil structural health monitoring*, vol. 3, no. 1, pp. 49–61, 2013.
- [193] L. Dong, H. Wang, G. Wang, and W. Qiu, «A wireless multifunctional monitoring system of tower body running state based on mems acceleration sensor,» in *Quality Electronic Design (ISQED), 2018 19th International Symposium on*, IEEE, 2018, pp. 357–363.
- [194] S.-H. Sung, J.-W. Park, T Nagayama, and H.-J. Jung, «A multi-scale sensing and diagnosis system combining accelerometers and gyroscopes for bridge health monitoring,» *Smart Materials and Structures*, vol. 23, no. 1, p. 015 005, 2013.
- [195] S. König and P. Leinfelder, «First results with mems tilt sensors on bridges,» in *Inertial Sensors and Systems (ISS), 2016 DGON*, IEEE, 2016, pp. 1–15.
- [196] C. Liu, J.-W. Park, B. Spencer Jr, D.-S. Moon, and J. Fan, «Sensor fusion for structural tilt estimation using an acceleration-based tilt sensor and a gyroscope,» *Smart Materials and Structures*, vol. 26, no. 10, p. 105 005, 2017.
- [197] J. O. Smith *et al.*, *Spectral audio signal processing*. W3K, 2011, vol. 1334027739.
- [198] R Crochiere, «A weighted overlap-add method of short-time fourier analysis/synthesis,» *IEEE Transactions on Acoustics, Speech, and Signal Processing*, vol. 28, no. 1, pp. 99–102, 1980.
- [199] F. G. Baptista and J. Vieira Filho, «A new impedance measurement system for pzt-based structural health monitoring,» *IEEE Transactions on Instrumentation and Measurement*, vol. 58, no. 10, pp. 3602–3608, 2009.
- [200] C. Trigona, B. Andò, and S. Baglio, «Performance measurement methodologies and metrics for vibration energy scavengers,» *IEEE Transactions on Instrumentation and Measurement*, vol. 66, no. 12, pp. 3327–3339, 2017.
- [201] G. Piana, E. Lofrano, A. Carpinteri, A. Paolone, and G. Ruta, «Experimental modal analysis of straight and curved slender beams by piezoelectric transducers,» *Mechanica*, vol. 51, no. 11, pp. 2797–2811, 2016.
- [202] B.-T. Wang and C.-C. Wang, «Feasibility analysis of using piezoceramic transducers for cantilever beam modal testing,» *Smart Materials and Structures*, vol. 6, no. 1, p. 106, 1997.

- [203] A. C. Okafor, K Chandrashekhara, and Y. Jiang, «Delamination prediction in composite beams with built-in piezoelectric devices using modal analysis and neural network,» *Smart materials and structures*, vol. 5, no. 3, p. 338, 1996.
- [204] B. Chapuis and E. Sjerve, *Sensors, algorithms and applications for structural health monitoring*. Springer, 2017.
- [205] G. Lacidogna, G. Piana, and A. Carpinteri, «Damage monitoring of three-point bending concrete specimens by acoustic emission and resonant frequency analysis,» *Engineering Fracture Mechanics*, vol. 210, pp. 203–211, 2019.
- [206] H. Wang and P. Chen, «Intelligent diagnosis method for a centrifugal pump using features of vibration signals,» *Neural Computing and Applications*, vol. 18, no. 4, pp. 397–405, 2009.
- [207] C. Devriendt, F. Magalhães, W. Weijtjens, G. De Sitter, Á. Cunha, and P. Guillaume, «Structural health monitoring of offshore wind turbines using automated operational modal analysis,» *Structural Health Monitoring*, vol. 13, no. 6, pp. 644–659, 2014.
- [208] K.-Y. Oh, J.-Y. Park, J.-S. Lee, B. I. Epureanu, and J.-K. Lee, «A novel method and its field tests for monitoring and diagnosing blade health for wind turbines,» *IEEE Transactions on Instrumentation and Measurement*, vol. 64, no. 6, pp. 1726–1733, 2015.
- [209] S. Heinrich and I. Dufour, «Toward higher-order mass detection: Influence of an adsorbate’s rotational inertia and eccentricity on the resonant response of a bernoulli-euler cantilever beam,» *Sensors*, vol. 15, no. 11, pp. 29 209–29 232, 2015.
- [210] C. Kexel, T. Maetz, M. Maelzer, and J. Moll, «Digital communication across orthotropic composite components using guided waves,» *Composite Structures*, vol. 209, pp. 481–489, 2019.
- [211] M. Mitra and S Gopalakrishnan, «Guided wave based structural health monitoring: A review,» *Smart Materials and Structures*, vol. 25, no. 5, p. 053 001, 2016.
- [212] Z. Su, L. Ye, and Y. Lu, «Guided lamb waves for identification of damage in composite structures: A review,» *Journal of sound and vibration*, vol. 295, no. 3-5, pp. 753–780, 2006.
- [213] S Pant, J. Laliberte, and M Martinez, «Structural health monitoring (shm) of composite aerospace structures using lamb waves,» in *Proc. Int. Conf. Compos. Mater.(Montreal, Canada, 28 July-2 August, 2013)*, 2013.
- [214] F. Xiong, *Digital Modulation Techniques, (Artech House Telecommunications Library)*. Artech House, Inc., 2006.
- [215] Y. Sun, Y. Xu, W. Li, Q. Li, X. Ding, and W. Huang, «A lamb waves based ultrasonic system for the simultaneous data communication, defect inspection, and power transmission,» *IEEE Transactions on Ultrasonics, Ferroelectrics, and Frequency Control*, vol. 68, no. 10, pp. 3192–3203, 2021.
- [216] C. Kexel, M. Mälzer, and J. Moll, «Guided wave based acoustic communications in structural health monitoring systems in the presence of structural defects,» in *IEEE International Symposium on Circuits and Systems*, 2018, pp. 1–4.
- [217] C. Kexel, M. Mälzer, and J. Moll, «Connecting physics to ict: Demonstrating a ‘data drawbridge’ by means of guided ultrasound waves,» *European Journal of Physics*, vol. 39, no. 5, p. 055 806, 2018.

- [218] J. Moll, C. Kexel, and M. Mälzer, «Complex intelligent structures with data communication capabilities,» in *9th European Workshop on Structural Health Monitoring*, Manchester (UK), 2018, pp. 1–7.
- [219] C. Kexel, T. Maetz, M. Mälzer, and J. Moll, «Digital communication across orthotropic composite components using guided waves,» *Composite Structures*, vol. 209, pp. 481–489, 2019.
- [220] M. Mälzer, C. Kexel, T. Maetz, and J. Moll, «Combined inspection and data communication network for lamb-wave structural health monitoring,» *IEEE transactions on ultrasonics, ferroelectrics, and frequency control*, vol. 66, no. 10, pp. 1625–1633, 2019.
- [221] F. Ritter, S. Krempel, S. Tietze, A. Backer, A. Wolfschmitt, and K. S. Drese, «Data transmission by guided acoustic waves,» in *Sensors and Measuring Systems; 19th ITG/GMA-Symposium*, VDE, 2018, pp. 1–4.
- [222] R. Mijarez, P. Gaydecki, and M. Burdekin, «Continuous monitoring guided wave encoded sensor for oil rig flooded member detection,» *Insight-Non-Destructive Testing and Condition Monitoring*, vol. 47, no. 12, pp. 748–751, 2005.
- [223] S. Chakraborty, G. J. Saulnier, K. W. Wilt, E. Curt, H. A. Scarton, and R. B. Litman, «Low-power, low-rate ultrasonic communications system transmitting axially along a cylindrical pipe using transverse waves,» *IEEE Transactions on Ultrasonics, Ferroelectrics, and Frequency Control*, vol. 62, no. 10, pp. 1788–1796, Oct. 2015, ISSN: 0885-3010. DOI: [10.1109/TUFFC.2015.007078](https://doi.org/10.1109/TUFFC.2015.007078). [Online]. Available: <http://ieeexplore.ieee.org/lpdocs/epic03/wrapper.htm?arnumber=7296567> (visited on 11/25/2015).
- [224] S. Chakraborty, G. J. Saulnier, K. W. Wilt, R. B. Litman, and H. A. Scarton, «Low-rate ultrasonic communication axially along a cylindrical pipe,» in *2014 IEEE International Ultrasonics Symposium*, IEEE, 2014, pp. 547–551.
- [225] K. Manolakis, U. Krüger, K. Krüger, M. Gutierrez-Estevez, S. Mikulla, and V. Jungnickel, «Borehole communication with acoustic ofdm,» in *Int. OFDM-Workshop (InOWo'11)*, 2011.
- [226] J. D. Ashdown, L. Liu, G. J. Saulnier, and K. R. Wilt, «High-rate ultrasonic through-wall communications using mimo-ofdm,» *IEEE Transactions on Communications*, vol. 66, no. 8, pp. 3381–3393, 2018.
- [227] T. J. Lawry, K. R. Wilt, J. D. Ashdown, H. A. Scarton, and G. J. Saulnier, «A high-performance ultrasonic system for the simultaneous transmission of data and power through solid metal barriers,» *IEEE transactions on ultrasonics, ferroelectrics, and frequency control*, vol. 60, no. 1, pp. 194–203, 2012.
- [228] M. Bielinski, G. Sosa, K. Wanuga, R. Primerano, M. Kam, and K. R. Dandekar, «Bit-loaded papr reduction for high-data-rate through-metal control network applications,» *IEEE Transactions on Industrial Electronics*, vol. 61, no. 5, pp. 2362–2369, 2013.
- [229] B. Wang, J. Saniie, S. Bakhtiari, and A. Heifetz, «Ultrasonic communication in solid channels using ofdm,» in *2020 IEEE International Ultrasonics Symposium (IUS)*, IEEE, 2020, pp. 1–3.

- [230] R. Mijarez and P. Gaydecki, «Automatic guided wave ppm communication system for potential shm of flooding members in sub-sea oilrigs,» *Smart Materials and Structures*, vol. 22, no. 5, p. 055 031, 2013.
- [231] Y. Jin, Y. Ying, and D. Zhao, «Data communications using guided elastic waves by time reversal pulse position modulation: Experimental study,» *Sensors*, vol. 13, no. 7, pp. 8352–8376, 2013.
- [232] Y. Jin, D. Zhao, and Y. Ying, «Time reversal data communications on pipes using guided elastic waves: Part i. basic principles,» in *Health Monitoring of Structural and Biological Systems 2011*, SPIE, vol. 7984, 2011, pp. 92–103.
- [233] Y. Jin, Y. Ying, and D. Zhao, «Time reversal data communications on pipes using guided elastic waves: Part II. Experimental studies,» in *Health Monitoring of Structural and Biological Systems 2011*, International Society for Optics and Photonics, vol. 7984, SPIE, 2011, pp. 104 –114. DOI: [10.1117/12.880273](https://doi.org/10.1117/12.880273). [Online]. Available: <https://doi.org/10.1117/12.880273>.
- [234] A. Wu, S. He, Y. Ren, N. Wang, S. C. M. Ho, and G. Song, «Design of a new stress wave-based pulse position modulation (ppm) communication system with piezoceramic transducers,» *Sensors*, vol. 19, no. 3, p. 558, 2019.
- [235] G. Trane, R. Mijarez, R. Guevara, and D. Pascacio, «PPM-based System for Guided Waves Communication Through Corrosion Resistant Multi-wire Cables,» en, *Physics Procedia*, vol. 70, pp. 672–675, 2015, ISSN: 18753892. DOI: [10.1016/j.phpro.2015.08.076](https://doi.org/10.1016/j.phpro.2015.08.076). [Online]. Available: <http://linkinghub.elsevier.com/retrieve/pii/S1875389215008172> (visited on 11/25/2015).
- [236] G. Trane, R. Mijarez, and J. A. Pérez-Díaz, «Automatic guided waves data transmission system using an oil industry multiwire cable,» *Sensors*, vol. 20, no. 3, p. 868, 2020.
- [237] Y. Jin, Y. Ying, and D. Zhao, «Time reversal enabled elastic wave data communications using sensor arrays,» en, *The Journal of the Acoustical Society of America*, vol. 134, no. 5, pp. 3980–3980, Nov. 2013, ISSN: 0001-4966. DOI: [10.1121/1.4830502](https://doi.org/10.1121/1.4830502). [Online]. Available: <http://scitation.aip.org/content/asa/journal/jasa/134/5/10.1121/1.4830502> (visited on 11/24/2015).
- [238] X. Huang, J. Saniie, S. Bakhtiari, and A. Heifetz, «Software-defined ultrasonic communication system based on time-reversal signal processing,» in *2020 IEEE International Ultrasonics Symposium (IUS)*, IEEE, 2020, pp. 1–4.
- [239] L. De Marchi, A. Marzani, and J. Moll, «Ultrasonic Guided waves Communications in smart materials: The case of tapered waveguides,» in *8th European Workshop on Structural Health Monitoring*, 2016, pp. 1–8.
- [240] J. Moll, L. De Marchi, and A. Marzani, «Transducer-to-Transducer Communication in Guided Wave Based Structural Health Monitoring,» in *19th World Conference on Non-Destructive Testing*, Munich, Germany, 2016, pp. 1–8.
- [241] L. De Marchi, A. Marzani, J. Moll, P. Kudela, M. Radzieński, and W. Ostachowicz, «A pulse coding and decoding strategy to perform lamb wave inspections using simultaneously multiple actuators,» *Mechanical Systems and Signal Processing*, vol. 91, pp. 111–121, 2017.

- [242] R. Primerano, M. Kam, and K. Dandekar, «High bit rate ultrasonic communication through metal channels,» in *2009 43rd Annual Conference on Information Sciences and Systems*, IEEE, 2009, pp. 902–906.
- [243] T. Hosman, M. Yearly, and J. K. Antonio, «Design and characterization of an mfsk-based transmitter/receiver for ultrasonic communication through metallic structures,» *IEEE Transactions on Instrumentation and Measurement*, vol. 60, no. 12, pp. 3767–3774, 2011.
- [244] H. Sakuma, K. Nakamura, and S. Ueha, «Two-way communication over gas pipeline using multicarrier modulated sound waves with cyclic frequency shifting,» *Acoustical science and technology*, vol. 27, no. 4, pp. 225–232, 2006.
- [245] R. Bahouth, F. Benmeddour, E. Moulin, and J. Assaad, «Transmission of digital data using guided ultrasonic waves in solid plates,» in *Proceedings of Meetings on Acoustics ICU*, Acoustical Society of America, vol. 38, 2019, p. 055 008.
- [246] —, «Lamb wave wireless communication in healthy plates using coherent demodulation,» *International Journal of Electronics and Communication Engineering*, vol. 15, no. 7, pp. 436–440, 2021.
- [247] B. Wang, J. Saniie, S. Bakhtiari, and A. Heifetz, «Ultrasonic communication systems for data transmission,» in *2019 IEEE International Conference on Electro Information Technology (EIT)*, IEEE, 2019, pp. 1–4.
- [248] R. Bahouth, F. Benmeddour, E. Moulin, and J. Assaad, «Wireless communication using ultrasonic guided waves in healthy and defected plates,» 2020.
- [249] D. J. Graham, J. A. Neasham, and B. S. Sharif, «Investigation of methods for data communication and power delivery through metals,» *IEEE Transactions on industrial electronics*, vol. 58, no. 10, pp. 4972–4980, 2011.
- [250] J. Moll, C. Kexel, H. Milanchian, M. B. Bhavsar, and J. H. Barker, «Ultrasound bone fracture sensing and data communication: Experimental results in a pig limb sample,» *Ultrasound in medicine & biology*, vol. 45, no. 2, pp. 605–611, 2019.
- [251] J. Saniie, B. Wang, and X. Huang, «Information transmission through solids using ultrasound,» in *2018 IEEE International Ultrasonics Symposium (IUS)*, IEEE, 2018, pp. 1–10.
- [252] G Trane, R Mijarez, R Guevara, and A Baltazar, «Guided wave sensor for simple digital communication through an oil industry multi-wire cable,» *Insight-Non-Destructive Testing and Condition Monitoring*, vol. 60, no. 4, pp. 206–211, 2018.
- [253] J. Moll, M. Mälzer, L. De Marchi, N. Testoni, and A. Marzani, «Experimental Analysis of Digital Data Communication in Intelligent Structures Using Lamb Waves,» in *11th International Workshop on Structural Health Monitoring (Stanford, USA)*, 2017, pp. 1654–1661.
- [254] L. De Marchi, N. Testoni, and A. Marzani, «A novel shaped piezoelectric sensor for impact localization in plate structures,» in *2015 XVIII AISEM Annual Conference*, IEEE, 2015, pp. 1–4.
- [255] C. Kexel, M. Mälzer, and J. Moll, «Guided wave based acoustic communications in structural health monitoring systems in the presence of structural defects,» in *2018 IEEE International Symposium on Circuits and Systems (ISCAS)*, IEEE, 2018, pp. 1–4.



- [256] L. De Marchi, A. Marzani, and J. Moll, «Ultrasonic guided waves communications in smart materials: The case of tapered waveguides,» in *Structural Health Monitoring*, 8th European Workshop, 2016, pp. 1–8.
- [257] U. Madhow and M. L. Honig, «Mmse interference suppression for direct-sequence spread-spectrum cdma,» *IEEE transactions on communications*, vol. 42, no. 12, pp. 3178–3188, 1994.
- [258] R. C. Dixon, *Spread spectrum systems: with commercial applications*. Wiley New York, 1994, vol. 994.
- [259] D. Torrieri, *Principles of spread-spectrum communication systems*. Springer, 2005, vol. 1.
- [260] R. Pickholtz, D. Schilling, and L. Milstein, «Theory of spread-spectrum communications-a tutorial,» *IEEE transactions on Communications*, vol. 30, no. 5, pp. 855–884, 1982.
- [261] T. Hong and F. De León, «Lissajous curve methods for the identification of nonlinear circuits: Calculation of a physical consistent reactive power,» *IEEE Transactions on Circuits and Systems I: Regular Papers*, vol. 62, no. 12, pp. 2874–2885, 2015.
- [262] I. Bartoli, A. Marzani, F. L. di Scalea, and E. Viola, «Modeling wave propagation in damped waveguides of arbitrary cross-section,» *Journal of Sound and Vibration*, vol. 295, no. 3-5, pp. 685–707, 2006.
- [263] L. De Marchi, A. Marzani, N. Speciale, and E. Viola, «A passive monitoring technique based on dispersion compensation to locate impacts in plate-like structures,» *Smart Materials and Structures*, vol. 20, no. 3, p. 035 021, 2011.
- [264] C.-b. Xu, Z.-b. Yang, X.-f. Chen, S.-h. Tian, and Y. Xie, «A guided wave dispersion compensation method based on compressed sensing,» *Mechanical Systems and Signal Processing*, vol. 103, pp. 89–104, 2018.
- [265] R. Gangadharan, C. Murthy, S. Gopalakrishnan, and M. Bhat, «Time reversal technique for health monitoring of metallic structure using lamb waves,» *Ultrasonics*, vol. 49, no. 8, pp. 696–705, 2009.
- [266] Y. Jin, Y. Ying, and D. Zhao, «Time reversal enabled elastic wave data communications using sensor arrays,» in *Proceedings of Meetings on Acoustics 166ASA*, ASA, vol. 20, 2013, p. 045 001.
- [267] Q. Ji, Q. Kong, and G. Song, «Study on energy focusing synthesis on pipe using time reversal technique,» in *Proceedings of the 11th IEEE International Conference on Networking, Sensing and Control*, IEEE, 2014, pp. 625–630.
- [268] Y. Jin, Y. Ying, and D. Zhao, «Data communications using guided elastic waves by time reversal pulse position modulation: Experimental study,» *Sensors*, vol. 13, no. 7, pp. 8352–8376, 2013.
- [269] G. Trane, R. Mijarez, and J. A. Pérez-Díaz, «Automatic guided waves data transmission system using an oil industry multiwire cable,» *Sensors*, vol. 20, no. 3, p. 868, 2020.
- [270] *Octal three-level/quad five-level high-voltage 2a digital pulsers with t/r switch*, Maxim Integrated Products, Inc., 2013.

- [271] *Tx7316 three-level, 16-channel or five-level, 8-channel transmitter with 2.4-a pulser, t/r switch, and integrated transmit beamformer*, Texas Instruments, 2019.
- [272] E. Baravelli, M. Senesi, M. Ruzzene, and L. De Marchi, «Fabrication and characterization of a wavenumber-spiral frequency-steerable acoustic transducer for source localization in plate structures,» *IEEE Transactions on Instrumentation and Measurement*, vol. 62, no. 8, pp. 2197–2204, 2013.
- [273] M. Li, «On performance of optical wireless communication with spatial multiplexing towards 5-g,» *IEEE Access*, vol. 6, pp. 28 108–28 113, 2018.
- [274] L. Hanzo, W. Webb, and T. Keller, *Single-and multi-carrier quadrature amplitude modulation: principles and applications for personal communications, WATM and broadcasting: 2nd*. IEEE Press-John Wiley, 2000.
- [275] M. Mälzer, C. Kexel, T. Maetz, and J. Moll, «Combined inspection and data communication network for lamb-wave structural health monitoring,» *IEEE Transactions on Ultrasonics, Ferroelectrics, and Frequency Control*, vol. 66, no. 10, pp. 1625–1633, 2019. DOI: [10.1109/TUFFC.2019.2925864](https://doi.org/10.1109/TUFFC.2019.2925864).
- [276] Y. Sun, Y. Xu, W. Li, Q. Li, X. Ding, and W. Huang, «A lamb waves based ultrasonic system for the simultaneous data communication, defect inspection, and power transmission,» *IEEE Transactions on Ultrasonics, Ferroelectrics, and Frequency Control*, pp. 1–1, 2021. DOI: [10.1109/TUFFC.2021.3087603](https://doi.org/10.1109/TUFFC.2021.3087603).
- [277] T. K. Lajos L. Hanzo Soon Xin Ng and W. Webb, *Quadrature Amplitude Modulation: From Basics to Adaptive Trellis-Coded, Turbo-Equalised and Space-Time Coded OFDM, CDMA and MC-CDMA Systems*. Wiley-IEEE Press, 2004, ISBN: 0470094680,9780470094686.
- [278] S. Gholizadeh, Z. Leman, and B. H. T. Baharudin, «A review of the application of acoustic emission technique in engineering,» *Structural Engineering and Mechanics*, vol. 54, no. 6, pp. 1075–1095, 2015.
- [279] A. Berkovits and D. Fang, «Study of fatigue crack characteristics by acoustic emission,» *Engineering Fracture Mechanics*, vol. 51, no. 3, pp. 401–416, 1995.
- [280] S. Chesné and A. Deraemaeker, «Damage localization using transmissibility functions: A critical review,» *Mechanical systems and signal processing*, vol. 38, no. 2, pp. 569–584, 2013.
- [281] P. L. Ainsleigh, «Acoustic echo detection and arrival-time estimation using spectral tail energy,» *The Journal of the Acoustical Society of America*, vol. 110, no. 2, pp. 967–972, 2001.
- [282] H. Vallen, «Ae testing fundamentals, equipment, applications,» *Journal of Nondestructive Testing(Germany)*, vol. 7, no. 9, pp. 1–30, 2002.
- [283] S. F. Wirtz and D. Söfker, «Improved signal processing of acoustic emission for structural health monitoring using a data-driven approach,» in *9th European Workshop on Structural Health Monitoring, Manchester, UK*, 2018.
- [284] J. Sikorska and D. Mba, «Challenges and obstacles in the application of acoustic emission to process machinery,» *Proceedings of the Institution of Mechanical Engineers, Part E: Journal of Process Mechanical Engineering*, vol. 222, no. 1, pp. 1–19, 2008.

- [285] S. Ramesh, *The T<sub>E</sub>X Applied Welding Engineering. Processes, Codes, and Standards*. Elsevier, 2012, pp. 307–319.
- [286] V. M. Karbhari *et al.*, *Non-destructive evaluation (NDE) of polymer matrix composites*. Elsevier, 2013.
- [287] S. Adrián-Martínez, M. Bou-Cabo, I. Felis, C. D. Llorens, J. A. Martínez-Mora, M. Saldaña, and M. Ardid, «Acoustic signal detection through the cross-correlation method in experiments with different signal to noise ratio and reverberation conditions,» in *International conference on Ad-Hoc Networks and wireless*, Springer, 2014, pp. 66–79.
- [288] X. Li, X. Shang, A. Morales-Esteban, and Z. Wang, «Identifying p phase arrival of weak events: The akaike information criterion picking application based on the empirical mode decomposition,» *Computers & Geosciences*, vol. 100, pp. 57–66, 2017.
- [289] M. R. Pearson, M. Eaton, C. Featherston, R. Pullin, and K. Holford, «Improved acoustic emission source location during fatigue and impact events in metallic and composite structures,» *Structural Health Monitoring*, vol. 16, no. 4, pp. 382–399, 2017.
- [290] Z. E. Ross, C. Rollins, E. S. Cochran, E. Hauksson, J.-P. Avouac, and Y. Ben-Zion, «Aftershocks driven by afterslip and fluid pressure sweeping through a fault-fracture mesh,» *Geophysical Research Letters*, vol. 44, no. 16, pp. 8260–8267, 2017.
- [291] Y. Chen, «Automatic microseismic event picking via unsupervised machine learning,» *Geophysical Journal International*, vol. 222, no. 3, pp. 1750–1764, 2020.
- [292] Z. E. Ross, M.-A. Meier, and E. Hauksson, «P wave arrival picking and first-motion polarity determination with deep learning,» *Journal of Geophysical Research: Solid Earth*, vol. 123, no. 6, pp. 5120–5129, 2018.
- [293] W. Zhu and G. C. Beroza, «Phasenet: A deep-neural-network-based seismic arrival-time picking method,» *Geophysical Journal International*, vol. 216, no. 1, pp. 261–273, 2019.
- [294] O. Rojas, B. Otero, L. Alvarado, S. Mus, and R. Tous, «Artificial neural networks as emerging tools for earthquake detection,» *Computación y Sistemas*, vol. 23, no. 2, pp. 335–350, 2019.
- [295] Z. Zhang, «Improved adam optimizer for deep neural networks,» in *2018 IEEE/ACM 26th International Symposium on Quality of Service (IWQoS)*, IEEE, 2018, pp. 1–2.
- [296] J. Lin, Y. Rao, J. Lu, and J. Zhou, «Runtime neural pruning,» in *Proceedings of the 31st International Conference on Neural Information Processing Systems*, 2017, pp. 2178–2188.
- [297] O. M. Saad and Y. Chen, «Capsphase: Capsule neural network for seismic phase classification and picking,» *IEEE Transactions on Geoscience and Remote Sensing*, 2021.
- [298] S. Sabour, N. Frosst, and G. E. Hinton, «Dynamic routing between capsules,» *arXiv preprint arXiv:1710.09829*, 2017.
- [299] B. Mandal, S. Dubey, S. Ghosh, R. Sarkhel, and N. Das, «Handwritten indic character recognition using capsule networks,» in *2018 IEEE Applied Signal Processing Conference (ASPCON)*, IEEE, 2018, pp. 304–308.

- [300] V. Barat, Y. Borodin, and A. Kuzmin, «Intelligent ae signal filtering methods,» *Journal of Acoustic Emission*, vol. 28, pp. 109–119, Jan. 2010.
- [301] Y. Jiang and F Xu, «Research on source location from acoustic emission tomography,» in *30th European Conference on Acoustic Emission Testing & 7th International Conference on Acoustic Emission, Granada, Spain, 2012*.
- [302] B. Li, *Uncertainty quantification in vibration-based structural health monitoring using Bayesian statistics*. University of California, Berkeley, 2016.
- [303] X. Liu and S. Rao, «Vibration analysis in the presence of uncertainties using universal grey system theory,» *Journal of Vibration and Acoustics*, vol. 140, no. 3, 2018.
- [304] D. Straub, E. Chatzi, E. Bismut, W. Courage, M. Döhler, M. H. Faber, J. Köhler, G. Lombaert, P. Omenzetter, M. Pozzi, *et al.*, «Value of information: A roadmap to quantifying the benefit of structural health monitoring,» in *ICOSSAR-12th international conference on structural safety & reliability, 2017*.
- [305] N. Testoni, L. De Marchi, and A. Marzani, «A stamp size, 40ma, 5 grams sensor node for impact detection and location,» in *European Workshop on SHM, 2016*.

## DECLARATION

---

I declare that this thesis was composed by myself, that the work contained herein is my own except where explicitly stated otherwise in the text, and that this work has not been submitted for any other degree or professional qualification except as specified.

*University of Bologna, February 2022*

Federica Zonzini

